

RELATIVE PERMEABILITY-SATURATION-CAPILLARY HEAD
RELATIONSHIPS FOR AIR SPARGING IN SOILS

by

Wilson S. Clayton

ProQuest Number: 10796658

All rights reserved

INFORMATION TO ALL USERS

The quality of this reproduction is dependent upon the quality of the copy submitted.

In the unlikely event that the author did not send a complete manuscript and there are missing pages, these will be noted. Also, if material had to be removed, a note will indicate the deletion.



ProQuest 10796658

Published by ProQuest LLC (2019). Copyright of the Dissertation is held by the Author.

All rights reserved.

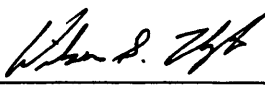
This work is protected against unauthorized copying under Title 17, United States Code
Microform Edition © ProQuest LLC.

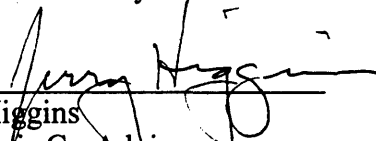
ProQuest LLC.
789 East Eisenhower Parkway
P.O. Box 1346
Ann Arbor, MI 48106 – 1346

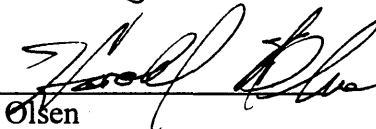
A thesis submitted to the Faculty and the Board of Trustees of the Colorado School of Mines in partial fulfillment of the requirements for the degree of Doctor of Philosophy (Geological Engineering).

Golden, Colorado

Date: May 30, 1996


Signed: 
Wilson S. Clayton

Approved: 
Dr. Jerry Higgins
Thesis Co-Advisor

Approved: 
Dr. Harold Olsen
Thesis Co-Advisor

Golden, Colorado

Date: 5/31/96


Dr. Roger Slatt
Professor and Head,
Department of Geology and Geological Engineering

ABSTRACT

The relative permeability-saturation-capillary head (k_r - S - h_c) relationships of soils are the soil properties which control air and water flow during *in-situ* air sparging. An unsteady state displacement experiment was developed to measure k_r - S - h_c relationships during displacement of water by air in soil core samples. The displacement experiments closely simulated the air flow rates, injection pressures, and gradients associated with *in-situ* air sparging in order to reflect the degree of pore-scale air fingering associated with the *in-situ* process and its impact on k_r - S - h_c .

Air sparging displacement experiments were conducted using five soil specimens of various texture and geologic origin. Few soils tested followed $k_{ra}(S)$ and $h_c(S)$ relationships derived from moisture retention data and functional relationships. However, water relative permeability (k_{rw}) generally followed functional relationships for $k_{rw}(S)$. For most soils tested, air relative permeability (k_{ra}) and h_c were found to be multi-valued functions of saturation. For these soils, $k_{ra}(S)$ and $h_c(S)$ frequently were up to an order of magnitude smaller than values derived from moisture retention data and common functional relationships for k_r - S - h_c . Also, $k_{ra}(S)$ sometimes increased by up to an order of magnitude at steady saturation values to approach $k_{ra}(S)$ functional relationships. In many instances, $k_{ra}(h_c)$ followed common functional relationships, while $k_{ra}(S)$ and $h_c(S)$ deviated from common functional relationships. Faster displacements resulted in lower k_{ra} and larger deviations from $k_{ra}(S)$ functional relationships.

The unique air flow behaviors observed for air sparging conditions are inferred to reflect the development and subsequent breakthrough of pore-scale dead-end air fingers, which initially do not conduct air flow. This hypothesis was tested by evaluating a hypothetical backbone air saturation (S_{ab}), which conducts air flow. Both k_{ra} and h_c were found to remain in equilibrium with hypothetical, calculated values of S_{ab} for many experiments where $k_{ra}(S)$ and $h_c(S)$ were very low. This result implies that dead-end air fingers existed, which did not contribute to k_{ra} or h_c . These results represent the first demonstration of the effects of pore-scale fingering on k_r - S - h_c relationships. The extremely low magnitude of air permeability and capillary head with respect to total fluid saturation for fingered flow during air sparging is likely to have a significant impact on the nature of field-scale air sparging and related mathematical modeling.

TABLE OF CONTENTS

	Page
Section 1 INTRODUCTION	1
<u>1.1 Background</u>	1
<u>1.2 Statement of Problem</u>	2
<u>1.3 Objectives</u>	3
<u>1.4 Scope</u>	3
Section 2 LITERATURE REVIEW	5
<u>2.1 Air Sparging Conceptual Models</u>	5
<u>2.2 Air and Water Flow in Partially Saturated Porous Media</u>	7
<u>2.3 Gas Flow in Porous Media</u>	18
<u>2.4 Displacement Phenomena of Immiscible Fluids</u>	19
<u>2.4.1 Pore-Scale Fingering</u>	20
<u>2.4.2 Macroscopic Displacement Phenomena</u>	25
<u>2.5 Laboratory Measurement of Two-Phase Flow Parameters</u>	27
<u>2.5.1 Steady State Techniques</u>	28
<u>2.5.2 Unsteady State Techniques</u>	30

Section 3 EXPERIMENTAL PROGRAM	33
<u>3.1 Experimental Strategy</u>	33
<u>3.2 Design of Air Injection Displacement Experiment</u>	36
<u>3.2.1 Air Injection Displacement Experiment Parameters</u>	36
<u>3.2.2 Sample Boundary Conditions</u>	38
<u>3.2.3 Air Injection System Components</u>	41
<u>3.2.4 System Measurements and Flow Parameter Calculations</u>	46
Section 4 METHODS	50
<u>4.1 Soil Grain Size Distribution</u>	50
<u>4.2 Soil Moisture Retention</u>	50
<u>4.3 Air Injection System Calibration and Error Analysis</u>	51
<u>4.3.1 Calibration of System Measurements</u>	51
<u>4.3.2 Propagation of Measurement Errors</u>	55
<u>4.3.3 Evaluation of Error Related to Non-Uniform Fluid Saturations</u> ...	58
<u>4.4 Relative Permeability and Air Injection Testing</u>	60
<u>4.5 Gas-Phase Tracer Evaluation of Pore Scale Fingering</u>	61
Section 5 RESULTS	65
<u>5.1 Soil Samples Tested</u>	65
<u>5.2 Physical Characterization of Test Specimens</u>	66

<u>5.3 Moisture Retention Data</u>	67
<u>5.4 Intrinsic Permeability Data</u>	75
<u>5.5 Air Injection Displacement Experiment Results</u>	78
<u>5.5.1 Temporal Two-Phase Flow Data</u>	79
<u>5.5.2 Unsteady State Capillary Head-Saturation Data</u>	96
<u>5.5.3 Air Relative Permeability Data</u>	100
<u>5.5.4 Water Relative Permeability Data</u>	127
<u>5.6 Gas-Phase Tracer Data</u>	131
<u>5.7 Similitude of Air Injection Displacement Experiments</u>	139
Section 6 DISCUSSION	142
<u>6.1 Possible Causes of Unique Flow Behaviors</u>	143
<u>6.1.1 Errors Related to Fluid Non-Uniformity</u>	145
<u>6.1.2 Transient Non-Equilibrium Conditions</u>	147
<u>6.1.3 Development of Pore-Scale Dead-End Air Fingers</u>	147
<u>6.2 Prediction of Fingered Flow Behaviors</u>	156
<u>6.3 Similitude of Air Injection Simulations</u>	157
<u>6.4 Gas-Phase Tracer Experiments</u>	161
Section 7 CONCLUSIONS	162
Section 8 NEEDS FOR ADDITIONAL RESEARCH	164

REFERENCES 166

LIST OF FIGURES

Figure 1. The capillary rise equation	8
Figure 2. Capillary head-saturation relationships	10
Figure 3. Relative permeability-saturation relationships	11
Figure 4. Relative permeability-capillary head relationships	12
Figure 5. Fingers of air displacing liquid epoxy	21
Figure 6. Phase-diagram for immiscible displacement	24
Figure 7. The experimental approach	34
Figure 8. Pressure head diagram depicting the displacement experiment design	39
Figure 9. The air injection displacement experiment apparatus	42
Figure 10. Soil sample test cell.	43
Figure 11. The pore fluid measurement and control system	45
Figure 12. Pressure transducer calibration data	52
Figure 13. Frequency histogram of residuals of V_{wd}	54
Figure 14. Frequency histogram of percent error of Q_a	54
Figure 15. The mathematical model for error analysis of non-uniform fluid saturation	59
Figure 16. The gas-phase tracer system	63
Figure 17. Calibration of percent recovery for tracer experiments	64
Figure 18. Soil grain size distribution curves	68
Figure 19. Soil moisture characteristic curve. Sample FLO.	69
Figure 20. Soil moisture characteristic curve. Sample COR.	70

Figure 21. Soil moisture characteristic curve. Sample COL.	71
Figure 22. Soil moisture characteristic curve. Sample CSM.	72
Figure 23. Soil moisture characteristic curve. Sample CHV	73
Figure 24. Typical data from a dry air conductivity test	76
Figure 25. Typical data from a saturated hydraulic conductivity test	76
Figure 26. Temporal fluid pressure head data. Experiment FLO_2L.	81
Figure 27. Temporal saturation and capillary head data. Experiment FLO_2L.	81
Figure 28. Temporal air flow data. Experiment FLO_2L.	83
Figure 29. Temporal water flow data. Experiment FLO_2L.	83
Figure 30. Temporal fluid pressure head data. Experiment COR_3E.	84
Figure 31. Temporal saturation and capillary head data. Experiment COR_3E.	84
Figure 32. Temporal air flow data. Experiment COR_3E.	86
Figure 33. Temporal water flow data. Experiment COR_3E.	86
Figure 34. Temporal fluid pressure head data. Experiment COR_3C.	87
Figure 35. Temporal saturation and capillary head data. Experiment COR_3C.	87
Figure 36. Temporal air flow data. Experiment COR_3C.	88
Figure 37. Temporal water flow data. Experiment COR_3C.	88
Figure 38. Temporal fluid pressure head data. Experiment COL_2G.	89
Figure 39. Temporal saturation and capillary head data. Experiment COL_2G.	89
Figure 40. Temporal air flow data. Experiment COL_2G.	91
Figure 41. Temporal water flow data. Experiment COL_2G.	91
Figure 42. Temporal fluid pressure head data. Experiment COL_1H.	92
Figure 43. Temporal saturation and capillary head data. Experiment COL_1H.	92
Figure 44. Temporal air flow data. Experiment COL_1H.	93
Figure 45. Temporal water flow data. Experiment COL_1H.	93
Figure 46. Temporal fluid pressure head data. Experiment COL_2C.	94

Figure 47. Temporal saturation and capillary head data. Experiment COL_2C.	94
Figure 48. Temporal air flow data. Experiment COL_2C.	95
Figure 49. Temporal water flow data. Experiment COL_2C.	95
Figure 50A. Pore fluid heads vs. water saturation. Experiment FLO_2P	97
Figure 50B. Capillary head-saturation data from experiment FLO_2P	97
Figure 51A. Pore fluid heads vs. water saturation. Experiment COR_3E.	98
Figure 51B. Capillary head-saturation data from experiment COR_3E.	98
Figure 52A. Pore fluid heads vs. water saturation. Experiment COR_3A.	99
Figure 52B. Capillary head-saturation data from experiment COR_3A	99
Figure 53A. Pore fluid heads vs. water saturation. Experiment COL_2C.	101
Figure 53B. Capillary head-saturation data from experiment COL_2C.	101
Figure 54A. Pore fluid heads vs. water saturation. Experiment COL_1H.	102
Figure 54B. Capillary head-saturation data from experiment COL_1H	102
Figure 55A. Pore fluid heads vs. water saturation. Experiment COL_2E.	103
Figure 55B. Capillary head-saturation data from experiment COL_2E	103
Figure 56A. Pore fluid heads vs. water saturation. Experiment CSM_1E	104
Figure 56B. Capillary head-saturation data from experiment CSM_1E	104
Figure 57A. Pore fluid heads vs. water saturation. Experiment CHV_1H.	105
Figure 57B. Capillary head-saturation data from experiment CHV_1H.	105
Figure 58. Air relative permeability-saturation data. Experiment FLO_2I.	107
Figure 59. Air relative permeability-capillary head data. Experiment FLO_2I.	107
Figure 60. Air relative permeability-saturation data. Experiment FLO_2L.	109
Figure 61. Air relative permeability-capillary head data. Experiment FLO_2L.	109
Figure 62. Air relative permeability-saturation data. Experiment FLO_2P.	110
Figure 63. Air relative permeability-capillary head data. Experiment FLO_2P.	110
Figure 64. Air relative permeability-saturation data. Experiment FLO_1K.	111

Figure 65. Air relative permeability-capillary head data. Experiment FLO_1K.	111
Figure 66. Air relative permeability-saturation data. Experiment COR_3A.	113
Figure 67. Air relative permeability-capillary head data. Experiment COR_3A.	113
Figure 68. Air relative permeability-saturation data. Experiment COR_3C.	114
Figure 69. Air relative permeability-capillary head data. Experiment COR_3C.	114
Figure 70. Air relative permeability-saturation data. Experiment COR_3E.	116
Figure 71. Air relative permeability-capillary head data. Experiment COR_3E.	116
Figure 72. Air relative permeability-saturation data. Experiment COL_2C.	117
Figure 73. Air relative permeability-capillary head data. Experiment COL_2C.	117
Figure 74. Air relative permeability-saturation data. Experiment COL_2E.	119
Figure 75. Air relative permeability-capillary head data. Experiment COL_2E.	119
Figure 76. Air relative permeability-saturation data. Experiment COL_2G.	120
Figure 77. Air relative permeability-capillary head data. Experiment COL_2G.	120
Figure 78. Air relative permeability-saturation data. Experiment COL_1H.	121
Figure 79. Air relative permeability-capillary head data. Experiment COL_1H.	121
Figure 80. Air relative permeability-saturation data. Experiment CSM_1E.	123
Figure 81. Air relative permeability-capillary head data. Experiment CSM_1E.	123
Figure 82. Air relative permeability-saturation data. Experiment CSM_1H.	124
Figure 83. Air relative permeability-capillary head data. Experiment CSM_1H.	124
Figure 84. Air relative permeability-saturation data. Experiment CHV_1H.	125
Figure 85. Air relative permeability-capillary head data. Experiment CHV_1H.	125
Figure 86. Air relative permeability-saturation data. Experiment CHV_1K.	126
Figure 87. Air relative permeability-capillary head data. Experiment CHV_1K.	126
Figure 88. Water relative permeability-saturation data. Experiment FLO_2P.	128
Figure 89. Water relative permeability-capillary head data. Experiment FLO_2P.	128
Figure 90. Water relative permeability-saturation data. Experiment COR_3B.	129

Figure 91. Water relative permeability-capillary head data. Experiment COR_3B. . .	129
Figure 92. Water relative permeability-saturation data. Experiment COR_3E.	130
Figure 93. Water relative permeability-capillary head data. Experiment COR_3E. . . .	130
Figure 94. Water relative permeability-saturation data. Experiment COL_1J.	132
Figure 95. Water relative permeability-capillary head data. Experiment COL_1J. . . .	132
Figure 96. Water relative permeability-saturation data. Experiment CSM_1H.	133
Figure 97. Water relative permeability-capillary head data. Experiment CSM_1H. . . .	133
Figure 98. Water relative permeability-saturation data. Experiment CHV_1F.	134
Figure 99. Water relative permeability-capillary head data. Experiment CHV_1F. . . .	134
Figure 100. Gas-phase tracer data. Experiment FLO_2P.	135
Figure 101. Gas-phase tracer data. Experiment FLO_2I.	135
Figure 102. Gas-phase tracer data. Experiment CSM_1E.	137
Figure 103. Gas-phase tracer data. Experiment CSM_1H.	137
Figure 104. Gas-phase tracer data. Experiment COL_2J.	138
Figure 105. Gas-phase tracer data. Experiment COR_4F.	138
Figure 106. Gas-phase tracer data. Experiment COR_4H.	140
Figure 107. Gas-phase tracer data. Experiment COR_4J.	140
Figure 108. Error analysis of non-uniform fluid saturation. Experiment FLO_2P. . . .	145
Figure 109. Error analysis of non-uniform fluid saturation. Experiment COR_3E. . . .	145
Figure 110. Error analysis of non-uniform fluid saturation. Experiment CHV_1H. . . .	146
Figure 111. Error analysis of non-uniform fluid saturation. Experiment COL_1H. . . .	146
Figure 112. Capillary head-saturation data. Experiment COL_2C.	150
Figure 113. Transformed capillary head data. Experiment COL_2C.	150
Figure 114. Capillary head-saturation data. Experiment COL_1H.	151
Figure 115. Transformed capillary head data. Experiment COL_1H.	151
Figure 116. Capillary head-saturation data. Experiment CHV_1H.	153

Figure 117. Transformed capillary head data. Experiment CHV_1H.	153
Figure 118. Capillary head-saturation data. Experiment COR_3E.	154
Figure 119. Transformed capillary head data. ExperimentCOR_3E.	154
Figure 120. Capillary head-saturation data. Experiment FLO_2P.	155
Figure 121. Transformed capillary head data. Experiment FLO_2P.	155
Figure 122. Phase diagram for the measured displacement data.	160

LIST OF TABLES

Table 1. Comparison of <i>in-situ</i> sparging conditions and the experimental system.	37
Table 2. Statistical summary of residuals of measured pressure heads	52
Table 3. Statistical description of residuals of V_{wd} (cm) and percent error of Q_d	53
Table 4. Summary of procedures used to evaluate the propagation of errors.	55
Table 5. Propagation of errors in permeability measurements	57
Table 6. Summary of physical soil characteristics.	68
Table 7. Summary of moisture retention characteristics	74
Table 8. Summary of dry air conductivities measured prior to air injection testing	77
Table 9. Summary of saturated hydraulic conductivities	77
Table 10. Intrinsic permeability data	78
Table 11. Experiment results which are described herein	80
Table 12. Summary of calculated values of Re and C	141
Table 13. Soil characteristics which may influence fingering	158

LIST OF SYMBOLS

α = inverse of air entry pressure head

γ = interfacial tension

ρ_d = dry bulk density

Δt = variable time interval

ΔV_{wd} = change in fluid volume in tube T-2

Θ_i = interfacial contact angle

λ = pore size distribution index

μ_i = viscosity of fluid i

ρ_i = density of fluid i

ϕ = porosity

B = ratio of buoyant forces to viscous forces

C = capillary number

C_c = coefficient of gradation

C_u = uniformity coefficient

D = characteristic dimension

D_{50} = mean grain size

f = mass flux

g = acceleration of gravity

g_x = acceleration of gravity in x direction

h_a = air pressure head (water equivalent)

h_c = capillary head
 h_{cb} = base Capillary Head
 h_{ct} = top Capillary Head
 h_o = characteristic capillary head (typically air entry pressure head)
 h_i = constant hydraulic head
 h_2 = pressure head measurement in tube T-2
 h_w = water pressure head
 I_a = air gradient, expressed in terms of cm water head per cm length
 I_w = hydraulic Gradient
 k = absolute permeability of medium
 $K_{a,dry}$ = dry air conductivity
 K_a = air conductivity
 k_{ra} = air relative permeability
 k_{rai} = air relative permeability of model increment i
 k_{ri} = relative permeability of fluid i
 k_{rw} = water relative permeability
 K_{sat} = saturated hydraulic conductivity
 K_w = hydraulic conductivity
 L = sample length
 L_i = length of model increment
 m = pore size distribution index
 M = viscosity ratio
 n = pore size distribution index
 n_i = number of model increments
 P_a = air pressure
 P_{et} = dynamic air entry pressure head of top porous boundary, expressed in cm water

q_a = darcy air velocity
 Q_a = air flow rate
 q_{ix} = volumetric flux of fluid i in x direction
 Q_w = water flow rate
 R_p = pore radius
 R = gas constant
 R_e = Reynolds number
 S = fluid saturation
 S_a = air Saturation
 S_{ab} = backbone air saturation
 S_e = effective saturation
 S_{ea} = effective air saturation
 S_{eab} = effective backbone air saturation
 S_{eaf} = effective free air saturation
 S_{eat} = effective trapped air saturation
 S_m = maximum water saturation
 S_r = residual water saturation
 S_w = water saturation
 T = absolute temperature
 U_{ab} = base pore air pressure head, expressed in cm water
 U_{at} = top pore air pressure head, expressed in cm water
 U_{wb} = base pore water pressure head, expressed in cm water
 U_{wt} = top pore water pressure head, expressed in cm water
 v = fluid velocity
 V_v = void volume of sample
 V_{wd} = volume of water displaced

ACKNOWLEDGMENTS

There were numerous individuals who supported the efforts involved in this thesis. First and foremost is my wife Karen who paid tuition and all the other bills for 5 years, while I worked toward the Ph.D. degree. However, her financial contributions were small compared to her overall level of hard work and support. While this research was under way, Karen worked long hours including extended overseas assignments, started a family, and allowed me to take advantage of the flexible schedule of a student. Without Karen's support, this thesis would never have been possible.

Groundwater Technology, Inc. funded the development and construction of the experimental apparatus. Thanks to Dr. Richard Brown, Vice President of Technology, and the corporate development committee for viewing this project as having value for the company.

Several individuals at the Colorado School of Mines provided valuable guidance and insight as the research proceeded. These especially include Dr. Helen Dawson, Dr. Jerry Higgins, Dr. Karl Nelson, and Dr. Hal Olsen who all helped solve numerous experimental problems along the way. John Jeseck provided much needed assistance machining the test cell as various prototype designs were developed.

Section 1

INTRODUCTION

1.1 Background

Subsurface remediation of organic chemical spills in groundwater and soil has become a principal activity of waste management. One of the most recent and significant advances in remediation technology has been the use of in-situ air sparging for aquifer remediation. Air sparging involves air injection below the water table in an unconfined aquifer. The induced air flow causes stripping of volatile compounds, provides additional oxygen for biodegradation, and allows the addition of gaseous phase chemicals for chemical or physical in situ treatment.

The nature of air flow is an important aspect of the effectiveness of sparging. The air flow properties of the soil determine the region over which air flow occurs, and therefore determine the requirements for injection well spacing and depth. Also, since injected air does not contact the entire soil matrix, the rate of cleanup by sparging is generally limited by diffusion through groundwater [*Ahlfeld et al.*, 1994, *Clayton and Nelson*, 1995, *Rutherford and Johnson*, 1995]. The air saturation (percentage of soil pore space which is air filled) and geometry of the air phase are important variables which control the rate of mass transfer during sparging [*Clayton and Nelson*, 1995, *Mohr*, 1995].

Air sparging has primarily been applied at sites with relatively homogeneous soils, since heterogeneity is frequently problematic. The contrasting air flow behaviors of different soil materials can result in stratigraphic control of air flow and uncontrolled lateral transport of air and hazardous vapors. These difficulties prohibit the use of air sparging at many sites with layered soils.

Air flow during air sparging has been a subject of debate among practitioners and researchers since its use began in the U.S. in the late 1980's. Early in its history, many practitioners held a conceptual model for sparging based on small bubbles driven upward through the soil by buoyancy. The bubble flow model has essentially been replaced by the more valid conceptual model of potential flow of a continuous air phase in a partially saturated porous media.

1.2 Statement of Problem

Air flow during air sparging is controlled by soil properties which govern the relationships between fluid relative permeability, saturation, and capillary head (k_r-S-h_c). Descriptions of these soil properties are required for the mathematical modeling of air and water flow during sparging. The indices which characterize these properties have been derived to date primarily from laboratory methods designed to characterize either vadose zone soil moisture retention or fluid flow in petroleum reservoirs. However, the applicability of vadose zone soil moisture retention relationships or petroleum reservoir characterization techniques to air sparging has not been demonstrated. Moreover, these methods do not take into account the unique behaviors of air sparging in soils, which are described herein.

An important aspect of air flow during air sparging is that injected air must displace water from the soil. This displacement process is unstable, and results in the development of pore-scale air fingering, which affects the k_r - S - h_c relationships. Several researchers have shown that the nature and degree of fluid fingering is unique for each displacement process involving different fluid pairs and displacement rates. Thus, we may expect pore-scale fingering during air sparging to result in a set of k_r - S - h_c relationships which are different than those for processes which occur in petroleum reservoirs or in the vadose zone. However, a technique to measure these relationships for air sparging which reflects the effects of pore-scale fluid fingering has not been available.

1.3 Objectives

The overall objective of the research was to evaluate the possibly unique flow behaviors which may be expected for air sparging based on the anticipated pore-scale instability associated with air displacing water from soils. A primary objective was to develop a laboratory experimental apparatus which takes into account the effects of pore-scale air fingering to measure k_r - S - h_c relationships for air sparging in soils. A secondary objective was to identify unique characteristics of the measured relationships for air sparging by comparison to estimates based on soil moisture retention data and previously published functional relationships. A tertiary objective was to assess the k_r - S - h_c relationships of a variety of soil types.

1.4 Scope

The research involved measurement of the laboratory scale air and water flow behaviors of air sparging. Relative permeability-saturation-capillary head relationships were measured in soil core samples using an experimental apparatus which simulated the air injection pressures, gradients, and flow rates associated with field air sparging. A computer automated system was developed to conduct unsteady state displacement experiments where air was injected into initially water saturated soil core samples. The system design incorporated aspects of various pre-existing permeability measurement techniques, as well as several innovative measurement techniques which improved the ability of the system to accurately simulate sparging conditions.

Estimated k_r - S - h_c relationships were obtained through measurement of soil moisture retention data in a tempe pressure cell appartus. From this data, air entry pressure heads and soil pore size distribution indices were obtained for input to previously published functional relationships for air and water relative permeability functions.

Extension of the k_r - S - h_c relationships obtained to model field scale air and water flow behavior was beyond the scope of this research. However, the relative importance of buoyant, inertial, capillary, and viscous forces was determined in order to evaluate the mechanisms of air invasion and air flow with respect to previously published studies, and to evaluate the similarity of the experimental results to field-scale air sparging.

Section 2

LITERATURE REVIEW

This literature review first considers the various conceptual models for air flow during air sparging, which have been adopted by practitioners. Second, the occurrence and flow of air and water in porous media is reviewed. Next, the implications of compressible gas flow are considered. Then, unstable fluid displacement processes, including the phenomenon of air fingering and its impact on k_r - S - h_c relationships are reviewed. Finally, techniques for the laboratory measurement of k_r - S - h_c relationships in core samples are reviewed.

2.1 Air Sparging Conceptual Models

A variety of published papers review the practice of air sparging [*Ardito and Billings*, 1990, *Brown et al.*, 1991, *Johnson et al.*, 1993, *Leonard and Brown*, 1992, *Lundegard and LaBrecque*, 1995, *Marley et al.*, 1992a, and *Marley and Bruell*, 1995]. From these papers several conceptual models have evolved to describe air flow during air sparging. The initial widely accepted conceptual model described small discrete air bubbles cascading upwards due to buoyancy, and distributing themselves outward as they rise due to mechanical dispersion. More recently *Ji et al.* [1993] and *Johnson et al.*, [1993] recognized that bubble flow is not typical, and that air flows as a continuous phase driven

by gradients of pressure. These authors proposed that air flow occurs in discrete channels, but did not describe the nature of these channels in quantitative terms. However, Ji et al. visualized air channels formed in glass beads in 2-dimensional lab scale experiments, and found channel widths on the order of a few grain diameters or less and channel spacing varying up to tens of centimeters. They also found that for uniform glass beads larger than 4 mm in diameter, bubble flow could occur.

A third conceptual model of uniform flow of a continuous air phase within a homogeneous partially saturated porous medium was used by *Beckett et al.* [1995], *Corey* [1994], *Hinkley et al.* [1995], *Lundegard and Andersen* [1993], *Marley et al.* [1992b], *McWhorter, pers. comm.* [1994] and *Thompson, pers. comm.* [1995] as a basis for modeling air flow during air sparging. Corey and McWhorter both considered one dimensional air flow during air sparging. Corey considered horizontal flow, while McWhorter considered vertical upward air flow. They developed mathematical solutions to determine the distribution of capillary pressure and air pressure during steady state air flow, assuming that the water flux is equal to zero as a condition of steady state flow. Their results indicated that for steady state conditions the gradient of capillary pressure (and therefore saturation) is relatively uniform over most of the flow length, and increases nonlinearly near the outlet face.

Lundegard and Andersen [1993] modified an existing three-dimensional numerical unsteady state petroleum reservoir simulator in order to evaluate how the air distribution changes in space and time at the site scale. Their results indicated that the air invasion front advances outward until air breakthrough to the vadose zone occurs. After air breakthrough, the air flow front recedes and air saturations are reduced until steady state conditions are achieved. *Acomb et al.* [1995], *Clayton et al.* [1995], and *Lundegard and*

LaBrecque [1995] have confirmed this behavior through field measurements of air saturations during air sparging.

2.2 Air and Water Flow in Partially Saturated Porous Media

For air and water in a partially saturated porous medium, as the water saturation is reduced, the fluid interfaces occupy smaller pores, and the capillary pressure (air pressure minus water pressure) increases. Capillary pressure will be expressed here in terms of capillary head (water equivalent). Capillary head (h_c) in an ideal cylindrical pore is described by the capillary rise equation, shown below. Figure 1 represents equation (1).

$$h_c = \frac{2\gamma}{\rho_w g R_p} \cos\theta_i \quad (1)$$

where, γ = interfacial tension
 ρ_w = density of water
 g = acceleration of gravity
 R_p = pore radius
 θ_i = interfacial contact angle
 and where, θ_i = zero for an air-water system

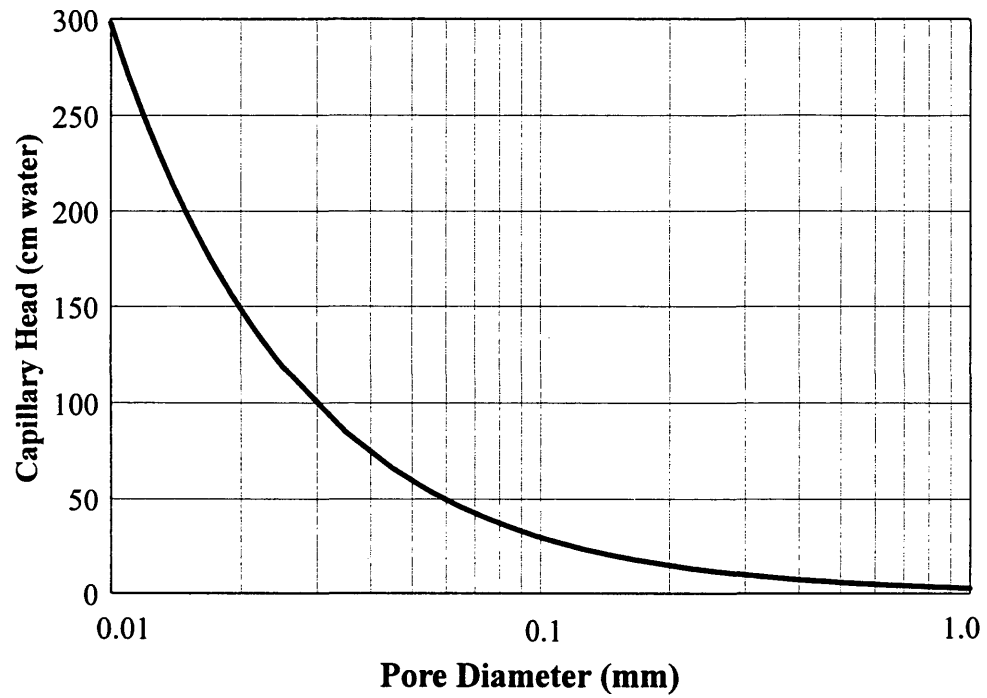


Figure 1. The capillary rise equation implies that for uniform cylindrical pores, the capillary head (air pressure head minus water pressure head) increases as the inverse of the pore size.

The permeability of air and water are also functions of saturation. The permeability of each fluid increases as a function of its saturation [Corey, 1994], and is zero below its residual saturation, where the fluid becomes discontinuous. The relationships between fluid saturation and capillary head and permeability in soils have been considered by a number of authors. Richards [1931] described the capillary conduction of water through a porous medium and established a functional relation between capillary head and soil moisture content.

Brooks and Corey [1964] measured air and liquid permeabilities, and developed equations which predict the relative permeability of each fluid as a function of capillary head or fluid saturation. They also described a procedure whereby capillary head-saturation data are used to derive the hydraulic properties required as input for the relative permeability functions. Parker *et al.* [1987] adapted the results of Van Genuchten [1980] and those of Mualem [1976] to derive functional relationships for capillary head and relative permeability of two fluid phases to fluid saturation. The functions developed by Brooks and Corey and by Parker *et al.* are given below in the context of an air-water system and are shown in Figures 2, 3, and 4.

Brooks-Corey:

$$S_e = \left(\frac{h_o}{h_c}\right)^\lambda \quad (2)$$

$$k_{rw} = S_e^{(2+3\lambda)/\lambda} \quad (3)$$

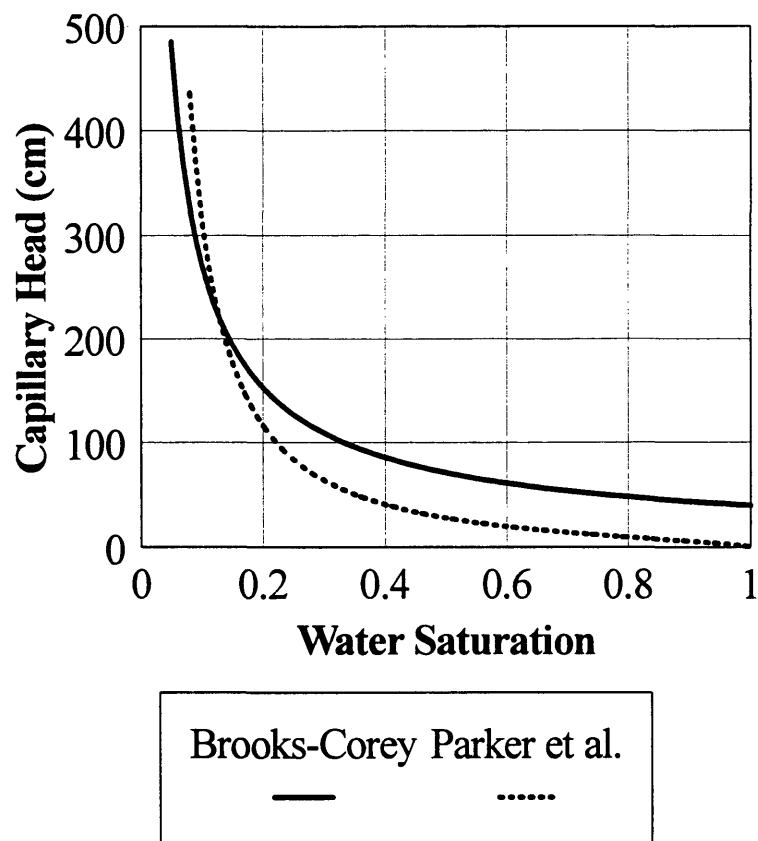


Figure 2. Functional relationships between capillary head and water saturation used by *Brooks and Corey* [1964] and *Parker et al.* [1987]. Porous medium properties as follows: $h_o = 40$, $S_r = 0.01$, $\lambda = 1.20$, $\alpha = 0.015$, $n = 1.7$.

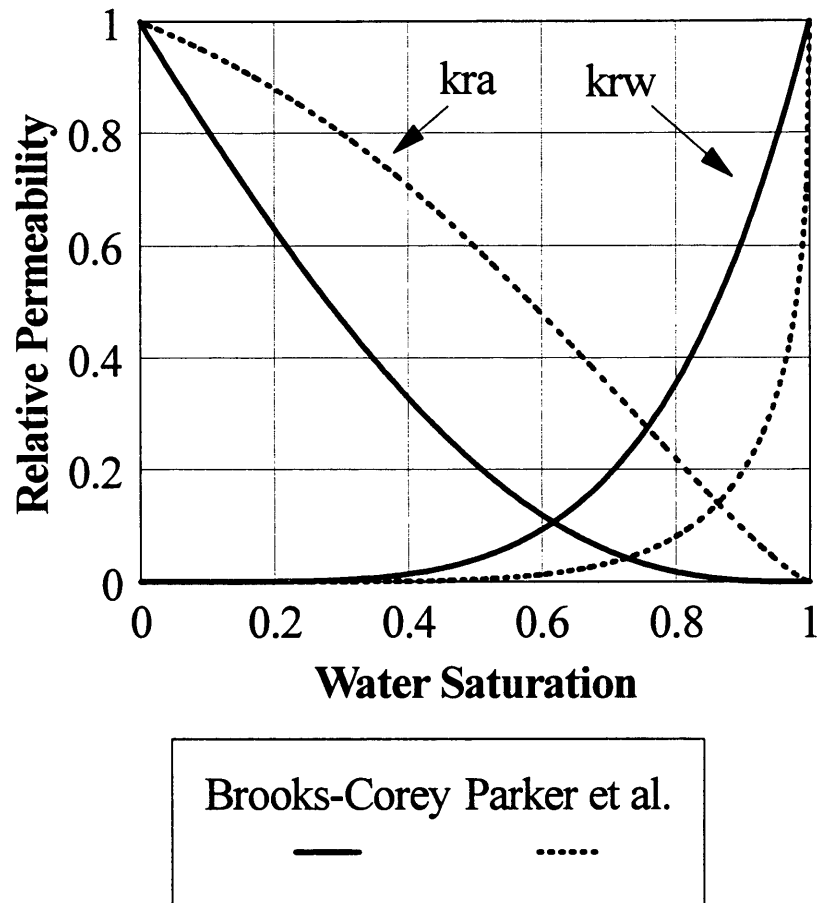


Figure 3. Functional relationships between air and water relative permeability (k_{ra} and k_{rw}) and water saturation and used by *Brooks and Corey* [1964] and *Parker et al.* [1987].

Porous medium properties as follows: $h_o = 40$, $S_r = 0.01$, $\lambda = 1.20$, $\alpha = 0.015$, $n = 1.7$.

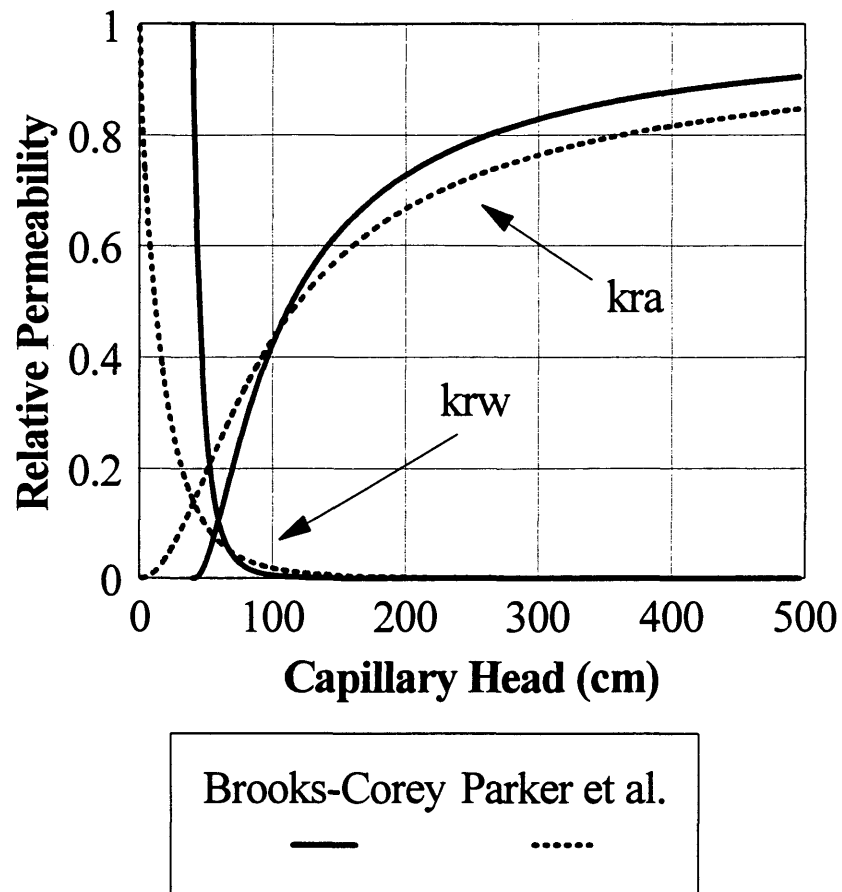


Figure 4. Functional relationships between air and water relative permeability (k_{ra} and k_{rw}) and capillary head used by *Brooks and Corey* [1964] and *Parker et al.* [1987].

Porous medium properties as follows: $h_o = 40$, $S_r = 0.01$, $\lambda = 1.20$, $\alpha = 0.015$, $n = 1.7$.

$$k_{rw} = \left(\frac{h_o}{h_c}\right)^{(2+3\lambda)} \quad (4)$$

$$k_{ra} = (1 - S_e)^2 (1 - S_e^{(2+\lambda)/\lambda}) \quad (5)$$

$$k_{ra} = \left[1 - \left(\frac{h_o}{h_c}\right)^\lambda\right]^2 \left[1 - \left(\frac{h_o}{h_c}\right)^{(2+\lambda)}\right] \quad (6)$$

Parker et al.:

$$S_e = [1 + (\alpha h_c)^n]^{-m} \quad (7)$$

$$k_{rw} = S_e^{1/2} [1 - (1 - S_e^{1/m})^m]^2 \quad (8)$$

$$k_{rw} = [1 + (\alpha h_c)^n]^{-\frac{m}{2}} (1 - \{1 - [1 + (\alpha h_c)^n]^{-1}\}^m)^2 \quad (9)$$

$$k_{ra} = (1 - S_e)^{1/2} (1 - S_e^{1/m})^{2m} \quad (10)$$

$$k_{ra} = \{1 - [1 + (\alpha h_c)^n]^{-m}\}^{\frac{1}{2}} \{1 - [1 + (\alpha h_c)^n]^{-1}\}^{2m} \quad (11)$$

where, S_e = effective saturation
 h_o = a characteristic capillary head (typically air entry pressure head)
 k_{rw} = water relative permeability ($0 < k_{rw} < 1$)
 k_{ra} = air relative permeability ($0 < k_{ra} < 1$)
and where, λ , α , m , and n are pore size distribution/curve fitting parameters
where, $m = 1 - 1/n$
and, $n = 1 + \lambda$

Effective saturation, capillary head, and relative permeability are defined as follows:

$$S_e = \frac{S_w - S_r}{S_m - S_r} \quad (12)$$

$$h_c = h_a - h_w \quad (13)$$

$$k_{rw} = \frac{K_w}{K_{sat}} \quad (14)$$

$$k_{ra} = \frac{K_a}{K_{a,dry}} \quad (15)$$

where, S_w = water saturation
 S_r = residual water saturation

- S_m = maximum water saturation
- h_a = air pressure head (water equivalent)
- h_w = water pressure head (water equivalent)
- K_w = hydraulic conductivity
- K_{sat} = saturated hydraulic conductivity
- K_a = air conductivity
- $K_{a,dry}$ = dry air conductivity

The curve fitting parameters (λ , α , or m) represent the pore-size distribution of the soil, which is the primary factor that controls the occurrence of partially saturated fluids in porous media. To apply equations (2) through (11), λ , α , or m are typically determined from laboratory data, or by calibration to field or model data. *Rawls and Brackensiek* [1988] presented estimates of these exponents and related parameters for vadose zone conditions in agricultural soils based on regression analysis of actual soil data.

Figures 2, 3, and 4 show that the curve shapes that correspond to the Brooks-Corey equations (equations (2) - (6)) differ from those for the Parker et al. equations (equations (7)-(11)). One fundamental difference relates to the fact that the Parker et al. equations represent fluid saturation as a continuous function of h_c for $h_c > 0$, while the Brooks-Corey relationships are only valid for $h_c > h_o$ (Figure 2). This allows the Parker et al. formulation to better handle fluid behaviors at very high water saturations. This is reflected in the shapes of the relative permeability curves as a function of h_c (Figure 4), where the Brooks-Corey $k_{ra} = 0$ and $k_{rw} = 1$ below h_o , while the Parker et al. $k_{ra} > 0$ for all $h_c > 0$.

Alternate wetting and drying, i.e. hysteresis in fluid saturation paths, can lead to non-wetting fluid trapping, which effects k_r - S - h_c relationships. *Parker and Lenhard* [1987] and *Lenhard and Parker* [1987] developed hysteretic constitutive relationships for air-water, two-phase systems, which considered a free air phase and a trapped air phase, defined as follows.

$$S_{ea} = S_{eaf} + S_{eat} \quad (16)$$

where, S_{ea} = effective air saturation
 S_{eaf} = effective free air saturation
 S_{eat} = effective trapped air saturation

Lenhard and Parker [1987] derived an air relative permeability function similar to equation (10) which accounts for the presence of trapped air. In this case, k_{ra} is a function of S_{eaf} , as follows.

$$k_{ra} = S_{eaf}^{\frac{1}{2}} [1 - (1 - S_{eaf})^{\frac{1}{m}}]^{2m} \quad (17)$$

For the simultaneous, one dimensional, low Reynolds number, incompressible flow of two immiscible fluids, the following flux equation can be applied to each fluid [*Corey*, 1994].

$$q_{ix} = \frac{\rho_i g k k_{ri}}{\mu_i} \left[\frac{\partial h_i}{\partial x} + \frac{g_x}{g} \right] \quad (18)$$

where, q_{ix} = volumetric flux of fluid i in x direction (darcy velocity)
 ρ_i = density of fluid i
 g_x = acceleration of gravity in x direction
 k = absolute permeability of medium
 k_{ri} = relative permeability of fluid i
 μ_i = viscosity of fluid i
 h_i = head of fluid i

and where,

$$\frac{\partial h_c}{\partial x} = \frac{\partial h_a}{\partial x} - \frac{\partial h_w}{\partial x} \quad (19)$$

and,

$$\frac{\partial q_w}{\partial x} = - \frac{\partial q_a}{\partial x} \quad (20)$$

Equation (18) is an extension of Darcy's law, which is only valid at low Reynolds number (Re). At high values of Re , the head loss through the porous medium does not increase linearly with flow rate, invalidating Darcy's law. *Corey* [1994] indicated that an appropriate maximum value of Re for Darcy flow is 1.0. The Reynolds number represents the ratio of inertial to viscous forces, and is defined as:

$$Re = \frac{vD\rho}{\mu} \quad (21)$$

where, v = fluid velocity
 D = characteristic dimension

Corey [1994] discussed various approaches to estimate the characteristic dimension (D). D is commonly considered to be equal to the mean grain diameter, but can also be considered to be a function of intrinsic permeability. For air flow during sparging, it seems that D should relate to the diameter of the pores through which air is flowing.

2.3 Gas Flow in Porous Media

The compressibility of a gas flowing in a porous medium results in volume change due to head loss along the flow path, such that for an ideal gas flowing in one dimension through a porous media of constant porosity and fluid saturation:

$$\frac{\partial q_a}{\partial x} = fRT \frac{\partial(1/P_a)}{\partial x} \quad (22)$$

where, f = mass flux
 R = gas constant
 T = absolute temperature
 P_a = air pressure

Gas flow in porous media generally does not meet the pore-scale boundary condition of zero fluid velocity at the solid or liquid interface, except at very high gas pressures [Klinkenberg, 1941]. This results in “gas slippage” or (in porous media) the Klinkenberg effect. Due to the Klinkenberg effect, the measured gas permeability and gas pressure are inversely related. Extrapolation of gas permeabilities measured at various pressures to an infinite pressure ($1/P = 0$) yields an equivalent liquid permeability. The Klinkenberg effect is considered to be relatively insignificant in coarse granular material. However,

Corey [1994] states that for silts or clays air permeabilities may be elevated by a factor of 2 or 3. This is related to the large specific surface of fine grained soils.

2.4 Displacement Phenomena of Immiscible Fluids

An important aspect of air sparging is that injected air must displace pore-water in order to establish air saturation and permeability. This contrasts to two-phase air-water flow in the vadose zone, where water movement is primarily related to gravity and capillary imbibition. During immiscible fluid displacement, interfacial instability can develop, which leads to development of preferential flow paths, or fingering of the displacing through the displaced fluid. Fluid fingering can be expected in cases where a viscosity difference exists between fluids [*Homsey*, 1987, *Wooding and Morel-Setoux*, 1976].

Fluid fingering can occur at the pore scale, or at a macroscopic scale. The viscosity ratio, interfacial tension, and wettability between fluids contribute to the degree and nature of fingering. *Stokes et al.* [1986] showed that higher interfacial tensions resulted in smaller finger widths. These authors, as well as *Homsey* [1987] and *Pavone* [1992], showed that a non-wetting displacing fluid tends to develop pore-sized fingers, whereas a wetting displacing fluid tends to develop macroscopic fingers. *Homsey* described the pattern of a non-wetting invading fluid as a probe of the topology of the microstructure of the porous medium. *Pavone* showed that in some cases both pore-scale and macroscopic fingering can occur for a non-wetting invading fluid.

2.4.1 Pore-Scale Fingering

For air sparging, the fluids have a very high interfacial tension (0.074 dyne/cm) , and air (the displacing fluid) is extremely non-wetting (contact angle = 0 degrees). Based on this, we would expect pore scale fingering to occur. In fact, the physics of pore scale fingering of gases displacing liquids has been investigated by numerous authors [*Brock and Orr*, 1991, *Chen and Wilkinson*, 1985, *Lenormand and Zarcone*, 1985, *Maloy et al.*, 1985, and *Oxaal*, 1991]. Their results reveal extreme pore-scale viscous fingering for air displacing liquids, with branching air fingers the width of a single pore diameter, where the density and geometry of the air fingers is a function of pore geometry and fluid saturation (Figure 5). Typically, a large percentage of the air branches terminate as “dead-ends”. The through going air fingers are referred to as “backbone” fingers.

Pore-scale fingering also implies that the invading fluid may only occupy a small percentage of the available pores. *Dullien* [1979] described the phenomena of hierarchal drainage, where invading fluid penetration occurs only in the largest available pores, even if the capillary head is sufficient to penetrate all pore diameters as defined by the capillary rise equation. *Dullien* indicated that hierarchal drainage may be expected and has been observed under conditions of a non-wetting displacing fluid (as during air sparging).

Hierarchal drainage occurs, according to *Dullien*, by equalization of wetting-phase pressure heads. Thus, the difference between pore fluid pressure heads across interfaces in intermediate size pores is less than that defined by equation (1) and drainage of many pores is prohibited. Hierarchal drainage may also represent the thermodynamic path of greatest efficiency, where any increase in air saturation requires additional thermodynamic work.

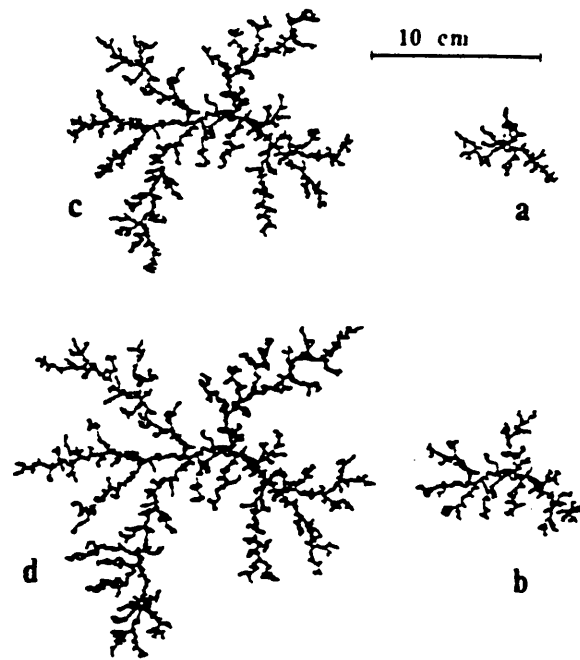


Figure 5. Fingers of air displacing liquid epoxy from a point source in a 2-D porous medium consisting of glass spheres [Maloy *et al.* 1985].

Maloy et al. [1985], *Lenormand and Zircon* [1985], *Chen and Wilkinson* [1985], *Oxaal* [1991], and others have investigated the fractal nature of pore-scale fluid fingering. These authors independently determined that a gas displacing a higher viscosity fluid by 1-dimensional flow in 2-dimensional networks in a variety of configurations resulted in pore-scale fingering with a fractal dimension ranging from 1.5 to 1.9. These authors showed that the fractal dimension is independent of pore geometry.

Numerous authors have mathematically simulated pore-scale fluid fingering. *Fatt* [1956] introduced the concept of a multidimensional network of capillary tubes as a basis for modeling multiphase flow. *Koplik* [1982], *Koplik and Lasseter* [1985], *Chen and Koplik* [1985], and *Chen* [1985] constructed small two-dimensional networks of etched glass, and studied the effects of network geometry on mechanisms of immiscible displacement. Mathematical representations of two- and three-dimensional pore networks have been developed by numerous authors including *Koplik and Lasseter* [1985], *Chatzis and Dullien* [1977], *Chen and Wilkinson*, [1985], and *Ferrand and Celia*, [1992].

Fatt [1960], *Witten and Kantor* [1984], and others have used network models to show that conductance occurs only through the system of backbone fingers and not through the dead-end fingers. *Fatt* used network models to generate relative permeability curves for fingered flow, and found that wetting-phase relative permeabilities were relatively unaffected by dead-end fingers, while non-wetting phase relative permeabilities are reduced significantly by the presence of dead-end fingers. *Fatt* also concluded that the increased tortuosity for non-wetting phase fingered flow resulted in lower relative permeabilities. This implies that for air sparging, if pore-scale fingering is well developed, we may expect lower air permeabilities than predicted based on the total fluid

saturation (i.e. equations (5) and (10)). In this case, an appropriate k_{ra} - S function should be similar to equation (17), where the free air saturation is a function of the backbone air volume.

Lenormand et al. [1988] showed that distinct fingering regimes exist for various combinations of viscosity ratio (M) and capillary number (C). M is defined as the ratio of displacing to displaced fluid viscosities (i.e. $M_{sparging} = \mu_d/\mu_w = 0.016$) (see Appendix A for a list of values of fluid properties and physical constants). C represents the ratio of viscous to capillary forces, and is defined as:

$$C = \frac{v\mu_w}{\gamma\cos\theta_i} \quad (23)$$

The results of *Lenormand et al.* are reproduced in Figure 6. Region I (low M) is where viscous forces in the displacing fluid are negligible relative to those in the displaced fluid. Region II is transitional, and Region III is where viscous forces in the displaced fluid are negligible. Then, considering capillary forces, *Lenormand* defines three domains for (1) stable displacements (high M and C), (2) viscous fingering (low M and high C), and (3) capillary fingering (high M and low C).

During viscous fingering, the invading fluid penetrates the medium primarily in the direction of bulk flow, and finger branching and tip splitting accounts for growth of the invading mass. During capillary fingering, invasion of the displacing fluid is controlled by capillary forces, and fingers may grow in directions opposite to the bulk flow in order to follow the path of least capillary resistance.

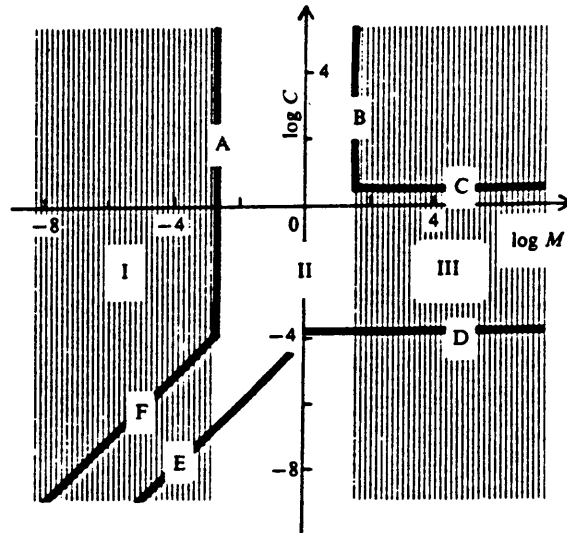


Figure 6. Phase-diagram for immiscible displacement showing domains for stable displacement (lines B and C) at high mobility ratio (M) and high capillary number (C), viscous fingering (lines A and F) at low mobility ratio and high capillary number, and capillary fingering (lines D and E) at high mobility ratio and low capillary number [Lenormand *et al.*, 1988]. In zone I, viscous forces are dominant in the displacing fluid, in zone III, viscous forces are dominant in the displaced fluid, and zone II is transitional.

Two additional approaches for the mathematical simulation of pore-scale fingering include Diffusion-Limited Aggregation (DLA) and percolation theory, both of which are stochastic algorithms. The DLA model of *Witten and Sander* [1981] was shown by *Paterson* [1984] to produce analogous patterns to immiscible fingering. DLA was subsequently used by numerous authors, including *Maloy et al.* [1985], *Murat and Aharony* [1986], and *Oxaal* [1991]. *Koplik et al.* [1983] established the similarities between immiscible displacement and percolation theory, and *Wilkinson and Willemsen* [1983] introduced the concept of invasion percolation to describe the immiscible displacement of fluids in porous media. *Lenormand and Zarcone* [1985], *Wilkinson* [1984], and others have used percolation models to evaluate the effects of pore-scale immiscible fingering.

2.4.2 Macroscopic Displacement Phenomena

Macroscopic fingering implies that for air sparging relatively large regions of the soil remain water saturated after air invasion. This condition develops as a result of uneven advance of a fluid displacement front. *Pavone* [1992] indicated that macroscopic fingering is favored by wetting fluid imbibition, but can also occur for a non-wetting displacing fluid. In this case (i.e. for air sparging), a zone of macroscopic fingers passes through the medium which is followed by a zone of macroscopically uniform saturation, where pore-scale fingering occurs. For a non-wetting invading fluid pore scale fingering presumably occurs within macroscopic fingers as well, and the macroscopic fingers can be visualized as zones of dense concentrations of pore-scale fingers.

Macroscopic fingering also occurs as a result of porous medium heterogeneity. *Brock and Orr* [1991] and *Dawe et al.* [1992] investigated the effects of heterogeneity in two-dimensional glass bead models of immiscible displacement. They found that heterogeneity generally controls the macroscopic flow pattern, whereas the flow pattern in a homogeneous medium is controlled by fingering mechanisms.

Hinkley et al. [1995] evaluated the development of macroscopic air fingering during air sparging through the use of high-resolution mathematical multiphase flow simulations. They determined that capillary heads suppress the development of air fingering at the macroscopic scale. They also evaluated the development of macroscopic fingering through X-ray computed tomography images of air injection into uniform sand packed columns. These results showed the development of macroscopic fingering in uniform Ottawa sand screened to a 0.6 mm diameter, while macroscopic fingering did not develop in Ottawa sand screened to a 0.1 mm. diameter. This may reflect that the reduced capillary heads required to drain the coarser material are insufficient to suppress macroscopic fingering.

McWhorter and Sunada [1990] developed a quasi-analytic mathematical solution for one-dimensional horizontal displacement of a wetting fluid by a non-wetting fluid in a porous medium. Their solution was based on applying the functional forms expressed in equations (2) through (7), above. They developed a fractional flow solution to simulate the process of penetration of a non-aqueous phase liquid (NAPL) into initially saturated porous media. Their results indicated rapid NAPL penetration and saturation profiles (saturation vs. distance) indicating maximum NAPL saturations less than 10% for some soils, and less than 50% in all cases. They found extreme sensitivity of the process to pore size distribution.

The results of McWhorter and Sunada were obtained using $M = 0.5$, while $M = 0.016$ air sparging. Additionally, water has a higher interfacial tension and greater wettability in the presence of air than in the presence of NAPL. As discussed above, these properties of the air sparging system lead to more extreme fingering and greater sensitivity to pore size distribution than NAPL-water systems.

2.5 Laboratory Measurement of Two-Phase Flow Parameters

Accurate representation of field conditions is an important condition for the validity of laboratory measurements of k_r - S - h_c relationships. The boundary and initial conditions imposed on a sample during a test must be designed to meet this condition. Appropriate conditions to be controlled include: capillary heads, fluid fluxes, gradients of fluid pressure, effective stress conditions, and the rate of change and history of these parameters.

Laboratory soil moisture retention measurements are typically conducted under conditions which are representative of *in-situ* vadose zone conditions, i.e. slow water drainage with air at uniform pressure throughout the sample [Corey, 1994]. Similarly, laboratory displacement experiments for petroleum reservoir characterization are typically conducted at high gradients, which are representative of reservoir conditions.

The effects of pore-scale and macroscopic displacement phenomena indicate that we should expect unique behaviors for different types of displacement processes. We should therefore expect distinctly different k_r - S - h_c relationships for air sparging than for unsaturated water flow or petroleum reservoir displacement processes. However, to date

tests to measure k_r - S - h_c relationships have been developed from vadose zone hydrologic research and petroleum reservoir characterization research. Laboratory techniques to quantify k_r - S - h_c relationships for air sparging conditions have not been developed prior to the research reported here.

Honarpoor and Mahmood [1988] and *Corey* [1994] provide useful overviews of laboratory methods for the measurement of relative permeability and fluid saturations in core samples. Laboratory methods can be broadly categorized into steady state and unsteady state methods. Steady state methods provide for constant capillary head, saturation, and flux during the test, while unsteady state techniques allow these parameters to vary throughout the test.

2.5.1 Steady State Techniques

Steady state techniques are considered highly reliable, but are inherently time consuming, since a separate experiment is required for each fluid saturation considered. Steady state techniques provide a uniform fluid saturation within the sample, so that the bulk measurements of saturation and relative permeability can be accurately correlated. The fluid saturations are generally controlled externally between individual experiments. Steady state methods may include simultaneous injection of two fluids under the same gradient (Hassler method) or under independently controlled flow rates (Penn State Method). Steady state air permeabilities can be measured by directing air flow vertically upward through a partially saturated sample with a static liquid phase (stationary-liquid method). In this case, the air pressure gradient is controlled to be equal to the hydrostatic gradient, providing a uniform capillary head and saturation in the sample.

Steady state techniques have been used by several authors including *Brooks and Corey* [1964] to investigate air permeabilities under partially-saturated conditions. Brooks and Corey used the stationary liquid method with oil as the liquid phase. The use of oil as a liquid phase minimized the effects of soil-water interactions such as shrink-swell, and the interfacial contact angle for air-oil systems is less susceptible to changes related to contaminants. In between each air permeability measurement, fluid saturations were changed by extracting liquid from the sample via a high air entry porous material. In this manner, Brooks and Corey controlled fluid saturations and measured capillary heads, based on the assumption of a hydrostatic distribution of liquid pressures in the sample.

Brooks and Corey also measured liquid permeabilities over a range of fluid saturations using a separate apparatus from that used for the air permeability measurements. Between liquid permeability measurements, they reduced liquid saturations in a similar manner as described above. Liquid permeabilities were measured using downward liquid flow with a gradient of 1.0 and air at atmospheric pressure in order to provide a uniform distribution of capillary head in the sample.

Roseberg and McCoy [1990] measured air permeabilities in soils with macropores using the stationary-liquid method. Their system involved external control of capillary head and measurement of air permeabilities over a range of flow rates. *McCarthy and Brown* [1992] measured air permeability over a wide range of fluid saturation. These authors did not observe the criteria for the stationary-liquid technique, but rather allowed air flow to equilibrate (as an apparent indication of uniform distribution of saturation) before measuring air permeability. They found an approximate linear relationship between saturation and air permeability at low to intermediate flow rates and water

saturations. However, they observed that at high flow rates and high water saturations, air permeability was not independent of flow rate. These data were eliminated from their consideration, but may have reflected the development of air fingering.

Since air sparging is a dynamic displacement process which likely involves pore-scale air fingering, we desire to employ laboratory techniques which will allow these effects to be manifested in the relative permeability measurements. Since steady state methods do not involve fluid displacement and the related fingering effects they are unlikely to accurately represent air sparging conditions. However, for this same reason they provide a standard against which the possible effects of fingered flow during air sparging can be compared.

2.5.2 Unsteady State Techniques

Unsteady state techniques generally are based on displacement experiments, where the core is initially saturated with one fluid, and a second fluid is injected which displaces the initial fluid [*Honarpoor and Mahmood, 1988*]. This has the advantage of allowing for the physical processes related to the fluid displacement process to be expressed in the data generated. However, the analysis of displacement experiments generally does not account for displacement instability and fluid fingering.

Displacement experiments result in non-uniform saturation and capillary head over the length of a core sample. For this reason, most unsteady state techniques rely on analyses which indirectly calculate the capillary head, saturation, and relative permeability at a specific point in the sample using curve-matching or analytical

solutions. Most displacement experiments maintain very high pressure gradients so that the effects of capillarity are minimized, and unsteady state flow equations can be solved to determine the relative permeabilities of the fluids. This has been shown to provide a reasonable representation of petroleum reservoir conditions, however it may not accurately reflect air sparging conditions since capillary effects may be important, and low flow rates and injection pressures are more representative of air sparging.

Johnson et al. [1959] presented a widely used method (JBN method) for determination of relative permeability from laboratory displacement experiments. The JBN method is based on solution of the Buckley-Leverett flow equation at the outlet face of a sample. However, where the boundary conditions do not satisfy the Buckley-Leverett flow equation, the analysis is not valid. The primary assumptions of the Buckley-Leverett equation are that both fluids flow under the same gradient, and that the gradient of capillary head is negligible [*Corey*, 1994].

Jones and Roszelle [1978] presented a graphical solution which is equivalent to the JBN method. *Kerig and Watson* [1987] proposed a parameter estimation technique, where relative permeabilities are estimated by fitting a functional form for the relative permeability curve to the time-history data from a displacement experiment. Their technique assumes that a valid functional form has been pre-determined, which is a reasonable assumption for petroleum reservoir simulations, which have been studied extensively.

Loomis and Crowell [1960] compared relative permeabilities calculated using the JBN method to those calculated from applying Darcy's law to the bulk measured values of flow rate and pressure drop at the average fluid saturation. They found relatively close

agreement between methods for air displacing oil.

Laboratory measurements of relative permeability are subject to errors caused by capillary and other end effects. *Kyte and Rapaport* [1958] described capillary end effects for waterflood experiments, where water displaces oil. In this case, capillary imbibition of wetting fluid into the sample at the inlet end, and retardation of wetting fluid breakthrough at the outlet end both occur. These effects influence the distribution of saturation and capillary head in the sample, and may lead to significant errors.

Peters and Khataniar [1985] evaluated the effects of fluid displacement instability on relative permeability curves. They compared relative permeabilities from dynamic displacement experiments to steady state relative permeabilities and found that the results deviated as the degree of displacement instability increased. They found that, in general, non-wetting phase relative permeabilities were reduced and wetting-phase relative permeabilities were increased. They concluded that dynamic displacement experiments should be conducted at the same degree of instability as occurs in-situ in order to obtain representative relative permeability curves.

Section 3

EXPERIMENTAL PROGRAM

3.1 Experimental Strategy

The experimental strategy involved the measurement of unsteady state k_r - S - h_c relationships under conditions which closely simulated the air flow rates, injection pressures, and gradients typical for field applications of air sparging. These measurements were compared to estimates based on soil moisture retention data. This comparison was used as a basis to evaluate the unsteady state behaviors involved in air sparging relative to the steady state behaviors which occur during free drainage, without fluid fingering. Additionally, gas-phase tracer experiments were conducted to evaluate the possible development of dead-end air fingers during air invasion.

The experimental approach and sequence of tests for each soil sample tested is depicted in Figure 7. For each soil tested, duplicate cores were obtained which were similar in composition and texture. One core was subjected to a sequence of air and water permeability testing and air injection displacement experiments to define the unsteady state k_r - S - h_c relationships. The second core was subjected to moisture retention, porosity, and dry bulk density measurements using a pressure cell. Both cores were subjected to grain size analysis after testing.

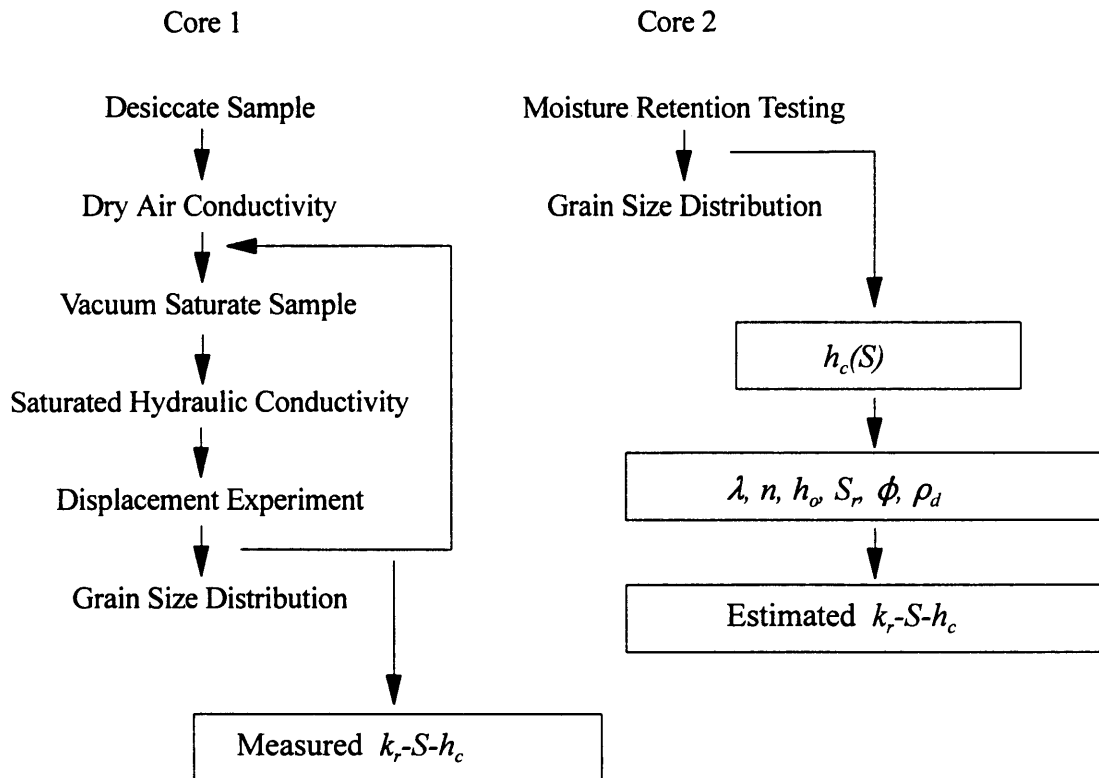


Figure 7. The experimental approach involved subjecting duplicate soil core samples to a series of tests to measure unsteady state relative permeability-saturation-capillary head (k_r-S-h_c) relationships and to generate estimates of k_r-S-h_c from moisture retention data. Parameters λ and n are pore size distribution indices, h_o = air entry pressure, S_r = residual saturation, ϕ = porosity, ρ_d = dry bulk density.

The measurement of unsteady state k_r - S - h_c under conditions representative of *in-situ* air sparging required the development of a unique air injection displacement experiment apparatus. The system allowed the measurement of bulk fluid saturation and relative permeability in order to account for the effects of fluid fingering and avoid the bias inherent in methods which rely on solution of unsteady state flow equations, described in section 2.2.2. This was accomplished by incorporating aspects of the steady state stationary-liquid technique into a new unsteady state displacement experiment where air displaces water from an initially water saturated sample.

The functional relationships for k_r - S - h_c provided by *Brooks and Corey* [1964] and *Parker et al.* [1987] were applied to the moisture retention data to provide estimated relative permeability functions against which to compare the air injection data. These relationships are hereinafter referred to as the Brooks-Corey and Parker et al. relationships. The Brooks-Corey relationships were based on empirical data for air permeabilities under stable (i.e. no air fingering) conditions, and therefore provided a comparable basis against which to illuminate the possible effects of air fingering on the air injection data. This research adopted their approach of determining the soil pore size distribution coefficient (λ) from measured $h_c(S)$ data using equation (2), and applying λ to equations (3) through (6) to estimate air and water relative permeabilities. The Parker et al. relationships were applied similarly using equations (7) and (8) through (11).

The use of gas-phase tracers to determine the presence of dead-end air fingers was based on the anticipated result that injected tracer gas may become trapped in dead-end pores. Therefore, less than 100 percent recovery of the tracer gas could be considered an indication of the development of dead-end air fingers. It was also anticipated that tracer gas would only become trapped if the tracer gas was present at the time when the dead-

end fingers developed. Thus, by injecting a series of finite slugs of tracer gas, the temporal variation in development of dead-ends could be discerned. Also, if dead-end air fingers do not develop, then near 100 percent tracer gas recovery would be expected.

The tracer experiments were designed solely to measure the percent recovery of each tracer slug injected since the magnitude and shape of the tracer breakthrough curve is governed by transport mechanisms which were not easily quantified for this system. These mechanisms include advection, dispersion, chemical diffusion, solubilization into water and re-volatilization, as well as gas dilution upon initial injection into the system.

3.2 Design of Air Injection Displacement Experiment

The following describes the air injection displacement experiment parameters, the boundary and internal conditions imposed during the displacement experiments, the system components which comprised the experimental apparatus, and how fluid permeabilities, saturations, and heads were measured and calculated.

3.2.1 Air Injection Displacement Experiment Parameters

The magnitude of air flow rates, air injection pressure heads, and gradients typical for field air sparging were considered in order to design the air injection displacement experiment to simulate the *in-situ* process. The ranges of these values for the *in-situ* and experimental systems are summarized in Table 1.

Table 1. Comparison of air flow parameters between typical *in-situ* sparging conditions and the conditions designed for the experimental system. Local *in-situ* conditions may vary over a wider range near the injection well, or near the water table

Air Flow Parameter	Darcy Velocity (cm/min)	Injection Pressure (psi)	Gradient (cm water/cm)
<i>In-Situ</i> Sparging	< 16	1 - 5	< 2
Experimental System	< 34	< 5	≈ 1

Typical field air sparging air injection rates range from 2 to 30 cubic feet per minute (cfm). Assuming that the air moves outward and upward across a semi-sphere, we may expect Darcy air velocities (q_a) of up to 16 cm/min at a 1 meter radius from the air injection point. For a core sample with 29 cm³ of cross sectional area, this corresponds to an air flow rate of 464 ml/min. The air injection system was designed to accommodate a maximum air flow rate (Q_a) of 1,000 ml/min. This air flow rate also represents the approximate upper limit for Darcy flow ($R_e \approx 1.0$, at $Q_a = 1,000$ ml/min and $S_w = 0.8$ for a medium sand).

Typical air sparging injection pressures are from 1 to 5 pounds per square inch above the “breakout” well head pressure, which equals the hydrostatic head at the well screen plus the air entry pressure of the soil. The air injection displacement experiment apparatus was designed to allow air injection pressures of up to 5 psi above the initial hydrostatic water pressure in the core sample.

During air sparging, air gradients vary spatially around the air injection well. *McWhorter* [1994] and *Corey* [1994] indicated that the air pressure entering the vadose zone during air sparging is expected to be approximately equal to the air entry pressure of the soil. They also indicate that the gradient of capillary head is largest near the water table for steady state air flow. Typical injection depths range from 10 to 30 feet below the water table. Considering a case of relatively high air gradients, with a 10 foot air injection depth and an injection pressure 5 psi above the breakout pressure, the average air pressure gradient from the injection point to the water table would be 1 psi/ft, or 2 ft. water/ft. While larger gradients may exist locally, either near the injection well or near the water table, this value represents an appropriate upper limit for the gradient over most of the region influenced. The experimental system was designed to approximate an air pressure gradient of 1.0 cm water/cm based on this and other considerations described below.

3.2.2 Sample Boundary Conditions

The boundary conditions imposed on the sample were designed to maintain relatively uniform capillary head and saturation within the sample, in order to allow the use of bulk measurements of fluid saturation and relative permeability. This was achieved by controlling the base and top air heads to induce upward vertical air flow at an air gradient which approximated the distribution of hydraulic head in the sample. A constant hydraulic head was maintained at the upper sample boundary, and as air invaded the base of the initially water saturated sample, water was allowed to drain only from the top of the sample, providing a no-flow boundary condition at the sample base. Figure 8 depicts a pressure head diagram of the boundary conditions, and the hypothetical internal

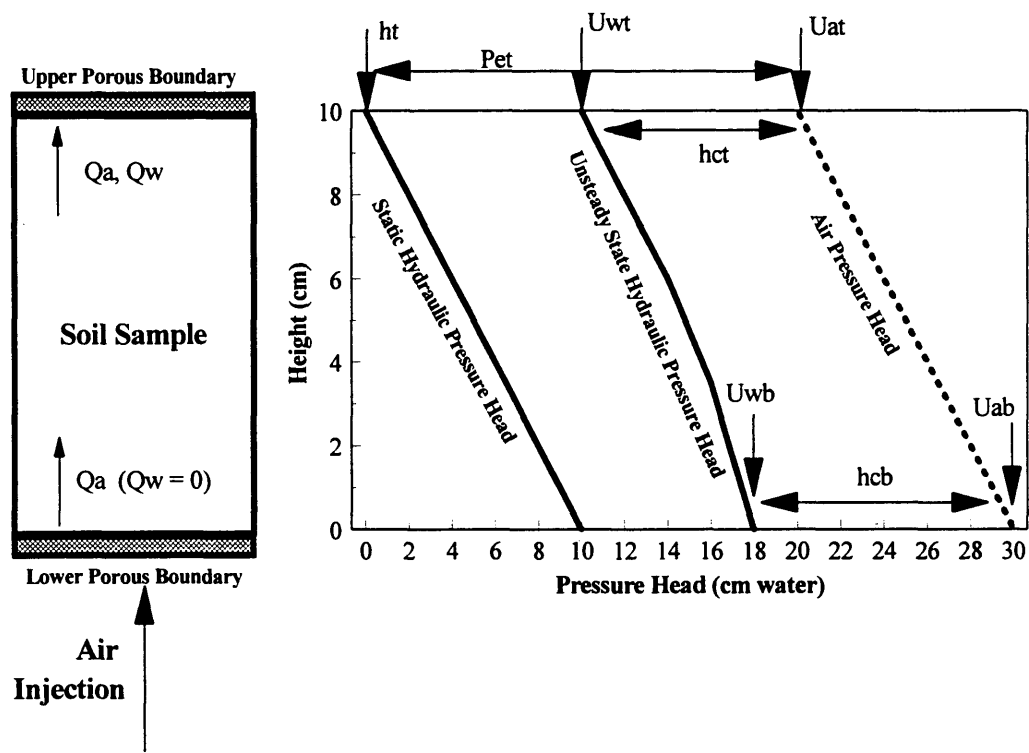


Figure 8. Pressure head diagram depicting the design of the air injection displacement experiments. Base and top pore air and water head (U_{ab} , U_{at} , U_{wb} , U_{wt} respectively) vary with the boundary air pressure head conditions and the distribution of capillary head (base (h_{cb}) and top (h_{ct}) capillary head are depicted here). The top pore air head is equal to the hydraulic head applied to the upper sample boundary (h_t) plus the dynamic air entry pressure head of the upper boundary (P_{et}), and the base pore air head is controlled by the air injection pressure head applied to the lower sample boundary. Q_a = air flow rate, Q_w = water flow rate.

distribution of air and water heads in a core sample during an air injection displacement experiment.

During the displacement experiments, control of base pore air head (U_{ab}) and top pore air head (U_{at}) was achieved using a computer data acquisition and control system to maintain an appropriate base air injection pressure head and by using a porous boundary with a specific air entry pressure head (P_{et}) on the top (outlet) end of a core sample to control the outlet air pressure head. During initial air invasion, prior to air breakthrough from the top of the sample, U_{at} was undefined, since the top of the sample was initially water saturated. After air breakthrough, U_{at} was controlled by the behavior of the upper porous boundary, and was equal to the hydraulic head maintained at the upper boundary (h_t) plus P_{et} . The applicable value of P_{et} is a dynamic air entry pressure head under conditions of air flow, where air emerges into the water filled chamber above the sample. Several upper boundaries were available, each having different values of P_{et} .

While a constant hydraulic head was maintained at the upper sample boundary, actual pore water heads varied during the displacement experiments as a function of water drainage from the top boundary (at a rate, Q_w), and the distribution of air pressure head and capillary head in the sample. As capillary head increased during an unsteady state experiment, the pore water pressure heads decreased, since air pressure heads were more or less constant. Where an upper boundary was used with a small value of P_{et} , h_{ct} had an upper limit of $h_{ct} = P_{et}$, and steady state S_w could be achieved at $U_{wt} = h_t$.

The effects of buoyancy were accounted for by the geometry of upward vertical air flow. In this case, buoyant forces and viscous forces acting on the air are collinear, and are inherent in the measurements of pore fluid pressure heads. The relative magnitude of

buoyant and viscous forces can be determined from measured data, since viscous forces were measured and buoyant forces are constant at $(\rho_u - \rho_w)ghA$.

3.2.3 Air Injection System Components

The experimental apparatus consisted of a soil sample test cell, air injection pump, pore fluid measurement and control system, and data acquisition and control system (Figure 9).

Soil cores tested were approximately 6 cm in diameter. Samples were contained within a latex membrane within a test cell (Figure 10) designed to control sample volume or confining stress, and provide connections for interface of the sample to the pore fluid measurement and control system. The sample cell was generally operated in constant volume mode in order to maintain volume balance of fluids. A stainless steel frame controlled the sample vertical dimension, while the essentially incompressible sample chamber fluid (water) provided approximate control of the lateral dimension.

The porous boundaries at the sample base and top (Figure 10) were sintered stainless steel, manufactured by Mott Metallurgical Corporation. Five materials were used, with nominal air entry pressure heads of 10, 17, 30, 60, 110, and 185 cm water. The 10 cm air entry pressure material was used at the base (inlet) end of the sample. This material provided minimal resistance to air flow, yet prevented air penetration into the sample prior to initiating a test. The higher air entry materials were used as the top (outlet) boundary to control the air pressure head at the outlet face during experiments.

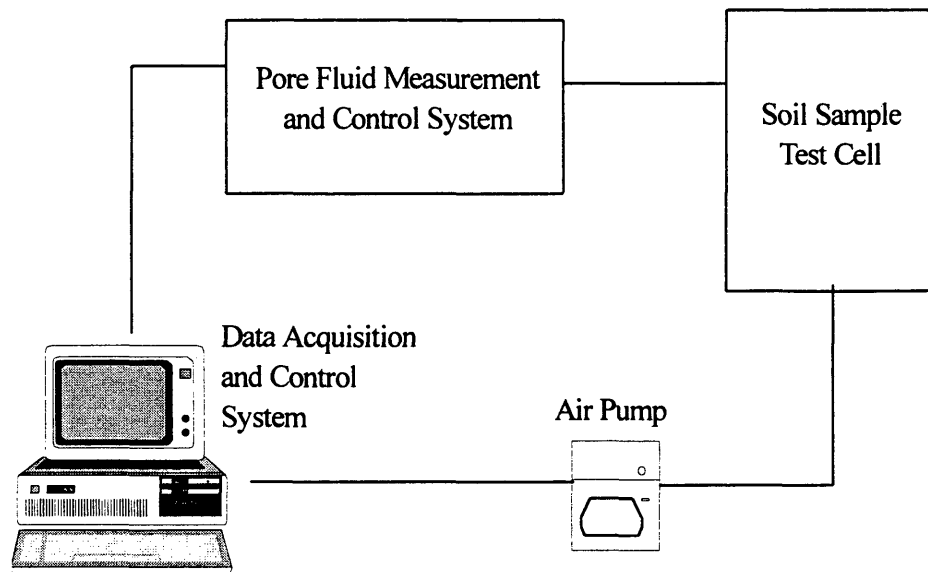


Figure 9. The air injection displacement experiment apparatus consisted of a data acquisition and control system, air pump, soil sample test cell, and pore fluid measurement and control system.

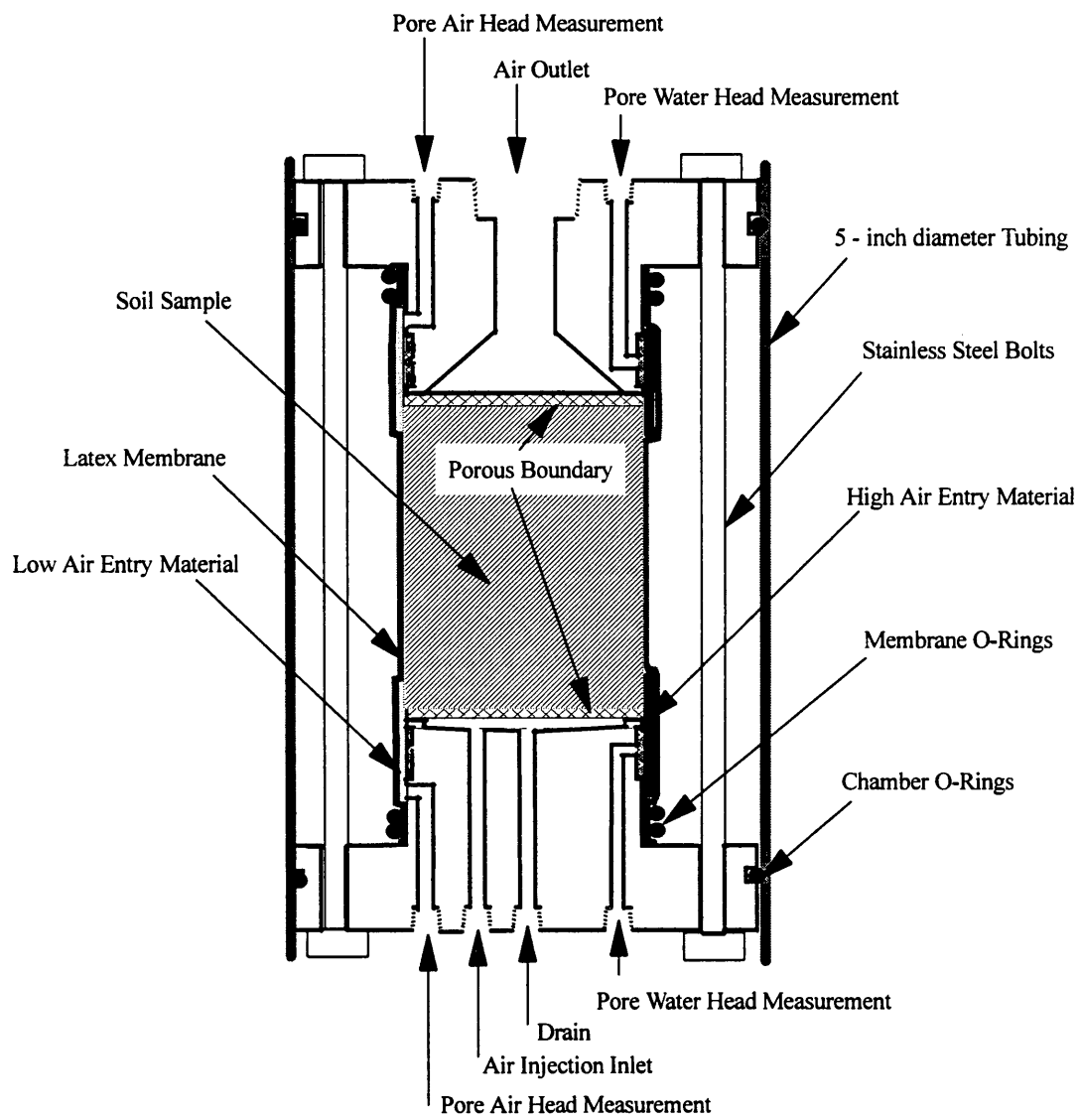


Figure 10. Soil sample test cell.

Pore-water and pore-air pressure heads were measured via the sample test cell at the base and top of the sample (Figure 10). Pore-water pressure heads were sensed directly via a flexible, high air entry pressure porous material wrapped around the side of the sample to avoid impedance of air flow during testing. The direct measurement of pore water pressure heads in this manner eliminated possible measurement errors related to end effects. The material used had an air entry pressure head of approximately 250 cm water. *McCoy* [1989] described the water retention characteristics and hydraulic properties of this material. Pore air pressure heads were sensed directly via a flexible, low air entry pressure (approximately 2 cm water) porous material.

A six-roller peristaltic pump, controlled externally by a 4-20 milliamp signal from the data acquisition and control system (Figure 11), was used as an air injection pump. The peristaltic pump tubing inlet was fed by pressure-regulated compressed air to achieve higher mass flow rates. A 2 liter air tank was used to buffer the pump outlet to minimize flow pulsation and to smooth the response of the system to changes in pump speed dictated by the control system. A second 3 liter humidification chamber was used to humidify the injected air in order to prevent evaporation from the sample.

The air flow rate through the sample was measured by a series of three flow transducers interfaced to the data acquisition system. The three flow transducers had measurement ranges of 20-100 ml/min, 40-500 ml/min, and 200-1,000 ml/min. A series of computer controlled electronic solenoid valves were used to switch to the appropriate flow transducer at set points of 100 ml/min and 500 ml/min. Flow rates greater than 1,000 ml/min were generally not allowed during the testing.

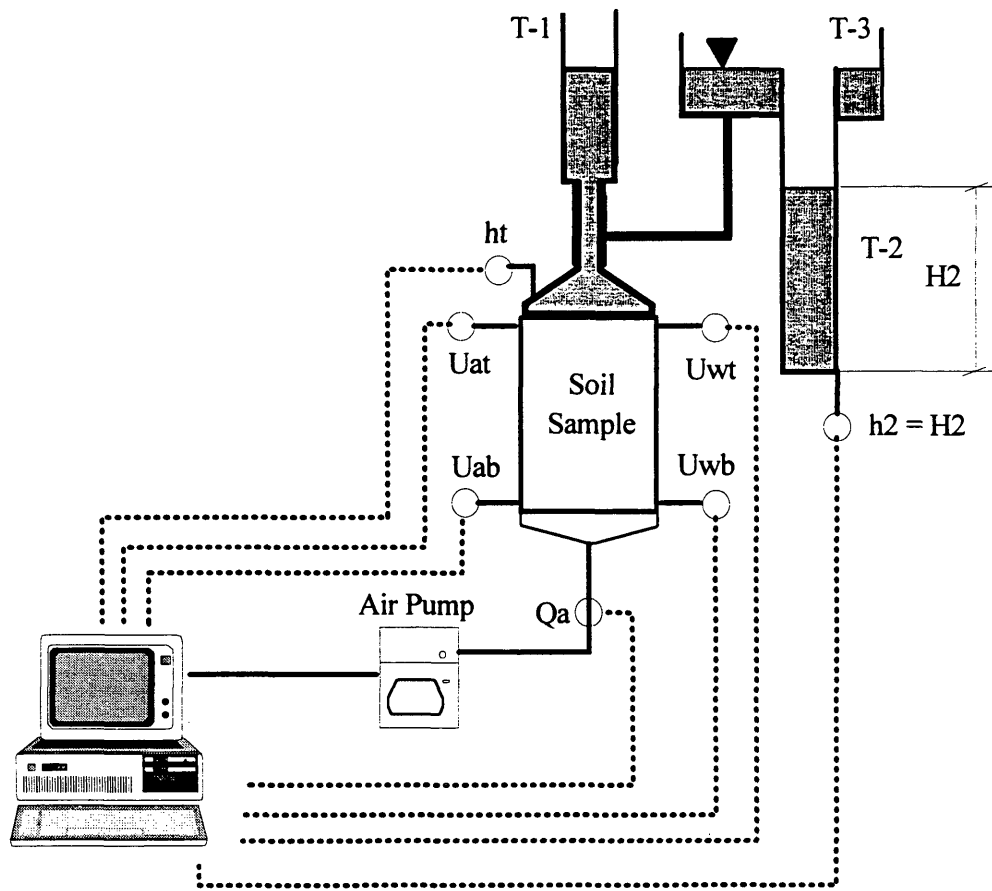


Figure 11. The pore fluid measurement and control system provided a constant hydraulic head (h_t) to the upper sample boundary via the overflow level in tube T-3. Pressure transducers interfaced to the computer measured h_t and the base and top pore air and water head (U_{ab} , U_{at} , U_{wb} , U_{wt} respectively), the air injection flow rate (Q_a), and the water level ($h_2 = H_2$) in overflow tube T-2. Air exited the system through tube T-1.

Figure 11 also depicts the pore fluid measurement and control system and its interface to the sample test cell and the data acquisition system. Tube T-3 consists of an overflow into tube T-2, which provided a constant hydraulic head to upper boundary material of the soil sample. Water displaced from the sample during an experiment overflowed from T-3 and the change in the level in T-2 was measured by a pressure transducer. This provided a volumetric measure of the amount of water displaced from the sample. At any time, the volume of air in a sample being tested was assumed to be equal to the volume of water displaced. Air which exited the sample rose up through tube T-1, and was released. The system also interfaced to the sample test cell to measure pore fluid heads using electronic pressure transducers.

The data acquisition and control system consisted of an analog to digital I/O board and data acquisition and control software installed in a computer. The system provided automated collection of transducer data and real time calculations of flow parameters, and controlled air injection conditions during the experiments based on the calculated data.

3.2.4 System Measurements and Flow Parameter Calculations

The system measurements consisted of the air flow rate (Q_a), the base pore air pressure head (U_{ab}), base pore water pressure head (U_{wb}), top pore air pressure head (U_{at}), top pore water pressure head (U_{wt}), the constant head applied to the top of the sample (H_t), and the level of water in T-2 (h_2).

Fluid saturation and pressure head parameters were calculated from the transducer data using the following equations.

Volume of water displaced (V_{wd}) (ml):

$$V_{wd} = 1.89 * h_2 \quad (24)$$

where, $1.89 =$ cross sectional area of tube T-2 (cm^2)

Air Saturation (S_a):

$$S_a = \frac{V_{wd}}{V_v} \quad (25)$$

Water Saturation (S_w):

$$S_w = 1 - \frac{V_{wd}}{V_v} \quad (26)$$

where, $V_v =$ void volume of sample, determined from sample dimensions and ϕ

Top Capillary Head (h_{ct}):

$$h_{ct} = U_{at} - U_{wt} \quad (27)$$

Base Capillary Head (h_{cb}):

$$h_{cb} = U_{ab} - U_{wb} \quad (28)$$

Air flow parameters were calculated using the following equations.

Air Gradient (I_a):

$$I_a = \frac{U_{ab} - U_{at}}{L} \quad (29)$$

where, I_a is expressed in terms of cm water head per cm length
 L = sample length

Air Conductivity (K_a):

$$K_a = \frac{Q_a \rho_a}{I_a A \rho_w} \quad (30)$$

where, A = sample cross-sectional area

Air Relative Permeability (k_{ra}):

$$k_{ra} = \frac{K_a}{K_{a,dry}} \quad (31)$$

Saturated hydraulic flow parameters were calculated using the following equations:

Water Flow Rate (Q_w):

$$Q_w = \frac{\Delta V_{wd}}{\Delta t} \quad (32)$$

where, ΔV_{wd} = change in fluid volume in tube T-2
 Δt = variable time interval

Hydraulic Gradient (I_w):

$$I_w = \frac{Uwb - Uwt - L}{L} \quad (33)$$

Saturated Hydraulic Conductivity (K_{sat}):

$$K_{sat} = \frac{Q_w}{I_w A} \quad (34)$$

Calculation of water relative permeability (k_{rw}) from the displacement data was based on a solution for unsaturated flow in core experiments with a boundary condition of zero flow at one end of the sample, as outlined by *Salehzadeh and Demond* [1994] and shown below.

$$k_{rw} = \frac{1}{2} \frac{Q_w}{K_{sat} I_w A} \quad (35)$$

Section 4

METHODS

4.1 Soil Grain Size Distribution

Soil grain size distribution was determined using the dry sieve method and hydrometer analysis (where appropriate) using the methods described by *Bowles* [1992]. From this data, the mean grain size (D_{50}), coefficient of uniformity (C_u), and the coefficient of gradation (C_c) were determined, and each sample was classified according to the Unified Soil Classification System (USCS).

4.2 Soil Moisture Retention

Soil moisture retention measurements were accomplished using a tempe pressure cell (model no. 1400) manufactured by Soil Moisture Equipment Corporation, together with the methods described by *Reginato and Van Bavel* [1962]. After completion of the moisture retention measurements, the sample was oven dried. From this, and the saturated sample weight the soil porosity (ϕ) and dry bulk density (dry bulk density, ρ_d) were determined from mass and volume relationships.

4.3 Air Injection System Calibration and Error Analysis

Calibration of the air injection system allowed the determination of errors in measurements and calculations which describe k_r - S - h_c relationships of the core samples tested. The errors in measurement of U_{ap} , U_{ab} , U_{wp} , U_{wb} and h_2 and the calculation of V_{wd} and Q_a were determined through specific calibration experiments. These data were used to estimate the uncertainty in calculations of fluid saturations, capillary heads, and relative permeabilities through analysis of the propagation of errors. Also, a method is described which was used to evaluate errors in k_{ra} - S correlations due to non-uniformity of fluid saturation along the length of the core sample.

4.3.1 Calibration of System Measurements

The pressure transducers were calibrated with a water manometer to read (via the data acquisition system) in units of cm water. The calibrations were checked periodically, and the transducers re-calibrated, as necessary. The electronic transducers which measured Q_a were calibrated using precision rotameters to read in units of ml/min..

The difference (or residual) between measured and actual values of U_{ap} , U_{ab} , U_{wp} and U_{wb} to h_t over a range of pressure heads (Figure 12) shows that each measurement included both random and systematic errors. The random errors reflect noise in the measurements while the systematic errors reflect non-linear transducer response. These errors sum to zero over the range of pressure heads considered and therefore, both types of errors were treated as random. Table 2 summarizes the statistical parameters which characterize the pressure head residuals for of U_{ap} , U_{ab} , U_{wp} and U_{wb} , as well as h_2 .

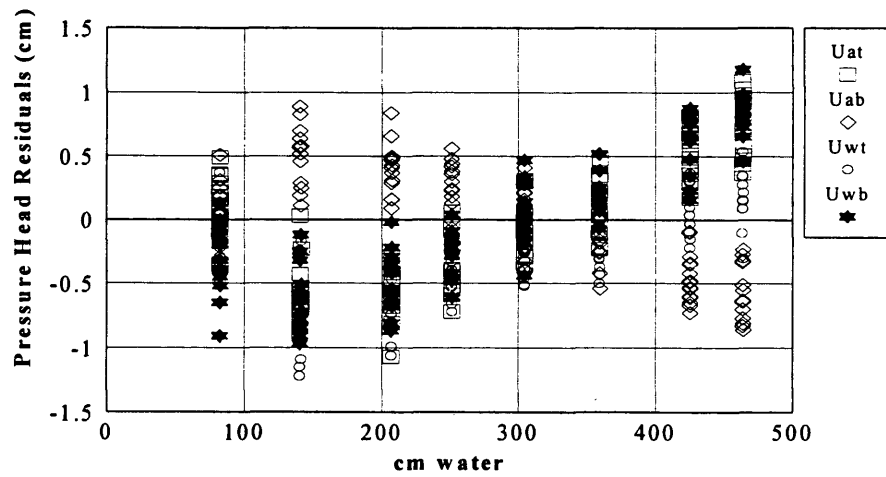


Figure 12. Pressure transducer calibration data. Residuals of measured values from transducers which measure the base and top pore air and water pressures (U_{ab} , U_{at} , U_{wb} , U_{wt} respectively) to the transducer which measures the constant head (h_1) over a range of values.

Table 2. Statistical summary of residuals of transducer values of U_{ab} , U_{at} , U_{wb} , and U_{wt} to h_1 and of transducer h_2 to manometer values.

Transducer	h_2	U_{ab}	U_{at}	U_{wt}	U_{wb}
Sample Size (N)	42	137	137	137	137
Minimum	-0.938	-0.860	-1.070	-1.220	-0.970
Maximum	0.582	0.890	1.090	0.540	1.180
Std. Deviation	0.323	0.413	0.503	0.373	0.528
Variance	0.104	0.171	0.253	0.139	0.278
Std. Error	0.063	0.035	0.043	0.032	0.045
Mean	-0.001	0.014	-0.022	-0.262	-0.015

A frequency histogram of V_{wd} residuals for experiments where $V_{wd} = 0$, is presented in Figure 13. Flow transducer measurements of Q_a were compared to values measured using precision air flow rotameters over a range of flow rates. A frequency histogram of the percent error in measurement of Q_a is presented in Figure 14. The error in Q_a was expressed as percent error, since the error is a fractional error, unlike pressure head measurements or calculation of V_{wd} . The statistical description of errors in V_{wd} and Q_a are summarized in Table 3.

Table 3. Statistical description of residuals of calculated values of the volume of water displaced (V_{wd}) to an actual value of zero, and percent error between transducer values of air flow rate (Q_a) and rotameter values.

Statistical Parameter	V_{wd} Residuals (cm ³)	Q_a Percent Error
Sample Size (N)	255	122
Minimum	-1.42	-6.80
Maximum	1.55	5.84
Std. Deviation	0.51	2.73
Variance	0.26	7.66
Std. Error	0.032	0.25
Mean	-0.124	-0.19

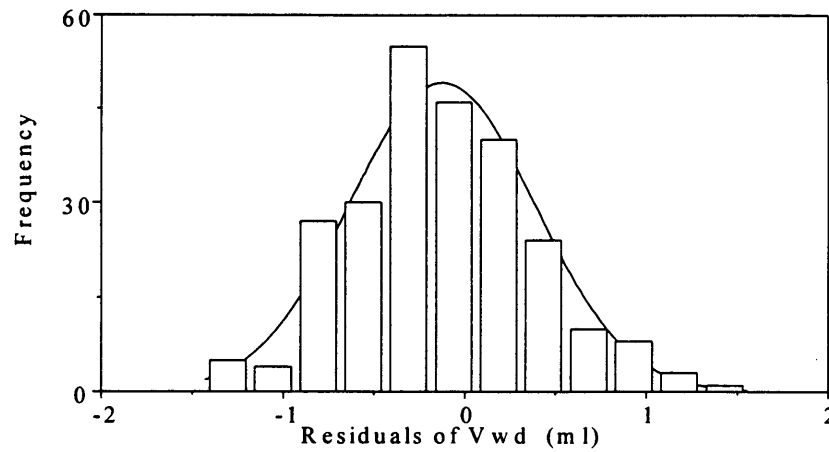


Figure 13. Frequency histogram of residuals of the volume of water displaced (V_{wd}) to an actual value of zero. The smooth curve represents a normal distribution fitted to the measured residuals.

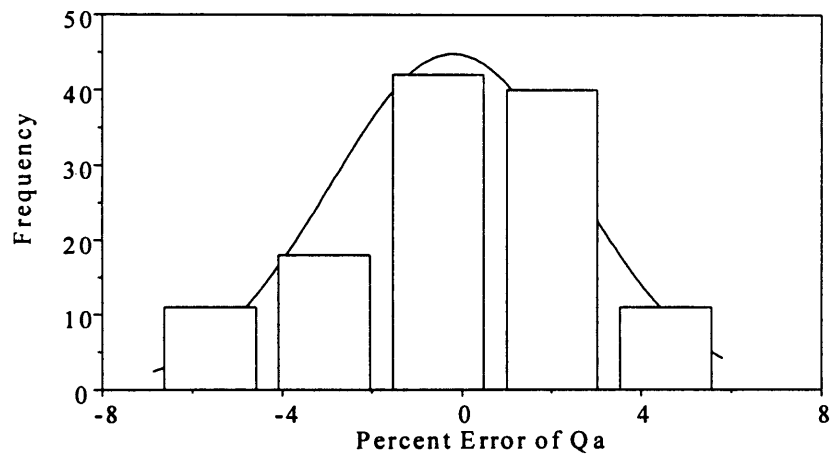


Figure 14. Frequency histogram of percent error of transducer values of air flow rate (Q_a) to rotameter values. The smooth curve represents a normal distribution fitted to the measured residuals.

4.3.2 Propagation of Measurement Errors

The estimated uncertainty in calculations of fluid saturations, capillary heads, and relative permeabilities was determined by evaluating the interactions (i.e. propagation) of measurement errors determined above using statistical methods described by *Taylor* [1982]. Table 4 summarizes the measurement errors considered in the calculated data.

Table 4. Summary of procedures used to evaluate the propagation of measurement errors through calculations of flow parameters.

Calculated Value	Procedure
air and water saturation	error analysis of volume of water displaced
top capillary head	error analysis of top pore air and water head
base capillary head	error analysis of base pore air and water heads
air gradient	error analysis of base and top pore air heads
air flow rate	residuals to rotameter values, error analysis of compressible flow
air permeability	error analysis of air gradient and air flow rate
hydraulic gradient	error analysis of base and top pore water head
water flow rate	error analysis of volume of water displaced
water permeability	error analysis of hydraulic gradient and water flow rate

A 70% confidence interval (one standard deviation) was applied to the calibration data. This relatively liberal confidence interval is justified by the fact that the

measurement errors included systematic errors as well as random errors, and that the random errors were reduced by the smoothing of calculated values using moving averages. For these reasons, the errors estimated here represent an estimate of the error in any single calculated value. However, the average of a series of real time calculations made with the data acquisition system will exhibit less error than that estimated.

Based on the 70% confidence interval, the estimated error in calculations of fluid saturation is ± 0.08 , and the estimated error in calculations of capillary heads is ± 0.86 cm. The error in calculation of water flow rate (Q_w) was estimated from the propagation of error in V_{wd} . The calculation of Q_w from equation (32) was generally accomplished using a minimum ΔV_{wd} of 10 ml. This implies a maximum percent error in Q_w of 12%.

The percent error in calculation of fluid gradients, the error introduced into measured air flow rates by air volume change resulting from head loss and the propagation of these and other errors described above into the error of fluid relative permeability calculations are summarized in Table 5. The error in calculations of fluid gradients is a non-linear function of the magnitude of the gradient, and is greatest for small gradients, where the error in measurement of fluid heads of approximately ± 0.5 cm is large relative to the head drop across the sample. Conversely, the error in Q_a related to air volume change resulting from head loss across the sample length is larger for larger gradients.

At low to moderate gradients, the errors in calculation of fluid relative permeability are largely attributable to the error in measurement of the gradient. The errors in calculation of water relative permeability are greater than for air relative permeability since the measurement of water flow rate has greater error than does air flow rate.

Table 5. Propagation of errors in air and water relative permeability measurements (k_{ra} and k_{rw} , respectively). The percent error in measurement of air and water flow rates (Q_a and Q_w , respectively) was taken as 2.7% and 10%, respectively. The errors estimated here represent an estimate of the error in any single calculated value. However, the average of a series of real time calculations made with the data acquisition system will exhibit less error than that estimated.

Fluid Gradient	% Error Gradient	% Error Q_a (head loss)	% error k_{ra}	% error k_{rw}
0.125	68.5%	0.1%	71.3%	78.5%
0.175	48.9%	0.1%	51.7%	58.9%
0.225	38.0%	0.2%	40.9%	48.0%
0.3	28.5%	0.2%	31.4%	38.5%
0.5	17.1%	0.4%	20.2%	27.1%
0.75	11.4%	0.6%	14.7%	21.4%
1	8.6%	0.8%	12.1%	18.6%
1.25	6.8%	1.0%	10.5%	16.8%
1.5	5.7%	1.2%	9.6%	15.7%
2	4.3%	1.6%	8.6%	14.3%
3	2.9%	2.4%	8.0%	12.9%

4.3.3 Evaluation of Error Related to Non-Uniform Fluid Saturations

The *Brooks and Corey* [1964] and *Parker et al.* [1987] functional relationships (equations (2) through (11)) imply that fluid permeability can be expressed as a single valued function of fluid saturation or capillary head. However, since these functions are non-linear, when fluid saturation varies along the length of a core sample, the bulk measured fluid permeability may be different than that which correlates to the bulk measured fluid saturation in the sample. The error attributable to this difference was evaluated for selected experiments using the following approach, which is outlined in Figure 15.

An error analysis model was developed which exploited the independent measurements of capillary head at the top and base of the sample (h_{ct} , h_{cb}). These measurements reflected the degree of non-uniformity of fluid saturation in the sample, since capillary head is a function of saturation. The model assumed that the Brooks-Corey equations for saturation-capillary head and air relative permeability-capillary head (equations (2) and (6)) were valid and accurate. The model consisted of 100 increments of length which represented the total length of the core sample.

Measured values of h_{ct} and h_{cb} were applied to equation (2) to determine “modeled” values of S_e at the base and top of the sample. The distribution of S_e over the sample length was varied by an exponent which allowed various shapes of the saturation distribution. From this distribution of S_e along the 100 increments of length, a “modeled” bulk value of S_e was determined. This bulk value of S_e was applied to equation (5) to determine the value of k_{ra} which would correlate to the bulk saturation in the sample. This is designated $k_{ra}(Bulk S_e)$.

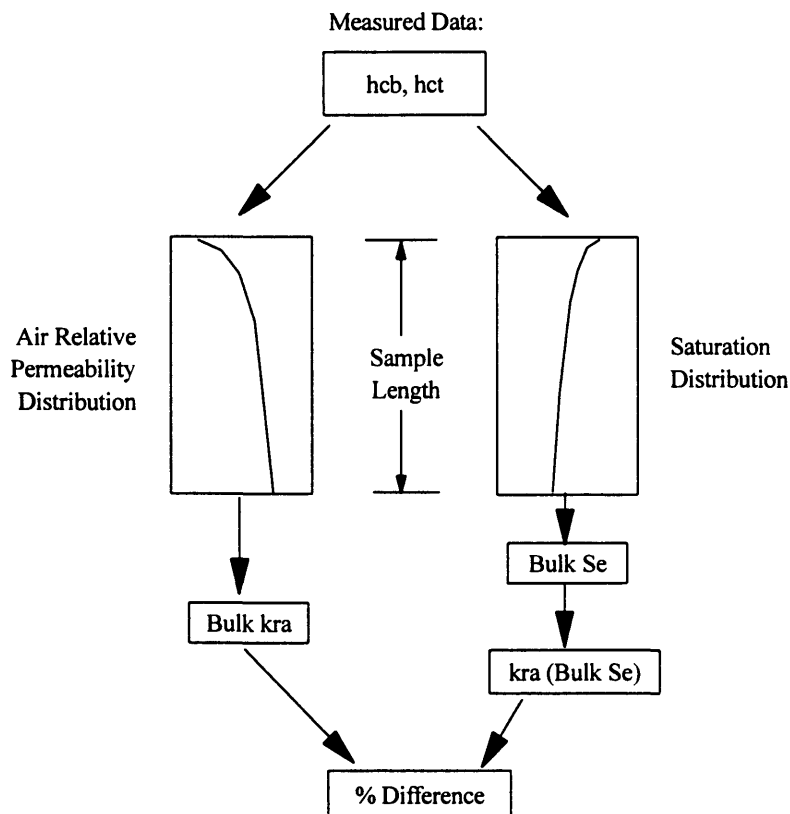


Figure 15. Schematic representation of data flow through the mathematical model for error analysis of non-uniform fluid saturation in core samples tested. Base and top capillary head data (h_{cb} and h_{ct}) were used to evaluate the possible distribution of air relative permeability (k_{ra}) and saturation in the sample using the Brooks-Corey functional relationships for $k_{ra}(h_c)$ and $S_e(h_c)$. From this, a bulk effective saturation ($Bulk S_e$) and a bulk air relative permeability ($Bulk k_{ra}$) were modeled. The modeled bulk air relative permeability was then compared to the air relative permeability which corresponds to the modeled bulk effective saturation ($kra(Bulk S_e)$) to estimate the percent error in kra attributable to non-uniform saturation in the core.

The distribution of k_{ra} along the sample length was modeled using equation (6) and the distribution of fluid saturation determined above. Considering the incremental permeabilities to act in series, the bulk value of k_{ra} which one would expect to measure was determined using the following equation.

$$\text{Bulk } k_{ra} = \frac{L}{\left(\frac{L_1}{k_{ra1}}\right) + \left(\frac{L_2}{k_{ra2}}\right) + \left(\frac{L_3}{k_{ra3}}\right) + \dots + \left(\frac{L_n}{k_{ran}}\right)} \quad (36)$$

where, L = sample length
 L_i = length of model increment i
 k_{rai} = relative air permeability of model increment i
 and, n = number of model increments = 100

The percent difference between the relative air permeability which correlates to the modeled bulk fluid saturation ($k_{ra}(\text{Bulk } S_e)$) and the anticipated measured air relative permeability ($\text{Bulk } k_{ra}$) provided an indication of the possible percent error in k_{ra} measurements related to non-uniform distribution of saturation in the core sample. These results are presented in section 6.1.1.

4.4 Relative Permeability and Air Injection Testing

The relative permeability and air injection testing of each sample was conducted in a sequence of steps outlined below:

- 1) Mount sample in test cell and dry sample using desiccated air.
- 2) Measure dry air conductivity ($K_{a,dry}$).
- 3) Vacuum saturate the sample using upward flow of deaired, deionized water.
- 4) Measure saturated hydraulic conductivity (K_{sat}).
- 5) Measure unsteady state air and water relative permeability (k_{ra}, k_{rw}), fluid saturation (S_w, S_a), and capillary heads (h_{ca}, h_{cb}) during air injection displacement experiment.
- 6) Repeat steps (3) through (5) for several different air injection conditions.

The air injection displacement experiments were generally controlled by the computer system to maintain a constant U_{ab} , which was sometimes manually adjusted during an experiment. This procedure was adopted, because the performance of the upper porous boundary materials frequently prevented condition for uniformity of capillary head ($I_a = I_w + 1$) from being strictly met. The measurement of $K_{a,dry}$ was conducted similarly, but without any water in the pore fluid measurement system. The measurement of K_{sat} was conducted using a constant flow test with upward water flow. The flow rate of water through the sample was regulated by a metering valve, and flow parameters were calculated using equations (37) through (39).

4.5 Gas-Phase Tracer Evaluation of Pore Scale Fingering

A gas-phase tracer was injected with air during several air injection displacement experiments in order to evaluate the possible occurrence of dead-end air fingers and air trapping. Methane (CH_4) gas was selected for use in the experiments for several reasons: CH_4 has relatively low aqueous solubility (approximately 24 mg/l) so that losses to water

were minimized, CH₄ is less dense than air (0.72 kg/m³ vs. 1.3 kg/m³) so that it did not get trapped within the testing apparatus, CH₄ is readily available in small quantities of known concentrations, and CH₄ is detected by an organic vapor analyzer (OVA) with a flame ionization detector (FID).

Methane was injected into the air stream at the base of the sample in 5 cm³ slugs of a 1.25% concentration, and detected by a Foxboro OVA/FID (model 128) which recovered the outlet air stream from the test apparatus (Figure 16). The OVA/FID was interfaced to the computer data acquisition system, so that the CH₄ concentration detected by the instrument was recorded during testing. The mass of CH₄ recovered from each slug injected was determined by integrating the measured concentration data over the flow rate through the instrument and time. For each test conducted, the first 5 cm³ slug of methane was injected with the initial air to invade the sample. After this slug of methane passed through the sample and the OVA/FID readings returned to zero, a series of calibration injections of 1cm³. of 1.25% CH₄ were injected directly into the instrument, and then another 5 cm³. slug was injected into the sample. This sequence was generally repeated from 4 to 6 times for each test conducted.

The percent recovery of each methane slug was calculated from the ratio of the mass recovered of the tracer injected into the sample and the preceding calibration injection into the OVA. Calibration of the percent of tracer recovered through the experimental system was achieved by injecting slugs of tracer gas into the experimental system, but without a soil sample present. These data (Figure 17), showed that tracer recovery was 89.8 ± 2.0 percent, at a 90% confidence interval. The loss of approximately 10% of the tracer slugs may be attributable to diffusion, solubilization, or absorption to the polyethylene and tubing where the tracer gas was injected.

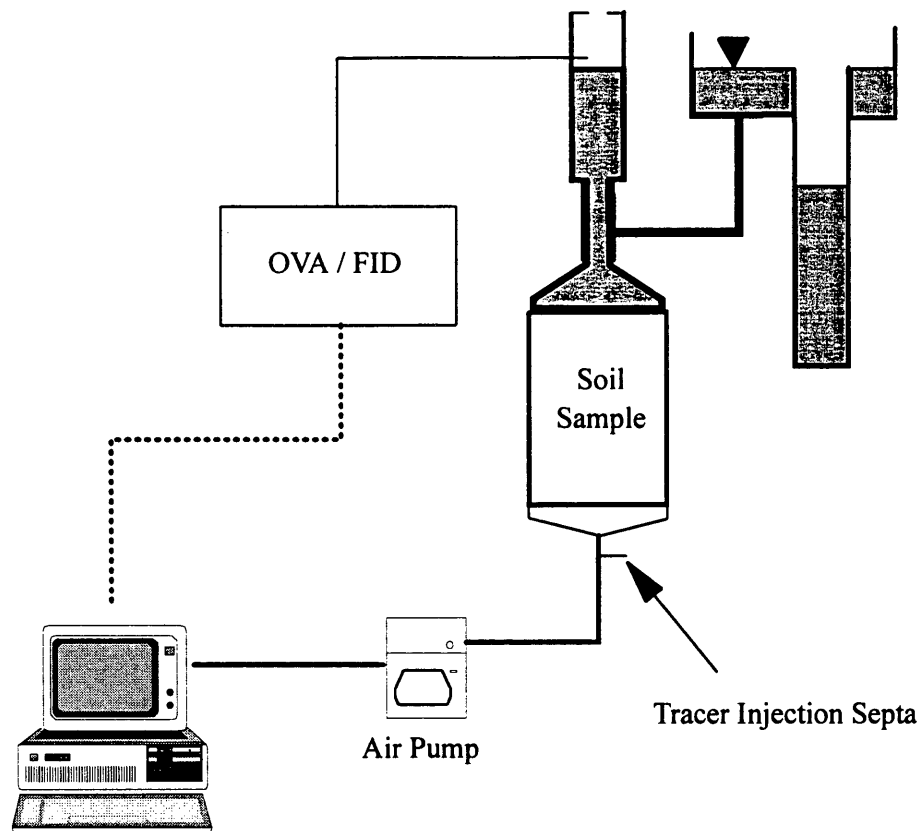


Figure 16. The gas-phase tracer system consisted of a tracer injection septa in the base air injection plumbing, and an OVA/FID which measured CH_4 in the outlet air stream from the pore fluid measurement and control system.

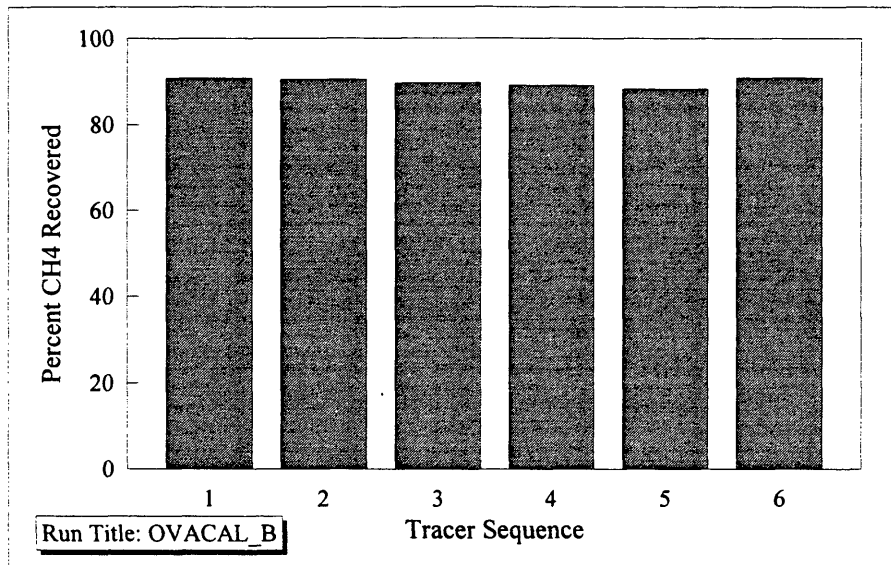


Figure 17. Calibration data for methane tracer recovery through the experimental system, without a soil sample present.

Section 5

RESULTS

5.1 Soil Samples Tested

The results of testing of five soil samples are presented. Three of the five samples consisted of duplicate specimens of natural subsurface geologic material. Two of the samples were remolded soils, for which duplicate specimen handling as shown in Figure 7 was not required. A brief discussion of each of the samples tested follows.

The sample identified as “FLO” was obtained from Dr. Paul Lundegard of Unocal Corporation and was collected from a site in Florence, Oregon which was the subject of extensive air sparging studies reported in *Lundegard and LaBrecque* [1995] and Lundegard and Anderson [1993]. These studies included field measurements of air saturations during air sparging using 3-D electrical resistance tomography (ERT), and numerical modeling of the air flow behaviors at the site. Soil at this site consists of dune sand. Duplicate samples were evaluated as shown in Figure 7.

The sample identified as “COR” was obtained from Groundwater Technology, Inc. from a government site air sparging project at Coronado Bay in San Diego, California. Air saturations at this site were measured during air sparging using time domain

reflectometry (TDR) as reported by *Clayton et al.* [1995]. Soil at this site consists of hydraulic fill, i.e. sediment dredged from San Diego Bay and emplaced in a slurry-phase. Core recovery from this site was poor, and samples analyzed were remolded approximately to the in-situ porosity measured using TDR, so specimens analyzed were not considered duplicates.

The sample identified as “COL” was also obtained from Groundwater Technology, Inc., from an industrial site air sparging project in Wichita, Kansas. TDR was also used at this site to measure air saturations during sparging [*Clayton and Nelson*, 1995]. Soils at this site consist of fluvial sedimentary deposits. Duplicate cores were analyzed.

The sample identified as “CSM” was designed at the Colorado School of Mines laboratory to achieve specific grain size criteria. The material consisted of a mixture of commercially available “play sand” and glacial till collected from Georgetown, Colorado. Specimens were remolded to a specific density and were not considered duplicates.

The sample identified as “CHV” was obtained from Groundwater Technology, Inc. from a retail petroleum site air sparging project in New Mexico. Soils at this site consisted of alluvial sedimentary deposits. Duplicate soil cores were analyzed.

5.2 Physical Characterization of Test Specimens

The grain size distributions for the five soils tested is shown in Figure 18. Samples which were analyzed from duplicate cores are designated with the subscripts “_smc” (for soil moisture characterization) and “_inj” (for air injection testing) to distinguish

between duplicates. Figure 18 also shows the mean grain size (D_{50}) and coefficient of uniformity (C_u) for each sample. Table 6 shows the D_{50} , C_u , C_c (coefficient of gradation), and USCS classification for each sample, as well as the porosity and dry bulk density which were determined from the tempe cell testing. Raw grain size distribution data are in Appendix B.

The grain size distribution of duplicate core samples was generally similar, except for sample COL_inj which was significantly coarser than sample COL_smc.

The samples tested represented a range of textures typical of granular soils. Sample FLO consisted of a uniform fine sand, composed primarily of sub-rounded, spherical soil grains. Sample COR consisted of a uniform fine sand composed largely of plate-structured grains derived from micaceous minerals and disintegrated shells. Sample COL consisted of a fine to coarse sand composed primarily of sub-rounded, spherical quartz and feldspar grains. Sample CSM consisted of a fine to coarse sand composed primarily of angular, non-spherical grains of quartz and feldspar. Sample CHV consisted of a silty fine to medium sand. The coarse fraction of this sample consisted primarily of well rounded, sub-angular grains.

5.3 Moisture Retention Data

Moisture retention data collected using the pressure cell apparatus (Appendix C) were plotted as h_c vs. S_w (Figures 19 - 23). The h_c - S functions of *Brooks and Corey* [1966] and *Parker et al.* [1987] (equations (2) and (7), respectively) were fit visually to the measured data in order to determine values of S_r , h_o , λ , α , and n (Table 7). Two curves based on the

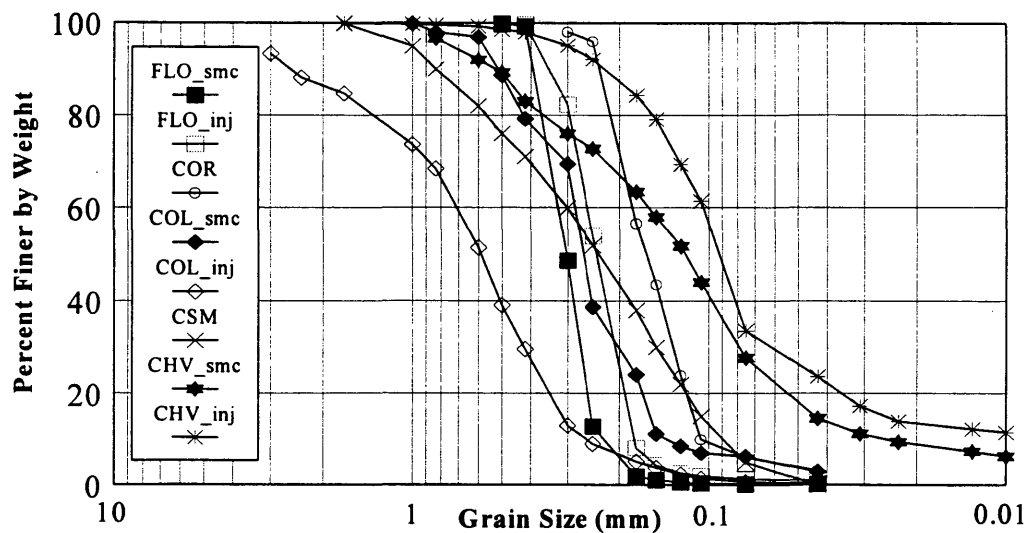


Figure 18. Soil grain size distribution curves for samples tested.

Table 6. Summary of physical soil characteristics. C_u = uniformity coefficient, C_c = coefficient of gradation, D_{50} = mean grain size, ϕ = porosity, ρ_d = dry bulk density, USCS = USCS soil classification.

Sample ID	C_u	C_c	D_{50} (mm)	ϕ	ρ_d (g/cm ³)	USCS
FLO_smc	1.5	1.1	0.30	0.398	1.58	SP
FLO_inj	1.5	0.8	0.24	--	--	SP
COR	1.7	0.9	0.16	0.45	1.42	SP-SM
COL_smc	1.7	1.2	0.26	0.38	1.60	SP-SM
COL_inj	2.7	1.0	0.61	--	--	SP
CSM	3.3	.08	0.24	0.37	1.63	SP
CHV_smc	4.8	1.2	0.12	0.33	1.78	SM
CHV_inj	3.2	1.4	0.09	--	--	SM

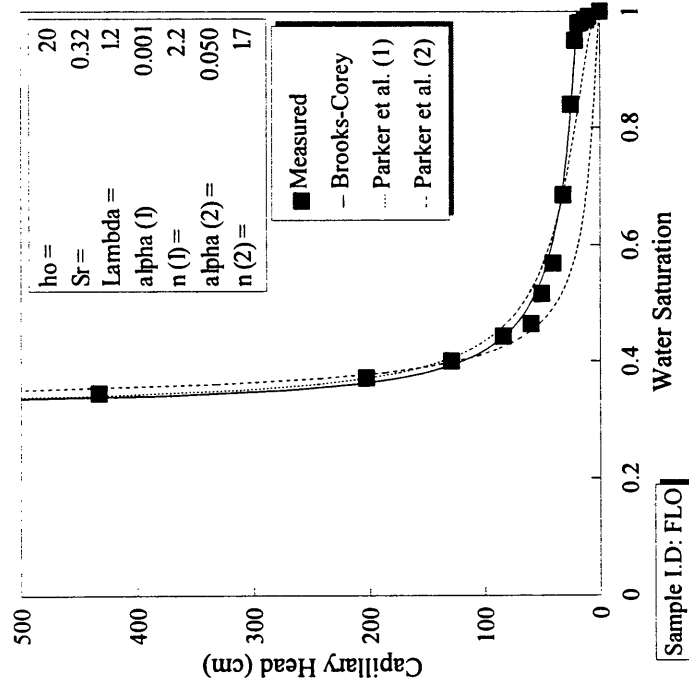


Figure 19A. Soil moisture retention data and Brooks-Corey and Parker et al. curves. Sample FLO. h_o = air entry pressure head, S_r = residual saturation, Lambda (λ) = Brooks-Corey pore size distribution index, alpha (α), and n are the Parker et al. indices for (1) best visual fit and (2) best fit with $\alpha = 1/h_o$.

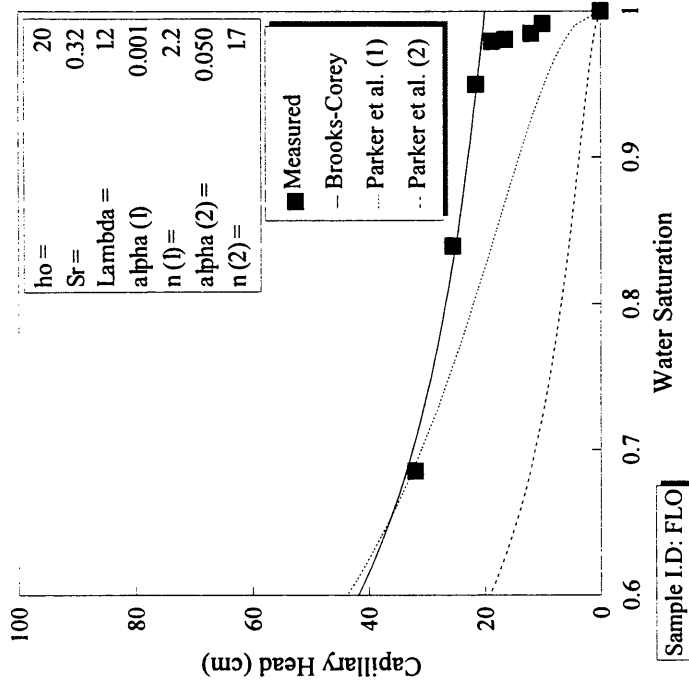


Figure 19B. Soil Moisture Retention Data and Brooks-Corey and Parker et al. curves at high Water Saturation. Sample FLO. h_o = air entry pressure head, S_r = residual saturation, Lambda (λ) = Brooks-Corey pore size distribution index, alpha (α), and n are the Parker et al. indices for (1) best visual fit and (2) best fit with $\alpha = 1/h_o$.

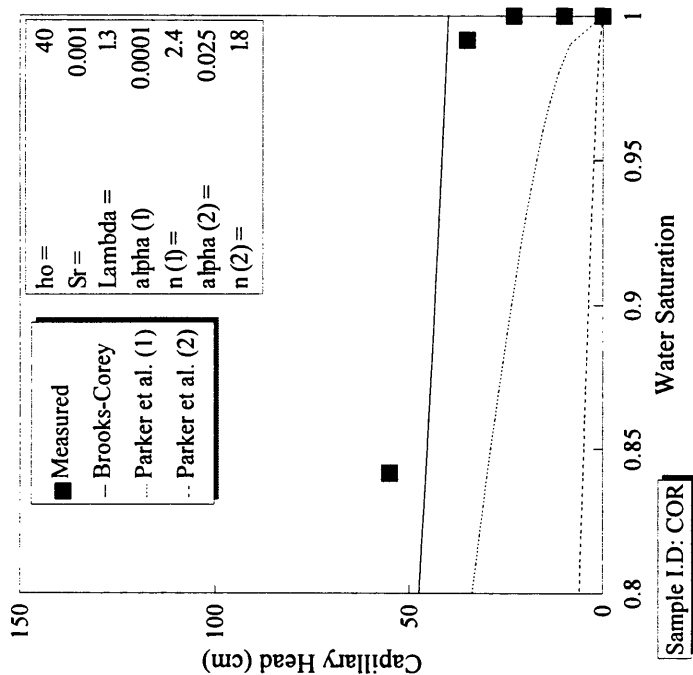


Figure 20A. Soil moisture retention data and Brooks-Corey and Parker et al. curves. Sample COR. h_o = air entry pressure head, S_r = residual saturation, Lambda (λ) = Brooks-Corey pore size distribution index, alpha (α), and n are the Parker et al. indices for (1) best visual fit and (2) best fit with $\alpha = 1/h_o$.

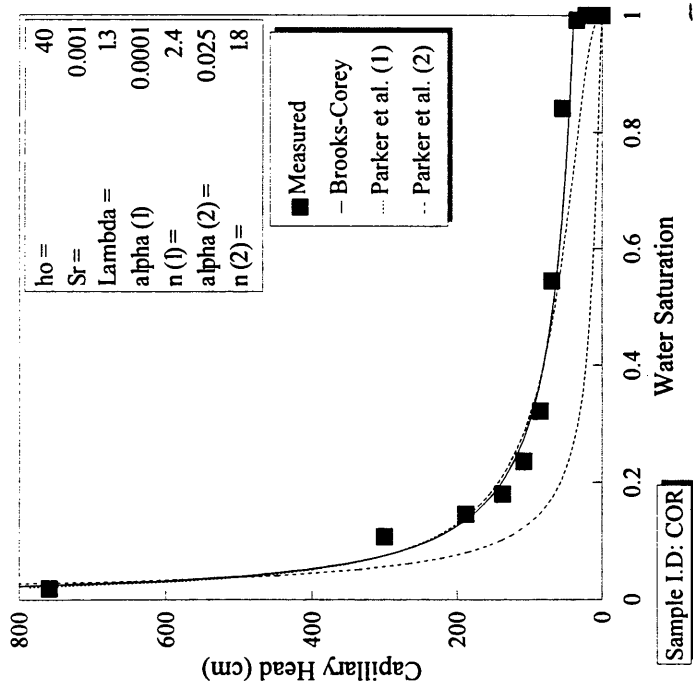


Figure 20B. Soil moisture retention data and Brooks-Corey and Parker et al. curves at high Water Saturation. Sample COR. h_o = air entry pressure head, S_r = residual saturation, Lambda (λ) = Brooks-Corey pore size distribution index, alpha (α), and n are the Parker et al. indices for (1) best visual fit and (2) best fit with $\alpha = 1/h_o$.

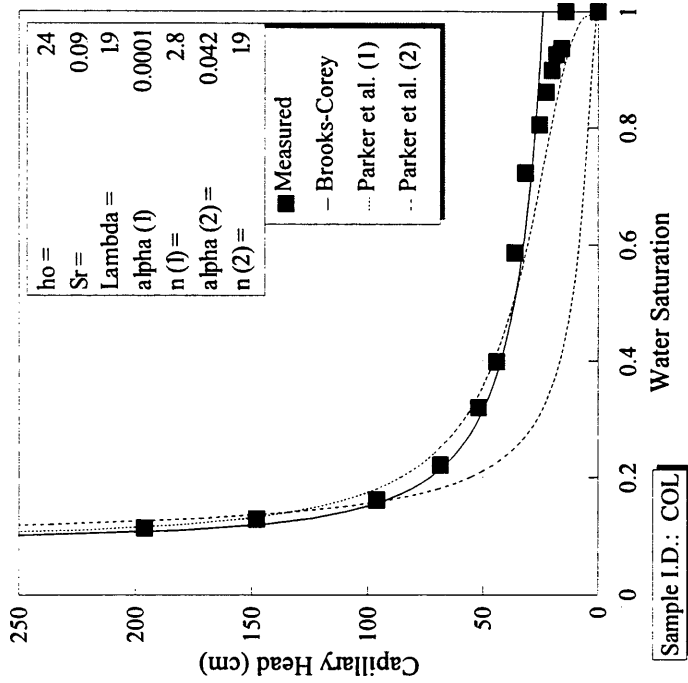


Figure 21A. Soil moisture retention data and Brooks-Corey and Parker et al. curves. Sample COL. h_o = air entry pressure head, S_r = residual saturation, Lambda (λ) = Brooks-Corey pore size distribution index, alpha (α), and n are the Parker et al. indices for (1) best visual fit and (2) best fit with $\alpha = 1/h_o$.

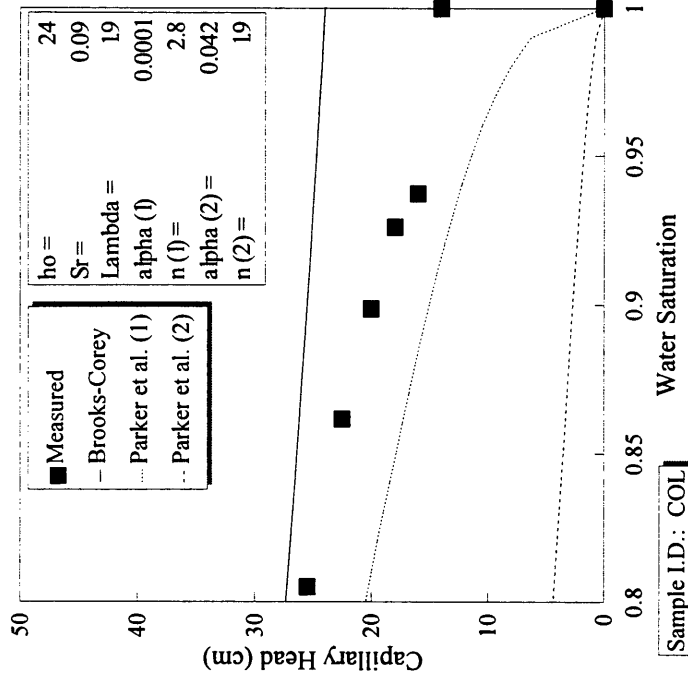


Figure 21B. Soil Moisture Retention Data and Brooks-Corey and Parker et al. curves at high Water Saturation. Sample COL. h_o = air entry pressure head, S_r = residual saturation, Lambda (λ) = Brooks-Corey pore size distribution index, alpha (α), and n are the Parker et al. indices for (1) best visual fit and (2) best fit with $\alpha = 1/h_o$.

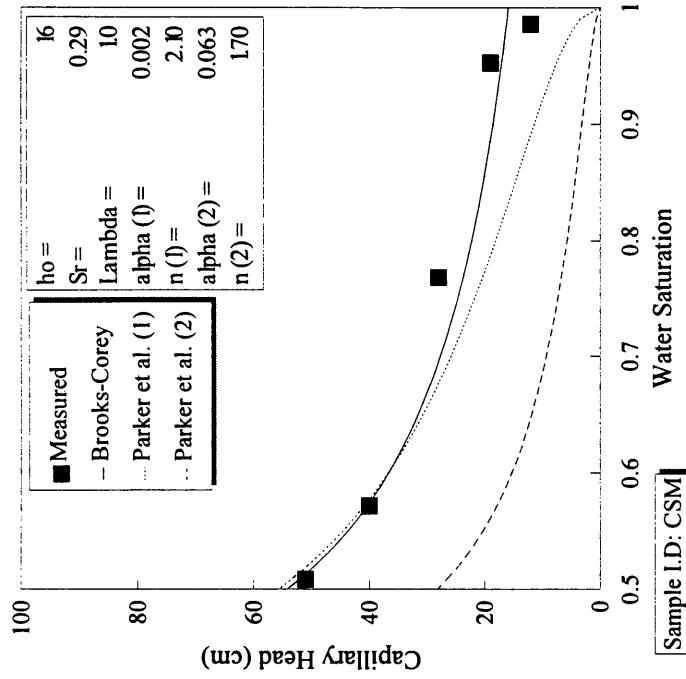


Figure 22A. Soil moisture retention data and Brooks-Corey and Parker et al. curves. Sample CSM. h_o = air entry pressure head, S_r = residual saturation, Lambda (λ) = Brooks-Corey pore size distribution index, alpha (α), and n are the Parker et al. indices for (1) best visual fit and (2) best fit with $\alpha = 1/h_o$.

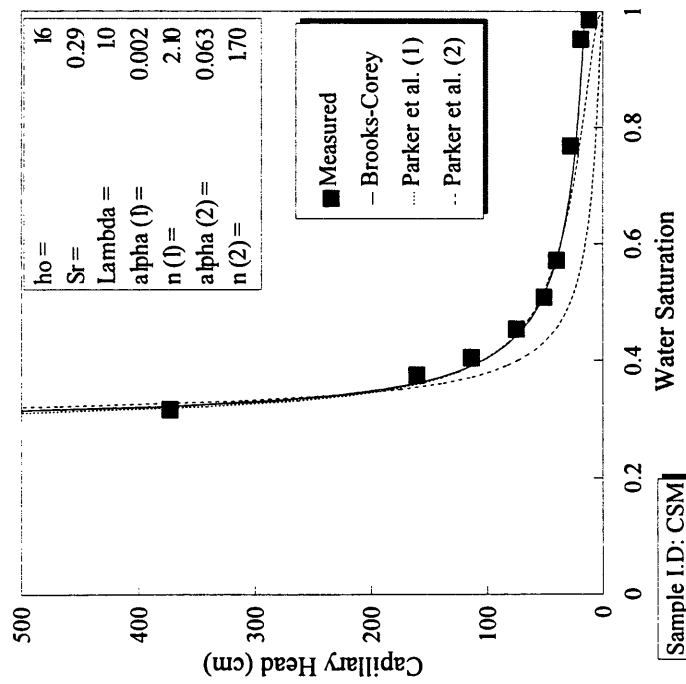


Figure 22B. Soil Moisture Retention Data and Brooks-Corey and Parker et al. curves at high Water Saturation. Sample CSM. h_o = air entry pressure head, S_r = residual saturation, Lambda (λ) = Brooks-Corey pore size distribution index, alpha (α), and n are the Parker et al. indices for (1) best visual fit and (2) best fit with $\alpha = 1/h_o$.

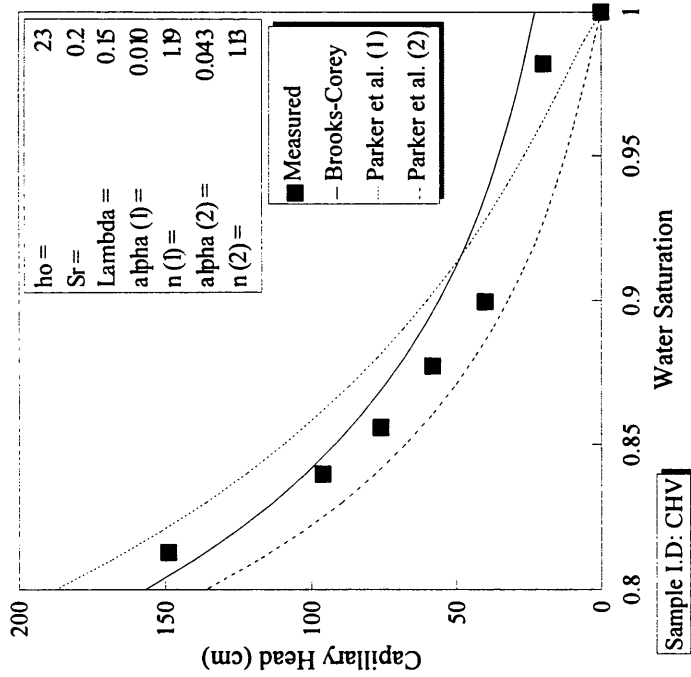


Figure 23A. Soil moisture retention data and Brooks-Corey and Parker et al. curves. Sample CHV. h_o = air entry pressure head, S_r = residual saturation, Λ = Brooks-Corey pore size distribution index, α and n are the Parker et al. indices for (1) best visual fit and (2) best fit with $\alpha = 1/h_o$.

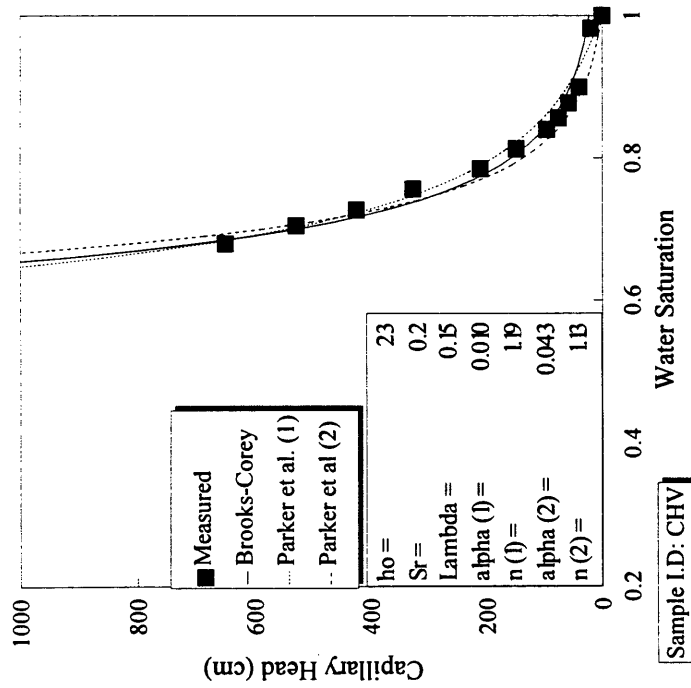


Figure 23B. Soil moisture retention data and Brooks-Corey and Parker et al. curves at high Water Saturation. Sample CHV. h_o = air entry pressure head, S_r = residual saturation, Λ = Brooks-Corey pore size distribution index, α and n are the Parker et al. indices for (1) best visual fit and (2) best fit with $\alpha = 1/h_o$.

Table 7. Summary of moisture retention characteristics. S_r = residual saturation, h_o = air entry pressure head, λ = Brooks-Corey pore size distribution index, and α and n are the Parker et al. pore size indices. Parker et al. indices (1) represent a best visual fit, while indices (2) are based on a visual best fit for $\alpha = 1/h_o$.

Sample ID	FLO	COR	COL	CSM	CHV
S_r	0.32	0.001	0.09	0.29	0.20
h_o	20	40	24	16	23
λ	1.2	1.3	1.9	1.0	0.15
α (1)	0.001	0.0001	0.0001	0.002	0.010
n (1)	2.2	2.4	2.8	2.10	1.19
α (2)	0.050	0.025	0.042	0.063	0.043
n (2)	1.7	1.8	1.9	1.70	1.13

Parker et al. equation were fit to the data for each sample: (1) a curve based on the best visual fit obtained, and (2) a curve based on $\alpha = 1/h_o$. While the set of curves based on (2) provides a poor fit to the measured data, the values of α and n are in closer agreement to values used by Parker et al. for sand and clay soils ($\alpha = 0.052$ and 0.032 , $n = 1.84$ and 1.86 , respectively). The values derived from (1) were also found to provide unreasonable estimates of relative permeability, while the values derived from (2) provided reasonable relative permeability estimates, as will be shown in section 5.5.3.

The Brooks-Corey pore size distribution index (λ) determined from the moisture retention data was between 1.0 and 1.9 for all soils tested, except sample CHV for which $\lambda = 0.15$. The values of λ determined for samples FLO, COR, COL, and CSM reflect the

sandy, relatively uniform grain size distribution of the materials, which is expressed in the relatively small slope of the drainage curves at high to moderate water saturations. The smaller value of λ determined for sample CHV reflects its finer grained, less uniform texture, which results in a steeper slope of the moisture retention curve.

5.4 Intrinsic Permeability Data

The intrinsic permeability of the soils was calculated from both the saturated hydraulic conductivity and the dry air conductivity of soil core samples in order to compare the air and water permeabilities. Saturated hydraulic conductivities were measured before each individual air injection experiment in order to determine the permeability changes which resulted from air sparging. Water intrinsic permeabilities were calculated from the saturated hydraulic conductivity value determined prior to air injection testing (K_{sat}).

Air and water conductivities were calculated with the data acquisition system, generally over a range of flow rates. Typical dry air conductivity and saturated hydraulic conductivity data are shown in Figures 24 and 25, respectively. For each test, these data were averaged to determine a representative value of the fluid conductivity. These values are summarized in Tables 8 and 9. Intrinsic permeabilities calculated from the fluid conductivity data are summarized in Table 10.

F-test and t-test statistics were evaluated to determine the similarity of measured air and water intrinsic permeabilities. The calculated F test statistic was 4.59, with a critical F-value of 6.39 (95 % confidence interval), indicating that the sample variances were not dissimilar. The calculated students t-test statistic was 0.885, at a critical value of 2.31,

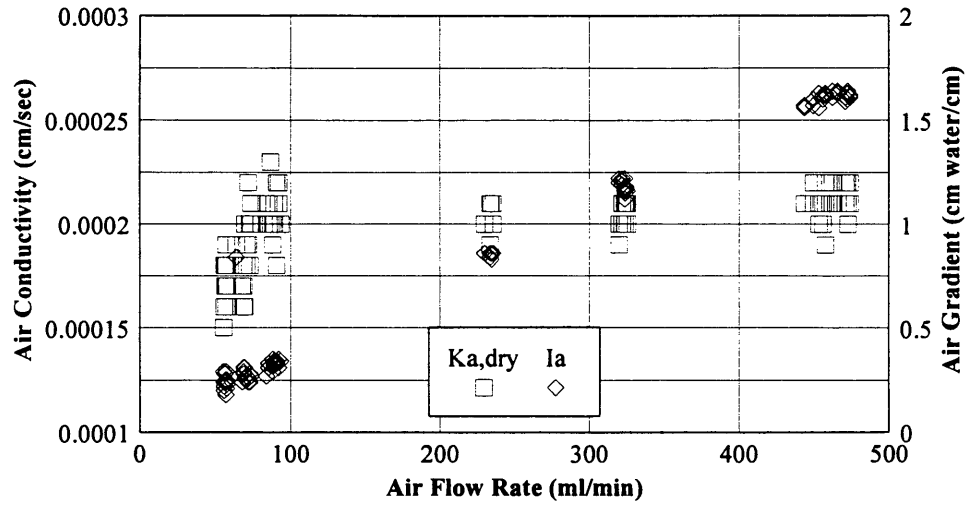


Figure 24. Typical data from a dry air conductivity ($K_{a,dry}$) test over a range of air flow rates and air gradients (I_a), sample CSM.

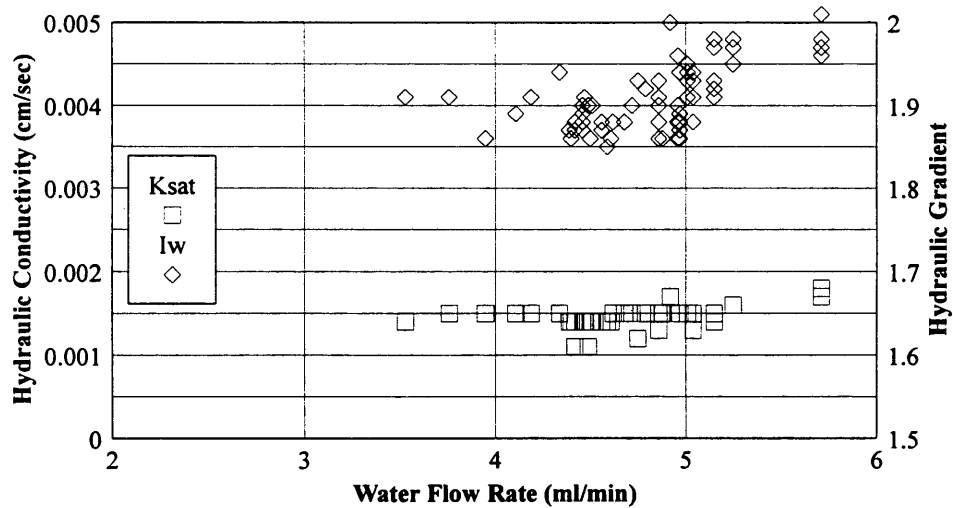


Figure 25. Typical data from a saturated hydraulic conductivity (K_{sat}) test over a range of flow rates and hydraulic gradients (I_w), sample CHV K_{sat} 1.

Table 8. Summary of dry air conductivities measured prior to air injection testing.

Sample ID	FLO	COR	COL	CSM	CHV
$K_{a,dry}$ (cm/sec)	0.0011	0.00055	0.0028	0.00020	0.00024

Table 9. Summary of saturated hydraulic conductivities measured prior to air injection testing (K_{sat} 1) and then sequentially (K_{sat} 2, K_{sat} 3, etc.) prior to multiple air injection tests.

Sample ID	FLO	COR	COL	CSM	CHV
K_{sat} 1 (cm/sec)	0.0633	0.0065	0.055	0.004	0.0014
K_{sat} 2 (cm/sec)	0.0640	0.0065	0.060	0.0042	0.0013
K_{sat} 3 (cm/sec)	0.054	0.0037	0.018	--	0.0017
K_{sat} 4 (cm/sec)	0.053	--	0.014	--	--
K_{sat} 5 (cm/sec)	0.052	--	0.012	--	--
K_{sat} 6 (cm/sec)	0.044	--	0.0064	--	--
K_{sat} 7 (cm/sec)	0.044	--	--	--	--
K_{sat} 8 (cm/sec)	0.045	--	--	--	--

Table 10. Intrinsic permeability data calculated from air and water fluid conductivities.

Sample	FLO	COR	COL	CSM	CHV
k (air) (cm ²)	1.6e-07	8.2e-08	4.2e-07	3.0e-08	3.6e-08
k (water) (cm ²)	7.2e-07	7.4e-08	6.3e-07	4.6e-08	1.6e-08

indicating that the means were not dissimilar. These results indicate that the air and water intrinsic permeabilities were essentially the same, which demonstrates that gas slippage, or the Klinkenberg effect was insignificant within the level of the error of the system. This observation is consistent with the relatively coarse texture of the samples tested, compared to the fine grained media which are susceptible to the Klinkenberg effect.

The sequence of saturated hydraulic conductivity data collected before each displacement experiment (Table 9) revealed a decreasing trend for sample COL, which may be attributable to the effects of air sparging. However, other samples did not show a significant trend, suggesting that the results from sample COL may represent errors such as incomplete saturation of the sample prior to testing.

5.5 Air Injection Displacement Experiment Results

Eighteen air injection displacement experiments were completed using 5 soil specimens. These 18 experiments generated data in each of the following 4 categories: (1) temporal two-phase flow data, (2) capillary head-saturation data, and (3) air and (4) water relative permeability data. Representative results were selected from each of these

four categories of data (Table 11) which illustrate the variety of behaviors observed in the 18 experiments. Sufficient results were selected to also show reproducibility of behaviors in certain samples, as well as sensitivity of the behaviors to different air injection conditions. The full set of data in all four categories for all 18 experiments is included in Appendix D.

5.5.1 Temporal Two-Phase Flow Data

The temporal two-phase flow data represent the changes in flow parameters over time during the experiments. The representative data presented here primarily reflect the varied and unique histories of the experiments. In many instances, these results show the response of pore fluid heads, saturations, and air and water flow parameters to changes in the air injection pressure head set-point. Additionally, some of the data reflect transient changes in state of the flow system and coupled air and water flow phenomena which were independent of any changes in experimental operating parameters.

Experiment FLO_2L involved a base air injection pressure head of approximately 175 cm (Figure 26), which was 33 cm above the initial base hydrostatic pressure head. The magnitude of U_{at} was externally controlled by the top porous boundary to be approximately equal to 165 cm. Both U_{wb} and U_{wt} decreased rapidly during the first hour, and reached more or less steady values after four hours. As the sample drained, S_w decreased non-linearly over the test, and reached a steady value of 0.36 after four hours (Figure 27). A brief increase in U_{ab} at two hours resulted in a coupled transient increase in the rate of drainage. Both h_{cb} and h_{ct} increased rapidly during the first minutes of the test, and stabilized after approximately one hour at values of 36 and 38 cm, respectively.

Table 11. Experiment results which are described herein. These results were selected to represent typical behaviors observed in each of the four categories of data.

Experiment	Temporal Data	h_c -S Data	k_{ra} Data	k_{rv} Data
FLO_2I			✓	
FLO_2L	✓		✓	
FLO_2P		✓	✓	✓
FLO_1K			✓	
COR_3A		✓	✓	
COR_3B				✓
COR_3C	✓		✓	
COR_3E	✓	✓	✓	✓
COL_2C	✓	✓	✓	
COL_2E		✓	✓	
COL_2G	✓		✓	
COL_1H	✓	✓	✓	
COL_1J				✓
CSM_1E		✓	✓	
CSM_1H			✓	✓
CHV_1F				✓
CHV_1H		✓	✓	
CHV_1K			✓	

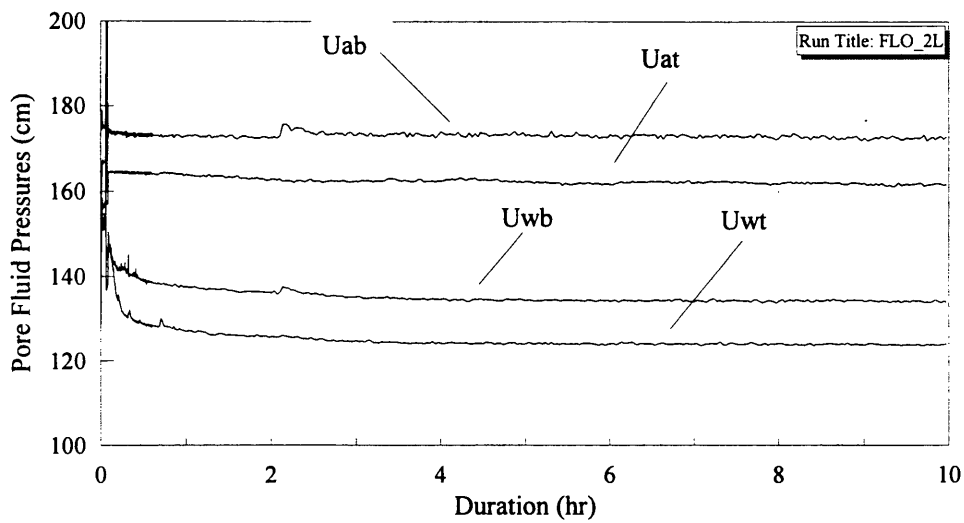


Figure 26. Temporal fluid pressure head data. Experiment FLO_2L. U_{ab} = base pore air head, U_{at} = top pore air head, U_{wb} = base pore water head, U_{wt} = top pore water head

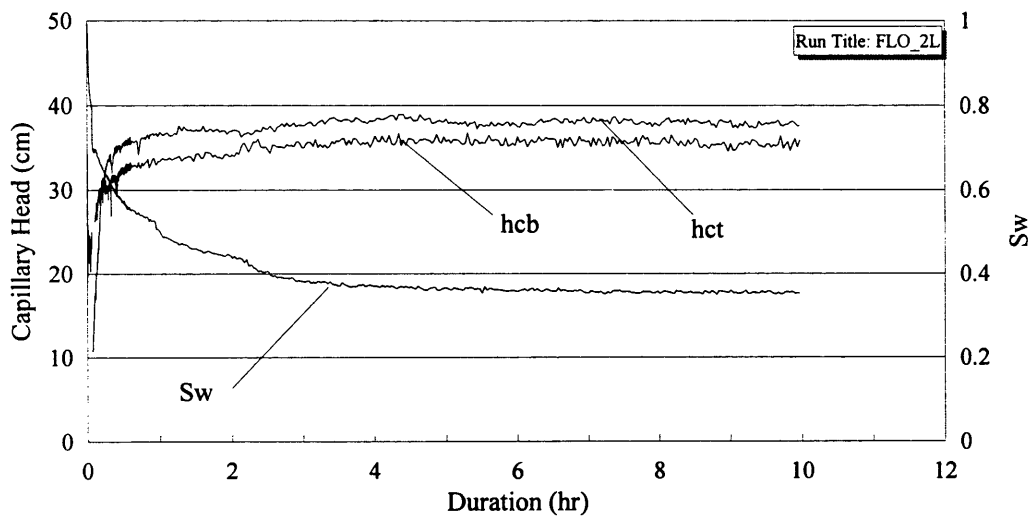


Figure 27. Temporal water saturation (S_w) and top and base capillary head (h_{ct} and h_{cb}) data. Experiment FLO_2L.

During the first four hours of experiment FLO_2L, k_{ra} increased to approximately 0.5 (Figure 28). During this period, Q_a generally increased and I_a generally decreased. The temporary increase in air injection pressure head at two hours resulted in an increase in I_a and Q_a . Approximately 15 minutes after this increase, k_{ra} experienced an incremental increase, which can be correlated to the decrease in S_w at this time.

The transient water flow behaviors during experiment FLO_2L were mostly manifested in the first hour of the test (Figure 29). After air injection was initiated, I_w was large, but after air breakthrough at the top of the sample, I_w became negative and then rose to values slightly above zero within the first hour. Note that during this period, water drainage continued despite the negative value of I_w . The increase in U_{ab} at two hours was accompanied by a transient increase in I_w .

During the first two hours of experiment COR_3E, U_{ab} was increased incrementally from 250 cm (107 cm above the hydrostatic base pore water head) to 280 (Figure 30). The magnitude of U_{at} increased with each incremental increase in U_{ab} , due to impedance of the top porous boundary which limited the rate of air flow through the sample. At approximately 10 hours, U_{at} increased without any change in air injection conditions. Over the duration of the experiment, U_{wb} and U_{wt} decreased to achieve capillary heads which rose from 30 cm to greater than 120 cm at the top and 70 cm at the base of the sample after 18 hours. After 10 hours, U_{wb} and U_{wt} showed brief, pulsed increases, which were coincident with the increase in U_{at} . Transient behaviors in capillary head data after 10 hours (Figure 31) are related to these pulses, as pore air pressure heads were relatively stable.

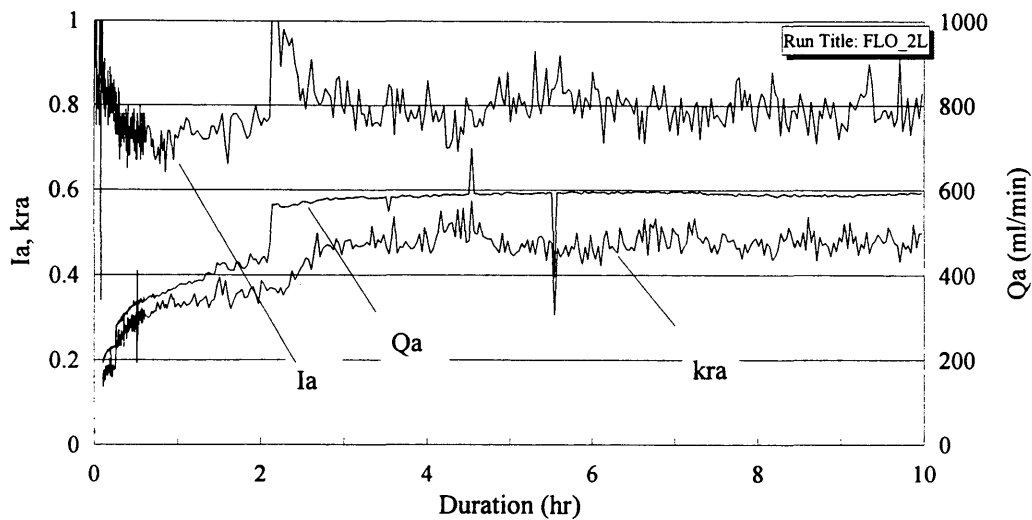


Figure 28. Temporal air flow data. Experiment FLO_2L. I_a = air gradient (cm water/cm), Q_a = air flow rate, k_{ra} = air relative permeability

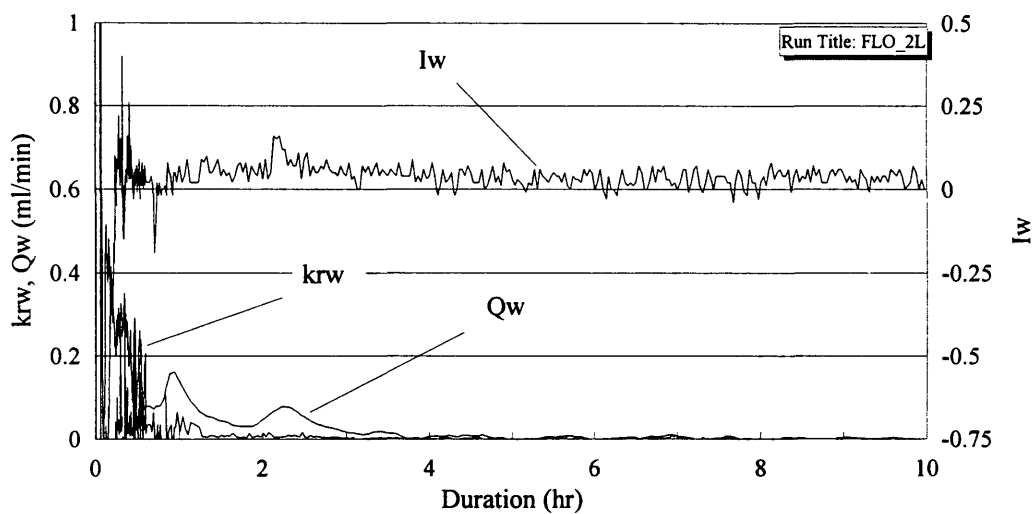


Figure 29. Temporal water flow data. Experiment FLO_2L. I_w = hydraulic gradient, Q_w = water flow rate, k_{rw} = water relative permeability

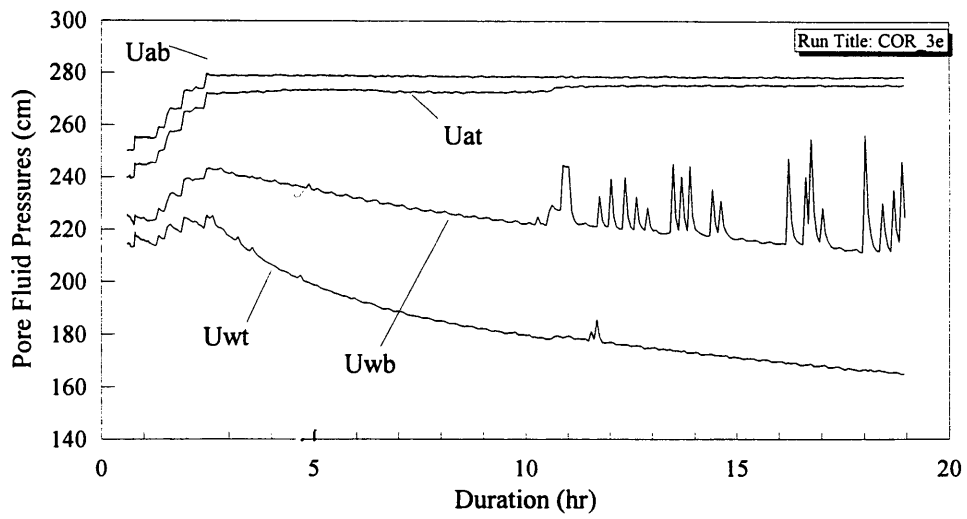


Figure 30. Temporal fluid pressure head data. Experiment COR_3E. U_{ab} = base pore air head, U_{at} = top pore air head, U_{wb} = base pore water head, U_{wt} = top pore water head

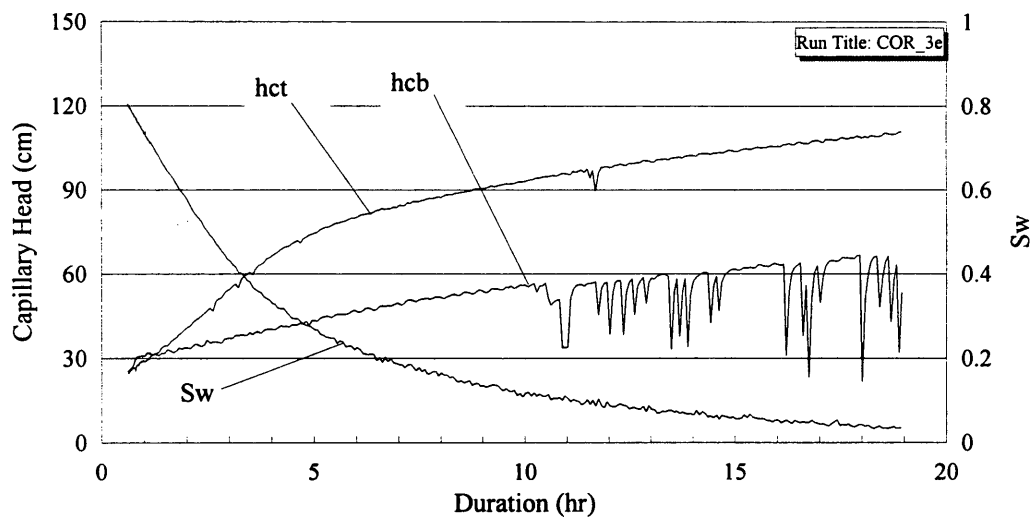


Figure 31. Temporal water saturation (S_w) and top and base capillary head (h_{ct} and h_{cb}) data. Experiment COR_3E.

The air pressure gradient generally decreased over time during experiment COR_3E (Figure 32), with the exception of an increase at approximately six hours, related to an increase in Q_a . At approximately 10 hours, I_a decreased dramatically, and k_{ra} increased dramatically, while Q_a remained essentially unchanged. Water flow behaviors were mostly manifested in the first five hours of the experiment, with the exception of pulses in I_w after 10 hours (Figure 33).

Experiment COR_3C was conducted in two phases. Initially, a low air injection pressure of 165 cm (20 cm above the hydrostatic base pore water head) was imposed on the sample, which resulted in drainage of the sample to a $S_w \approx 0.8$ over a period of four hours (Figures 34 and 35). After S_w stabilized at 0.8, U_{ab} was increased to approximately 185 cm. This resulted in increased water drainage, down to $S_w \approx 0.35$ after 20 hours.

Capillary heads during the first phase of experiment COR_3C were approximately equal to 20 cm (Figure 35) with h_{ct} slightly larger than h_{cb} . In the second phase of the experiment, h_{ct} rose to above 40 cm, while h_{cb} rose to about 30 cm.

At the beginning of the second phase of experiment COR_3C, I_a increased in a step-like manner, while Q_a and k_{ra} increased steadily and began to stabilize after 30 hours (Figure 36). Also, I_w increased at the beginning of the second phase, and as drainage occurred k_{rw} decreased (Figure 37).

Experiment COL_2G was conducted at $U_{ab} \approx 500$ cm (356 cm above the base hydrostatic pore water head) (Figure 38). At approximately 32 hours, U_{at} experienced a step increase. Over the full 55-hour duration of the test, S_w decreased to approximately 0.1 (Figure 39), while h_{cb} rose to 30 cm, and h_{ct} rose to more than 100 cm. At

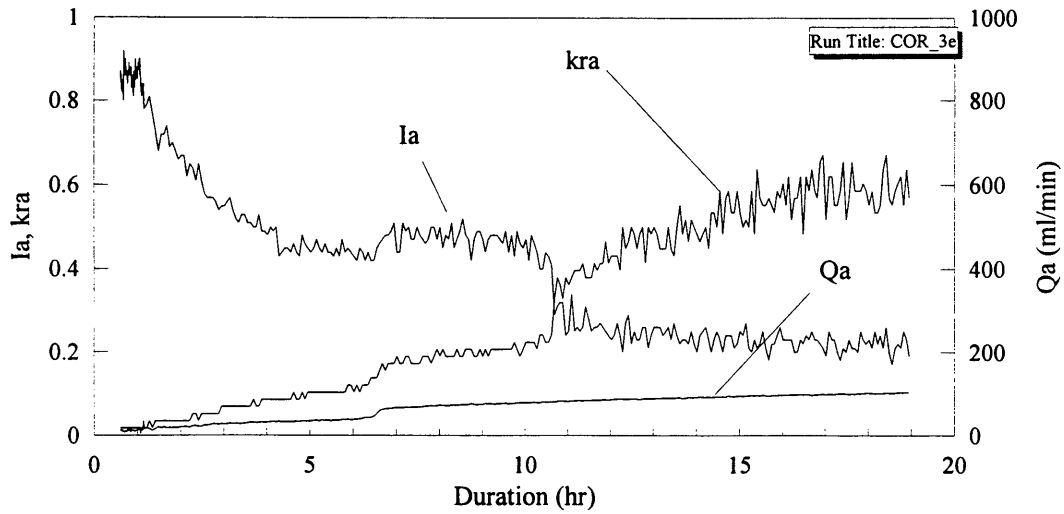


Figure 32. Temporal air flow data. Experiment COR_3E. I_a = air gradient (cm water/cm), Q_a = air flow rate, k_{ra} = air relative permeability

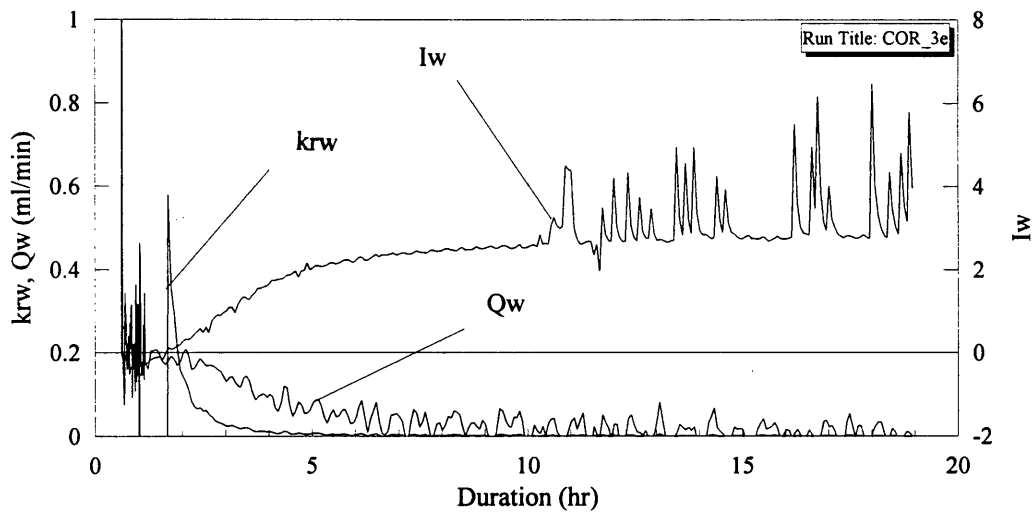


Figure 33. Temporal water flow data. Experiment COR_3E. I_w = hydraulic gradient, Q_w = water flow rate, k_{rw} = water relative permeability

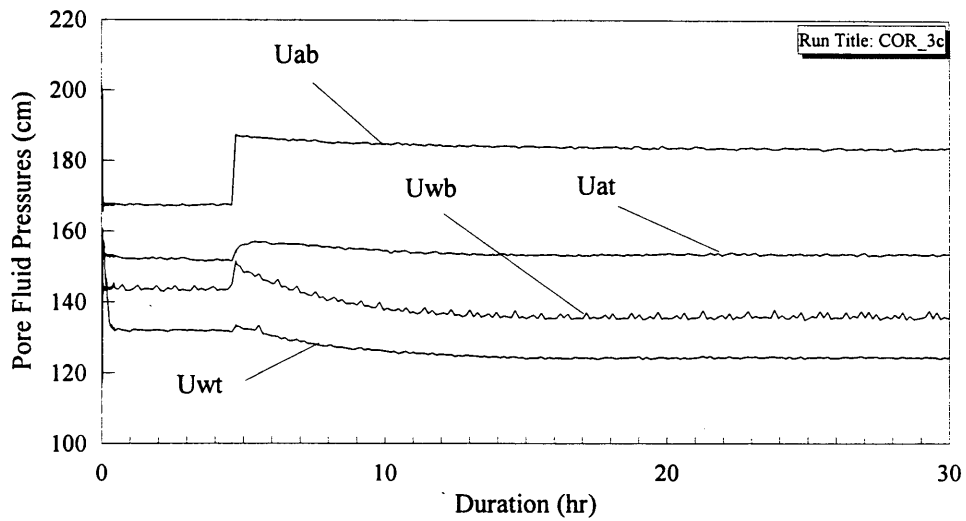


Figure 34. Temporal fluid pressure head data. Experiment COR_3C. U_{ab} = base pore air head, U_{at} = top pore air head, U_{wb} = base pore water head, U_{wt} = top pore water head

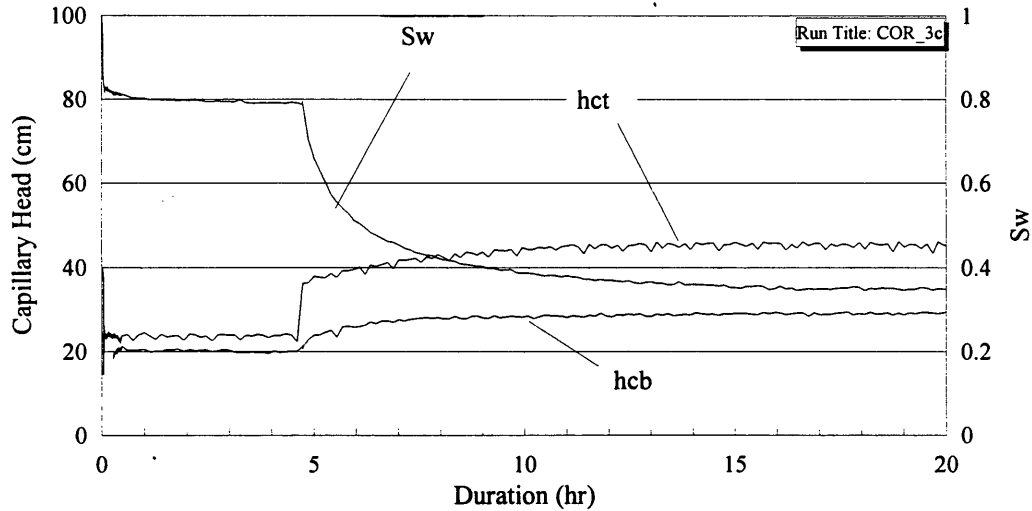


Figure 35. Temporal water saturation (S_w) and top and base capillary head (h_{ct} and h_{cb}) data. Experiment COR_3C.

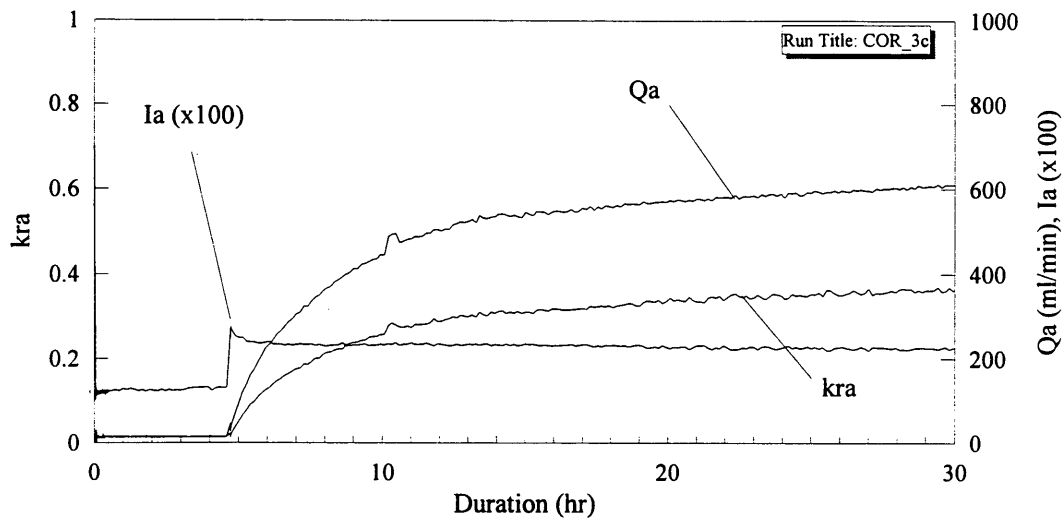


Figure 36. Temporal air flow data. Experiment COR_3C. I_a = air gradient (cm water/cm), Q_a = air flow rate, k_{ra} = air relative permeability

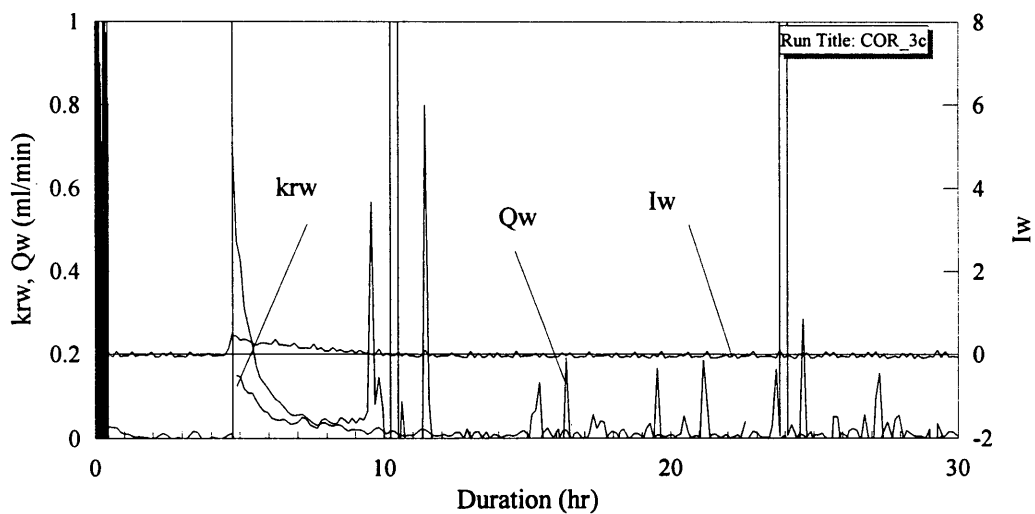


Figure 37. Temporal water flow data. Experiment COR_3C. I_w = hydraulic gradient, Q_w = water flow rate, k_{rw} = water relative permeability

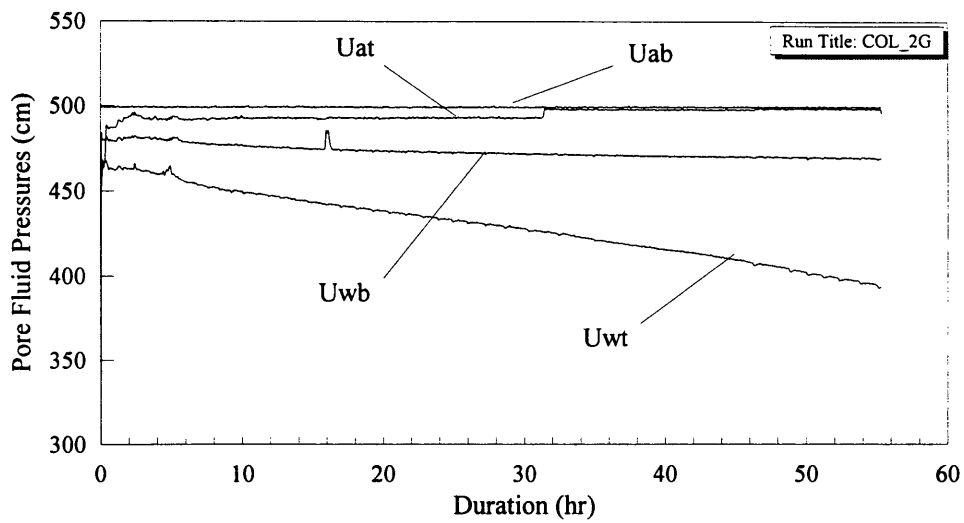


Figure 38. Temporal fluid pressure head data. Experiment COL_2G. U_{ab} = base pore air head, U_{at} = top pore air head, U_{wb} = base pore water head, U_{wt} = top pore water head

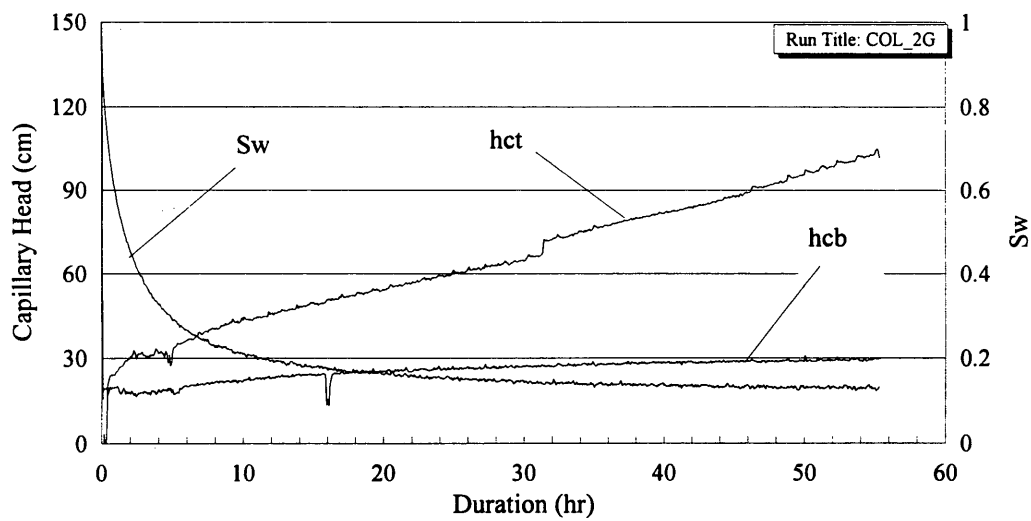


Figure 39. Temporal water saturation (S_w) and top and base capillary head (h_{ct} and h_{cb}) data. Experiment COL_2G.

approximately 32 hours, I_a decreased dramatically as Q_a and k_{ra} rose (Figure 40). The decrease in I_a introduced random errors to the k_{ra} data, as described for the propagation of errors summarized in Table 5. Note that the random errors tended to introduce “noise” to the data, while the trend of the mean of k_{ra} was discernable. The rate of water drainage decreased steadily and I_w increased steadily, while k_{rw} was reduced over the duration of the test (Figure 41).

Experiment COL_1H was conducted initially at $U_{ab} \approx 225$ cm (154 cm above the hydrostatic base pore water head), and was increased to $U_{ab} \approx 180$ cm (Figure 42). During the experiment, S_w decreased to approximately 0.3, h_{cb} rose to 30 cm, and h_{ci} rose to 40 cm (Figure 43). Between 20 and 22 hours, Q_a and k_{ra} increased rapidly (Figure 44), while I_w experienced a transient increase (Figure 45). After 30 hours, I_w stabilized at about 0.5.

Experiment COL_2C was conducted at an initial U_{ab} of 300 cm (154 cm above the hydrostatic base pore water head) which was increased incrementally to 350 cm over a 150-hour duration (Figure 46). At 40 hours, 90 hours, and 115 hours, U_{ab} was increased in increments. After 20 hours, S_w had decreased to 0.2, where it stabilized (Figure 47). Both Q_a and k_{ra} showed incremental increases at 90 hours and 120 hours (Figure 48), which were accompanied by increases in I_w (Figure 49).

The temporal data presented above showed that the nature of changes over time in fluid heads, saturation, and flow parameters were generally similar between samples. Differences were primarily related to the rate of water displacement and experiment set-point conditions. Several of the experiments (such as COR_3E at 10 hours, Figures 30 - 33) showed abrupt changes in state reflected in both fluid head and flow parameters.

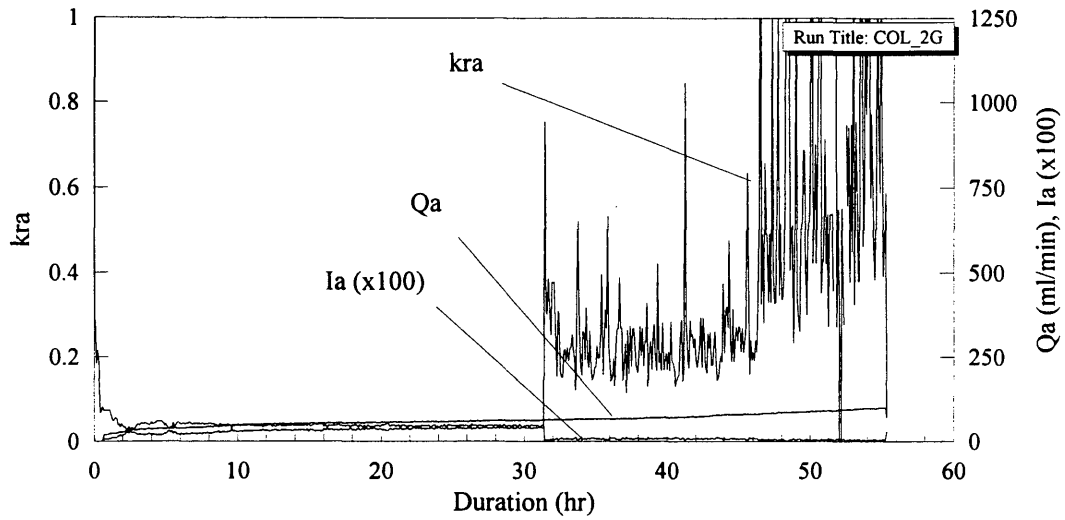


Figure 40. Temporal air flow data. Experiment COL_2G. I_a = air gradient (cm water/cm), Q_a = air flow rate, k_{ra} = air relative permeability

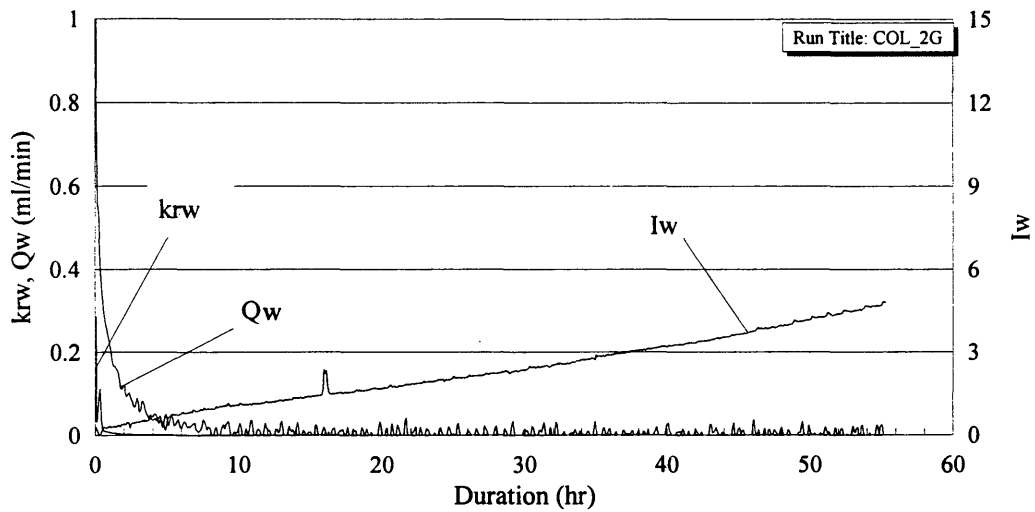


Figure 41. Temporal water flow data. Experiment COL_2G. I_w = hydraulic gradient, Q_w = water flow rate, k_{rw} = water relative permeability

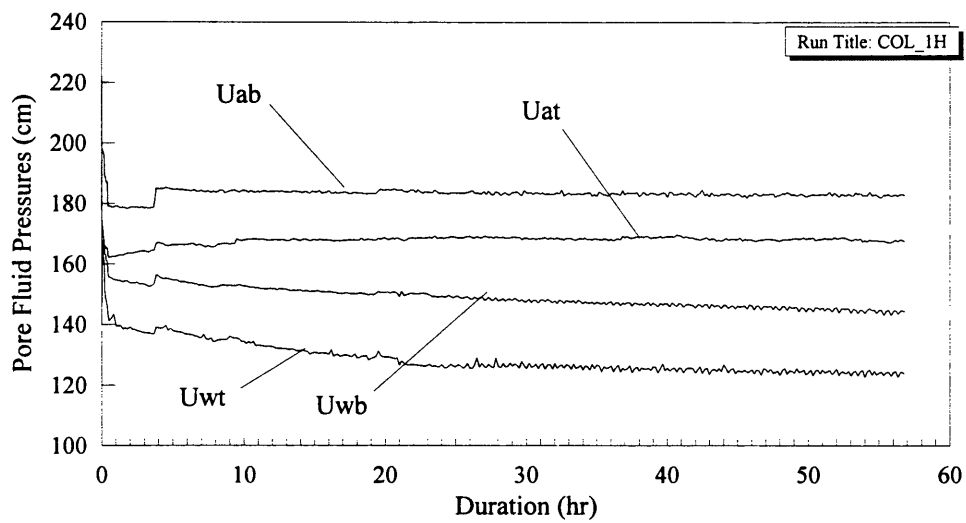


Figure 42. Temporal fluid pressure head data. Experiment COL_1H. U_{ab} = base pore air head, U_{at} = top pore air head, U_{wb} = base pore water head, U_{wt} = top pore water head

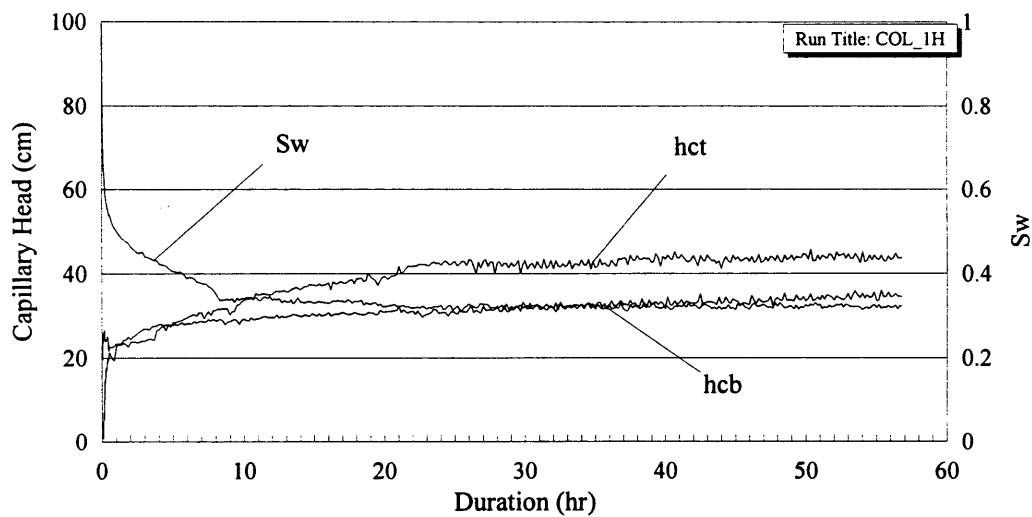


Figure 43. Temporal water saturation (S_w) and top and base capillary head (h_{ct} and h_{cb}) data. Experiment COL_1H.

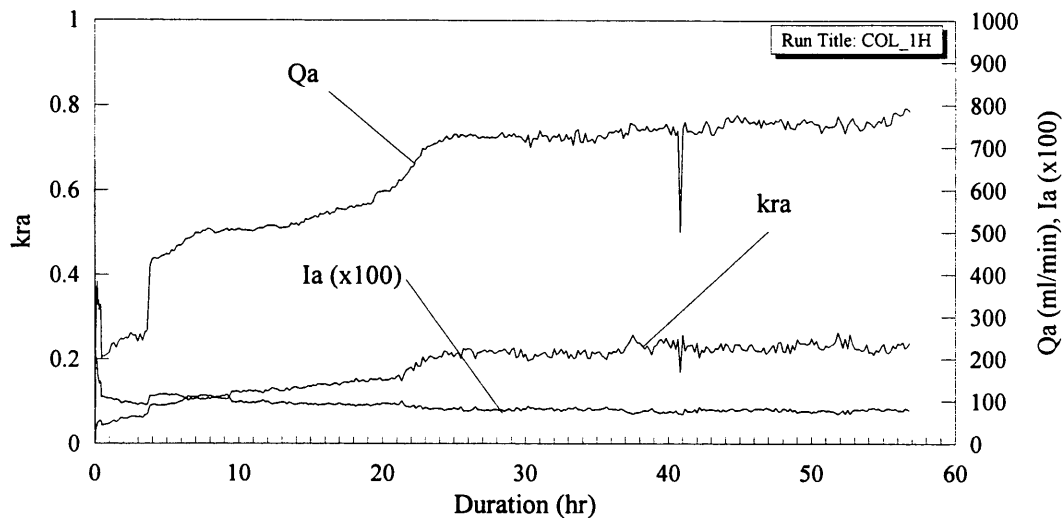


Figure 44. Temporal air flow data. Experiment COL_1H. I_a = air gradient (cm water/cm), Q_a = air flow rate, k_{ra} = air relative permeability

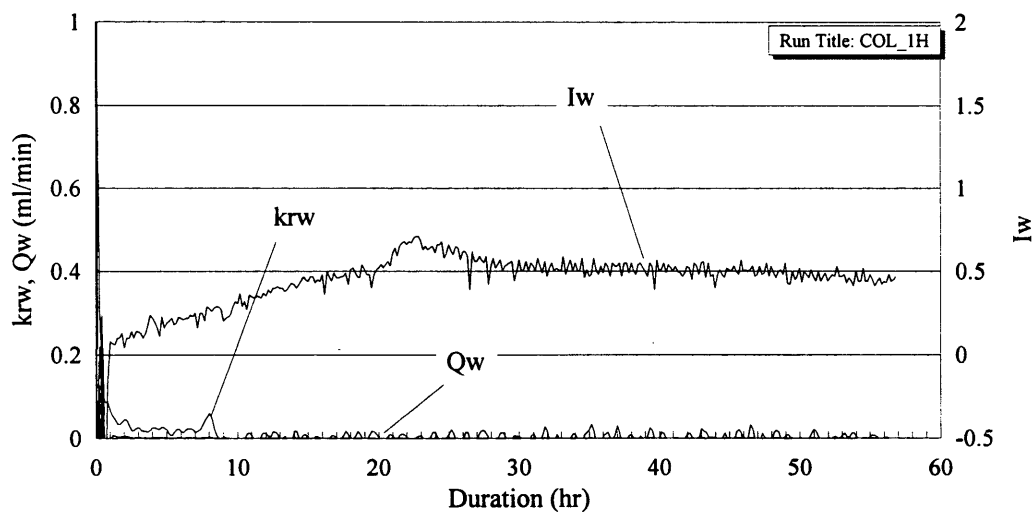


Figure 45. Temporal water flow data. Experiment COL_1H. I_w = hydraulic gradient, Q_w = water flow rate, k_{rw} = water relative permeability

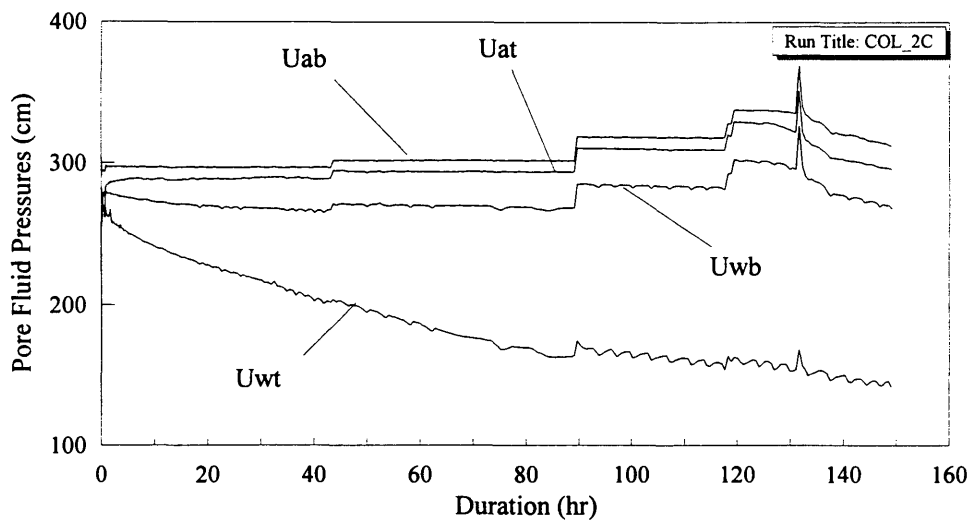


Figure 46. Temporal fluid pressure head data. Experiment COL_2C. U_{ab} = base pore air head, U_{at} = top pore air head, U_{wb} = base pore water head, U_{wt} = top pore water head

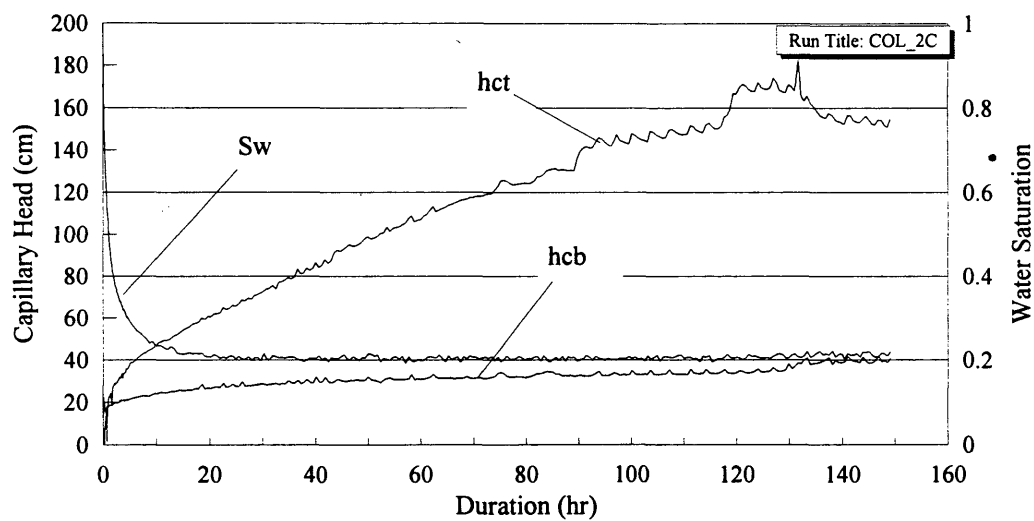


Figure 47. Temporal water saturation (S_w) and top and base capillary head (h_{ct} and h_{cb}) data. Experiment COL_2C.

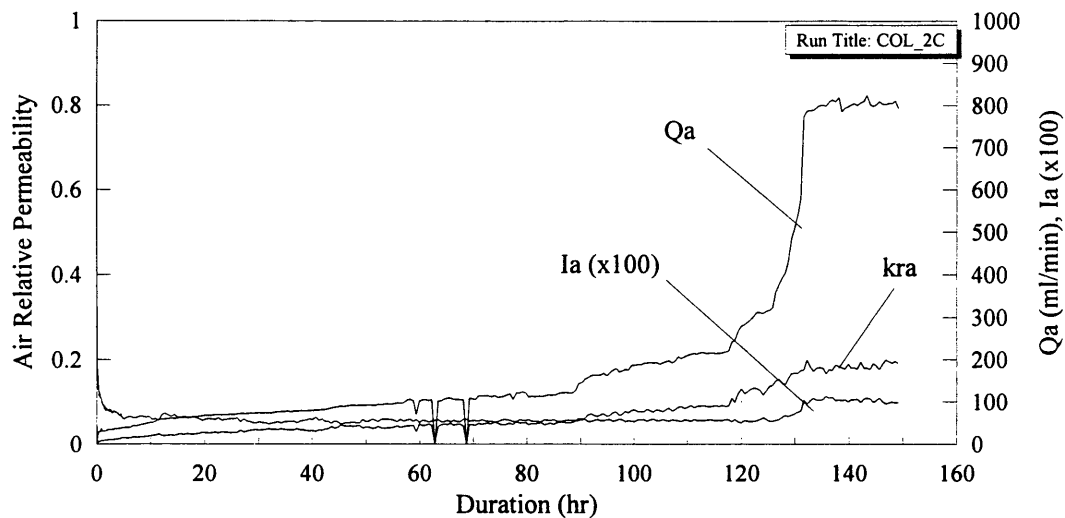


Figure 48. Temporal air flow data. Experiment COL_2C. I_a = air gradient (cm water/cm), Q_a = air flow rate, k_{ra} = air relative permeability

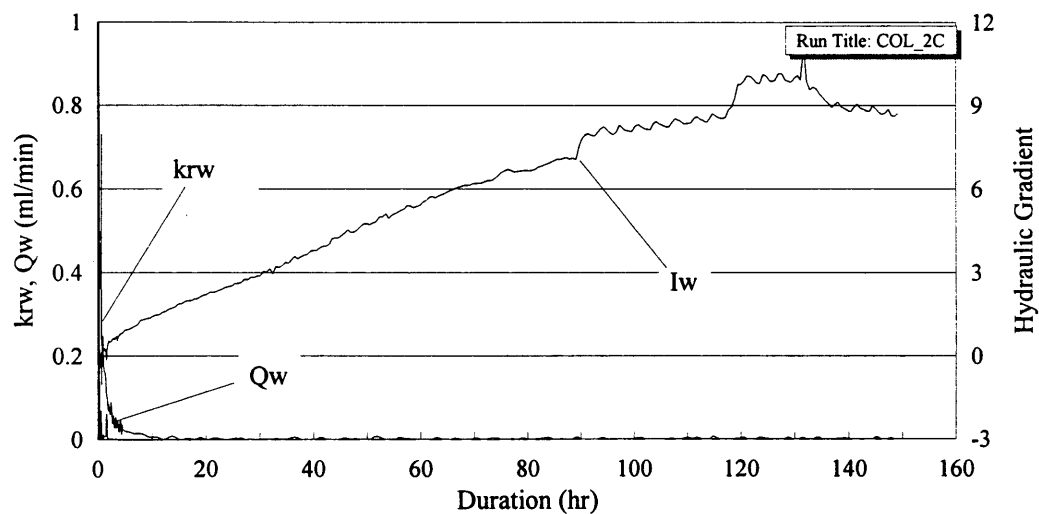


Figure 49. Temporal water flow data. Experiment COL_2C. I_w = hydraulic gradient, Q_w = water flow rate, k_{rw} = water relative permeability

5.5.2 Unsteady State Capillary Head-Saturation Data

The capillary head-saturation data (Figures 50 - 57) are presented as plots of top and base capillary head (h_{ct} and h_{cb}) vs. water saturation. Pore fluid pressure head-saturation data were also presented on accompanying plots in order to represent the raw data and the relative roles of water vs. air heads in controlling capillary heads. These plots include moisture retention data from section 5.3, to depict differences between the relationships measured for air injection and moisture retention relationships for the same sample.

The measured $h_c(S_w)$ relationships during experiment FLO_2P (Figure 50) are representative of those measured in all experiments involving sample FLO. Above $S_w \approx 0.8$, h_{ct} was small, but h_{cb} closely followed the measured moisture retention data. As the sample drained, h_{ct} rose to equal h_{cb} . Below saturations of 0.7, the capillary heads were nearly equal and increased linearly as S_w decreased, while moisture retention data increased non linearly to greater values than h_{ct} or h_{cb} .

Measured capillary heads during experiment COR_3E increased as saturations decreased, and showed transient pulsed behaviors at $S_w < 0.1$ (Figure 51). These data fell below the measured moisture retention data for sample COR. The pore fluid pressure data reflect that U_{ab} was increased in multiple increments during this experiment. While the $h_c(S_w)$ data do not reflect these changes in test conditions, the capillary head data do reflect the transient pulses in pore water pressure at $Sw < 0.1$.

During experiment COR_3A, h_{cb} was approximately equal to the air entry pressure derived from moisture retention data (h_o), and increased very little as the sample drained (Figure 52). In contrast, h_{ct} was equal to about half that value (20 cm) below a $S_w \approx 0.8$.

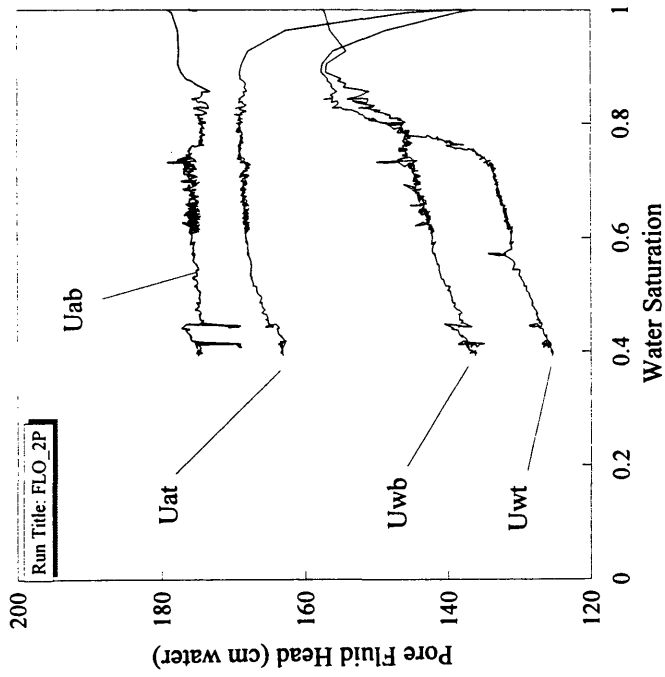


Figure 50A. Pore fluid heads vs. water saturation. Experiment FLO_2P. U_{ab} = base pore air head, U_{at} = top pore air head, U_{wb} = base pore water head, U_{wt} = top pore water head

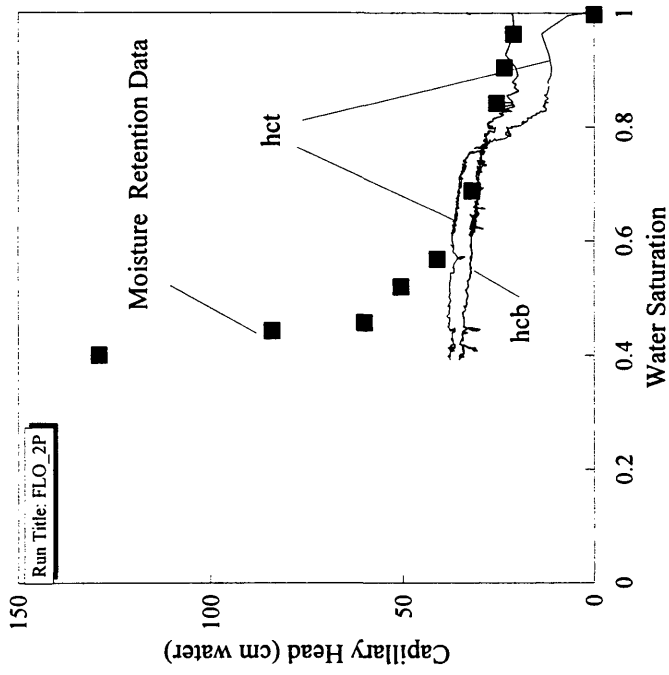


Figure 50B. Capillary head-saturation data from experiment FLO_2P, and moisture retention data. h_{ct} = top capillary head, h_{cb} = base capillary head.

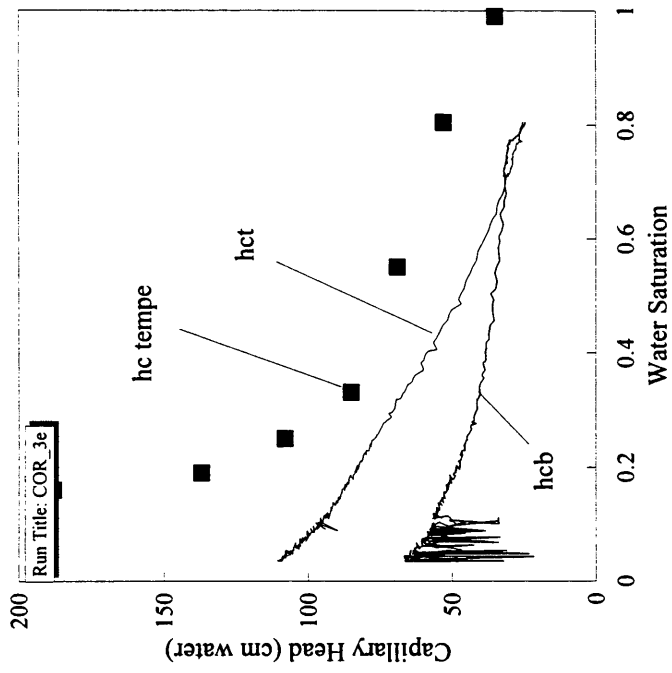


Figure 51B. Capillary head-saturation data from experiment COR_3E, and moisture retention data. h_{ct} = top capillary head, h_{cb} = base capillary head.

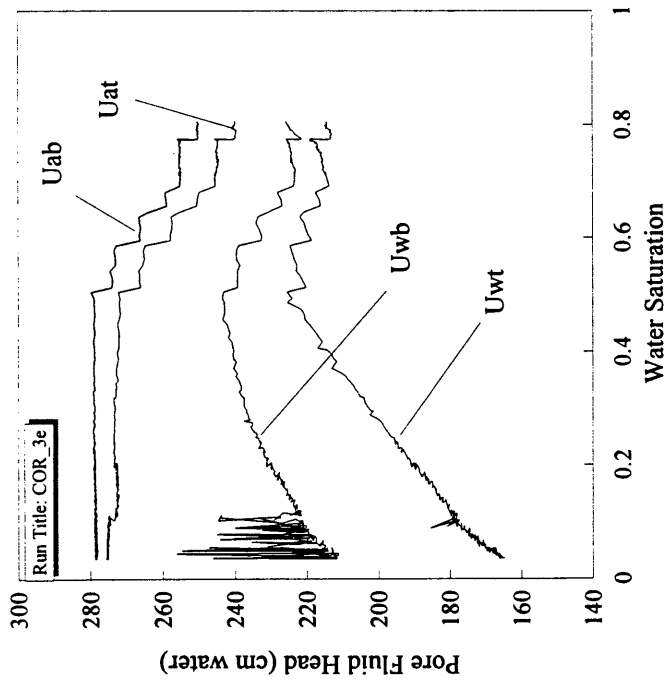


Figure 51A. Pore fluid heads vs. water saturation. Experiment COR_3E. U_{ab} = base pore air head, U_{at} = top pore air head, U_{wb} = base pore water head, U_{wt} = top pore water head

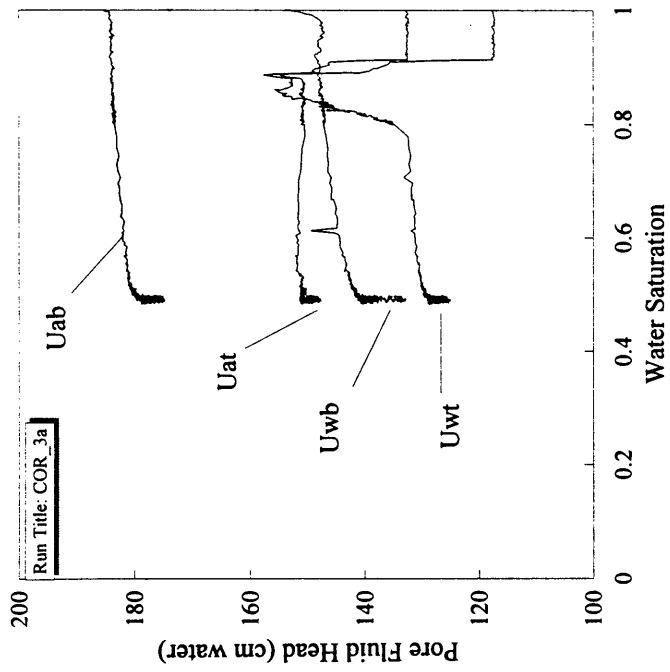


Figure 52A. Pore fluid heads vs. water saturation. Experiment COR_3A. U_{ab} = base pore air head, U_{at} = top pore air head, U_{wb} = base pore water head, U_{wt} = top pore water head

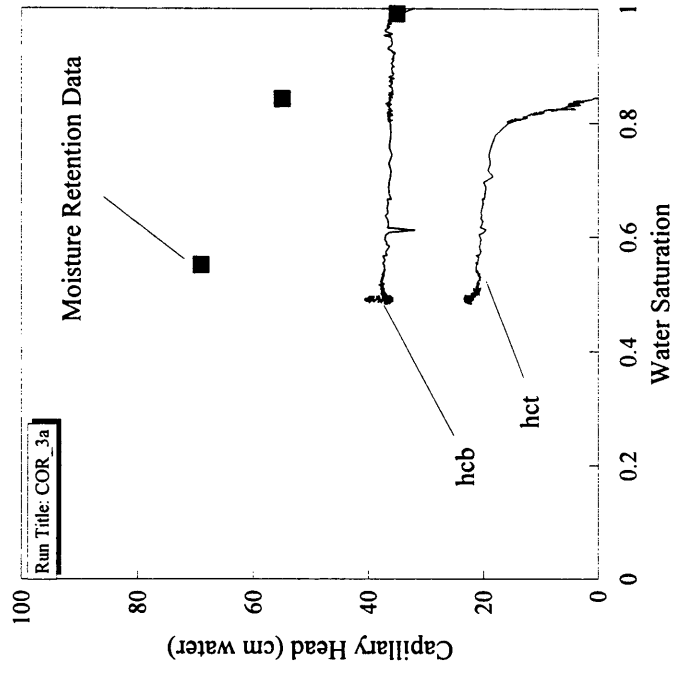


Figure 52B. Capillary head-saturation data from experiment COR_3A, and moisture retention data. h_{ct} = top capillary head, h_{cb} = base capillary head.

Also, during experiment COR_3A, both h_{cb} and h_{ct} showed an increase at the steady state $S_w \approx 0.5$, after an extended time period.

The $h_c(S_w)$ relationships measured during experiments with sample COL all showed similar behaviors. During experiment COL_2C, h_{cb} and h_{ct} (Figure 53) generally fell below the moisture retention data for the sample, except at very high and very low S_w . At high S_w , h_{cb} approximated the moisture retention data, while at S_w , h_{ct} approximated the moisture retention data. At $S_w \approx 0.2$, h_{cb} and h_{ct} increased as the air injection experiment proceeded at a steady value of S_w . During experiments COL_1H (Figure 54) and COL_2E (Figure 55) h_{cb} approximated the moisture retention data at high S_w , while at low S_w , h_{ct} increased to approach the moisture retention data. Capillary heads in these experiments also increased at a steady state S_w .

The measured capillary heads during experiment CSM_1E (Figure 56) followed the moisture retention data relatively closely above a $S_w \approx 0.5$. At $S_w < 0.5$, h_{cb} and h_{ct} increased little as the sample drained, while the moisture retention data increased rapidly.

During experiment CHV_1H, h_{ct} approximated the moisture retention data at high saturations, but increased little as the sample drained (Figure 57). As the sample drained, h_{cb} increased significantly, but remained well below the moisture retention data.

5.5.3 Air Relative Permeability Data

Air and water relative permeability data (Figures 58 - 86) are presented on plots of relative permeability vs. S_w and vs. arithmetic mean of the base and top capillary head.

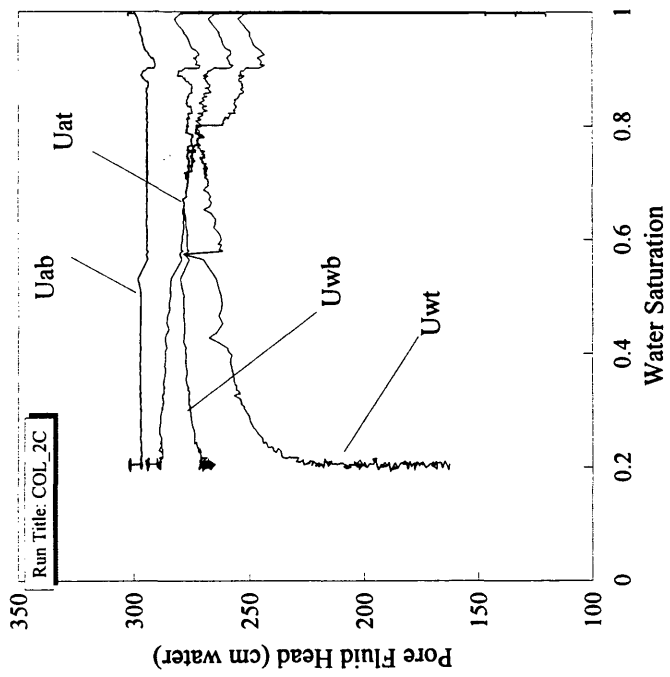


Figure 53A. Pore fluid heads vs. water saturation. Experiment COL_2C. U_{ab} = base pore air head, U_{at} = top pore air head, U_{wb} = base pore water head, U_{wt} = top pore water head

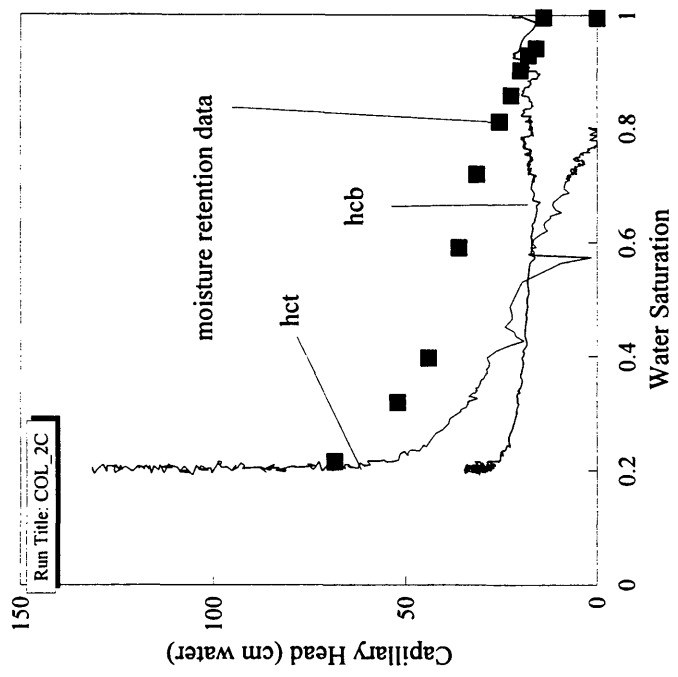


Figure 53B. Capillary head-saturation data from experiment COL_2C, and moisture retention data. h_{ct} = top capillary head, h_{cb} = base capillary head.

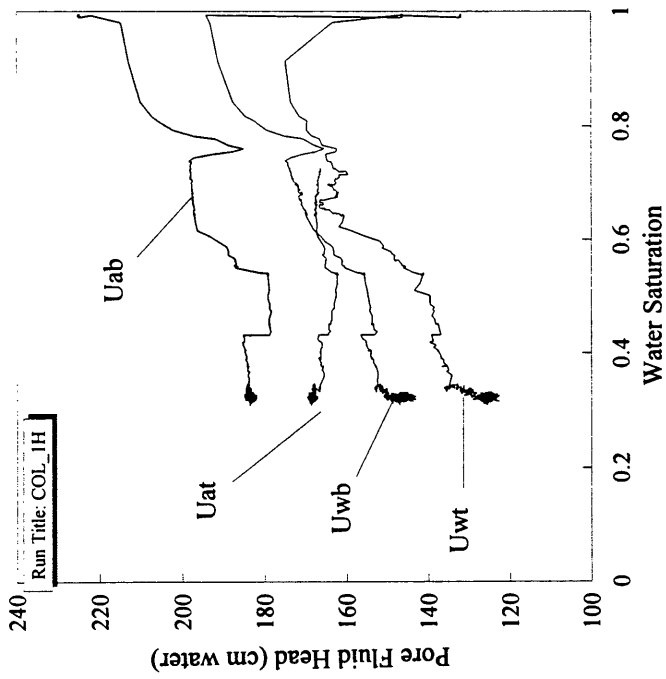


Figure 54A. Pore fluid heads vs. water saturation. Experiment COL_1H. U_{ab} = base pore air head, U_{at} = top pore air head, U_{wb} = base pore water head, U_{wt} = top pore water head

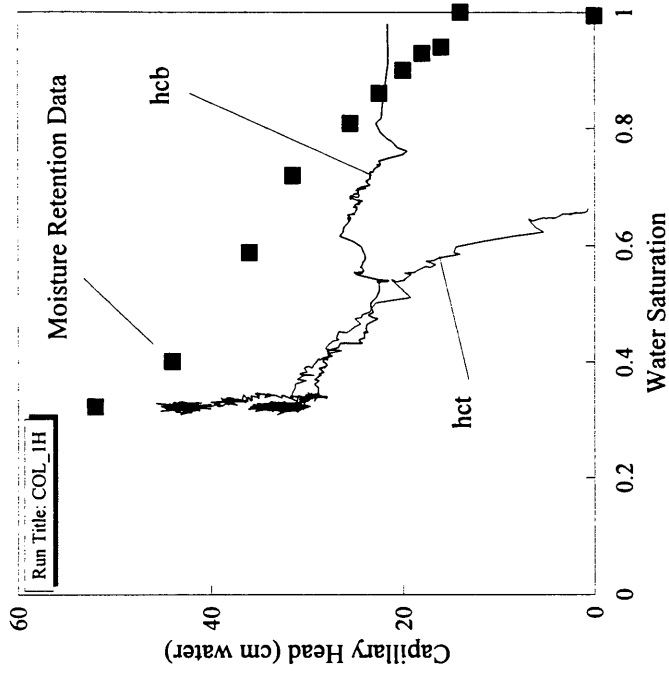


Figure 54B. Capillary head-saturation data from experiment COL_1H, and moisture retention data. h_{ct} = top capillary head, h_{cb} = base capillary head.

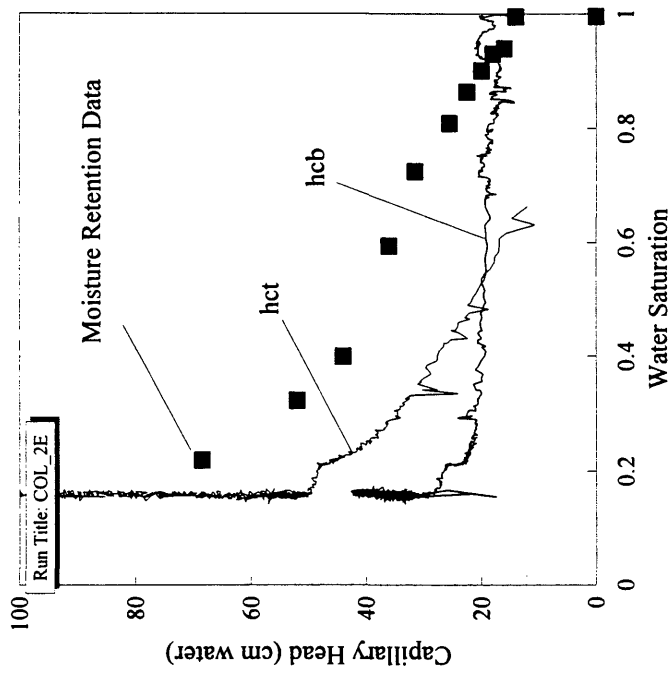


Figure 55B. Capillary head-saturation data from experiment COL_2E, and moisture retention data. h_{ct} = top capillary head, h_{cb} = base capillary head.

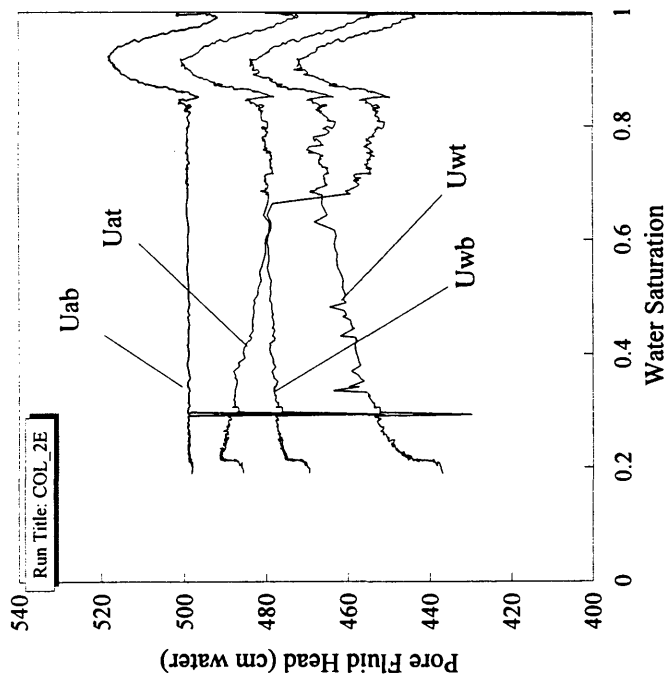


Figure 55A. Pore fluid heads vs. water saturation. Experiment COL_2E. U_{ab} = base pore air head, U_{at} = top pore air head, U_{wb} = base pore water head, U_{wt} = top pore water head

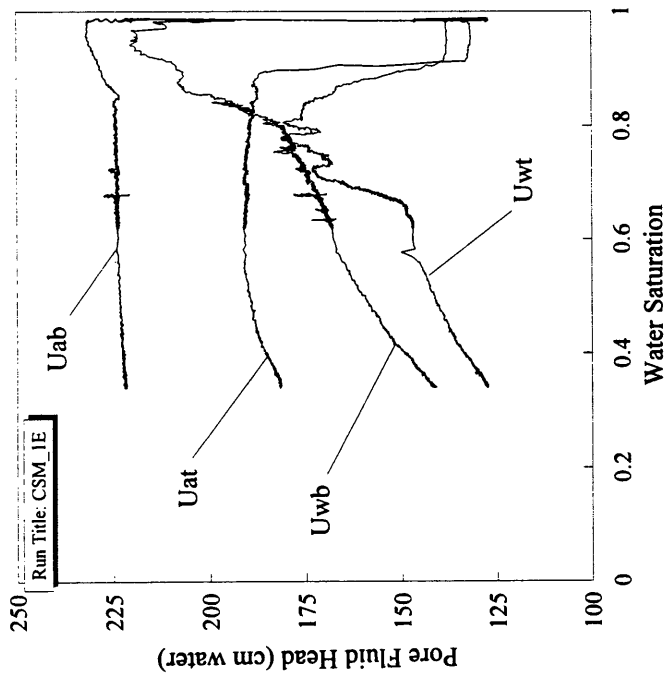


Figure 56A. Pore fluid heads vs. water saturation. Experiment CSM_1E. U_{ab} = base pore air head, U_{at} = top pore air head, U_{wb} = base pore water head, U_{wt} = top pore water head

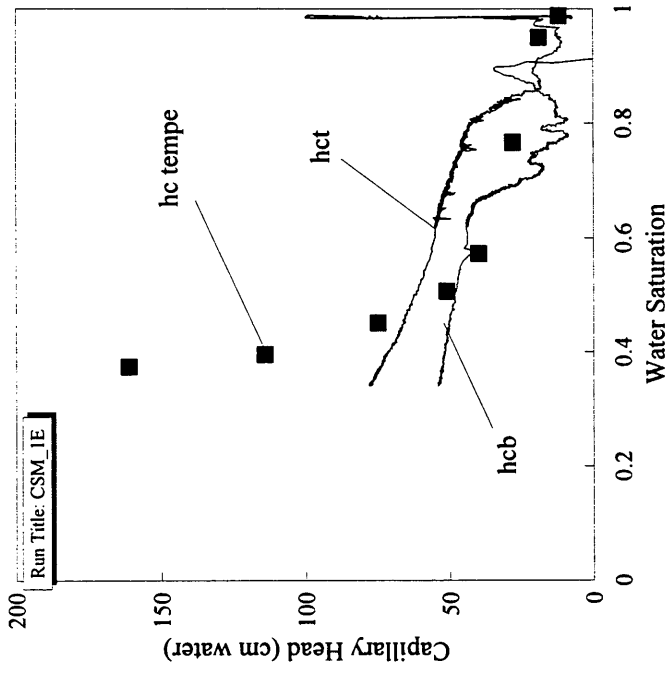


Figure 56B. Capillary head-saturation data from experiment CSM_1E, and moisture retention data. h_{ct} = top capillary head, h_{cb} = base capillary head.

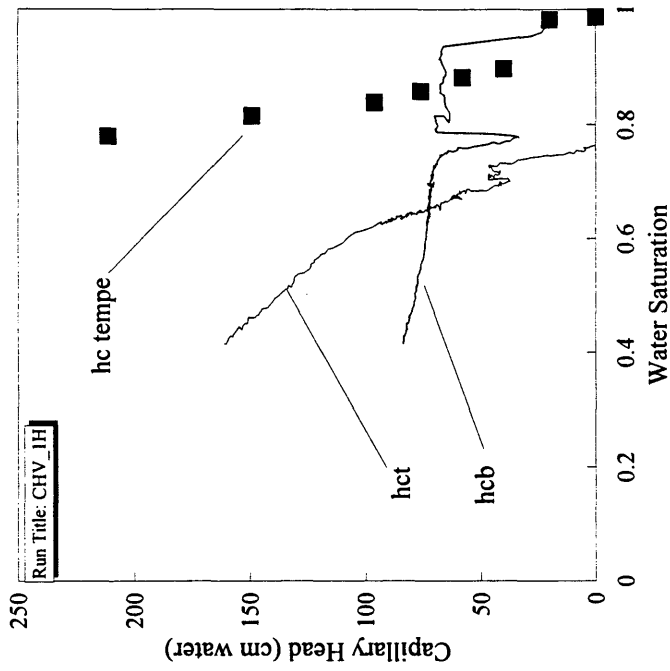


Figure 57B. Capillary head-saturation data from experiment CHV_1H, and moisture retention data. h_{ct} = top capillary head, h_{cb} = base capillary head.

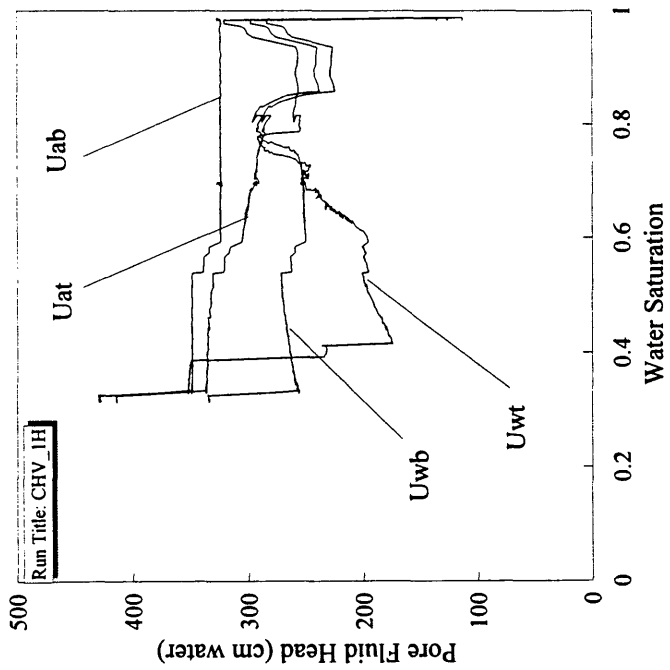


Figure 57A. Pore fluid heads vs. water saturation. Experiment CHV_1H. U_{ab} = base pore air head, U_{at} = top pore air head, U_{wb} = base pore water head, U_{wt} = top pore water head

The use of the arithmetic mean was based on the lack of any *a priori* knowledge of the distribution of capillary head in the sample. Without such knowledge, the use of another mean value was rejected to avoid introducing bias into the data. The relative permeability plots also include curves derived from the *Brooks and Corey* [1964] and *Parker et al.* [1987] functional relationships (equations (3) through (6) and (8) through (11)). Values of h_o , λ , α , and n used for these plots were those derived from the moisture retention data (Table 7).

As discussed in section 5.3, two sets of values of the Parker et al. indices (α and n) were derived from the moisture retention data: a set based on the best visual fit to the moisture retention data, and a set based on $\alpha = 1/h_o$. The values of α and n derived from $\alpha = 1/h_o$ were closer to values used by Parker et al. Also, the set of curves based on the best visual fit to measured moisture retention data provided invalid estimates of relative permeability functions. For these reasons, only the set of curves based on $\alpha = 1/h_o$ are shown with the air relative permeability data.

The $k_{ra}(S_w)$ data measured during experiment FLO_2I (Figure 58) followed the Brooks-Corey functional relationship closely above $S_w \approx 0.6$. Below $S_w \approx 0.6$, k_{ra} was lower than the Brooks-Corey relationship. When S_w stabilized at 0.30, k_{ra} continued to increase from approximately 0.6 to 0.7. The Parker et al. relationships over estimated k_{ra} at all saturations. During experiment FLO_2I, $k_{ra}(h_c)$ data (Figure 59) showed a distinct change in slope at $k_{ra} \approx 0.3$. This value corresponds to k_{ra} at $S_w \approx 0.6$. Below $k_{ra} \approx 0.3$, $k_{ra}(h_c)$ data were essentially bounded by the Parker et al. and Brooks-Corey functional relationships.

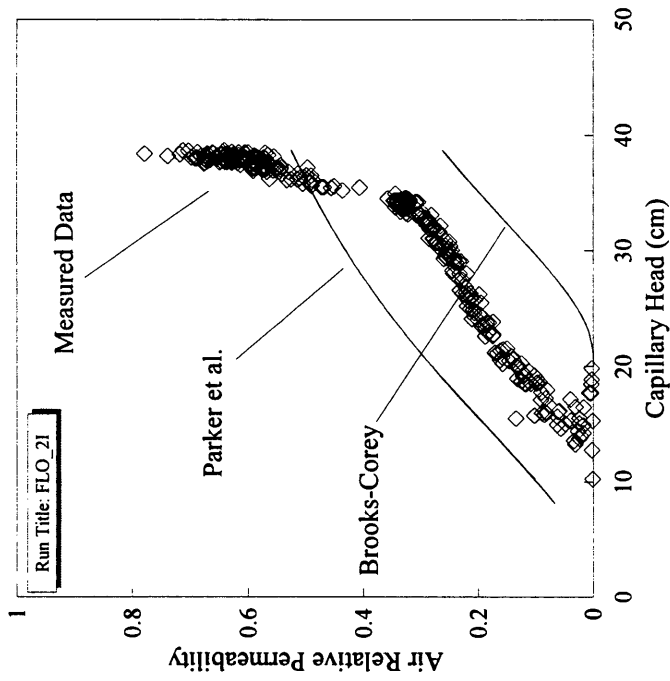


Figure 58. Air relative permeability-saturation data and Brooks-Corey and Parker et al. functions derived from moisture retention data. Experiment FLO_2I. Experimental conditions: $U_{ab} \approx 180 - 175$ cm, Steady $S_w \approx 0.3$ at 3.5 hrs. $k_{ra} \approx 0.65$ at 4 - 40 hours.

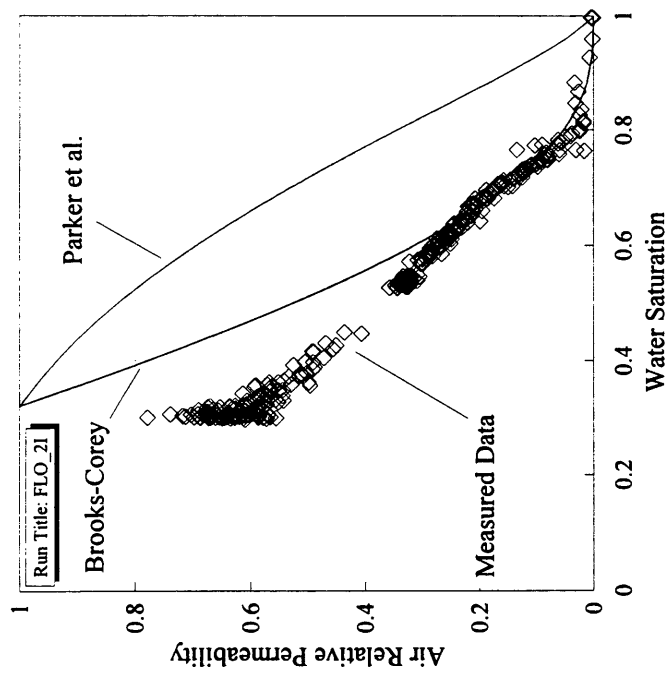


Figure 59. Air relative permeability-capillary head data and Brooks-Corey and Parker et al. functions derived from moisture retention data. Experiment FLO_2I. Experimental conditions: $U_{ab} \approx 180 - 175$ cm, Steady $S_w \approx 0.3$ at 3.5 hrs. $k_{ra} \approx 0.65$ at 4 - 40 hours.

Air relative permeability data from experiment FLO_2L were similar to the data from FLO_2I. The Brooks-Corey functional relationship provided a good estimate of $k_{ra}(S_w)$ above $S_w \approx 0.6$ (Figure 60), while for $S_w < 0.6$, the data showed step-like behavior. For $0.4 < S_w < 0.6$, k_{ra} increased very little, then at $S_w \approx 0.4$, k_{ra} increased from 0.35 to 0.5, with little change in S_w . The $k_{ra}(h_c)$ data for experiment FLO_2L (Figure 61) were bounded by the Brooks-Corey and Parker et al. functions.

The measured $k_{ra}(S_w)$ and $k_{ra}(h_c)$ data for experiment FLO_2P (Figures 62 and 63) were similar to those for experiments FLO_2I and FLO_2L. At $S_w > 0.6$, the measured data closely follow the Brooks-Corey functional form, while at lower saturations, the measured data fall below the Brooks-Corey curve. The data show a distinct change in slope with respect to capillary head at $h_c \approx 32$ cm, which corresponds to the measured capillary head at a $S_w \approx 0.6$, where the $k_{ra}(S_w)$ data diverged from the Brooks-Corey curve.

The measured $k_{ra}(S_w)$ data for experiment FLO_1K (Figure 64) were similar to those measured during experiments FLO_2I, FLO_2L, and FLO_2P, except that the deviation from the Brooks-Corey functional form at saturations below 0.6 was less pronounced. However, the data below $S_w \approx 0.6$ do show a step-like pattern, where k_{ra} increases occur between intervals of drainage. Also, the measured $k_{ra}(h_c)$ relationships (Figure 65) did not show a single distinct change in slope, but showed step-like behavior.

The experiments involving sample FLO showed the general reproducibility of air permeability measurements, as well as discontinuities and steps in $k_{ra}(S_w)$ and $k_{ra}(h_c)$. The $k_{ra}(S_w)$ discontinuity at $S_w \approx 0.6$ was common to all the experiments, but each experiment displayed unique transient steps at $S_w < 0.6$. The transient steps in $k_{ra}(S_w)$ and the usefulness of the Brooks-Corey relation as an estimate of $k_{ra}(S_w)$ at high S_w are two

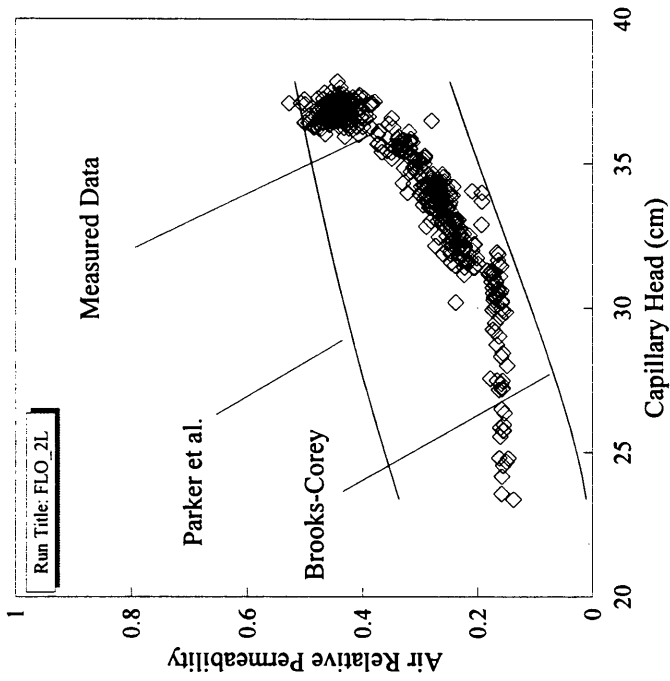


Figure 60. Air relative permeability-saturation data and Brooks-Corey and Parker et al. functions derived from moisture retention data. Experiment FLO_2L. Experimental conditions: $U_{ab} \approx 180 - 175$ cm, Steady $S_w \approx 0.35$ at 4 hrs. $k_{ra} \approx 0.45$ to 0.55 at 3 - 40 hours.

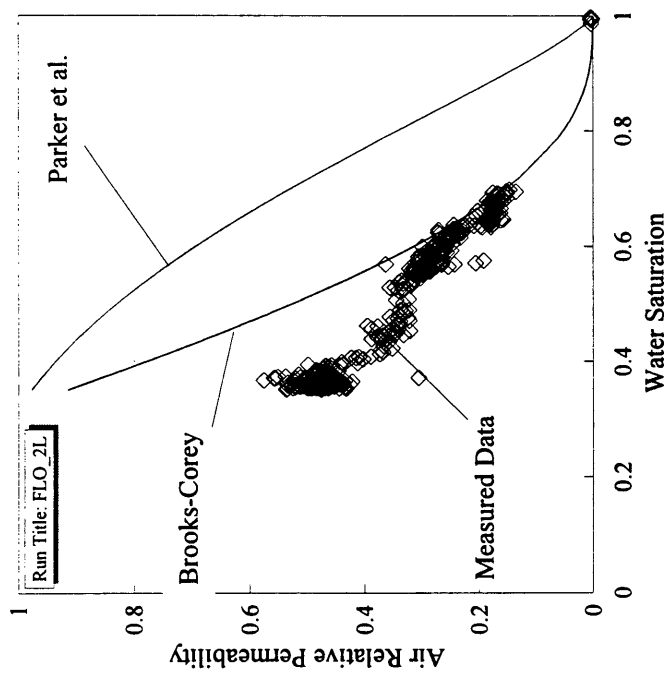


Figure 61. Air relative permeability-capillary head data and Brooks-Corey and Parker et al. functions derived from moisture retention data. Experiment FLO_2L. Experimental conditions: $U_{ab} \approx 180 - 175$ cm, Steady $S_w \approx 0.35$ at 4 hrs. $k_{ra} \approx 0.45$ to 0.55 at 3 - 40 hours.

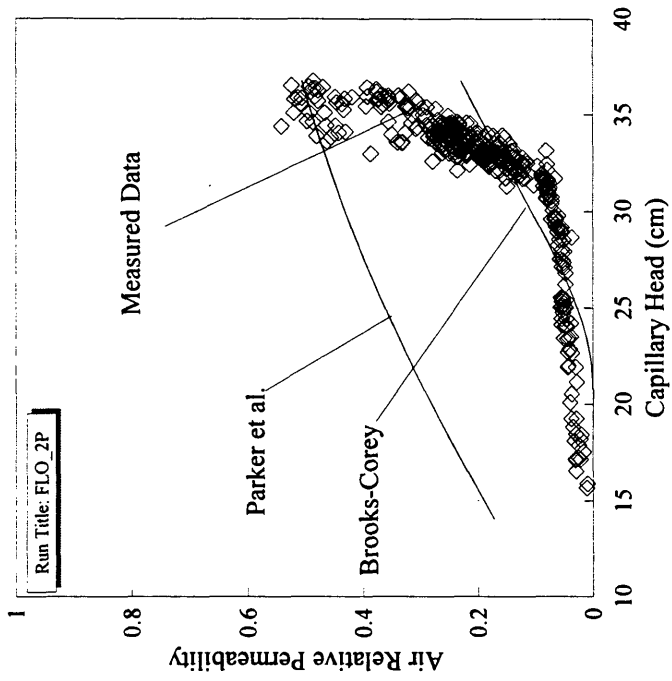


Figure 62. Air relative permeability-saturation data and Brooks-Corey and Parker et al. functions derived from moisture retention data. Experiment FLO_2P. Experimental conditions: $U_{ab} \approx 170 - 175$ cm, $S_w \approx 0.4$ at 3 hrs. $k_{ra} \approx 0.55$ at 3 hours.

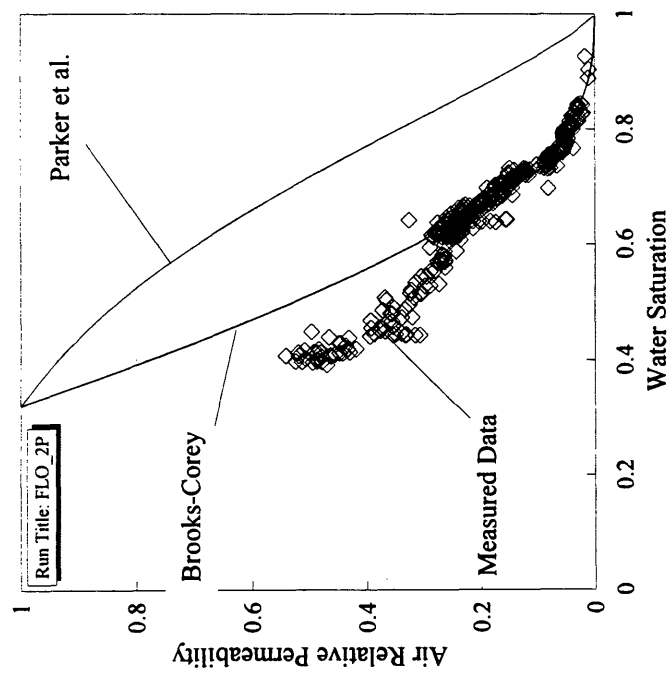


Figure 63. Air relative permeability-capillary head data and Brooks-Corey and Parker et al. functions derived from moisture retention data. Experiment FLO_2P. Experimental conditions: $U_{ab} \approx 170 - 175$ cm, $S_w \approx 0.4$ at 3 hrs. $k_{ra} \approx 0.55$ at 3 hours.

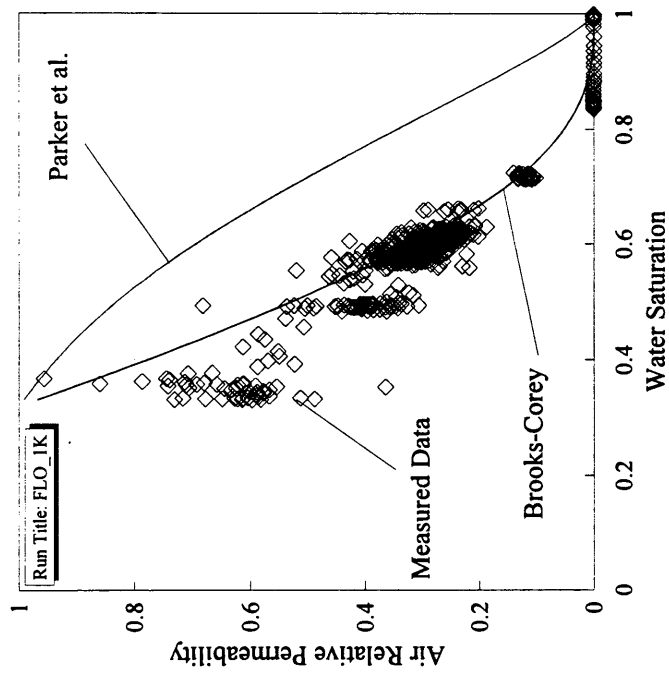


Figure 64. Air relative permeability-saturation data and Brooks-Corey and Parker et al. functions derived from moisture retention data. Experiment FLO_1K. Experimental conditions: $U_{ab} \approx 185 - 190$ cm, $S_w \approx 0.35$ at 2 hrs. $k_{ra} \approx 0.55$ at 2 hours.

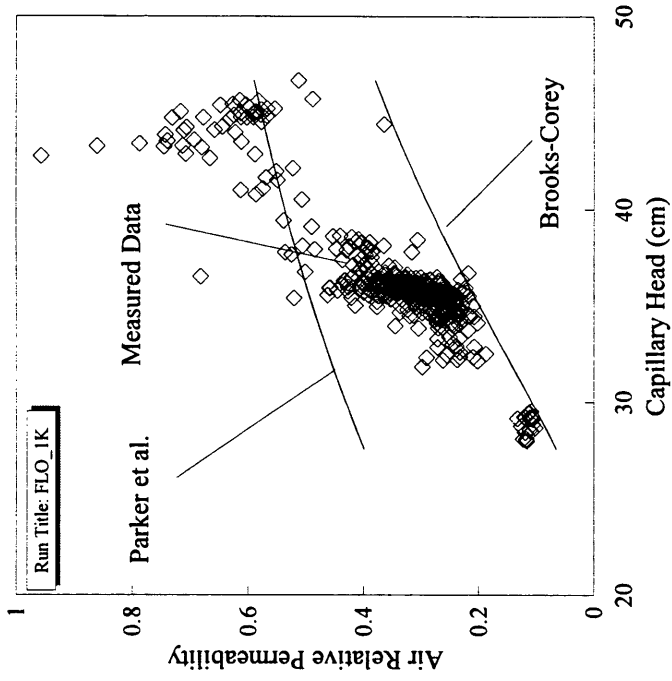


Figure 65. Air relative permeability-capillary head data and Brooks-Corey and Parker et al. functions derived from moisture retention data. Experiment FLO_1K. Experimental conditions: $U_{ab} \approx 185 - 190$ cm, $S_w \approx 0.35$ at 2 hrs. $k_{ra} \approx 0.55$ at 2 hours.

fundamental air relative permeability behaviors which were also encountered during experiments involving other soils.

The measured $k_{ra}(S_w)$ data from experiment COR_3A (Figure 66) fell below the Brooks-Corey curve down to a steady state $S_w \approx 0.5$. After 35 hours, k_{ra} increased at constant $S_w \approx 0.5$ to approximate the Brooks-Corey relation. This “air permeability breakthrough” behavior shows that k_{ra} can be a multi-valued function of S_w . This behavior is essentially opposite to that observed during experiments involving sample FLO, where the Brooks-Corey relation provided a good estimate of $k_{ra}(S_w)$ at high S_w . The $k_{ra}(h_c)$ data for experiment COR_3A (Figure 67) showed a distinct change in slope at $h_c \approx 30$ cm, above which the data fall on the Parker et al. curve. The Brooks-Corey $k_{ra}(h_c)$ curve was undefined for this test, since the mean capillary head (h_c) was below the air entry pressure derived from moisture retention data (h_o).

The measured $k_{ra}(S_w)$ data for experiment COR_3C (Figure 68) fell below the Brooks-Corey curve, but followed it more closely than experiment COR_3A. When steady saturation was reached at $S_w \approx 0.35$, k_{ra} continued to increase, and approached the Brooks-Corey curve. This experiment was conducted at a slower displacement rate than experiment COR_3A, and shows less pronounced air permeability breakthrough. The sensitivity to displacement rate is also a behavior observed with other samples. The measured $k_{ra}(h_c)$ data for experiment COR_3C (Figure 69) followed a trend below the Parker et al. curve, but rose to approximate the Parker et al. function at high h_c and k_{ra} . The Brooks-Corey $k_{ra}(h_c)$ curve is undefined for this test, since h_c was below h_o .

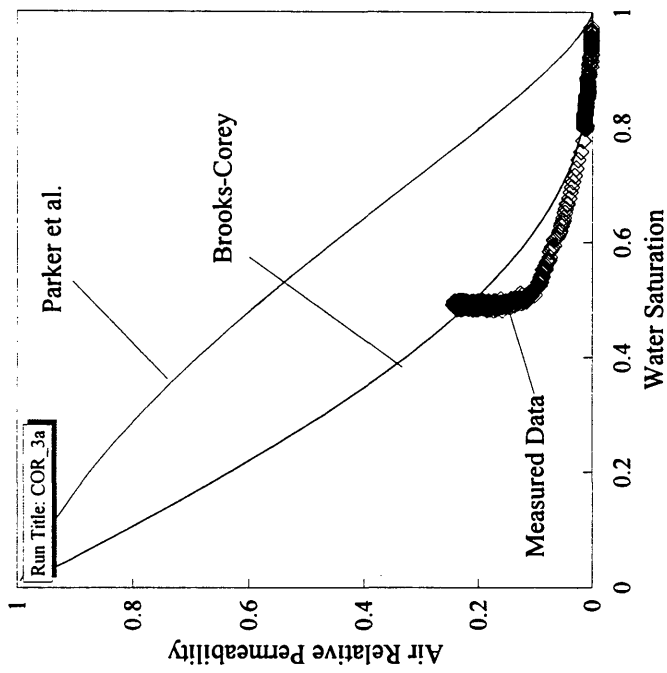


Figure 66. Air relative permeability-saturation data and Brooks-Corey and Parker et al. functions derived from moisture retention data. Experiment COR_3A. Experimental conditions: $U_{ab} \approx 185 - 175$ cm, Steady $S_w \approx 0.5$ at 10 hrs. $k_{ra} \approx 0.25$ at 40 hours.

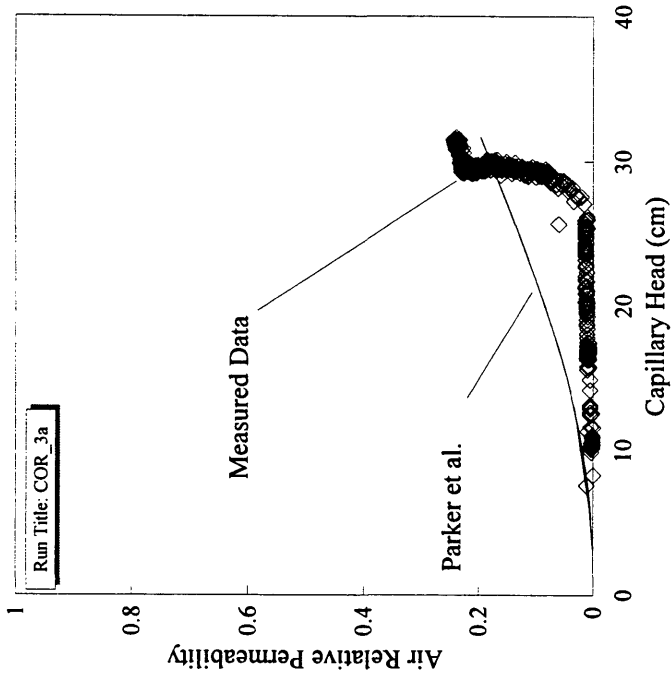


Figure 67. Air relative permeability-capillary head data and Brooks-Corey and Parker et al. functions derived from moisture retention data. Experiment COR_3A. Experimental conditions: $U_{ab} \approx 185 - 175$ cm, Steady $S_w \approx 0.5$ at 10 hrs. $k_{ra} \approx 0.25$ at 40 hours.

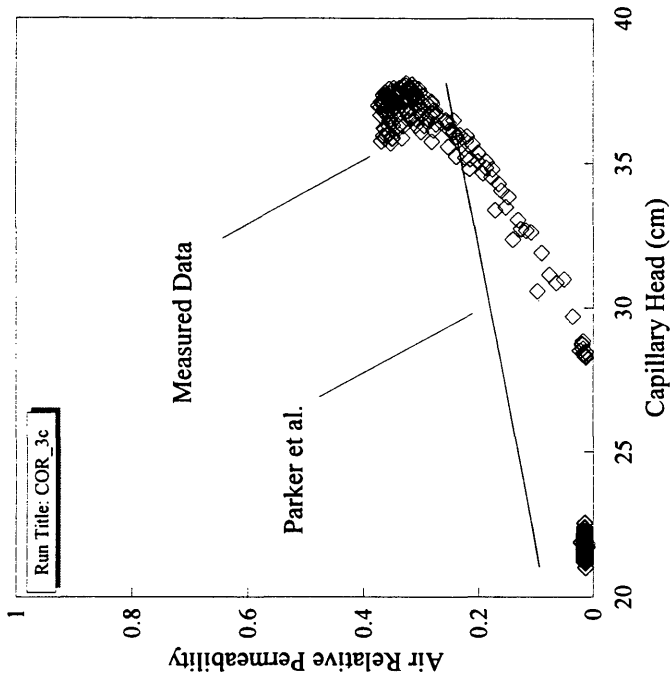


Figure 68. Air relative permeability-saturation data and Brooks-Corey and Parker et al. functions derived from moisture retention data. Experiment COR_3C. Experimental conditions: $U_{ab} \approx 165$ cm at 0 - 4.5 hrs and 185 cm at 4.5 - 30 hrs., Steady $S_w \approx 0.8$ at 4 hrs and 0.35 at 30 hrs. $k_{ra} \approx 0.02$ at 4 hours and 0.37 at 30 hrs.

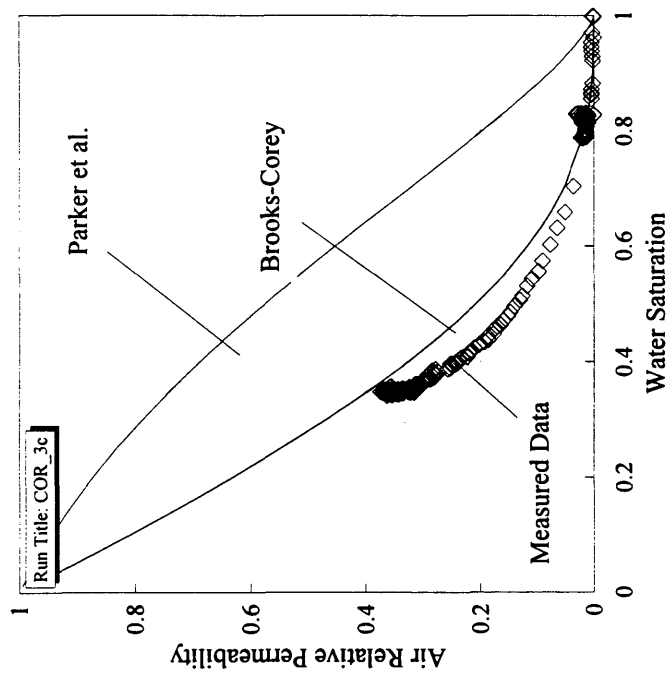


Figure 69. Air relative permeability-capillary head data and Brooks-Corey and Parker et al. functions derived from moisture retention data. Experiment COR_3C. Experimental conditions: $U_{ab} \approx 165$ cm at 0 - 4.5 hrs and 185 cm at 4.5 - 30 hrs., Steady $S_w \approx 0.8$ at 4 hrs and 0.35 at 30 hrs. $k_{ra} \approx 0.02$ at 4 hours and 0.37 at 30 hrs.

Experiment COR_3E was conducted at a higher air injection pressure head, and therefore a faster displacement rate than both experiments COR_3A and COR_3C, and showed more pronounced air permeability breakthrough (i.e., lower k_{ra} at intermediate S_w , and a larger increase in k_{ra} at relatively constant S_w). The $k_{ra}(S_w)$ data for experiment COR_3E (Figure 70) showed an a slow increase in k_{ra} above $S_w \approx 0.2$. Step increases in k_{ra} occurred at $S_w \approx 0.2$ and 0.1. At $S_w \approx 0.05$, k_{ra} rose to 0.6. The data points shown in Figure 70 were collected at 4 minute intervals, and the abrupt nature of the step changes in $k_{ra}(S_w)$ is indicated by the gap in measured $k_{ra}(S_w)$ data at $S_w \approx 0.2$, and 0.1. The step-change in $k_{ra}(S_w)$ at $S_w \approx 0.1$ was coincident with the onset of a period of intermittent instability in U_{wb} , which is reflected in I_w and h_{cb} (Figures 31, 32, and 33, at 6.5 hours and 11 hours). These data reflect a coupled instability in the air and water flow in conjunction with air permeability breakthrough.

The measured $k_{ra}(h_c)$ data (Figure 71) for experiment COR_3E followed close to the Brooks-Corey curve for low and intermediate values of k_{ra} . However, the data showed a discontinuity at $k_{ra} \approx 0.3$, and deviated from the Brooks-Corey curve. At $k_{ra} > 0.3$, the data rose closer to the Parker et al. curve. The apparent noise in $k_{ra}(h_c)$ data at $k_{ra} > 0.3$ resulted from the instability in capillary heads after air permeability breakthrough (Figures 31 and 51).

The experiments involving sample COL all displayed air permeability breakthrough similar to that observed for sample COR, but in many cases to a more extreme degree. During experiment COL_2C, the $k_{ra}(S_w)$ data (Figure 72) and the $k_{ra}(h_c)$ data (Figure 73) were both significantly below the Brooks-Corey and Parker et al. curves. Steady state saturation was reached at $S_w \approx 0.2$, and $k_{ra}(S_w)$ data increased from 0.05 to 0.2.

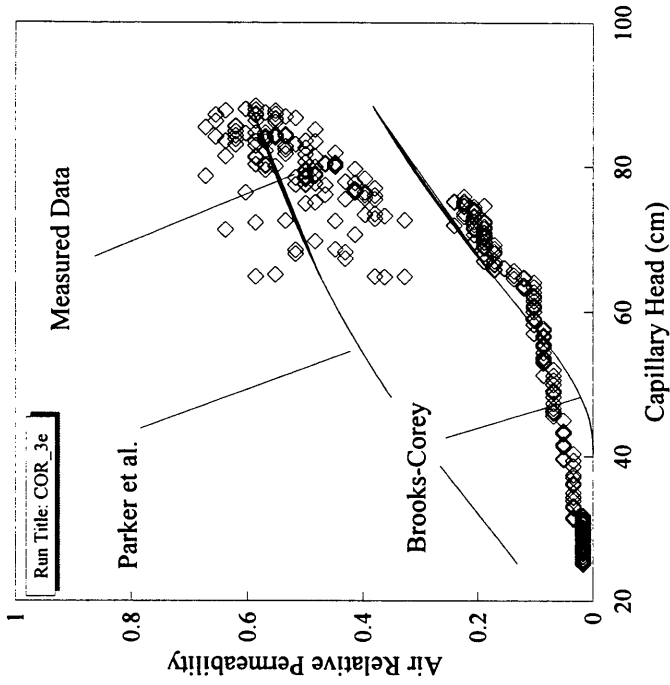


Figure 70. Air relative permeability-saturation data and Brooks-Corey and Parker et al. functions derived from moisture retention data. Experiment COR_3E. Experimental conditions: $U_{ab} \approx 250 - 280$ cm, increasing from 0 to 3 hrs., and 280 cm from 3 - 19 hrs., $S_w \approx 0.4$ at 3 hrs and 0.1 at 10 hrs. $k_{ra} \approx 0.02$ at 4 hrs. and 0.2 at 10 hrs.

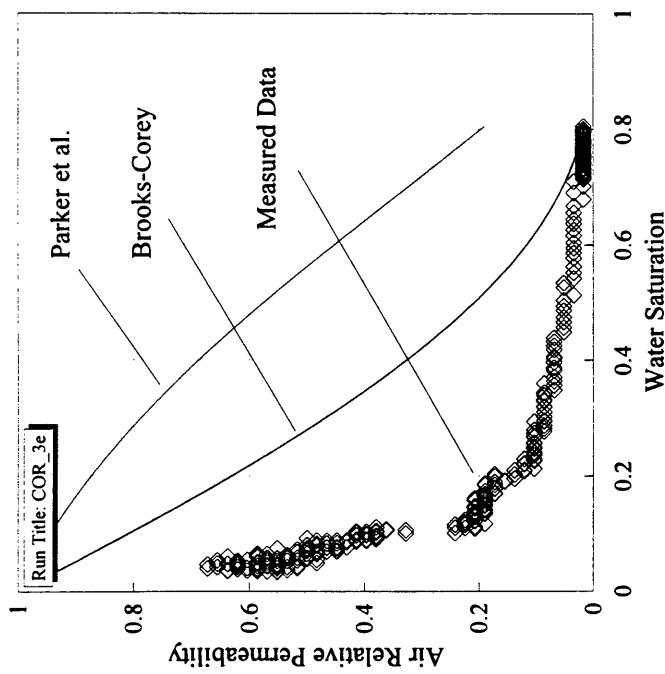


Figure 71. Air relative permeability-capillary head data and Brooks-Corey and Parker et al. functions derived from moisture retention data. Experiment COR_3E. Experimental conditions: $U_{ab} \approx 250 - 280$ cm, increasing from 0 to 3 hrs., and 280 cm from 3 - 19 hrs., $S_w \approx 0.4$ at 3 hrs and 0.1 at 10 hrs. $k_{ra} \approx 0.02$ at 4 hrs. and 0.2 at 10 hrs.

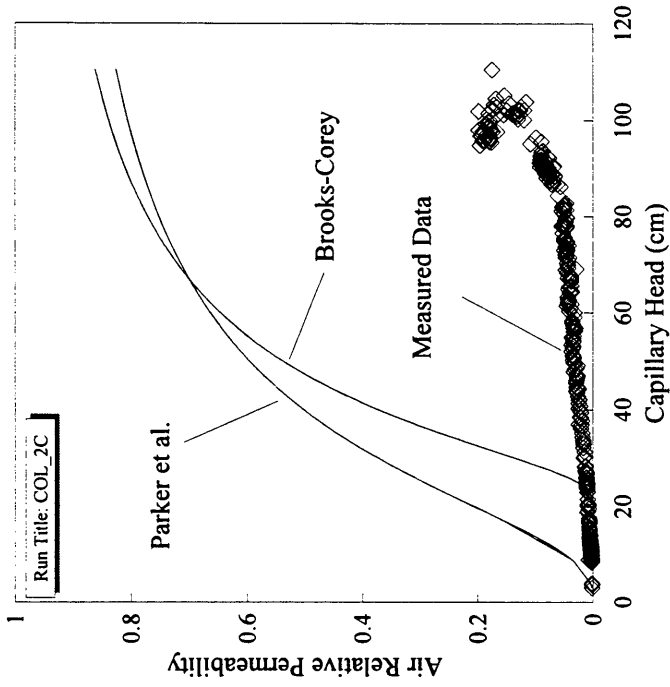


Figure 72. Air relative permeability-saturation data and Brooks-Corey and Parker et al. functions derived from moisture retention data. Experiment COL_2C. Experimental conditions: $U_{ab} \approx 300 - 350$ cm, increasing over 150 hrs. Steady $S_w \approx 0.2$ at 20 hrs. $k_{ra} \approx 0.1$ at 120 hrs. and 0.2 at 150 hrs.

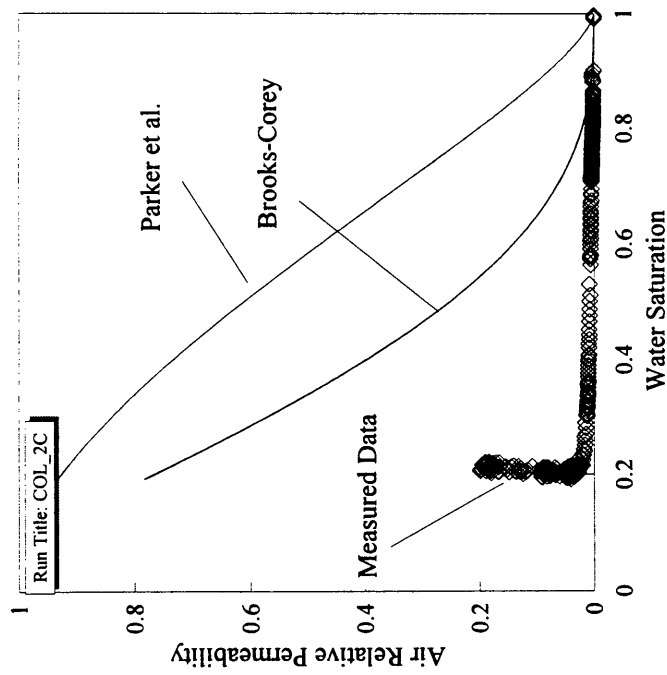


Figure 73. Air relative permeability-capillary head data and Brooks-Corey and Parker et al. functions derived from moisture retention data. Experiment COL_2C. Experimental conditions: $U_{ab} \approx 300 - 350$ cm, increasing over 150 hrs. Steady $S_w \approx 0.2$ at 20 hrs. $k_{ra} \approx 0.1$ at 120 hrs. and 0.2 at 150 hrs.

The measured $k_{ra}(S_w)$ data for experiment COL_2E (Figure 74) showed both air permeability breakthrough and step-changes as were observed for sample FLO and COR. Above $S_w \approx 0.3$, k_{ra} increased little, and was significantly below the Brooks-Corey and Parker et al. curves. At $S_w \approx 0.3, 0.2$, and 0.15 , k_{ra} increased in discreet steps, without change in S_w . Steady state saturation was reached at $S_w \approx 0.15$, where k_{ra} increased from 0.1 to 0.25. The measured $k_{ra}(h_c)$ data also fell significantly below the Brooks-Corey and Parker et al. curves (Figure 75).

The measured $k_{ra}(S_w)$ data for experiment COL_2G (Figure 76) were similar to experiment COL_2C and COL_2E, and showed extreme air permeability breakthrough without intermediate step-changes in k_{ra} . Steady state saturation was achieved at $S_w \approx 0.15$. At higher S_w , k_{ra} increased little, and at $S_w \approx 0.15$, k_{ra} increased by more than an order of magnitude. Data “noise” introduced by low I_u (Figure 40) were present, such that the mean final value of k_{ra} was approximately 0.6. The measured $k_{ra}(h_c)$ data (Figure 77) showed a distinct trend at low k_{ra} values. The k_{ra} values exhibited noise from experimental errors as the k_{ra} and h_c increased.

The measured $k_{ra}(S_w)$ data for experiment COL_1H (Figure 78) also showed air permeability breakthrough. The discontinuous trend in $k_{ra}(S_w)$ from $0.55 > S_w > 0.42$, represents the propagation of measurement errors of I_u and Q_u during the transient decrease in air injection pressure head from one to four hours during the experiment (Figures 42 and 44). After steady saturation was reached at $S_w \approx 0.3$, k_{ra} increased from 0.1 to 0.25. The $k_{ra}(h_c)$ data (Figure 79) closely approximated the Brooks-Corey and Parker et al. curves.

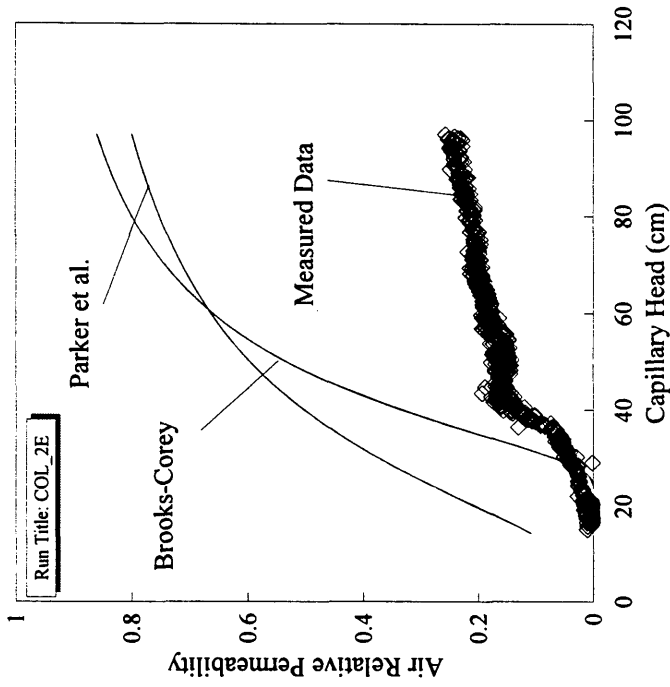


Figure 74. Air relative permeability-saturation data and Brooks-Corey and Parker et al. functions derived from moisture retention data. Experiment COL_2E. Experimental conditions: $U_{ab} \approx 500 - 450$ cm, Steady $S_w \approx 0.15$ at 15 hrs. $k_{ra} \approx 0.15$ at 15 hrs. and 0.25 at 70 hrs.

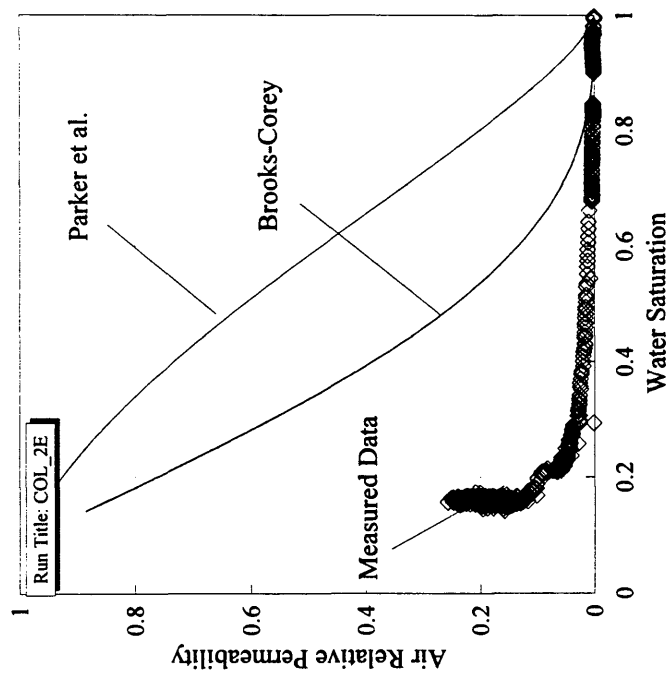


Figure 75. Air relative permeability-capillary head data and Brooks-Corey and Parker et al. functions derived from moisture retention data. Experiment COL_2E. Experimental conditions: $U_{ab} \approx 500 - 450$ cm, Steady $S_w \approx 0.15$ at 15 hrs. $k_{ra} \approx 0.15$ at 15 hrs. and 0.25 at 70 hrs.

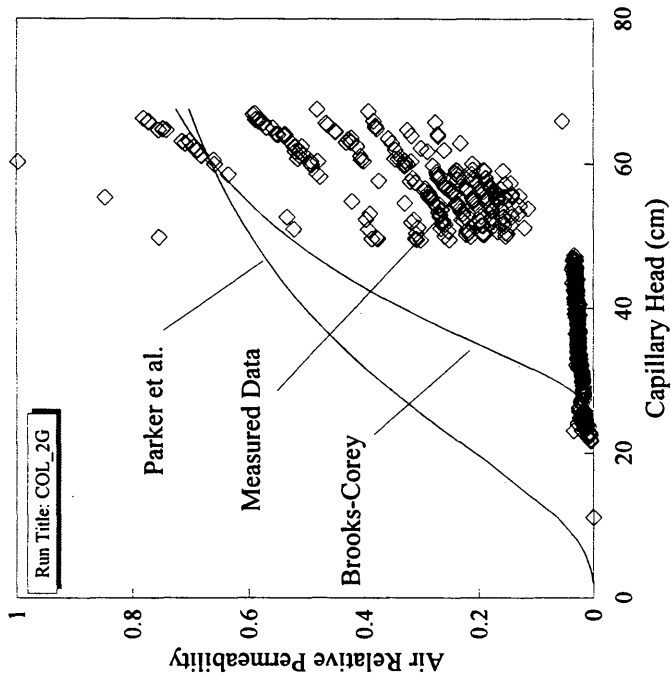


Figure 76. Air relative permeability-saturation data and Brooks-Corey and Parker et al. functions derived from moisture retention data. Experiment COL_2G. Experimental conditions: $U_{ab} \approx 500$ cm, $S_w \approx 0.15$ at 20 hrs. $k_{ra} \approx 0.03$ at 30 hrs and 0.75 at 55 hrs., permeability breakthrough at 31hrs.

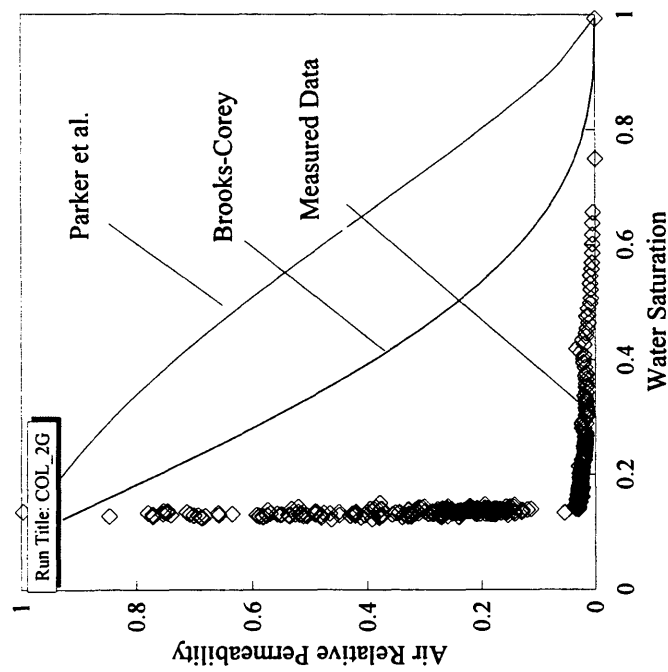


Figure 77. Air relative permeability-capillary head data and Brooks-Corey and Parker et al. functions derived from moisture retention data. Experiment COL_2G. Experimental conditions: $U_{ab} \approx 500$ cm, $S_w \approx 0.15$ at 20 hrs. $k_{ra} \approx 0.03$ at 30 hrs and 0.75 at 55 hrs., permeability breakthrough at 31hrs.

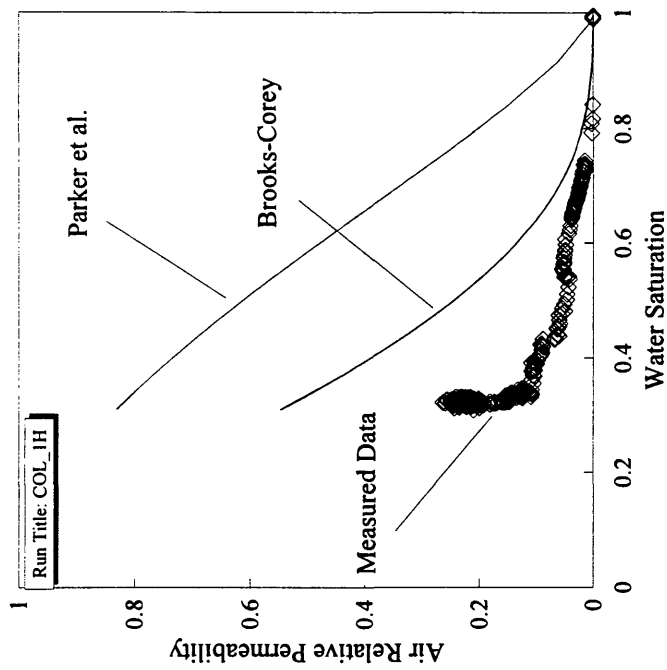


Figure 78. Air relative permeability-saturation data and Brooks-Corey and Parker et al. functions derived from moisture retention data. Experiment COL_IH. Experimental conditions: $U_{ab} \approx 180$ cm, Steady $S_w \approx 0.3$ at 25 hrs. $k_{ra} \approx 0.1$ at 10 hrs, 0.2 at 25 hrs., and 0.25 at 50 hrs.

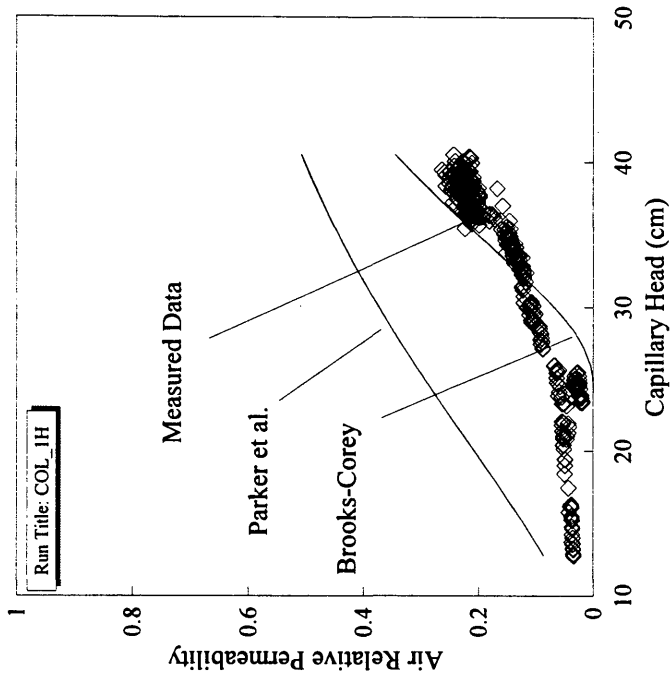


Figure 79. Air relative permeability-capillary head data and Brooks-Corey and Parker et al. functions derived from moisture retention data. Experiment COL_IH. Experimental conditions: $U_{ab} \approx 180$ cm, Steady $S_w \approx 0.3$ at 25 hrs. $k_{ra} \approx 0.1$ at 10 hrs, 0.2 at 25 hrs., and 0.25 at 50 hrs.

The $k_{ra}(S_w)$ and $k_{ra}(h_c)$ data from experiments CSM_1E (Figures 80 and 81) and CSM_1H (Figures 82 and 83) were similar to those involving sample FLO. Data for $k_{ra}(S_w)$ from experiments CSM_1E (Figure 80) and CSM_1H (Figure 82) both followed the Brooks-Corey relation above $S_w \approx 0.6$, and at $S_w \approx 0.6$, a discontinuity in the measured relation was observed. At $S_w < 0.6$, k_{ra} was lower than the Brooks-Corey function for experiment CSM_1E, while $k_{ra}(S_w)$ data for experiment CSM_1H closely followed the Brooks-Corey curve for $0 < k_{ra} < 0.82$. This was the only experiment where $k_{ra}(S_w)$ was accurately estimated by either the Parker et al. or Brooks-Corey relationships over a wide range of S_w . The $k_{ra}(h_c)$ data for both experiments involving sample CSM (Figures 81 and 83) showed a distinct change in slope which correlates to the discontinuity in $k_{ra}(S_w)$ at $S_w \approx 0.6$.

The experiments involving sample CHV showed air permeability breakthrough similar to samples COR and COL, and showed sensitivity to displacement rate, as was shown by sample COR. The $k_{ra}(S_w)$ data for experiment CHV_1H (Figure 84) were well below the Brooks-Corey curve for $S_w > 0.3$. At $S_w \approx 0.3$, k_{ra} increased in a step without change in S_w . The $k_{ra}(h_c)$ data (Figure 85) followed the Brooks-Corey curve closely over the range of saturations experienced.

Experiment CHV_1K was conducted at a slower rate of displacement than CHV_1H, and showed less pronounced air permeability breakthrough. The $k_{ra}(S_w)$ data for experiment CHV_1K (Figure 86) followed the Brooks-Corey curve more closely than experiment CHV_1H, yet still showed a distinct change in slope, in this case at $S_w \approx 0.5$. Below this saturation, the $k_{ra}(S_w)$ data rose to approximate the Brooks-Corey curve. The $k_{ra}(h_c)$ data (Figure 87) were very similar to those for experiment CHV_1H, and followed the Brooks-Corey curve closely for all saturations experienced.

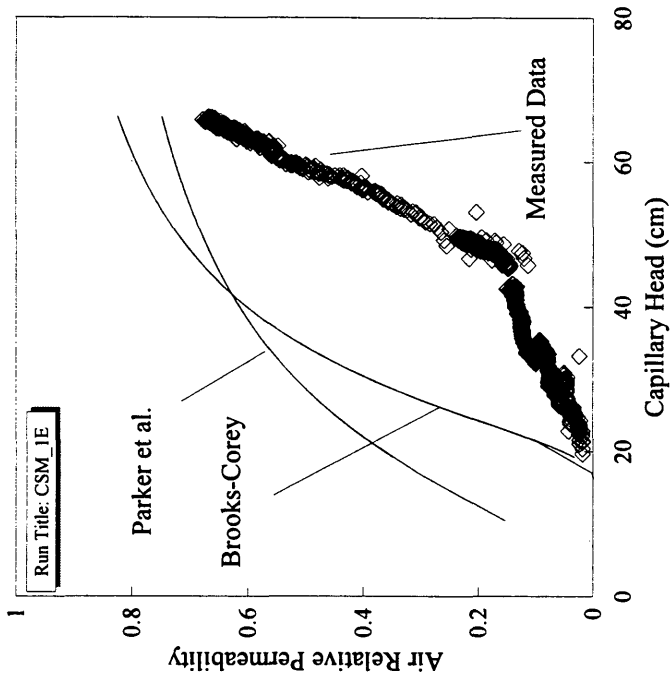


Figure 81. Air relative permeability-capillary head data and Brooks-Corey and Parker et al. functions derived from moisture retention data. Experiment CSM_1E. Experimental conditions: $U_{ab} \approx 225$ cm, $S_w \approx 0.35$ at 12 hrs. $k_{ra} \approx 0.3$ at 1 hr. and 0.6 at 7 hrs.

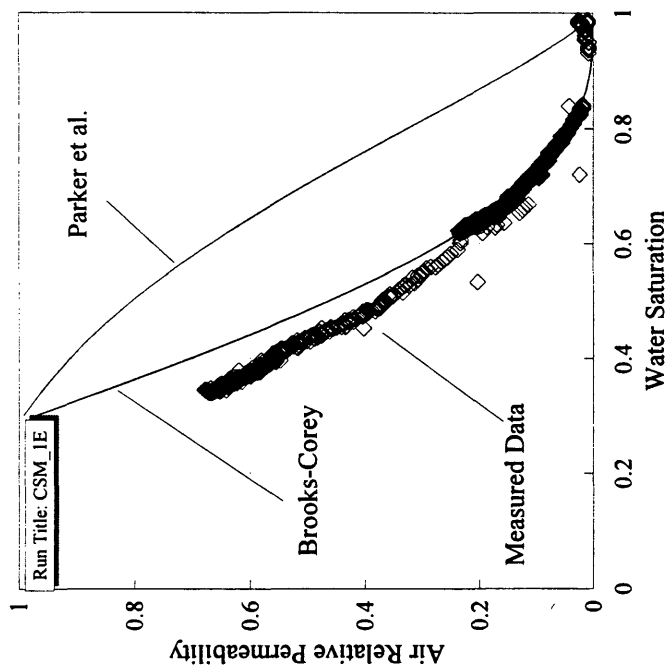


Figure 80. Air relative permeability-saturation data and Brooks-Corey and Parker et al. functions derived from moisture retention data. Experiment CSM_1E. Experimental conditions: $U_{ab} \approx 225$ cm, $S_w \approx 0.35$ at 12 hrs. $k_{ra} \approx 0.3$ at 1 hr. and 0.6 at 7 hrs.

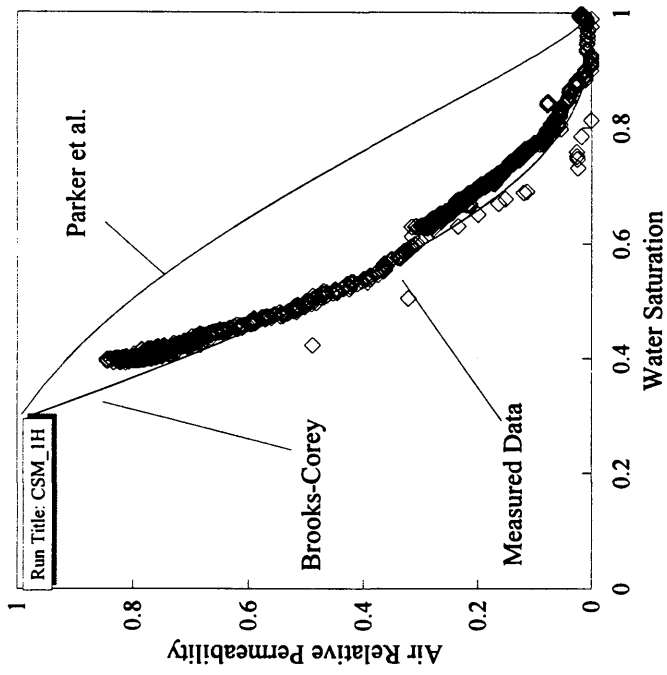


Figure 82. Air relative permeability-saturation data and Brooks-Corey and Parker et al. functions derived from moisture retention data. Experiment CSM_1H. Experimental conditions: $U_{ab} \approx 310$ at 0 - 0.4 hrs. and 240 cm at 0.4 - 23 hrs., $S_w \approx 0.6$ at 0.4 hrs. $k_{ra} \approx 0.6$ at 5 hrs. and 0.8 at 20 hrs.

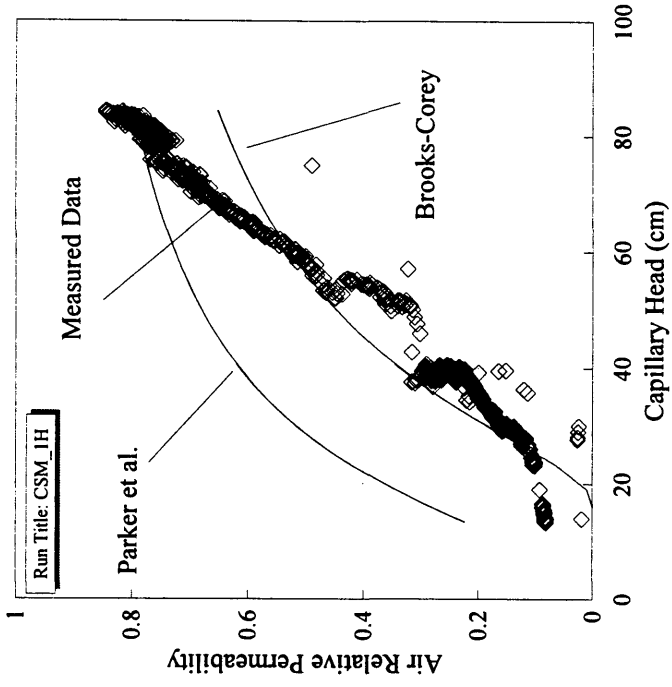


Figure 83. Air relative permeability-capillary head data and Brooks-Corey and Parker et al. functions derived from moisture retention data. Experiment CSM_1H. Experimental conditions: $U_{ab} \approx 310$ at 0 - 0.4 hrs. and 240 cm at 0.4 - 23 hrs., $S_w \approx 0.6$ at 0.4 hrs. $k_{ra} \approx 0.6$ at 5 hrs. and 0.8 at 20 hrs.

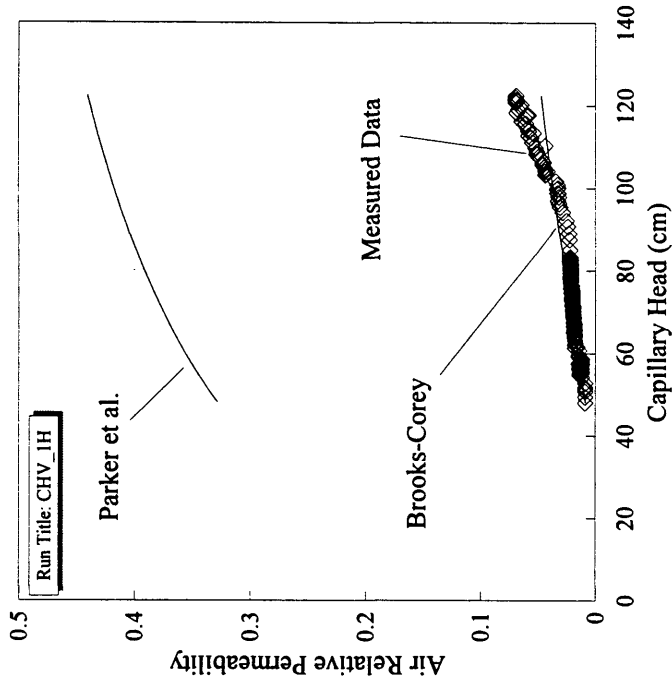


Figure 84. Air relative permeability-saturation data and Brooks-Corey and Parker et al. functions derived from moisture retention data. Experiment CHV_1H. Experimental conditions: $U_{ab} \approx 325$ at 0 - 2 hrs., 350 cm at 2 - 23 hrs., and 425 at 23 - 26 hrs. $S_w \approx 0.5$ at 5 hrs. and 0.3 at 26 hrs. $k_{ra} \approx 0.08$ at 23 hrs. and 0.17 at 23 - 26 hrs.

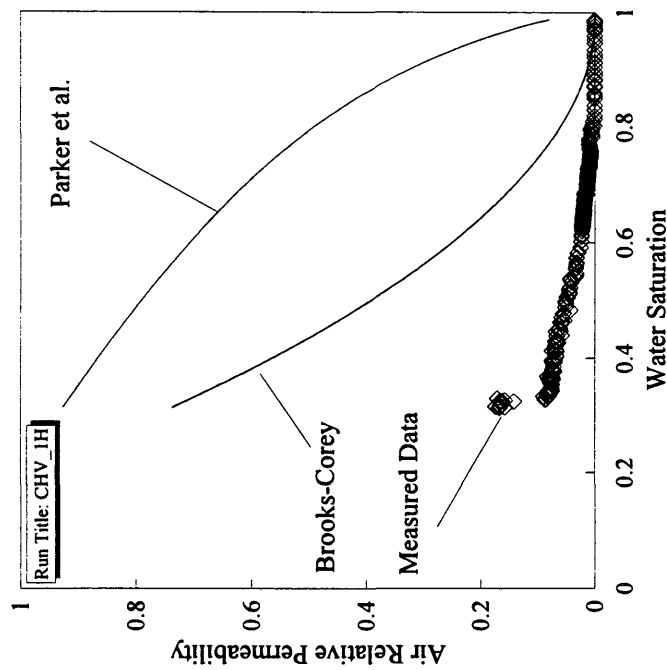


Figure 85. Air relative permeability-capillary head data and Brooks-Corey and Parker et al. functions derived from moisture retention data. Experiment CHV_1H. Experimental conditions: $U_{ab} \approx 325$ at 0 - 2 hrs., 350 cm at 2 - 23 hrs., and 425 at 23 - 26 hrs. $S_w \approx 0.5$ at 5 hrs. and 0.3 at 26 hrs. $k_{ra} \approx 0.08$ at 23 hrs. and 0.17 at 23 - 26 hrs.

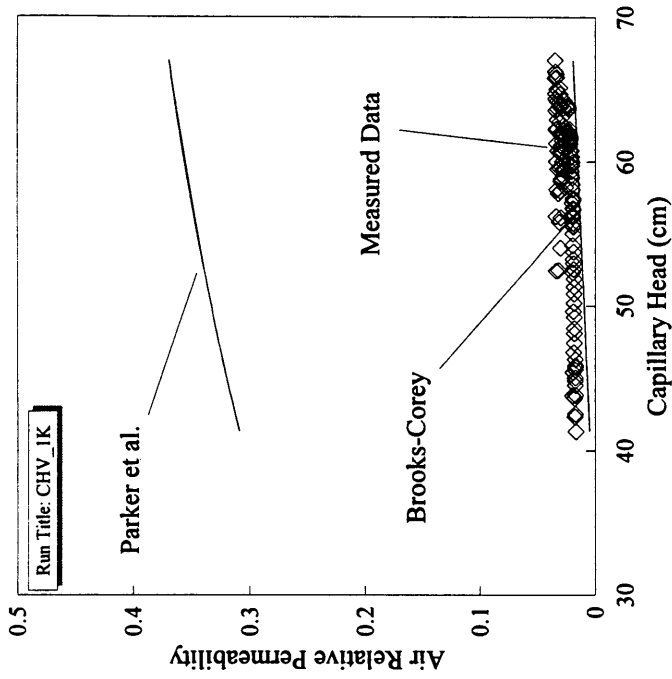


Figure 86. Air relative permeability-saturation data and Brooks-Corey and Parker et al. functions derived from moisture retention data. Experiment CHV_1K. Experimental conditions: $U_{ab} \approx 300$ cm. $S_w \approx 0.5$ at 20 hrs. and steady at 0.45 at 40 hrs. $k_{ra} \approx 0.2$ at 20 hrs. and 0.4 at 70 - 90 hrs.

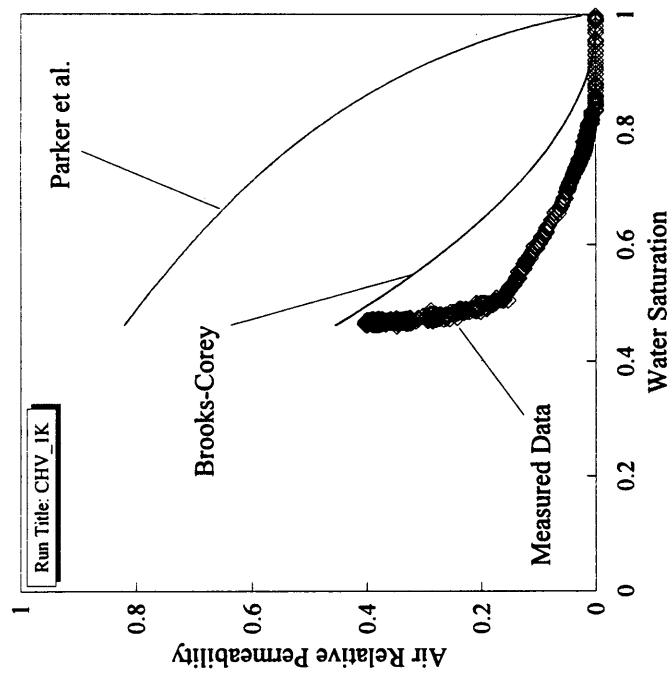


Figure 87. Air relative permeability-capillary head data and Brooks-Corey and Parker et al. functions derived from moisture retention data. Experiment CHV_1K. Experimental conditions: $U_{ab} \approx 300$ cm. $S_w \approx 0.5$ at 20 hrs. and steady at 0.45 at 40 hrs. $k_{ra} \approx 0.2$ at 20 hrs. and 0.4 at 70 - 90 hrs.

5.5.4 Water Relative Permeability Data

Water relative permeability data (Figures 88 - 99) are presented for a limited number of experiments due to the effects of transient I_w after air breakthrough. Transient reversals in I_w frequently occurred without corresponding changes in the rate of water drainage from the sample. These effects resulted in errors in calculation of k_{rw} , and tended to occur early in the experiments, where k_{rw} was changing rapidly. For those tests where relevant k_{rw} data were obtained, the results were consistent with either or both the Brooks-Corey and Parker et al. functions.

The measured $k_{rw}(S_w)$ and $k_{rw}(h_c)$ data for experiment FLO_2P (Figures 88 and 89) were bounded by the Brooks-Corey and Parker et al. curves. Data at $S_w > 0.75$ were not presented due to errors resulting from transient negative values of I_w in the early portion of the experiment.

During experiment COR_3B, $k_{rw}(S_w)$ data (Figure 90) were approximated by the Parker et al. curve, with deviations resulting from transients in I_w following air breakthrough. The measured $k_{rw}(h_c)$ data (Figure 91) also followed the Parker et al. curve, with transient deviations. The Brooks-Corey curve for $k_{rw}(h_c)$ was far removed from the measured relative permeability data, since h_c was generally below the entry pressure (h_0) derived from moisture retention data.

The measured $k_{rw}(S_w)$ relationships from experiment COR_3E (Figure 92) followed the Brooks-Corey curve, with some transient deviations, while the $k_{rw}(h_c)$ data (Figure 93) followed the Parker et al. curve. As with experiment COR_3B, the Brooks-Corey relation for $k_{rw}(h_c)$ provided a poor estimate, since h_c was below h_0 for most values of k_{rw} .

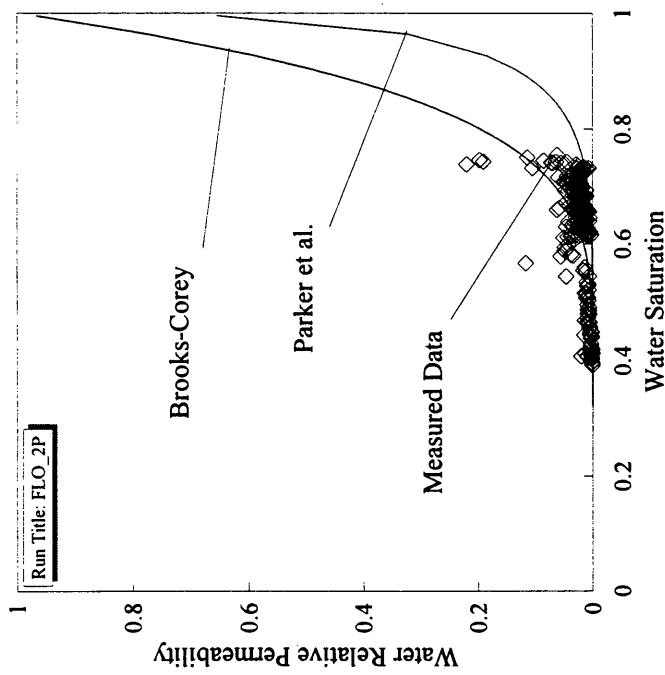


Figure 88. Water relative permeability-saturation data and Brooks-Corey and Parker et al. functions derived from moisture retention data. Experiment FLO_2P. Experimental conditions: $U_{ab} \approx 170 - 175$ cm, $S_w \approx 0.4$ at 3 hrs. $k_{ra} \approx 0.55$ at 3 hours.

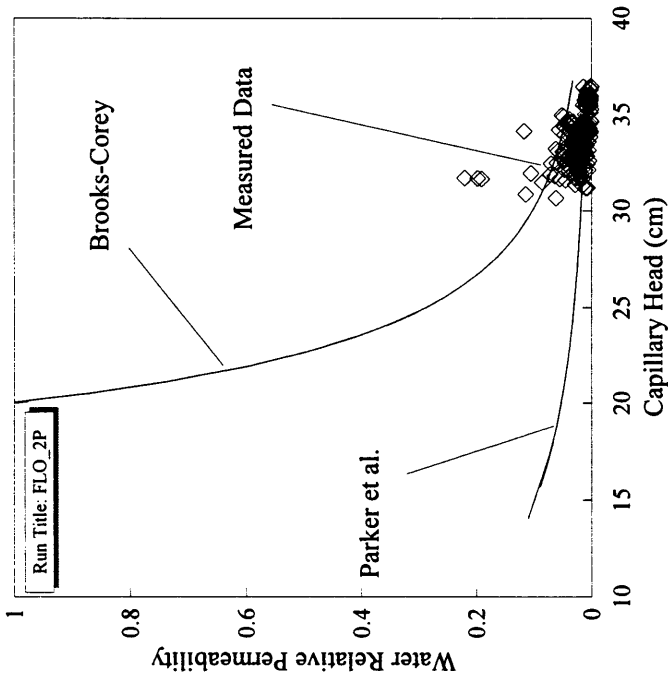


Figure 89. Water relative permeability-capillary head data and Brooks-Corey and Parker et al. functions derived from moisture retention data. Experiment FLO_2P. Experimental conditions: $U_{ab} \approx 170 - 175$ cm, $S_w \approx 0.4$ at 3 hrs. $k_{ra} \approx 0.55$ at 3 hours.

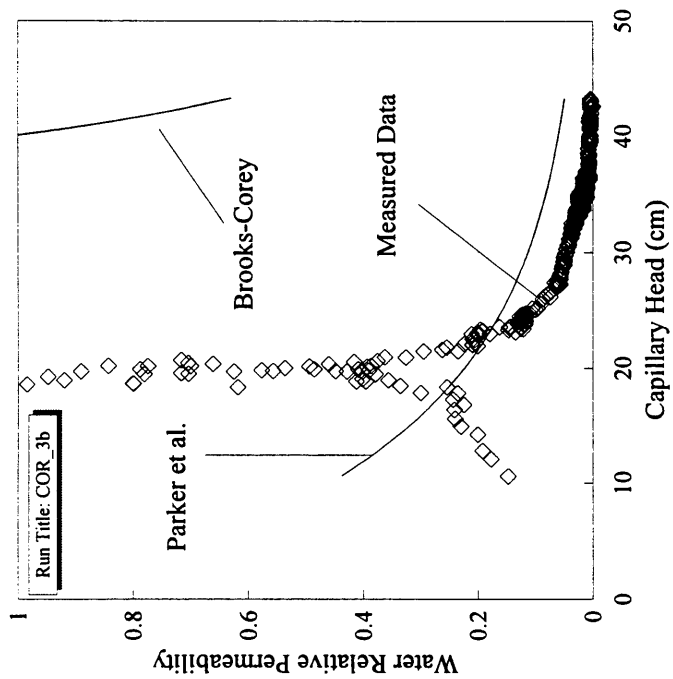


Figure 90. Water relative permeability-saturation data and Brooks-Corey and Parker et al. functions derived from moisture retention data. Experiment COR_3B. Experimental conditions: $U_{ab} \approx 225$ cm, $S_w \approx 0.5$ at 0.5 hrs. $k_{rw} \approx 0.1$ at 0.2 hrs.

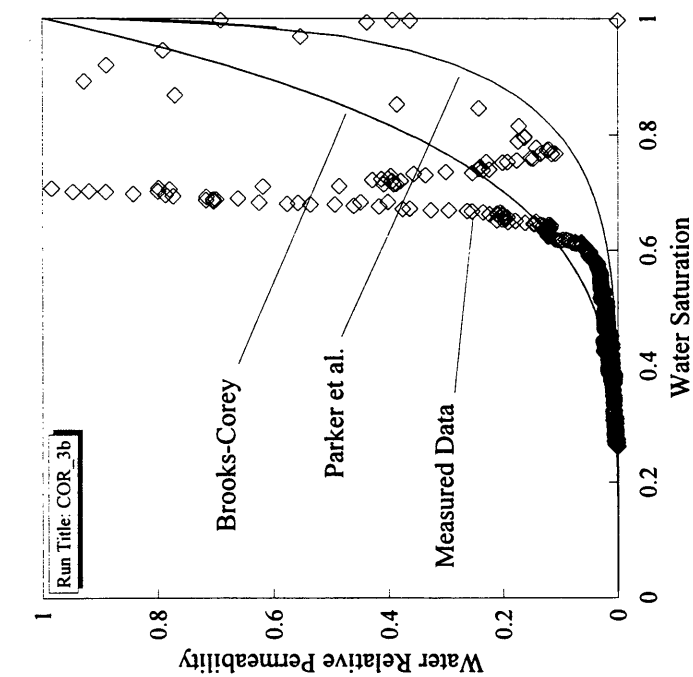


Figure 91. Water relative permeability-capillary head data and Brooks-Corey and Parker et al. functions derived from moisture retention data. Experiment COR_3B. Experimental conditions: $U_{ab} \approx 225$ cm, $S_w \approx 0.5$ at 0.5 hrs. $k_{rw} \approx 0.1$ at 0.2 hrs.

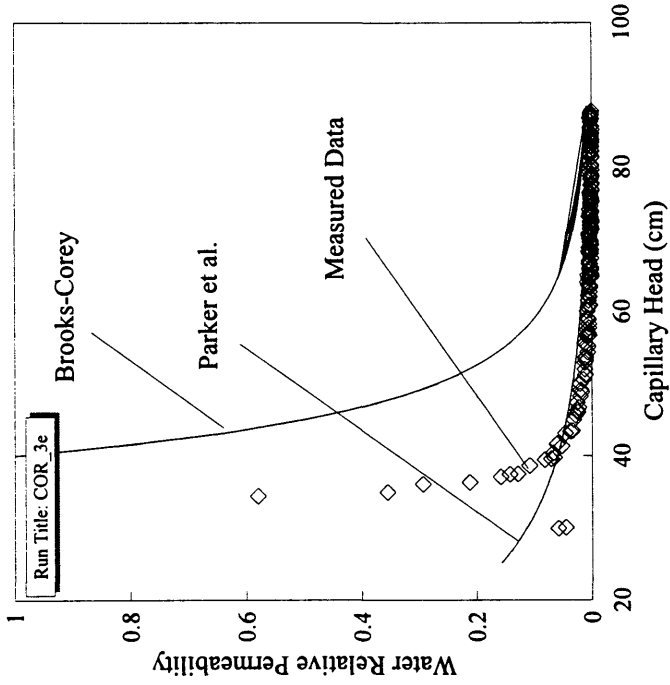


Figure 92. Water relative permeability-saturation data and Brooks-Corey and Parker et al. functions derived from moisture retention data. Experiment COR_3E. Experimental conditions: $U_{ab} \approx 250 - 280$ cm, increasing from 0 to 3 hrs., $S_w \approx 0.4$ at 3 hrs., $k_{rw} \approx 0.2$ at 2 hrs. and 0.02 at 3 hrs.

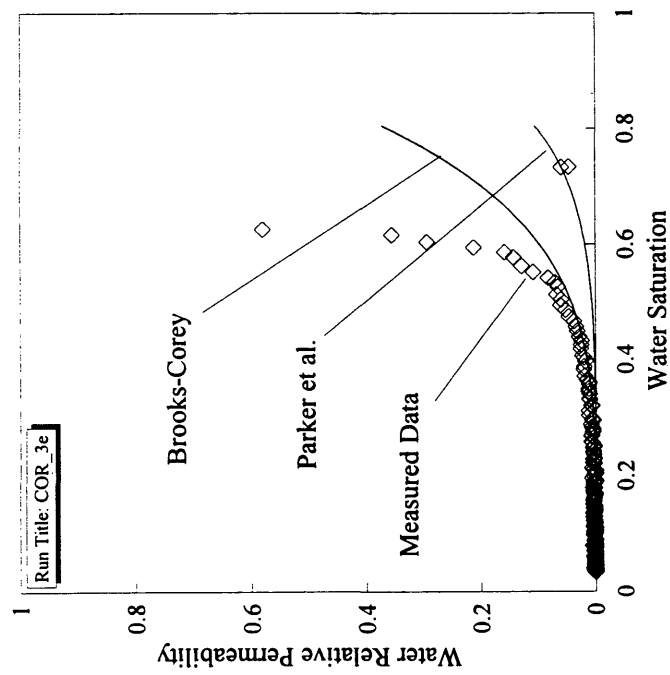


Figure 93. Water relative permeability-capillary head data and Brooks-Corey and Parker et al. functions derived from moisture retention data. Experiment COR_3E. Experimental conditions: $U_{ab} \approx 250 - 280$ cm, increasing from 0 to 3 hrs., $S_w \approx 0.4$ at 3 hrs., $k_{rw} \approx 0.2$ at 2 hrs. and 0.02 at 3 hrs.

The measured $k_{rw}(S_w)$ data for experiment COL_1J (Figure 94) were obscured by transient effects, but were frequently approximated by the Parker et al. curve, especially below $S_w \approx 0.7$. The $k_{rw}(h_c)$ data (Figure 95) did not follow the Brooks-Corey or Parker et al. curves.

The measured $k_{rw}(S_w)$ data for experiment CSM_1H (Figure 96) showed transient effects, but followed the Parker et al. curve closely for $0.25 > k_{rw} > 0.1$. The $k_{rw}(h_c)$ data (Figure 97) were generally bounded by the Parker et al. and Brooks-Corey curves.

The measured $k_{rw}(S_w)$ data for experiment CHV_1F (Figure 98) displayed noise from transient gradients, but seemed to generally follow the Brooks-Corey curve. The $k_{rw}(h_c)$ data (Figure 99) were generally bounded by the Parker et al. and Brooks-Corey curves.

5.6 Gas-Phase Tracer Data

Gas-phase tracer data from experiment FLO_2P (Figure 100) show that relatively consistent tracer recovery of 95 to 97 percent was achieved after 93 percent recovery of the initial slug injected. Compared to the calibration recovery of $89.9 \text{ percent} \pm 2.0$ (Figure 17), these data do not reflect air trapping, and therefore do not suggest the development of pore-scale dead-end air fingers. Since these data were collected at $S_w > 0.6$, where $k_{ra}(S_w)$ was approximated by the Brooks-Corey function (Figure 62), the air relative permeability data also do not suggest the development of dead-end air fingers.

Gas-phase tracer data for experiment FLO_2I (Figure 101) were collected under similar experimental conditions as experiment FLO_2P, except tracer data were

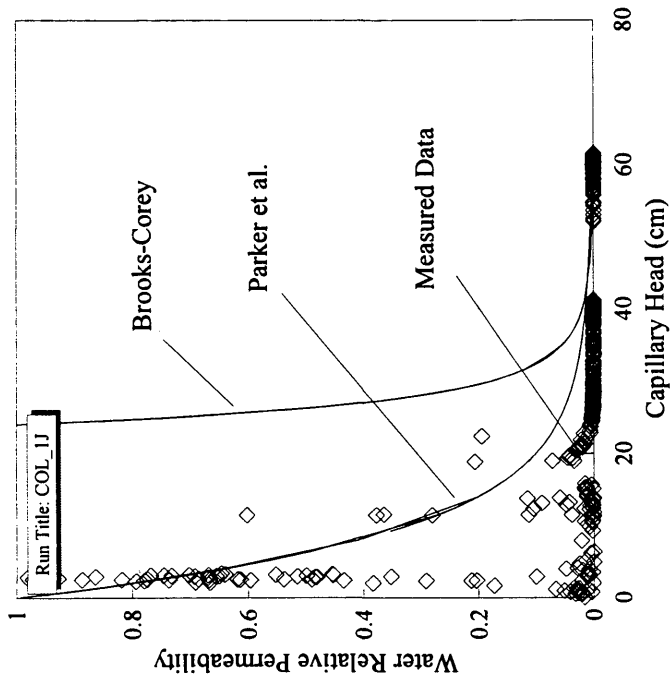


Figure 94. Water relative permeability-saturation data and Brooks-Corey and Parker et al. functions derived from moisture retention data. Experiment COL_1J. Experimental conditions: $U_{ab} \approx 180 - 190$ cm, increasing from 0 to 5 hrs., $S_w \approx 0.5$ at 0.5 hrs. $k_{rw} \approx 0.1$ at 2 hrs. and 0.02 at 5 hrs.

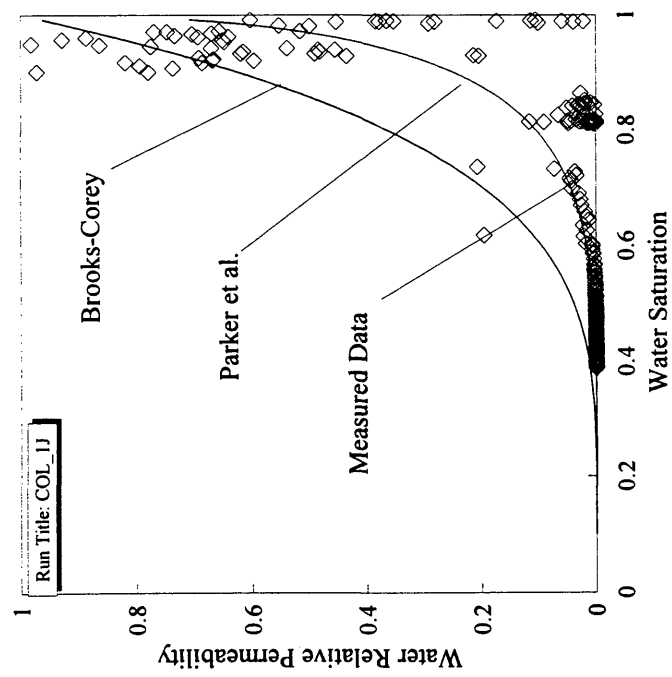


Figure 95. Water relative permeability-capillary head data and Brooks-Corey and Parker et al. functions derived from moisture retention data. Experiment COL_1J. Experimental conditions: $U_{ab} \approx 180 - 190$ cm, increasing from 0 to 5 hrs., $S_w \approx 0.5$ at 0.5 hrs. $k_{rw} \approx 0.1$ at 2 hrs. and 0.02 at 5 hrs.

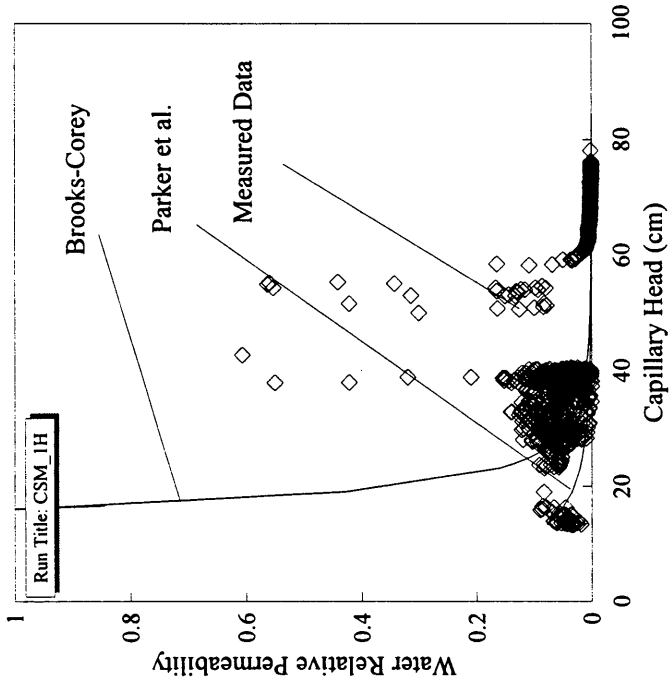


Figure 96. Water relative permeability-saturation data and Brooks-Corey and Parker et al. functions derived from moisture retention data. Experiment CSM_1H. Experimental conditions: $U_{ab} \approx 310$ at 0 - 0.4 hrs. and 240 cm at 0.4 - 23 hrs., $S_w \approx 0.6$ at 0.4 hrs.

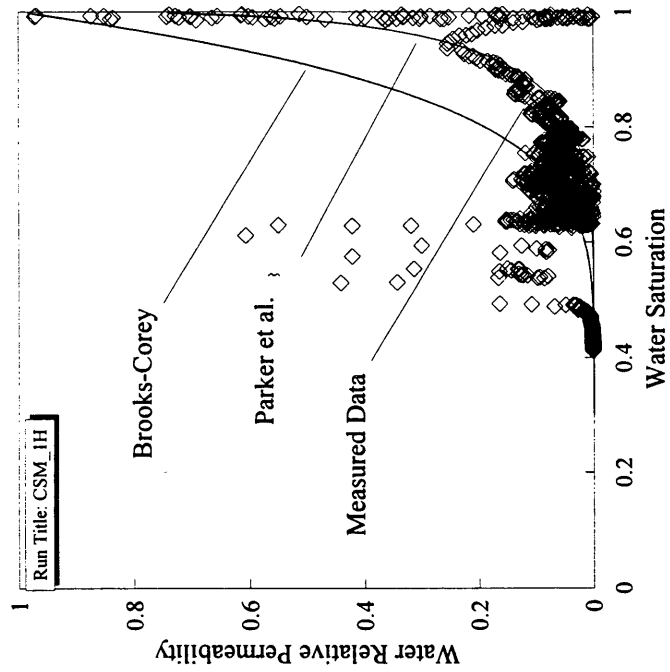


Figure 97. Water relative permeability-capillary head data and Brooks-Corey and Parker et al. functions derived from moisture retention data. Experiment CSM_1H. Experimental conditions: $U_{ab} \approx 310$ at 0 - 0.4 hrs. and 240 cm at 0.4 - 23 hrs., $S_w \approx 0.6$ at 0.4 hrs.

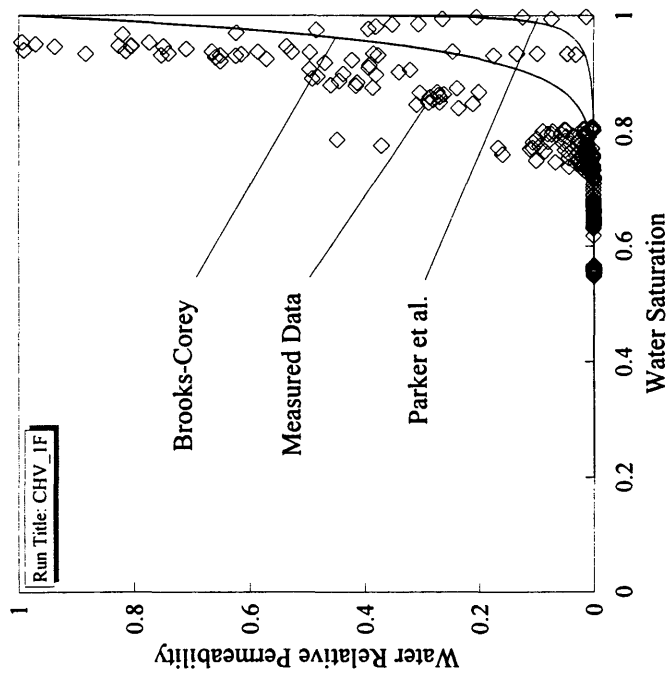


Figure 98. Water relative permeability-saturation data and Brooks-Corey and Parker et al. functions derived from moisture retention data. Experiment CHV_1F. Experimental conditions: $U_{ab} \approx 200$, $S_w \approx 0.8$ at 0.5 hrs., 0.62 at 20 hrs.

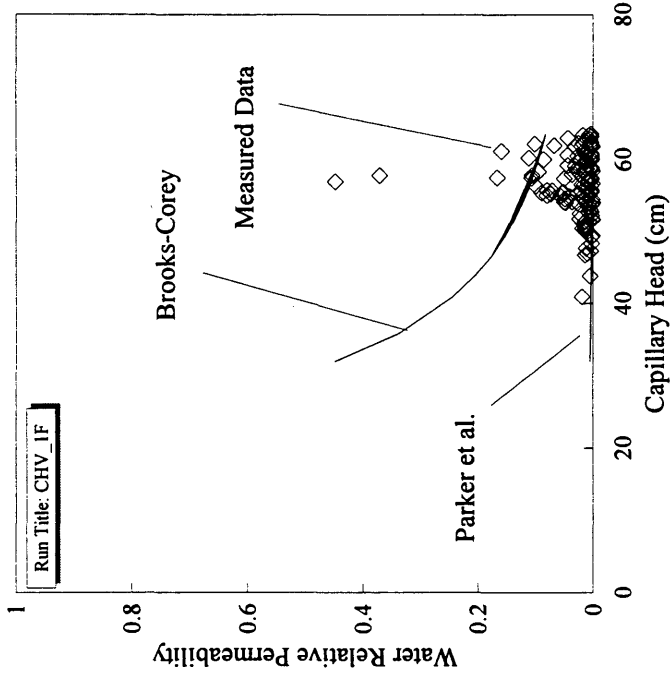


Figure 99. Water relative permeability-capillary head data and Brooks-Corey and Parker et al. functions derived from moisture retention data. Experiment CHV_1F. Experimental conditions: $U_{ab} \approx 200$, $S_w \approx 0.8$ at 0.5 hrs., 0.62 at 20 hrs.

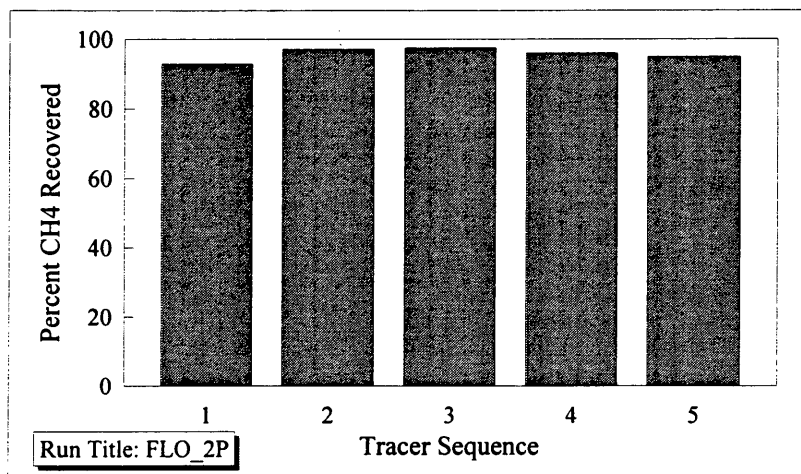


Figure 100. Gas-phase tracer data. Experiment FLO_2P. Experimental conditions: $U_{ab} \approx 175$ cm, $Q_a = 50 - 250$ ml/min, S_w range 1.0 to 0.68, duration 0.5 hr.

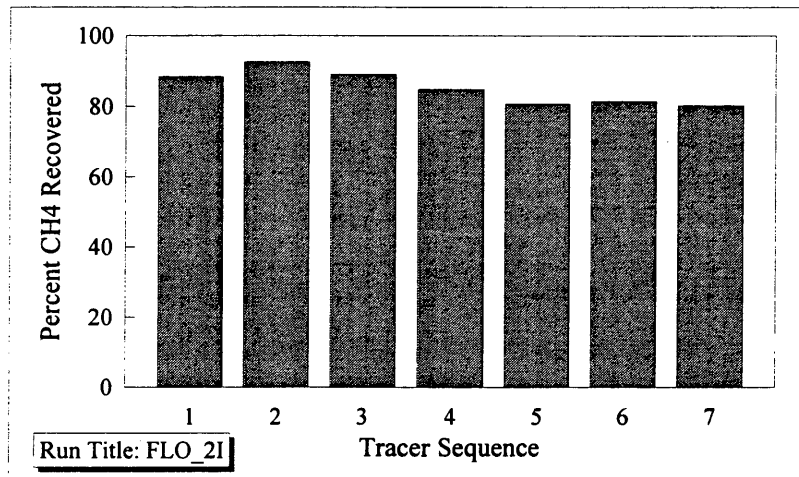


Figure 101. Gas-phase tracer data. Experiment FLO_2I. Experimental conditions: $U_{ab} \approx 175$ cm, $Q_a = 50 - 500$ ml/min, S_w range 1.0 to 0.51, duration 0.42 hr.

collected over a wider range of saturations, down to $S_w = 0.53$. Also, during this experiment, $k_{ra}(S_w)$ deviated from the Brooks-Corey relationship for $S_w < 0.6$ (Figure 58). Tracer slugs four through seven (Figure 101) represent portions of the experiment where $S_w < 0.6$, and where low $k_{ra}(S_w)$ data suggest the possible development of dead-end air fingers. In fact, the tracer data show approximately 90 percent recovery at $S_w > 0.6$, and approximately 80 percent recovery at $S_w < 0.6$. Compared to the approximately 90 percent calibration recovery, these data indicate possible air trapping at $S_w < 0.6$, which may reflect the development of pore-scale dead-end air fingers.

Gas-phase tracer data collected during experiments CSM_1E and CSM_1H reflect poor reproducibility of the tracer experiment results. The tracer data from experiment CSM_1E (Figure 102) showed a trend of increasing tracer recovery over time, while during experiment CSM_1H (Figure 103) tracer recovery decreased over time. These data were collected under similar experimental conditions, and over the same range of saturations ($0.6 < S_w < 1$). These tracer data are considered to be inconclusive, since they suggest air trapping, while $k_{ra}(S_w)$ data for both experiments followed the Brooks-Corey relationship, suggesting an absence of air trapping.

Gas-phase tracer data collected during experiment COL_2J (Figure 104) show a consistent trend of increasing tracer recovery over time, from 80 to 100 percent, which indicates possible air trapping during the early portion of the experiment. This suggests the possible development of dead-end air fingers during initial air invasion. Due to experimental errors after completion of the tracer testing, k_r - S - h_c data from this experiment were not presented. However, sample COL consistently showed extremely low $k_{ra}(S_w)$ and air permeability breakthrough at low S_w , which also suggests the possible development of dead-end air fingers during air invasion.

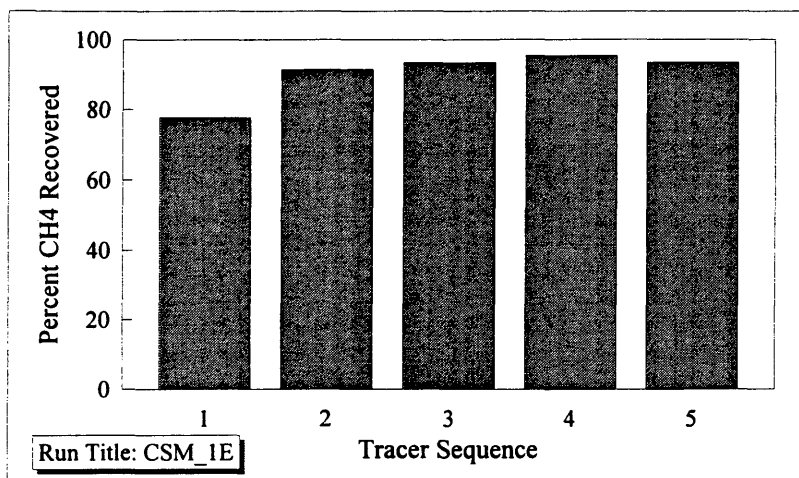


Figure 102. Gas-phase tracer data. Experiment CSM_1E. Experimental conditions: $U_{ab} \approx 225$ cm, $Q_a = 20 - 160$ ml/min, S_w range 1.0 to 0.62, duration 0.5 hr.

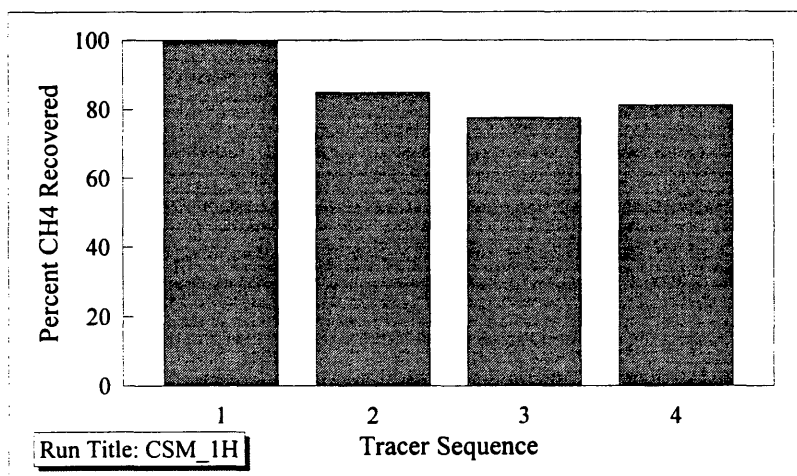


Figure 103. Gas-phase tracer data. Experiment CSM_1H. Experimental conditions: $U_{ab} \approx 310$ cm, $Q_a = 40 - 450$ ml/min, S_w range 1.0 to 0.63, duration 0.3 hr.

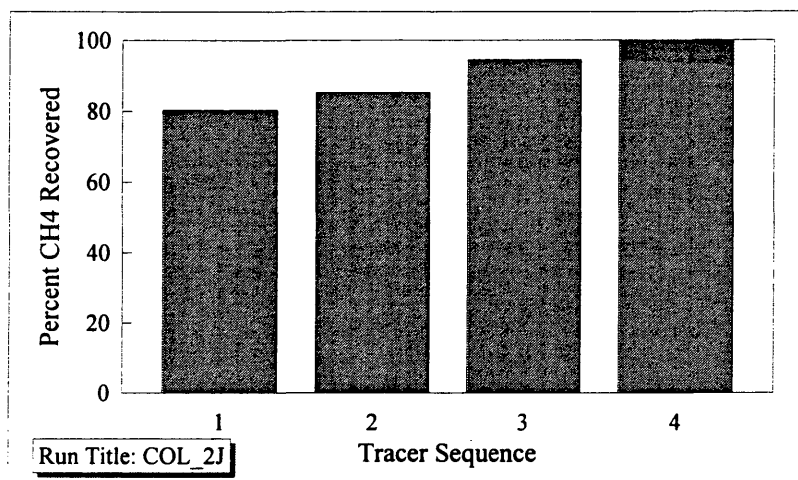


Figure 104. Gas-phase tracer data. Experiment COL_2J. Experimental conditions: $U_{ab} \approx 340$ cm, $Q_a = 5 - 12$ ml/min, S_w range 1.0 to 0.5, duration 2 hr.

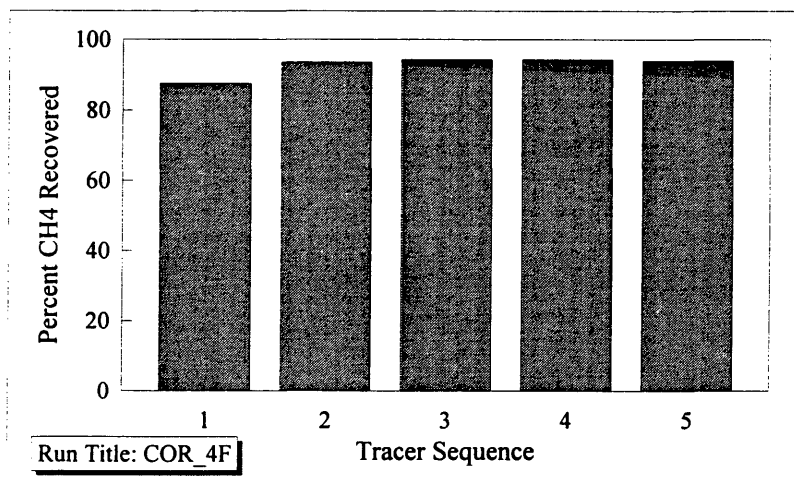


Figure 105. Gas-phase tracer data. Experiment COR_4F. Experimental conditions: $U_{ab} \approx 225$ cm, $Q_a = 10 - 100$ ml/min, S_w range 1.0 to 0.62, duration 0.42 hr.

Gas-phase tracer data from three experiments using sample COR generally showed inconsistent results. These experiments were conducted using a specimen for which k_r - S_h data were not presented, however, sample COR consistently showed low $k_{ra}(S_w)$ and air permeability breakthrough at low S_w . Experiment COR_4F (Figure 105) showed approximately 87 percent recovery of the initial tracer slug injected, and approximately 93 percent recovery of all the following tracer slugs. This data may indicate air trapping during initial air invasion. Experiment COR_4H (Figure 106) showed similar results as COR_4F for the first three slugs injected, with recoveries of 81, 88, and 88 percent, respectively. However, 70 and 85 percent recovery of tracer slugs four and five were obtained. Experiment COR_4J (Figure 107) showed 90 percent recovery of the initial slug injected, and from 83 to 85 percent recovery of the following four slugs.

5.7 Similitude of Air Injection Displacement Experiments

The values of Re and C calculated from the air injection displacement data are summarized in Table 12. The value of both parameters is a function of air velocity, which varies with Q_a and S_w during an experiment. The maximum value of Re encountered during the series of 18 tests was 0.86 for test COL_2E. Since the criteria for Darcy (i.e. laminar) flow is $Re < 1$, Darcy's law can be considered valid for the experiments, and inertial forces in flowing air were insignificant. The magnitude of C ranged from 4×10^{-8} to 1×10^{-6} for the 18 tests. For sandy soils, a limit of $C \leq \sim 10^{-6}$ is imposed by the limit on air velocity for Darcy flow.

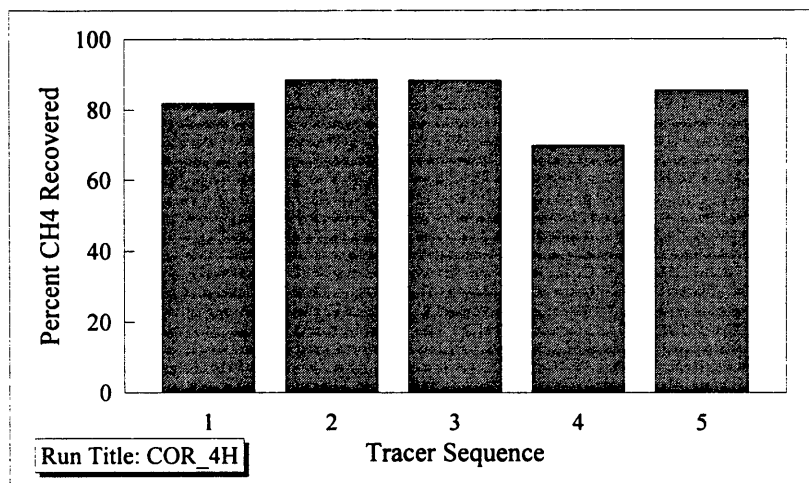


Figure 106. Gas-phase tracer data. Experiment COR_4H. Experimental conditions: $U_{ab} \approx 275$ cm, $Q_a = 10 - 400$ ml/min, S_w range 1.0 to 0.3, duration 0.5 hr.

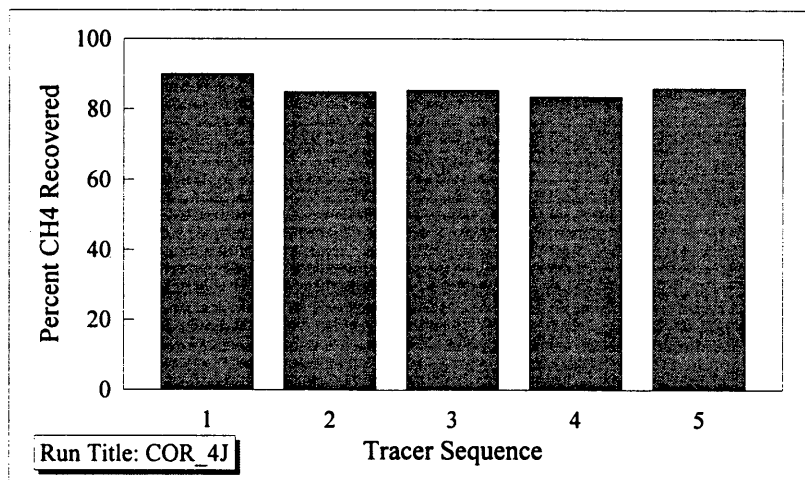


Figure 107. Gas-phase tracer data. Experiment COR_4J. Experimental conditions: $U_{ab} \approx 230$ cm, $Q_a = 10 - 125$ ml/min, S_w range 1.0 to 0.4, duration 0.5 hr.

Table 12. Summary of calculated values of Re and C for the 18 experiments.

Test	Re (min)	Re (max)	C (min)	C (max)
FLO_2I	0.05	0.27	2.50e-07	1.50e-06
FLO_2L	0.12	0.22	9.00e-07	1.30e-06
FLO_2P	0.03	0.30	5.00e-07	8.00e-07
FLO_1K	0.04	0.32	2.60e-07	1.80e-06
COR_3A	0.01	0.09	1.30e-07	9.80e-07
COR_3B	0.09	0.13	1.20e-06	1.40e-06
COR_3C	0.01	0.12	1.00e-07	1.30e-06
COR_3E	0.006	0.014	5.10e-08	1.50e-07
COL_2C	0.05	0.62	1.50e-07	1.40e-06
COL_2E	0.11	0.86	3.00e-07	2.00e-06
COL_2G	0.02	0.25	8.00e-08	5.70e-07
COL_1H	0.39	0.72	8.90e-07	1.60e-06
COL_1J	0.06	0.63	1.40e-07	1.40e-06
CSM_1E	0.018	0.21	1.30e-07	1.20e-06
CSM_1H	0.05	0.15	3.60e-07	8.40e-07
CHV_1F	0.005	0.09	9.00e-08	1.70e-06
CHV_1H	0.003	0.015	4.00e-08	1.50e-07
CHV_1K	0.01	.05	1.30e-07	6.80e-07

Section 6

DISCUSSION

This research provided measurements of k_r - S - h_c relationships for the air sparging process, which differed from estimates based on common functional forms in four ways: (1) values of $k_{ra}(S_w)$ and $h_c(S_w)$ which were significantly lower than expected for non-fingered flow, (2) step-like independent changes in air permeability and fluid saturation, (3) large increases in air permeability at steady state saturation (i.e., air permeability breakthrough), and (4) displacement rate dependence of air relative permeability relationships.

Errors related to fluid non-uniformity, the effects of transient non-equilibrium, and the development of pore-scale dead-end air fingers are examined as possible causes of the discrepancies between measured and estimated k_r - S - h_c relationships. The rate of water displacement and relevant physical soil properties are examined as predictors of the unique behaviors observed. Finally, the relative importance of buoyant, viscous, and capillary forces are examined with respect to the mechanisms of air invasion and the similarity of the physical experimental model to field-scale air sparging

6.1 Possible Causes of Unique Flow Behaviors

6.1.1 Errors Related to Fluid Non-Uniformity

The experimental system was designed to achieve uniform capillary head, and therefore saturation, in core samples tested so that errors related to the measurement of bulk sample properties were eliminated. However, for many experiments, the condition of uniform capillary head, defined by the criterion $I_a = I_w + 1$, described in section 3.2.2, was not met due to performance limitations of the system. In some instances, for soils with high air conductivity, in order to meet the uniformity criterion, air flow rates would have exceeded the system limitation of 1,000 ml/min. In other instances, for experiments where an upper boundary was used which had higher P_{et} , impedance of the upper porous boundary to air flow would sometimes limit the air gradient which could be achieved. This is illustrated by the transient data during the first 3 hours of experiment COR_3E, where the air flow rate increased linearly over time, the air gradient decreased, and h_{ct} and h_{cb} began to diverge, despite incremental increases in U_{ab} (Figures 30, 31, and 32).

In other cases, the two-phase flow behavior of the soils prevented the uniformity criterion from being met. In these cases, increasing U_{ab} to achieve the criterion $I_a = I_w + 1$ increased the rate of water drainage from the soil, and increased I_w , so that $I_a = I_w + 1$ became larger and more difficult to maintain. Also as S_w and k_{rw} decreased, I_w frequently increased, making the uniformity criterion more difficult to achieve. This is illustrated by experiment COL_2C (Figures 46 - 49).

As a result of the limitations described above, use of the computer system to maintain $I_a = I_w + 1$ was not feasible. This generally resulted in $I_a < I_w + 1$, and $h_{ci} > h_{cb}$ as the experiments proceeded. However, in some tests, U_{ab} was controlled at early times so that $I_a > I_w + 1$, and $h_{cb} > h_{ci}$. Then, at later times the system limitations described above would result in $I_a < I_w + 1$ such that $h_{ci} > h_{cb}$. For experiments FLO_2P, COR_3E, COL_2C, and COL_2E (Figures 50, 51, 53, and 55) this provided an opportunity to achieve uniform capillary heads where $I_a = I_w + 1$ at intermediate values of S_w .

The potential error in k_{ra} measurements due to non-uniform fluid saturation in the core samples was evaluated by applying the measured values of h_{ci} and h_{cb} to model the effects of non-uniformity of fluid saturation, as described in section 4.3.1. The results of this analysis for selected experiments are presented here on graphs which depict the measured $k_{ra}(S_w)$ data, an upper error bound (UEB) on $k_{ra}(S_w)$ based on the error analysis, and the Brooks-Corey functional relation derived from the moisture retention data. Tables of the values presented in the graphs and intermediate calculations are in Appendix E.

The error analysis of $k_{ra}(S_w)$ data from experiment FLO_2P (Figure 108) indicated that the error related to non-uniform fluid saturation was minimal, and did not change below $S_w \approx 0.6$, where k_{ra} deviated from the Brooks-Corey function by nearly 50%. Error analysis of fluid non-uniformity during experiment COR_3E (Figure 109) showed that these errors were insignificant relative to the deviation of measured $k_{ra}(S_w)$ from the Brooks-Corey relation. Similar results were obtained for experiments COL_1H and CHV_1H (Figures 110 and 111).

The error analysis suggests that the deviation of measured $k_{ra}(S_w)$ from the Brooks-Corey functional relationship cannot be accounted for by errors related to non-uniformity

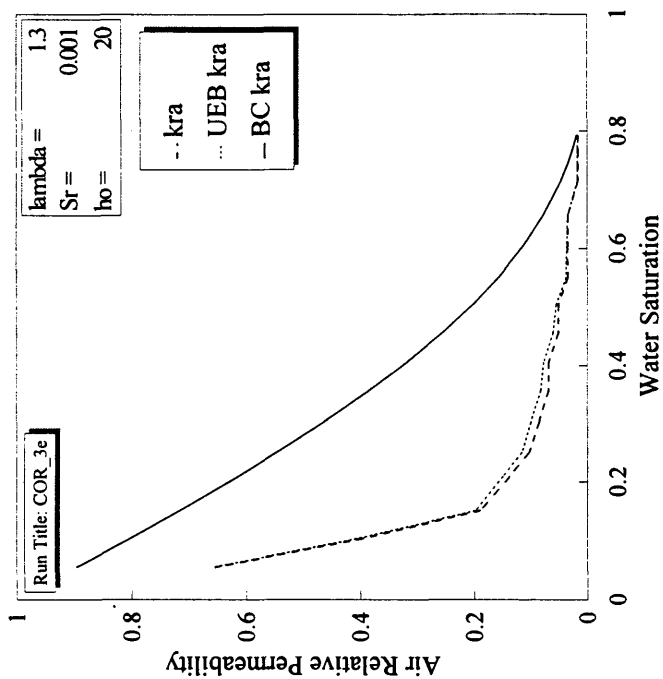


Figure 109. Error analysis of non-uniform fluid saturation. Experiment COR_3E. Air relative permeability (k_{ra}) and an upper error bound (UEB) are compared to the Brooks-Corey functional form.

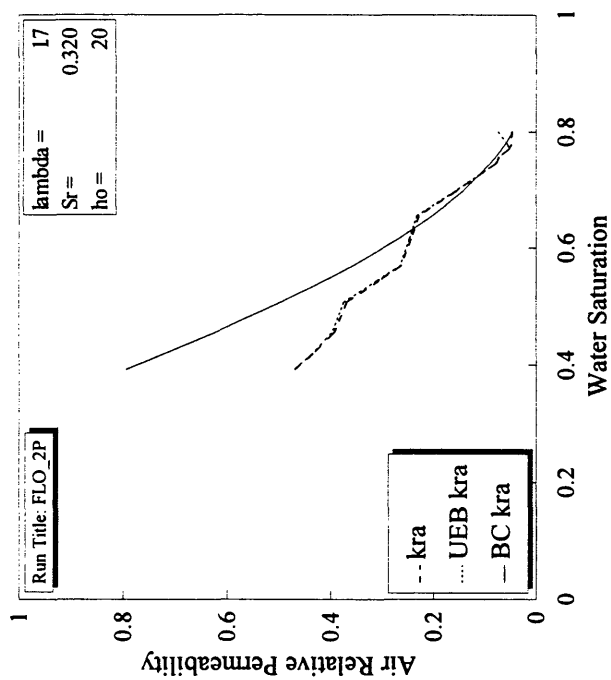


Figure 108. Error analysis of non-uniform fluid saturation. Experiment FLO_2P. Air relative permeability (k_{ra}) and an upper error bound (UEB) are compared to the Brooks-Corey functional form.

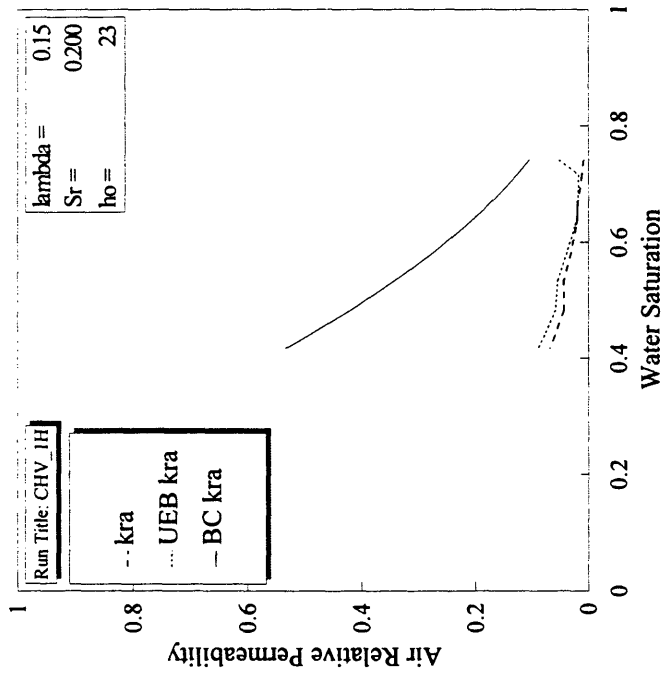


Figure 110. Error analysis of non-uniform fluid saturation. Experiment CHV_1H. Air relative permeability (k_{ra}) and an upper error bound (UEB) are compared to the Brooks-Corey functional form.

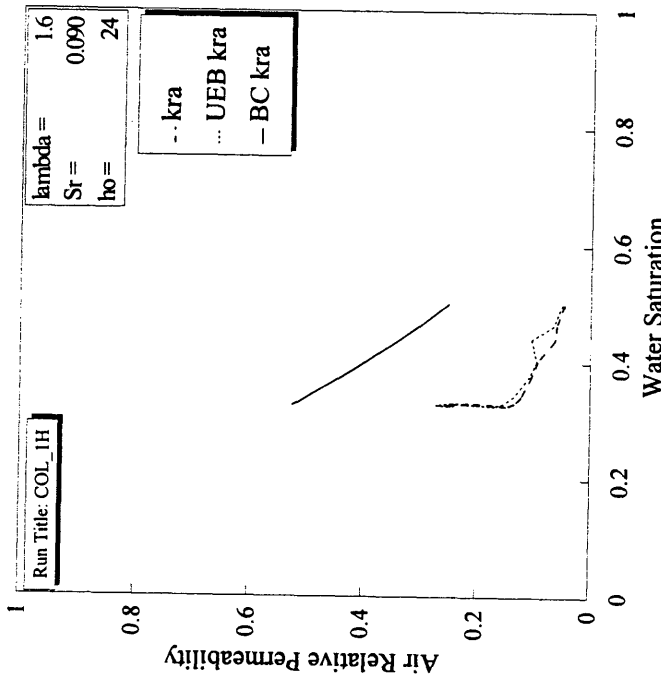


Figure 111. Error analysis of non-uniform fluid saturation. Experiment COL_1H. Air relative permeability (k_{ra}) and an upper error bound (UEB) are compared to the Brooks-Corey functional form.

of saturation. Modeled errors were generally less than 5%, while measured values of k_{ra} were frequently 50% to an order of magnitude lower than the functional relationship. Additionally, the highest modeled errors were frequently in portions of the tests other than those where the permeability deviated greatly from the Brooks-Corey curve.

6.1.2 Transient Non-Equilibrium Conditions

The low $k_{ra}(S_w)$ and the air permeability breakthrough behaviors are transient effects, which are history dependent. However, the air permeability breakthrough behaviors are unlikely to represent an expression of transient non-equilibrium conditions. In fact, in petroleum reservoir characterization methods, the unsteady state (i.e. JBN) relative permeability obtained from displacement experiments is generally verified by comparison to steady state (i.e. Hassler or Penn state method) results. Since the JBN method involves faster displacement rates than the experiments conducted here, the observed low $k_{ra}(S_w)$ are unlikely to be related purely to transient non-equilibrium.

6.1.3 Development of Pore-Scale Dead-End Air Fingers

The development and subsequent breakthrough of pore-scale dead-end air fingers is a possible explanation for the observed low $k_{ra}(S_w)$ and $h_c(S_w)$, step-changes in $k_{ra}(S_w)$, and air permeability breakthrough. This implies that the backbone air fingers which conducted flow controlled both the air permeability and capillary head. This is consistent with the suggestion of *Dullien* [1979] that capillary head and saturation are not in equilibrium during hierarchal drainage resulting from invasion of a non-wetting fluid.

The above hypothesis is supported by the observation that for many samples where low air permeability-saturation data were observed, low capillary head-saturation data were also observed, and air permeability-capillary head data were frequently close to values estimated by the Brooks-Corey or Parker et al. relationships. For example, the $k_{ra}(S_w)$ and $h_c(S_w)$ data from experiment COR_3E were much smaller than the Brooks-Corey functional form and moisture retention data, respectively. However, the $k_{ra}(h_c)$ data closely followed the Brooks-Corey functional form, prior to air permeability breakthrough (Figures 51, 70, and 71). Similar results were observed for experiments COL_1H, CHV_1H, and CHV_1K. In fact, experiments CHV_1H and CHV_1K, which were performed at different displacement rates, showed quite different the $k_{ra}(S_w)$ data, while the $k_{ra}(h_c)$ data for both experiments closely followed the Brooks-Corey relationship (Figures 84 - 87).

In contrast, for samples where $k_{ra}(S_w)$ closely followed the Brooks-Corey functional relationships, $h_c(S_w)$ approximate the moisture retention data, such as during experiment FLO_2P, at $S_w > 0.6$ (Figures 62 and 50). Similar results were obtained for sample CSM (Figures 82 and 56).

The $k_{ra}-S_w-h_c$ data were evaluated to examine the possibility that both k_{ra} and h_c were varying as a function of backbone air saturation (S_{ab}), as opposed to total fluid saturations. The hysteretic $k_{ra}(S)$ functional form given by *Lenhard and Parker* [1987] (eq. (17)) considered a free and a trapped air saturation. Since the Brooks-Corey functional relationships were found to fit measured $k_{ra}(S_w)$ data better than the Parker et al. relationships for samples which did not show low $k_{ra}(S_w)$, the Brooks-Corey $k_{ra}(S_w)$ function (equation (5)) was solved similarly to equation (17) to obtain the $k_{ra}(S_{ab})$ functional form shown below.

$$k_{ra} = S_{eab}^2 [1 - (1 - S_{eab})^{(2+\lambda)/\lambda}] \quad (37)$$

where, S_{eab} = effective backbone air saturation

Equation (37) was used to in conjunction with the residual saturation determined from the moisture retention data to solve $S_{ab} = f(k_{ra})$ using measured k_{ra} data from selected experiments. The calculated S_{ab} represents the conductive backbone air saturation which would provide the measured k_{ra} . Capillary head data were then plotted as a function of $(1-S_{ab})$, which represents the water saturation plus the dead-end air saturation. These data were compared to moisture retention data plotted as a function of S_w in order to evaluate the possibility that the capillary heads were in equilibrium with the backbone air saturation during the air injection displacement experiments.

Figures 112 and 113 show h_{ct} and h_{cb} plotted vs S_w and $(1-S_{ab})$, respectively, and moisture retention data plotted vs. S_w for experiment COL_2C. While the $h_c(S_w)$ data are lower than the moisture retention data, the transformed $h_c(1-S_{ab})$ data show remarkable correlation to the moisture retention data. $h_{cb}(1-S_{ab})$ closely follows the moisture retention data, while h_{ct} deviates strongly from the moisture retention data, suggesting that the base capillary head and saturation were more representative of the bulk sample properties. The data from experiment COL_1H (Figures 114 and 115) also show the improved correlation of data transformed from $h_c(S_w)$ to $h_c(1-S_{ab})$. In this instance, h_{cb} seems to correlate early in the test, while h_{ct} correlates at later times. This reflects the transient effects of moisture redistribution, where $h_{cb} > h_{ct}$ during the early portion of the test and $h_{cb} < h_{ct}$ at later time.

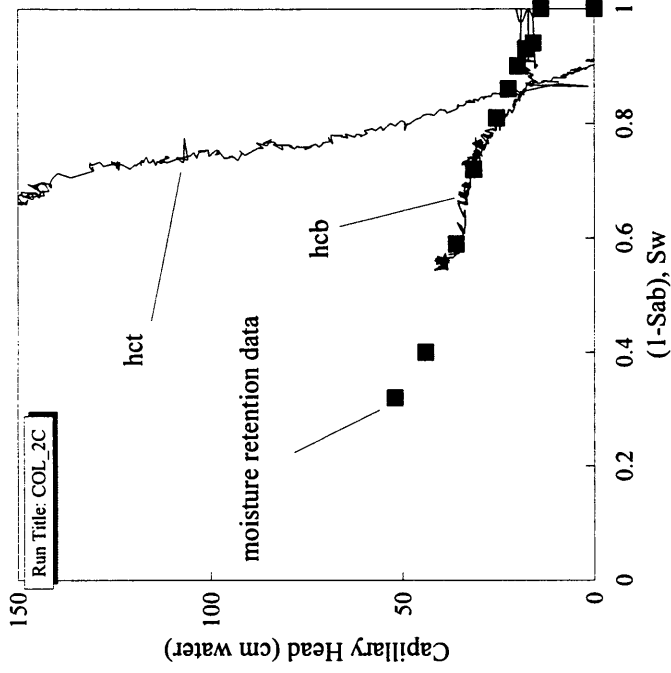


Figure 112. Capillary head-saturation data and moisture retention data plotted vs. water saturation (S_w). Experiment COL_2C. h_{ct} = top capillary head, h_{cb} = base capillary head

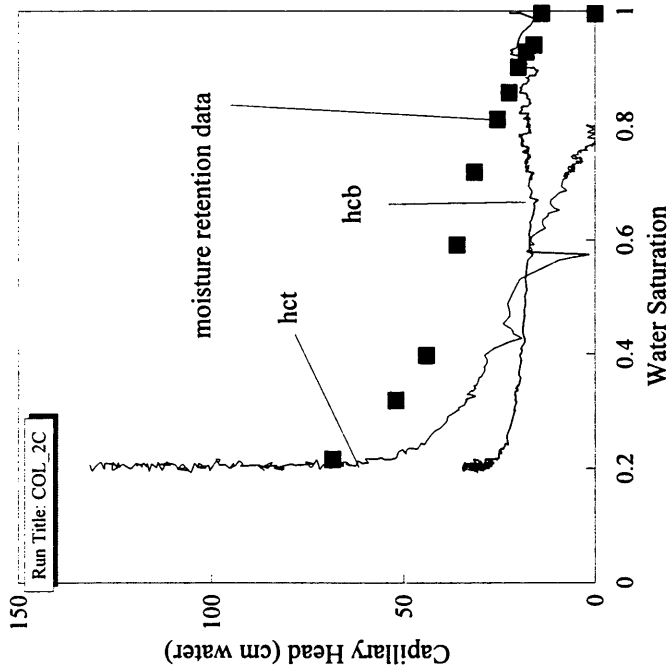


Figure 113. Transformed capillary head data plotted vs. one minus backbone air saturation ($1-S_{ab}$) and moisture retention data plotted vs. water saturation (S_w). Experiment COL_2C. h_{ct} = top capillary head, h_{cb} = base capillary head

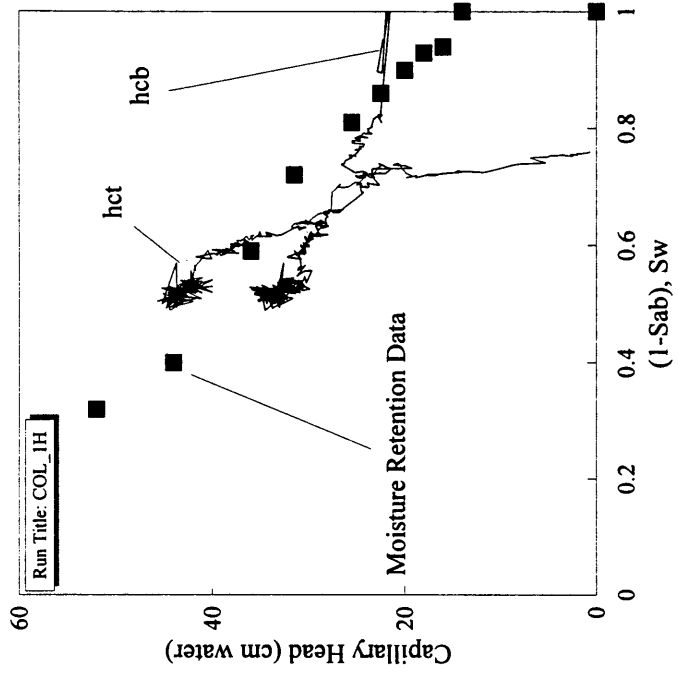


Figure 114. Capillary head-saturation data and moisture retention data plotted vs. water saturation (S_w). Experiment COL_1H. h_{ct} = top capillary head, h_{cb} = base capillary head

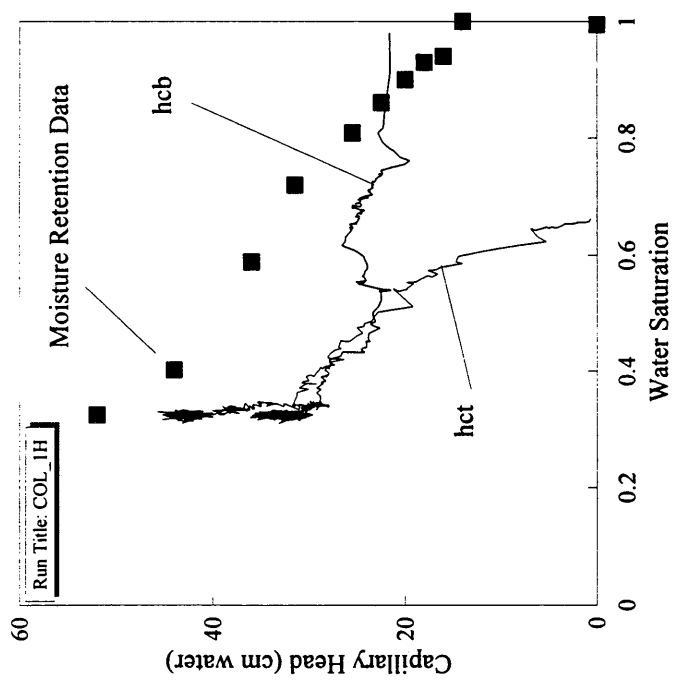


Figure 115. Transformed capillary head data plotted vs. one minus backbone air saturation ($1-S_{ab}$) and moisture retention data plotted vs. water saturation (S_w). Experiment COL_1H. h_{ct} = top capillary head, h_{cb} = base capillary head

Transformation of $h_c(S_w)$ data to $h_c(1-S_{ab})$ for experiment CHV_1H (Figures 116 and 117) shows excellent correlation of h_{ct} to moisture retention data, again suggesting that h_{ct} represented the bulk sample properties. $h_c(S_w)$ and transformed $h_c(1-S_{ab})$ data from experiment COR_3E (Figures 118 and 119) also show the improved correlation of transformed data to moisture retention data. The transformed h_{ct} and h_{cb} bound the moisture retention data, suggesting that the bulk sample properties were intermediate to those at the base and top.

For experiment FLO_2P, $k_{ra}(S_w)$ and $h_c(S_w)$ correlated well to the Brooks-Corey relation and moisture retention data, respectively above $S_w \approx 0.6$. Transformation of the $h_c(S_w)$ data to $h_c(1-S_{ab})$ (Figures 120 and 121) did not affect the data for $S_w > 0.6$, but resolved some of the poor correlation of $h_c(S_w)$ to moisture retention data for $S_w < 0.6$, where $k_{ra}(S_w)$ was below the Brooks-Corey functional form.

The good correlation of transformed $h_c(1-S_{ab})$ data to moisture retention data requires that both k_{ra} and h_c were in equilibrium with the calculated value of S_{ab} . Since the transformation involves both k_{ra} and h_c , if either k_{ra} or h_c were not in equilibrium with S_{ab} , we would expect more random results than were obtained. This hypothesis seems especially tenable since k_{ra} and h_c were calculated from independent measurements.

This result also specifically implies the development of pore-scale air fingering as opposed to macroscopic air fingering. Macroscopic fingering would not cause h_c to remain near h_o , as was observed in conjunction with extreme air fingering, inferred by low $k_{ra}(S_w)$.

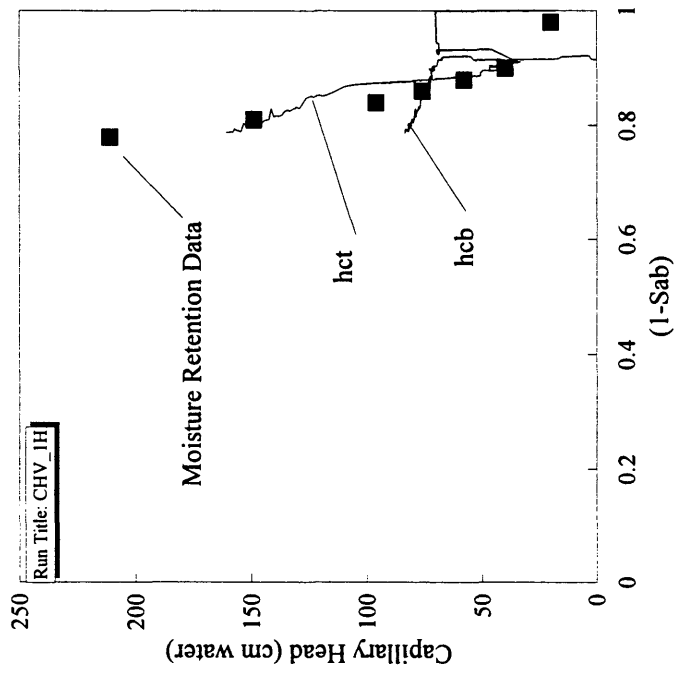


Figure 116. Capillary head-saturation data and moisture retention data plotted vs. water saturation (S_w). Experiment CHV_1H. h_{ct} = top capillary head, h_{cb} = base capillary head

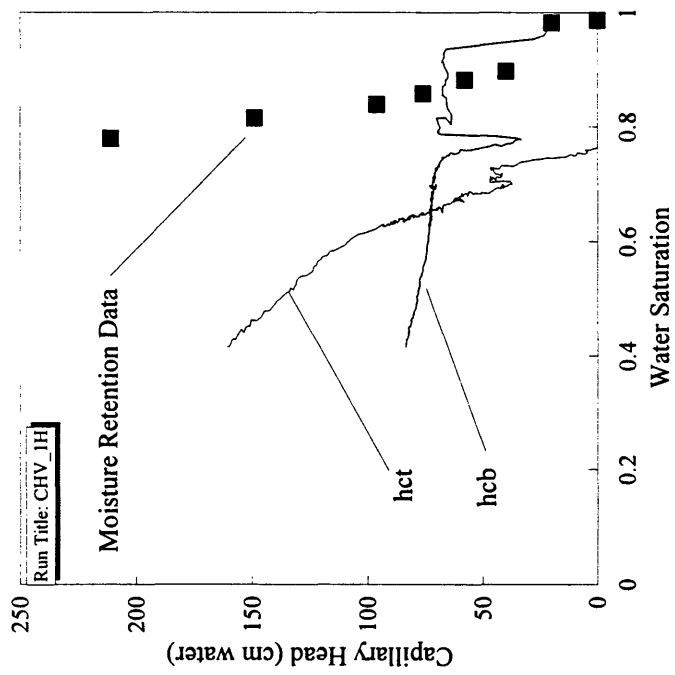


Figure 117. Transformed capillary head data plotted vs. one minus backbone air saturation ($1 - S_{ab}$) and moisture retention data plotted vs. water saturation (S_w). Experiment CHV_1H. h_{ct} = top capillary head, h_{cb} = base capillary head

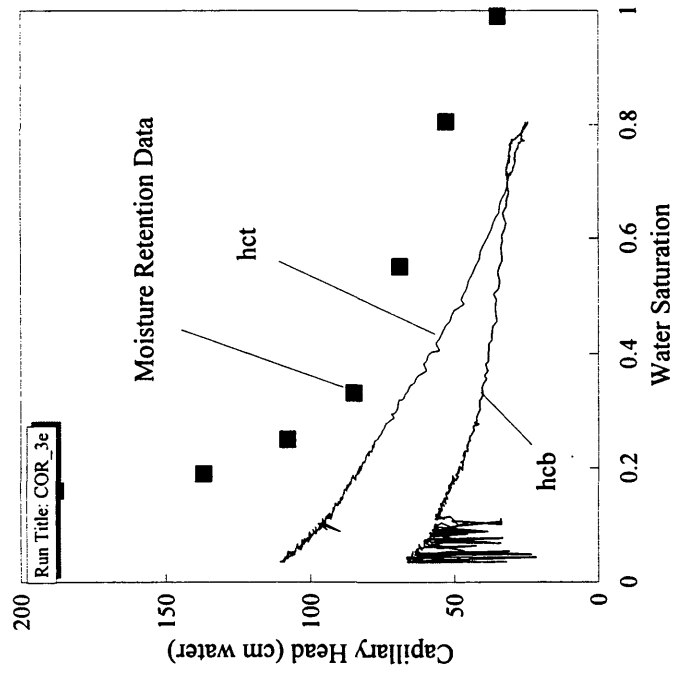


Figure 118. Capillary head-saturation data and moisture retention data plotted vs. water saturation (S_w). Experiment COR_3E. h_{ct} = top capillary head, h_{cb} = base capillary head

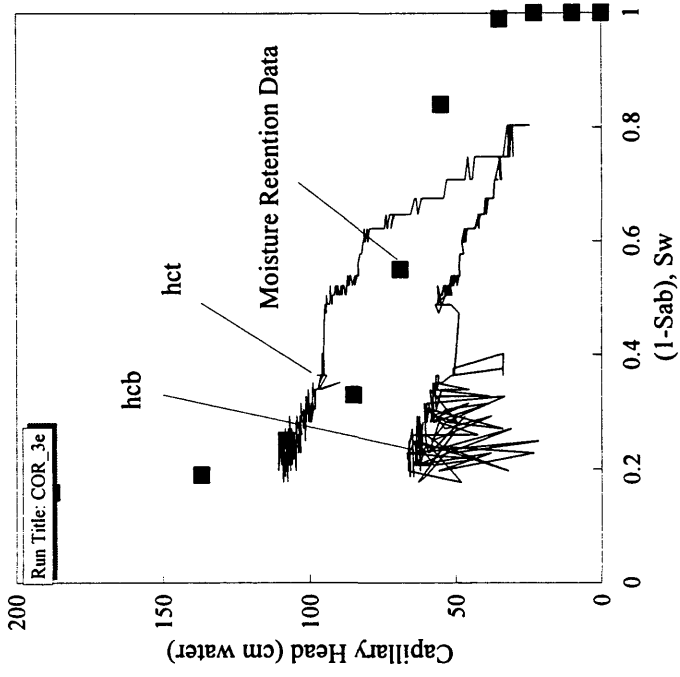


Figure 119. Transformed capillary head data plotted vs. one minus backbone air saturation ($1-S_{ab}$) and moisture retention data plotted vs. water saturation (S_w). Experiment COR_3E. h_{ct} = top capillary head, h_{cb} = base capillary head

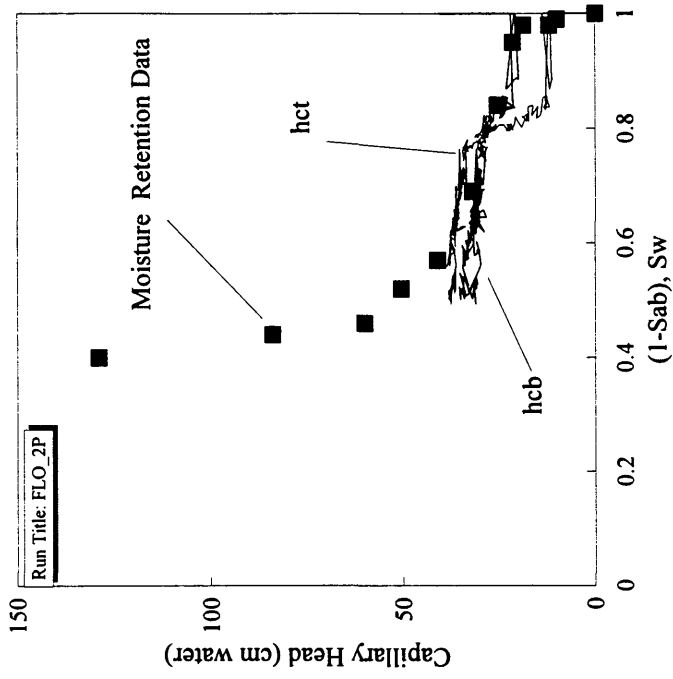


Figure 121. Transformed capillary head data plotted vs. one minus backbone air saturation ($1-S_{ab}$) and moisture retention data plotted vs. water saturation (S_w). Experiment FLO_2P. h_{ct} = top capillary head, h_{cb} = base capillary head

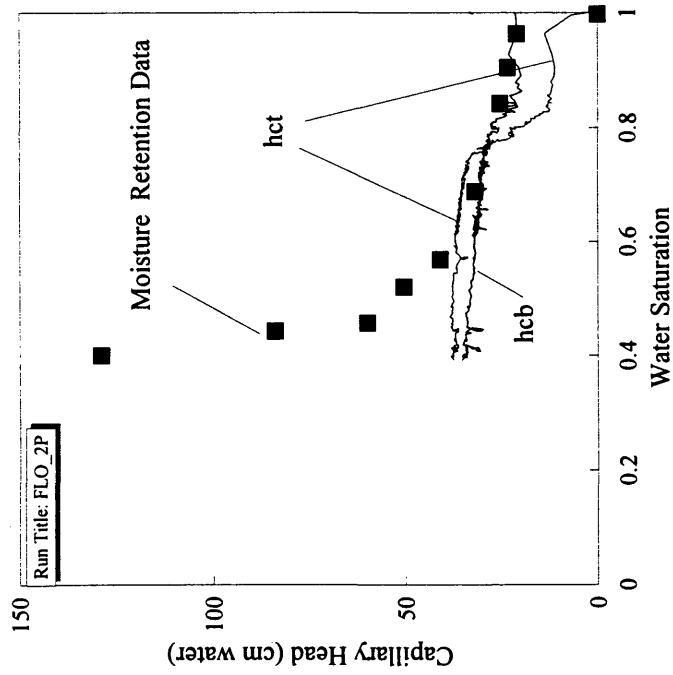


Figure 120. Capillary head-saturation data and moisture retention data plotted vs. water saturation (S_w). Experiment FLO_2P. h_{ct} = top capillary head, h_{cb} = base capillary head

6.2 Prediction of Fingered Flow Behaviors

The results showed that the rate of displacement during the experiments appeared to control the magnitude of the deviation of $k_{ra}(S_w)$ from the Brooks-Corey relationship, for samples which displayed low $k_{ra}(S_w)$ and air permeability breakthrough. In contrast, where the Brooks-Corey relation for $k_{ra}(S_w)$ was a good predictor of measured data, the results were generally insensitive to displacement rate. Displacement rate is an important factor which controls the geometry of viscous fingering [Pavone, 1992, and Lenormand, *et al.*, 1988]. Therefore, we can expect that for samples where fingered flow develops, that the displacement rate will affect the degree of fingering. Apparently, for the displacement mechanisms associated with air sparging, faster displacement rates result in development of a larger proportion of pore-scale, dead-end air fingers, which results in reduced air permeability.

Physical soil properties may also have influenced the development of low $k_{ra}(S_w)$ and air permeability breakthrough during the experiments. Relevant physical soil properties are summarized in Table 13, in order to evaluate their usefulness as predictors of the air permeability breakthrough behavior. Inspection of the data show no patterns which may discriminate samples which showed low $k_{ra}(S_w)$ and air permeability breakthrough from those that followed functional relationships derived from moisture retention data. Also, statistical discriminant analysis for various combinations of parameters resulted in a maximum calculated F-test statistic of 0.625, for $F_{critical} = 18.5$ at a 95% confidence interval. This implies that there is no statistical basis to discriminate the samples which showed air permeability breakthrough, based on these physical soil properties.

While pore size distribution can be anticipated to control the air permeability breakthrough behavior, grain size distribution, porosity, and density do not always correlate to pore size distribution. Nonetheless, the soil pore size distribution indices λ and m were also poor predictors of the permeability breakthrough behavior. The extreme sensitivity of pore-scale air fingering on pore size distribution implies that minor irregularities in pore size distribution may lead to the development of dead-end fingers. *McWhorter and Sunada* [1990] suggested that non-wetting fluid invasion is controlled by variations in the size distribution of the largest fraction of pores, which controls $h_c(S_w)$ behavior near h_o . Since the indices λ and m were derived by curve-matching to moisture retention curves, they do not specifically reflect the pore size distribution near h_o , and may not be expected to predict the air permeability breakthrough behavior.

6.3 Similitude of Air Injection Simulations

The design of the air injection displacement experiment provided for vertical upward air flow, so that buoyant and viscous forces were collinear and were not competing forces. However, for 3-dimensional air flow during field air sparging, buoyant and viscous forces do compete, and their ratio is an important criteria which controls the overall air flow pattern. Where buoyant forces dominate, air flow is generally upward. However, where viscous forces dominate, porous medium anisotropy and/or heterogeneity may control air flow, and lateral air flow may predominate.

The ratio of buoyant to viscous forces acting on air over the length of a core sample for upward vertical air flow in the experiments can be derived as follows:

Table 13. Soil characteristics which may influence fingering. The physical soil characteristics were poor predictors of the occurrence of air permeability breakthrough behavior in samples tested.

Sample	FLO	COR	COL	CSM	CHV
Air Permeability Breakthrough?	N	Y	Y	N	Y
S_r	0.32	0.01	0.09	0.3	0.2
h_o (cm)	20	40	18	16	23
λ	1.2	1.2	1.5	1.1	0.16
m	0.46	0.47	0.524	0.44	0.14
C_u	1.5	1.7	2.7	3.3	3.2
C_c	0.8	0.9	1	0.08	1.4
D_{50} (mm)	0.24	0.16	0.61	0.24	0.09
ϕ	0.398	0.45	0.38	0.37	0.33
ρ_d (g/cc)	1.58	1.42	1.6	1.63	1.78
k (cm ²)	4.4e-007	7.8e-008	5.3e-007	3.8e-008	2.6e-007

$$B = \frac{\text{buoyant force}}{\text{viscous force}} = \frac{(\rho_w - \rho_a)gL}{\rho_w g(U_{ab} - U_{at})} \approx \frac{L}{U_{ab} - U_{at}} = \frac{1}{I_a} \quad (38)$$

This derivation implies that for upward vertical flow, if $I_a > 1$, then $B < 1$ and viscous forces are greater than buoyant forces, and if $I_a < 1$, then $B > 1$ and buoyant forces are greater than viscous forces. Also, for the special case of a hydrostatic gradient ($I_w = 0$), the criterion of uniformity of capillary head of $I_a = I_w + 1$ is also the criteria for buoyant forces being equal to viscous forces.

These results have important implications for the impact of soil permeability on air sparging. Air sparging in more permeable soils generally involves lower air injection pressures, and therefore smaller gradients than sparging in less permeable soils. Therefore, we may expect vertical air flow to be more dominant in more permeable soils. By contrast air sparging in less permeable soils generally results in larger gradients, and we may expect lateral air flow to be more likely, since buoyancy becomes less important.

The maximum and minimum values of C determined for each experiment (Table 12) were plotted on the phase diagram for immiscible displacement (Figure 122) proposed by *Lenormand et al.* [1988]. These results show that the experiments were within the realm of capillary fingering as opposed to viscous fingering or stable displacements. This implies that for Darcy air flow during air sparging, air invasion will generally proceed in the direction of the lowest capillary resistance as opposed to primarily in the direction of bulk flow, since viscous forces are small relative to capillary forces.

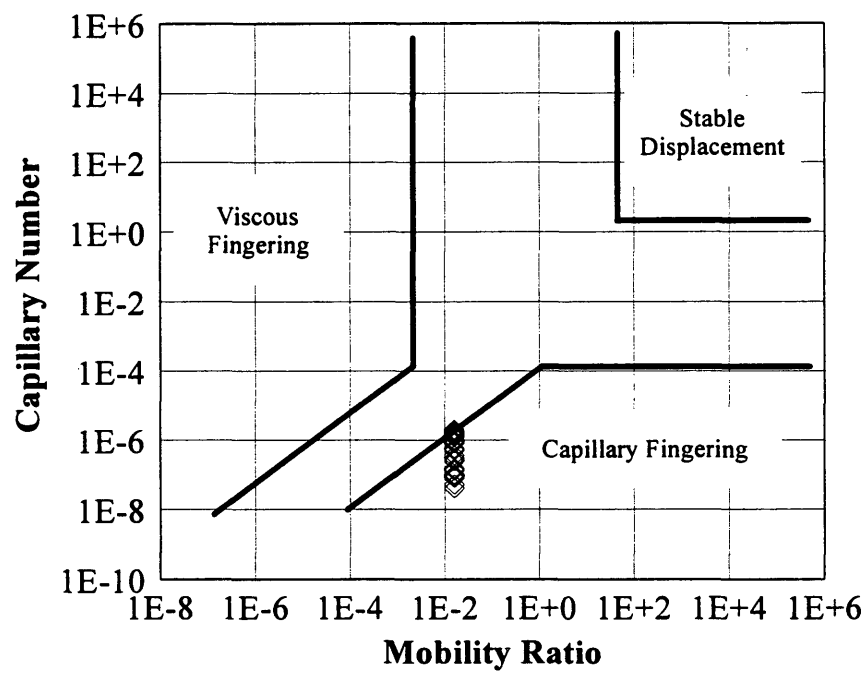


Figure 122. Capillary number and mobility ratio plotted on the phase diagram proposed by *Lenormand et al.* [1988] for behavior of immiscible displacements.

6.4 Gas-Phase Tracer Experiments

While the tracer experiments were designed to detect air trapping as a reflection of the development of dead-end air fingers, partial recovery of gas-phase tracer may also potentially reflect errors introduced by the experimental system or variability resulting from the specific experimental conditions during injection of each tracer slug. The inconsistencies in the data probably reflect the effects of the experimental system and variability in experimental conditions. While these inconsistencies rendered the data inconclusive, the correlation of selected tracer data to air flow behaviors suggests that further refinements to the experimental procedure and system configuration may result in the generation of more conclusive data.

Section 7

CONCLUSIONS

The evidence presented shows that the two-phase, air-water flow behaviors associated with air sparging in soil core samples differ from estimates based on steady state moisture retention data. These differences included, (1) values of $k_{ra}(S_w)$ and $h_c(S_w)$ which were significantly lower than expected for non-fingered flow, (2) step-like independent changes in k_{ra} and S_w , and (3) large increases in air permeability at steady state saturation (i.e., air permeability breakthrough). In contrast, $k_{ra}(h_c)$ and $k_{rw}(S_w)$ were found to be estimated reasonably well by common functional forms derived from moisture retention data.

Analysis of the possible causes of the deviations in $k_{ra}(S_w)$ and $h_c(S_w)$ from functional relationships showed that; (1) measurement errors related to non-uniform saturations were too small to account for the deviations, (2) transient non-equilibrium cannot account for the deviations, and (3) the development and subsequent breakthrough of pore-scale dead-end air fingers is a reasonable explanation which is also consistent with anticipated behaviors based on previous studies. The correction of $h_c(S_w)$ data by transformation to be a function of a hypothetical backbone air saturation calculated from the $k_{ra}(S_w)$ data suggests that both k_{ra} and h_c were in equilibrium with pore-scale backbone air fingers.

The water relative permeability relationships were not effected by the development of pore-scale air fingering. This result reflects that the development of air fingering does not result in the development of a trapped water phase.

Capillary forces were dominant over inertial forces and viscous forces during the experiments. This implies that the soil pore size distribution is the primary soil property which controls the mechanisms of air invasion, and the development of pore-scale air fingering during in-situ air sparging. The difficulty in predicting the development of pore-scale air fingering based on physical soil properties, including common pore size distribution indices, reflects that air fingering is controlled by the size distribution of the largest pores, at h_c near h_o . This is further supported by the observation that h_c frequently remained near h_o , when extreme air fingering was inferred by low $k_{ra}(S_w)$.

Section 8

NEEDS FOR ADDITIONAL RESEARCH

From the results of this research we can infer the existence of pore-scale dead-end air fingers, but the actual volume of dead-end vs. backbone air fingers remains unquantified. Gas-phase tracer experiments were conducted as part of this research in an attempt to show air trapping during air invasion. While these experiments were inconclusive due to irreproducibility of the data, the results indicated that air trapping may possibly occur during air invasion. Modifications can be made to the experimental apparatus which will minimize diffusion of the tracer gas. This will allow the collection of more definitive tracer data to confirm and quantify the existence of dead-end air fingers. *Fatt* [1960] also described tracer injection experiments to quantify the volume of dead-end fingers of an invading fluid. However, the design of these experiments poses specific difficulties for air as an invading fluid.

The ability to discriminate between samples which exhibit air permeability breakthrough from those which follow common functional forms for $k_{ra}(S_w)$, is necessary to evaluate the effects of heterogeneity on in-situ air sparging. Laboratory methods to measure the size distribution of the largest pores and to predict $h_c(S_w)$ near h_o are probably required to determine the properties which discriminate these soils. Also, the testing of a large suite of samples in a factorial experiment design may be required after relevant soil

properties are identified.

Useful functional forms for $k_{ra}(S_w)$, $k_{ra}(h_c)$, and $h_c(S_w)$ for air sparging should predict the onset of air permeability breakthrough as a function of the displacement history. While the history dependence may prove difficult or impossible to predict, systematic testing of soil samples over a wide range of air injection histories may be a productive approach to develop such functional forms.

The effects of low $k_{ra}(S_w)$ during the transient phase of air invasion have important implications for the prediction of the region of air flow and the related effects of heterogeneity during in-situ air sparging. The in-situ measurement of fluid saturations conducted by *Acomb* [1995], *Clayton et al.* [1995], *Clayton and Nelson* [1995], and *Lundegard and LaBrecque* [1995], can be combined with measurements of pore air and pore water pressure heads, as was done here in the core samples. Such a combination of measurements would provide an avenue to calculate capillary heads and air and water gradients in-situ, which can then be correlated to fluid saturation, to provide a complete set of constraints for calibration of mathematical flow models.

REFERENCES

- Acomb, L. J., D. McKay, P. Currier, S. T. Berglund, T. V. Sherhart, and C. V., Benediktsson, Neutron Probe Measurements of Air Saturation Near an Air Sparging Well, in *In-Situ Aeration: Air Sparging, Bioventing, and Related Remediation Processes*, eds. R. E. Hinchee, R. N. Miller, and P. C. Johnson, Battelle Press, Columbus, OH, 1995.
- Ahlfeld, D. P. , A. Dahmani, and W. Ji, A Conceptual Model of Field Behavior of Air Sparging and Its Implications for Application, *Ground Water Monitoring and Remediation*, fall, 1994.
- Ardito, C. P., and J. F. Billings, J. F. Alternative Remediation Strategies: The Subsurface Volatization and Ventilation System, in *Proceedings of The Conference on Petroleum Hydrocarbons and Organic Chemicals in Ground Water: Prevention, Detection, and Restoration*, National Water Well Association, Dublin, Ohio, 1990.
- Beckett, G. D., D. Huntley, and S. Panday, Air Sparging: A Case Study in Characterization, Field Testing, and Modeling Design, in *Proceedings of the 1995 Petroleum Hydrocarbons and Organic Chemicals in Ground Water: Prevention, Detection, and Remediation Conference and Exposition*, p. 207-221, Ground Water Publishing Company, 1995.
- Bowles, J. E., *Engineering Properties of Soils and Their Measurement*, 4th ed., McGraw-Hill, New York, 240 p., 1992.
- Brock, D. C., and F. M. Orr, Flow Visualization of Viscous Fingering in Heterogeneous Porous Media, *Pap 22614 Soc. Pet. Eng.*, Richardson, Tex., 1991.
- Brooks, R. H., and A. T. Corey, Hydraulic Properties of Porous Media, *Hydrol. Pap. 3*, Colorado State Univ., 27 pp., Fort Collins, 1964.
- Brown, R. A., C. Herman, and E. Henry, The Use of Aeration in Environmental Cleanups, in *Proceedings of Haztech International Pittsburgh Waste Conference*, Haztech International, Cleveland, Ohio. 1991.

Chatzis, I., and F. A. L. Dullien, Modeling Pore Structure by 2-D and 3-D Networks with Application to Sandstones, *J. Can. Pet. Technol.*, Jan.-Mar., 1997.

Chen, J. D., Some Mechanisms of Immiscible Fluid Displacement in Small Networks, *J. Coll. Int. Sc.*, v. 110, n. 2, p. 488-503, 1985.

Chen, J. D., and J. Koplik, Immiscible Fluid Displacements in Small Networks, *J. Coll. Int. Sc.*, v.108, n. 2. p. 304-331, 1985.

Chen, J. D., and D. Wilkinson, Pore-Scale Viscous Fingering in Porous Media, *Phys. Rev. Let.*, v. 55, n. 18, p. 1892-1895, 1985.

Clayton, W. S., R. A. Brown, and D. Bass, Air Sparging and Bioremediation: The Case for In-Situ Mixing, in *In-Situ Aeration: Air Sparging, Bioventing, and Related Remediation Processes*, eds. R. E. Hinchee, R. N. Miller, and P. C. Johnson, Battelle Press, Columbus, OH, 1995.

Clayton, W. S., and C. H. Nelson. In-Situ Sparging: Managing Chemical Transport and Mass Transfer, in *proceedings of the 1995 Superfund Conference and Exhibition*, E. J. Krause and Assoc., Bethesda, 1995.

Corey, A. T., *Mechanics of Immiscible Fluids in Porous Media*, Water Resources Publications, Littleton, Colorado, 1994.

Dawe, R. A., M. R. Wheat, and M. S. Bidner, Experimental Investigation of Capillary Pressure Effects on Immiscible Displacement in Lensed and Layered Porous Media. *Transp. Porous Media*, 7, 83-101, 1992.

Dullien, F. A. L., *Porous Media, Fluid Transport and Pore Structure*, Academic Press Inc., San Diego, California, 1979.

Fatt, I., The Network Model of Porous Media I-III, *Trans. Am. Inst. Min. Metall. Pet. Eng.*, 207, p. 144-181, 1956.

Fatt, I., The Influence of Dead-End Pore Volume of Relative Permeability. *Pap 1660-G. Soc. Pet. Eng.*, Richardson, Tex., 1960.

Ferrand, L. A., and M. A. Celia, The Effect of Heterogeneity on the Drainage Capillary Pressure-Saturation Relation, *Water Resour. Res.* (28)3, 859-870, 1992.

- Hinkley, R.E., Chen, M.R., and J.E. Killough, 1995, High Resolution, Two- and Three-Dimensional Simulation of Air Sparging, in *Proceedings of the 1995 Petroleum Hydrocarbons and Organic Chemicals in Ground Water: Prevention, Detection, and Remediation Conference and Exposition*, p. 223-237, Ground Water Publishing Company, 1995.
- Homsey, G. M., Viscous Fingering in Porous Media, *Ann. Rev. Fluid Mech.*, 19, p. 271-311, 1987.
- Honarpour, M., and S. M. Mahmood, Relative Permeability Measurements: An Overview, *J. Pet. Techn.*, p.963-966, August, 1988.
- Ji, W., A. Dahmani, D. P. Ahlfield, J. D. Lin, and E. Hill, Laboratory Study of Air Sparging: Air Flow Visualization, *Groundwater Monitoring and Remediation*, p. 115-126, Fall, 1993.
- Johnson, E. F., C. P. Bossler, and V. O. Naumann, Calculation of Relative Permeability from Displacement Experiments, *Trans.*, AIME, 216, 370-372, 1959.
- Johnson, R.L., R. C. Johnson, D. B. McWhorter, R. E. Hinchee, and I. Goodman, An Overview of In Situ Air Sparging, *Groundwater Monitoring and Remediation*, p. 127-135, Fall, 1993.
- Jones, S. C., and W. O. Roszelle, Graphical Techniques for Determining Relative Permeability from Displacement Experiments, *J. Pet. Technol.*, p. 807-817, May, 1978.
- Kerig, P. D., and A. T. Watson, A New Algorithm for Estimating Relative Permeabilities from Displacement Experiments, *SPE Res. Engr.*, p. 103-112, February, 1987.
- Klinkenberg, L. J., The Permeability of Porous Media to Liquids and Gases, *Drill. and Prod. Prac.*, p. 200-213, 1941.
- Koplik, J., Creeping Flow in Two-Dimensional Networks, *J. Fluid Mech.*, 119, p. 219-247, 1982.
- Koplik J., D. Wilkinson, and J. F. Willemsen, Percolation and Capillary Fluid Displacement, in *The Mathematics and Physics of Disordered Media: Percolation, Random Walk, Modeling, and Simulation*. Eds. B. D. Hughes and B. W. Ninham, Springer Verlag, New York, 1983.

Koplik, J., and Lasseter, T.J., 1985. Two-Phase Flow in Random Network Models of Porous Media, *SPE Journal*, p. 89-100, February, 1985.

Kyte, J. R., and L. A. Rapaport, Linear Waterflood Behavior and End Effects in Water-Wet Porous Media, *AIME Tech. Note 2020*, p. 47-50, October, 1958.

Lenormand, R., and C. Zarcone, Invasion Percolation in an Etched Network: Measurement of a Fractal Dimension, *Phys. Rev. Lett.*, 54, n. 20, p. 2226-2229, 1985.

Lenormand, R., E. Touboul, and C. Zarcone, Numerical Models and Experiments on Immiscible Displacements in Porous Media, *J. Fluid Mech.*, 189, pp. 165-187, 1988.

Lenhard, R. J., and J. C. Parker, A Model for Constitutive Relations Governing Multiphase Flow 2. Permeability-Saturation Relations, *Water Resour. Res.*, 23(12), p. 2197-2206, 1987.

Leonard, W. C., and R. A. Brown, Air Sparging: An Optimal Solution, in *Proceedings of The Conference on Petroleum Hydrocarbons and Organic Chemicals in Ground Water: Prevention, Detection, and Restoration*, National Water Well Association, Dublin, Ohio. 1992.

Loomis, A. G., and D. C. Crowell, Calculation of Relative Permeabilities from Displacement Measurements of Their Ratios, *Pap. 1611-G*, Soc. Pet. Eng., Richardson, Tex., 1960.

Lundegard, P.D., and Andersen, G. Numerical Simulation of Air Sparging Performance, in *Proceedings of The Conference on Petroleum Hydrocarbons and Organic Chemicals in Ground Water: Prevention, Detection, and Restoration*, National Water Well Association, Dublin, Ohio, pp. 461-476.1993.

Lundegard and LaBrecque, Air Sparging in a Sandy Aquifer (Florence, Oregon): Actual and Apparent Radius of Influence, *J. Contam. Hydrol.*, 19(1), 1995.

Maloy, K. J., J. Feder, and T. Jossang, Viscous Fingering Fractals in Porous Media, *Phys. Rev. Lett.*, 55(24). p. 2688-2691, 1985.

Marley, M. C., D. J. Hazebrouk, and M. T. Walsh, The Application of In Situ Air Sparging as an Innovative Soils and Groundwater Remediation Technology, *Groundwater Mon. Rev.*, National Water Well Association, Dublin, Ohio. Spring, 1992a.

Marley, M. C., F. Li, S. Magee, and D. E. Medina, Application of Models in the Design of Air Sparging Systems, *HMC/SUPERFUND '92*, Dec. 1-3, 1992, Washington D.C., Hazardous Materials Institute, Greenbelt, Maryland, p. 853-857, 1992b.

Marley, M. C., and C. J. Bruell, *In-Situ Air Sparging: An Evaluation of Petroleum Industry Sites and Considerations for Applicability, Design, and Operation*. American Petroleum Institute Publication number 4609, 1995.

McCarthy, K. P., and K. W. Brown, Soil Gas Permeability as Influenced by Soil Gas-Filled Porosity, *Soil Sc. Soc. Am. J.*, 56(4), 1992.

McCoy, E. L., Wettable Porous Plastic For Use As A Porous Barrier in Soil Hydraulic Studies, *Soil Sc. Soc. Am. J.*, 53, p. 979-981, 1989.

McWhorter D. B., and D. K. Sunada, Exact Integral Solutions for Two-Phase Flow, *Water Resour. Res.*, 26(3), p. 399-413, 1990.

Mohr, D., 1995, Mass Transfer Concepts Applied to Air Sparging, in *In-Situ Aeration: Air Sparging, Bioventing, and Related Remediation Processes*, eds. R. E. Hincbee, R. N. Miller, and P. C. Johnson, Battelle Presss, Columbus, OH, 1995.

Mualem, Y., A New Model for Predicting the Hydraulic Conductivity of Unsaturated Porous Media, *Water Resour. Res.*, 12, 513-522, 1976.

Murat, M. , and A. Aharony, Viscous Fingers and Diffusion-Limited Aggregates near Percolation, *Water Resour. Res.*, (57)15, p. 1875-1878, 1986.

Oxaal, U., Fractal Viscous Fingering in Inhomogeneous Porous Media, *Phys. Rev. A*, (44)8, p. 5038-5051, 1991.

Paterson, L., Diffusion-Limited Aggregation and Two-Fluid Displacements in Porous Media, *Phys. Rev. Lett.*, (52)18, p. 1621-1624, 1984.

Parker, J. C., R. J. Lenhard, and T. Kuppusamy, A Parametric Model for Constitutive Properties Governing Multiphase Flow in Porous Media, *Water Resour. Res.*, (23)4, p. 618-624, 1987.

Parker, J. C., and R. J. Lenhard, A Model for Constitutive Relations Governing Multiphase Flow 1. Saturation-Pressure Relations, *Water Resour. Res.*, (23)12, p. 2187-

2196, 1987.

Pavone, D., Observations and Correlations for Immiscible Viscous-Fingering Experiments, *SPE Res. Engr.*, May 1992, p. 187-194, 1992.

Peters, E. J., and S. Khataniar, The Effect of Instability on Relative Permeability Curves Obtained by the Dynamic Displacement Method, *Pap. 14713*, Soc. Pet. Eng., Richardson, Tex., 1985.

Rawls, W. J., and D. L. Brakensiek, Estimation of Soil Water Retention and Hydraulic Properties, in *Unsaturated Flow in Hydrologic Modeling, Theory and Practice*, Morel-Setoux, H. J., ed., Kluwer Academic Publishers, Dordrecht, Netherlands, 1988.

Reginato, R. J. , and C. H. M. Van Bavel, Pressure Cell for Soil Cores, *Soil. Sc. Soc. Am. J.*, 26(1), p. 1 - 3, 1962.

Richards, L. A., Capillary Conduction of Liquids Through Porous Mediums, *Physics*, V. 1, p.318-333, 1931.

Roseberg R. J., and E. L. McCoy, Measurement of Soil Macropore Air Permeability, *Soil Sc. Soc. Am. J.*, V. 54, p. 969-974, 1990.

Rutherford, K., and P. C. Johnson, Interfacial Mass Transfer Rates During In Situ Air Sparging - Effects of Process Control Changes and Lithology, in *Proceedings of the 1995 Petroleum Hydrocarbons and Organic Chemicals in Ground Water: Prevention, Detection, and Remediation Conference and Exposition*, Ground Water Publishing Company, p. 129-143, 1995.

Salehzadeh, A. and A. H. Demond, Apparatus for the Rapid Automated Measurement of Unsaturated Soil Transport Properties, *Water Resour. Res.*, (30)10, p.2679-2690, 1994.

Stokes, J. P., D. A. Weitz, J. P. Gollub, A. Dougherty, M. O. Robbins, P. M. Chaikin, and H. M. Lindsay, Interfacial Instability of Immiscible Displacement in a Porous Medium, *Phys. Rev. Lett.*, (57)14, p. 1718-1721, 1986.

Taylor, J. R., *An Introduction to Error Analysis*, University Science Books, Mill Valley, CA, 1982.

Van Genuchten M. Th., A Closed Form Equation for Predicting the Hydraulic Conductivity of Unsaturated Soils, *Soil Sc. Soc. Am. J.*, 44, p. 892-898, 1980.

Wilkinson, D., Percolation Model of Immiscible Displacement in the Presence of Buoyant Forces, *Phys. Rev. A*, (30)1, p. 520-531, 1984.

Wilkinson, D. and J. F. Willemsen, Invasion Percolation: A New Form of Percolation Theory, *J. Phys. A*, 16, p. 3365-3376, 1983.

Witten, T. A., and Y. Kantor, Space-Filling Constraint on Transport in Random Aggregates, *Phys. Rev. B*, (30)7, p. 4093-4095, 1984.

Witten, T. A., and L. M. Sander, Diffusion-Limited Aggregation, a Kinetic Critical Phenomenon, *Phys. Rev. Lett.*, (47)19, p. 1400-1403, 1981.

Wooding, R. A., and H. J. Morel-Seytoux, Multiphase Flow Through Porous Media, in *Annual Review of Fluid Mechanics*, eds. M. Van Dyke, W. G. Vincenti, and J. V. Wehausen, Annual Reviews Inc., Palo Alto, California, 1976.

APPENDIX A

List of Values of Fluid Properties and Physical Constants

$$\rho_a = 1.21 \times 10^{-3} \text{ g/ml}$$

$$\rho_w = 0.99 \text{ g/ml}$$

$$\mu_a = 1.6 \times 10^{-4} \text{ g/(s}\cdot\text{cm)} = 1.6 \times 10^{-2} \text{ cp}$$

$$\mu_w = 1.0 \text{ cp}$$

$$T = 293^\circ \text{ K}$$

atmospheric pressure = 0.803 atm (at 6,000 feet above sea level)

$$\gamma_{aw} = 72.8 \text{ dyne/cm}$$

APPENDIX B

Grain Size Distribution Data

Sample ID	FLO smc	FLO inj	COR	COL smc	COL inj	CSM	CHV smc	CHV inj
Cu	1.5	1.5	1.7	1.7	2.7	3.3	4.8	3.2
Cc	1.1	0.8	0.9	1.2	1.0	0.8	1.2	1.4
D50	0.30	0.24	0.16	0.26	0.61	0.24	0.12	0.09
Particle Dia. (mm)	Percent Finer							
3.000					93.4			
2.362					88.1			
1.700					84.7	99.9		100.0
1.000				99.9	73.7	95.0		99.8
0.833				98.0	68.4	90.0	96.7	99.6
0.600				97.0	51.5	82.0	92.0	99.3
0.500	99.9	99.8		88.7	39.1	76.0	89.3	98.6
0.417	99.3	99.7		79.2	29.6	71.0	83.0	98.0
0.300	48.7	82.3	98.1	69.4	13.0	60.0	76.0	95.1
0.246	12.8	54.0	96.0	38.7	9.0	52.0	72.7	92.1
0.175	1.9	8.1	56.6	24.1	5.1	38.0	63.4	84.3
0.150	1.1	4.3	43.5	11.2	3.8	30.0	58.0	79.1
0.124	0.6	2.6	23.9	8.5	2.3	22.0	51.8	69.3
0.106	0.4	2.0	10.0	7.0	1.4	15.0	44.0	61.4
0.075	0.2	1.3	6.1	6.2	0.7	5.0	27.7	33.6
0.043	0.2	1.0	3.1	2.9	0.4	0.0	14.5	23.6
0.031							11.2	17.2
0.023							9.4	13.9
0.013							7.3	12.2
0.010							6.2	11.5

APPENDIX C

Moisture retention Data

Capillary Head-Saturation Data
tempe cell apparatus

Sample I.D: FLO
Date: 1/26/96 - 2/9/96

754.11 = Initial weight of cell with sample (g)
136.7 = cell volume (cm³)
485.56 = cell weight (g)

Pc (cm water)	weight (g)	water expelled	water remaining	moisture content	water saturation	air saturation
0	754.11	na	54.37	39.77	1.00	0.00
10	753.65	0.46	53.91	39.43	0.99	0.01
12	753.29	0.82	53.55	39.17	0.98	0.02
16.5	753.06	1.05	53.32	39.00	0.98	0.02
18.75	752.99	1.12	53.25	38.95	0.98	0.02
21.5	751.40	2.71	51.66	37.79	0.95	0.05
25.5	745.38	8.73	45.64	33.38	0.84	0.16
32	737.00	17.11	37.26	27.26	0.69	0.31
41	730.65	23.46	30.91	22.61	0.57	0.43
50.5	727.80	26.31	28.06	20.53	0.52	0.48
60	725.00	29.11	25.26	18.48	0.46	0.54
84	723.83	30.28	24.09	17.62	0.44	0.56
129	721.53	32.58	21.79	15.94	0.40	0.60
203	719.92	34.19	20.18	14.76	0.37	0.63
433	718.53	35.58	18.79	13.74	0.35	0.65

330.03 = weight of dish (g) 365.59 = weight of solids (g)
714.41 = dish + moist soil (g) 54.37 = initial moisture (g)
695.62 = dish + dry soil (gg) 0.398 = porosity
18.79 = residual water (g)

Capillary Head-Saturation Data
tempe cell apparatus

Sample I.D: COR
Date: 9/1/94 - 9/22/94

760.61 = Initial weight of cell with sample (g)
129.9 = cell volume (cm³)
506.3 = cell weight (g)

Pc (cm water)	weight (g)	water expelled	water remaining	moisture content	water saturation	air saturation
0	760.61	na	58.14	44.76	1.00	0.00
10	760.61	0.00	58.14	44.76	1.00	0.00
23	760.61	0.00	58.14	44.76	1.00	0.00
35	760.12	0.49	57.65	44.38	0.99	0.01
55	751.40	9.21	48.93	37.67	0.84	0.16
69	734.09	26.52	31.62	24.34	0.54	0.46
85	721.13	39.48	18.66	14.36	0.32	0.68
108	716.16	44.45	13.69	10.54	0.24	0.76
137	712.92	47.69	10.45	8.04	0.18	0.82
188	710.91	49.70	8.44	6.50	0.15	0.85
300	708.65	51.96	6.18	4.76	0.11	0.89
759	703.58	57.03	1.11	0.85	0.02	0.98

4.3 = weight of dish (g) 195.30 = weight of solids (g)
200.71 = dish + moist soil (g) 58.14 = initial moisture (g)
199.6 = dish + dry soil (gg) 0.45 = porosity
1.11 = residual water (g)

Capillary Head-Saturation Data
tempe cell apparatus

Sample I.D.: COL
Date: 8/95

777.75 = Initial weight of cell with sample (g)
136.7 = cell volume (cm³)
506.3 = cell weight (g)

Pc (cm water)	weight (g)	water expelled	water remaining	moisture content	water saturation	air saturation
0	777.75	na	52.31	38.26	1.00	0.00
14	777.75	0.00	52.31	38.26	1.00	0.00
16	774.46	3.29	49.02	35.86	0.94	0.06
18	773.88	3.87	48.44	35.43	0.93	0.07
20	772.45	5.30	47.01	34.39	0.90	0.10
22.5	770.51	7.24	45.07	32.97	0.86	0.14
25.5	767.55	10.20	42.11	30.80	0.81	0.19
31.5	763.25	14.50	37.81	27.66	0.72	0.28
36	756.10	21.65	30.66	22.43	0.59	0.41
44	746.30	31.45	20.86	15.26	0.40	0.60
52	742.16	35.59	16.72	12.23	0.32	0.68
68.5	737.00	40.75	11.56	8.46	0.22	0.78
96	733.90	43.85	8.46	6.19	0.16	0.84
148	732.21	45.54	6.77	4.95	0.13	0.87
196	731.38	46.37	5.94	4.35	0.11	0.89

242 = weight of dish (g) 368.28 = weight of solids (g)
616.22 = dish + moist soil (g) 52.31 = initial moisture (g)
610.28 = dish + dry soil (gg) 0.38 = porosity
5.94 = residual water (g)

Capillary Head-Saturation Data
tempe cell apparatus

Sample I.D: CSM
Date: 2/8/96 - 2/18/96

756.33 = Initial weight of cell with sample (g)
136.7 = cell volume (cm³)

Pc (cm water)	weight (g)	water expelled	water remaining	moisture content	water saturation	air saturation
0	756.33	na	51.10	37.38	1.00	-0.00
12	755.61	0.72	50.38	36.85	0.99	0.01
19	753.91	2.42	48.68	35.61	0.95	0.05
28	744.49	11.84	39.26	28.72	0.77	0.23
40	734.44	21.89	29.21	21.37	0.57	0.43
51	731.20	25.13	25.97	19.00	0.51	0.49
75	728.40	27.93	23.17	16.95	0.45	0.55
114	725.89	30.44	20.66	15.11	0.40	0.60
161	724.37	31.96	19.14	14.00	0.37	0.63
373	721.40	34.93	16.17	11.83	0.32	0.68

212.39 = weight of dish (g)
601 = dish + moist soil (g)
584.83 = dish + dry soil (g)
16.17 = residual water (g)
51.10 = initial moisture (g)
0.37 = porosity

Capillary Head-Saturation Data
tempe cell apparatus

Sample I.D: CHV
Date: 9/1/94-9/22/94

775.38 = Initial weight of cell with sample (g)

136.7 = cell volume (cm³)

485.56 = cell weight (g)

Pc (cm water)	weight (g)	water expelled	water remaining	moisture content	water saturation	air saturation
0	775.38	na	45.45	33.25	1.00	0.00
20	774.56	0.82	44.63	32.65	0.98	0.02
40	770.82	4.56	40.89	29.91	0.90	0.10
58	769.80	5.58	39.87	29.16	0.88	0.12
76	768.83	6.55	38.90	28.45	0.86	0.14
96	768.10	7.28	38.17	27.92	0.84	0.16
149	766.87	8.51	36.94	27.02	0.81	0.19
211	765.60	9.78	35.67	26.09	0.78	0.22
327	764.32	11.06	34.39	25.16	0.76	0.24
425	763.00	12.38	33.07	24.19	0.73	0.27
529	761.99	13.39	32.06	23.45	0.71	0.29
650	760.85	14.53	30.92	22.62	0.68	0.32

149.11 = weight of dish (g)

424.4 = dish + moist soil (g)

393.48 = dish + dry soil (gg)

30.92 = residual water (g)

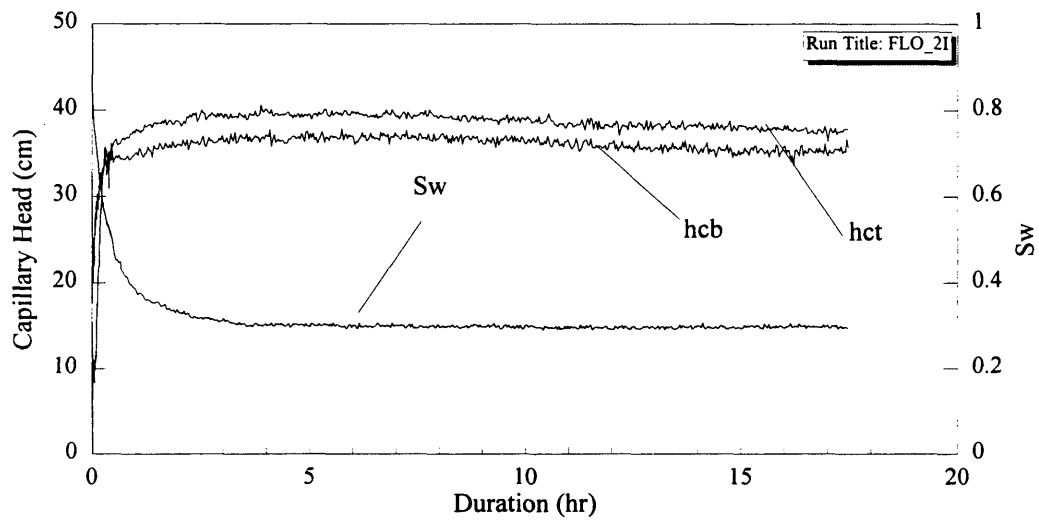
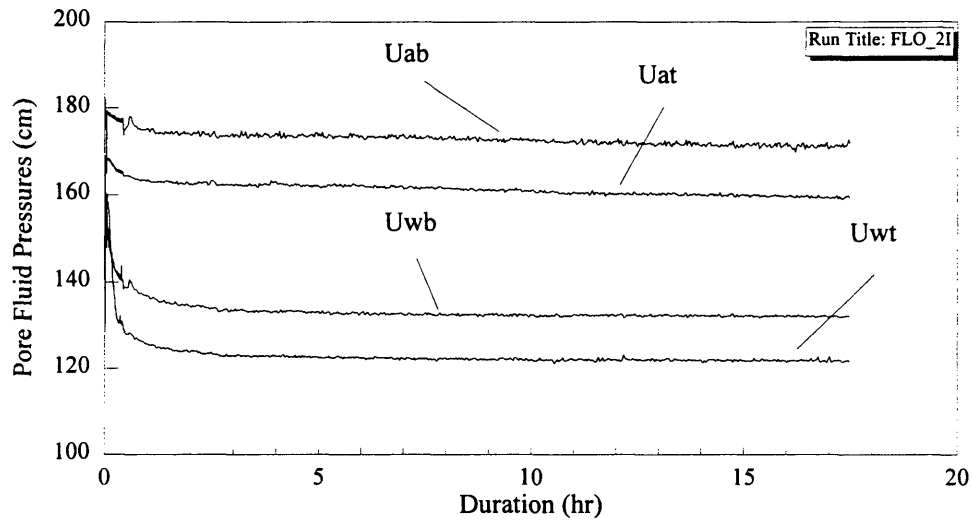
244.37 = weight of solids (g)

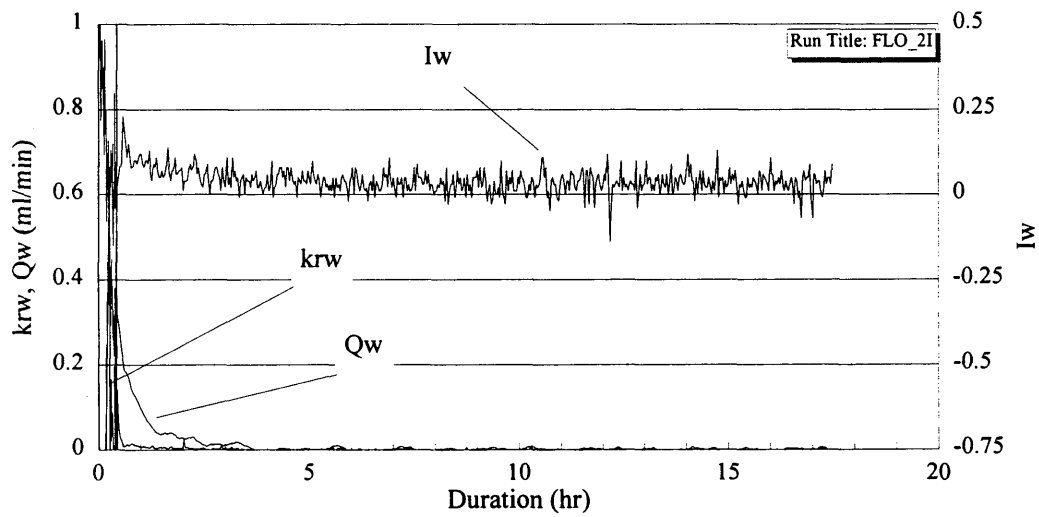
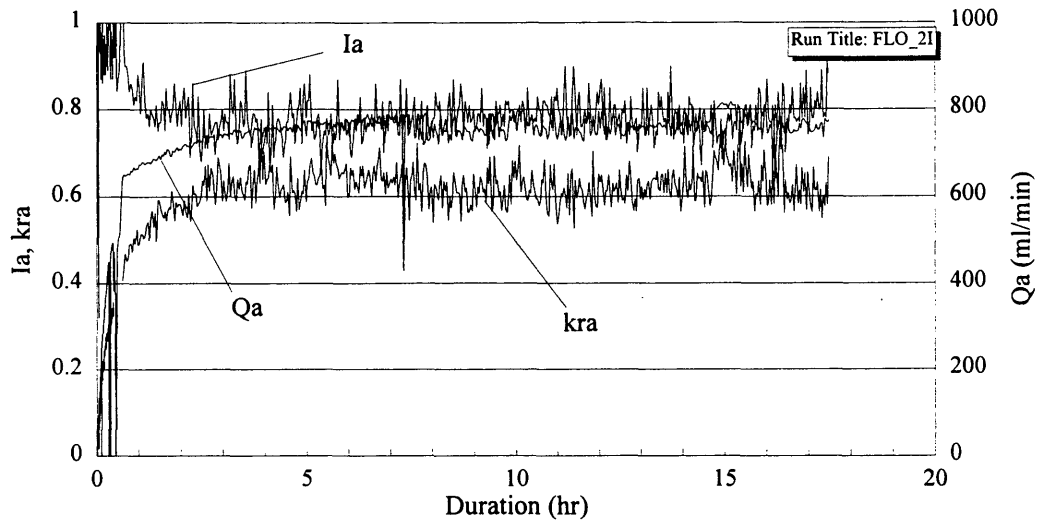
45.45 = initial moisture (g)

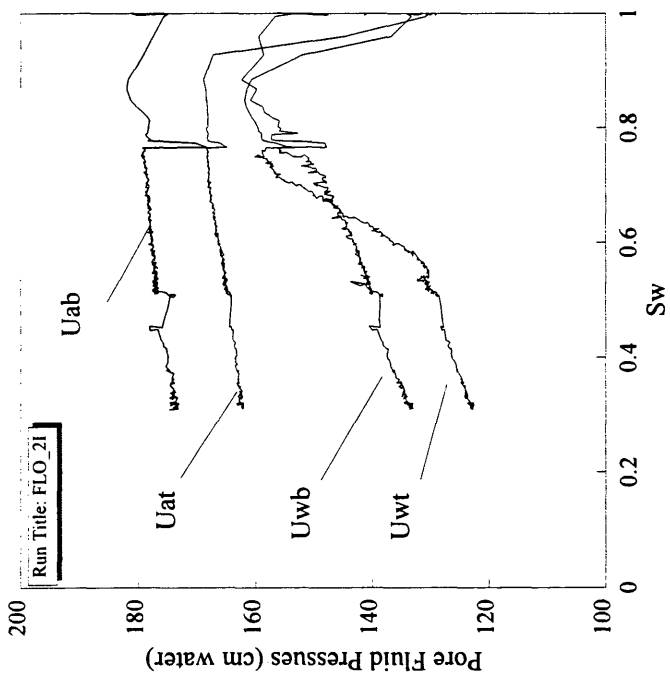
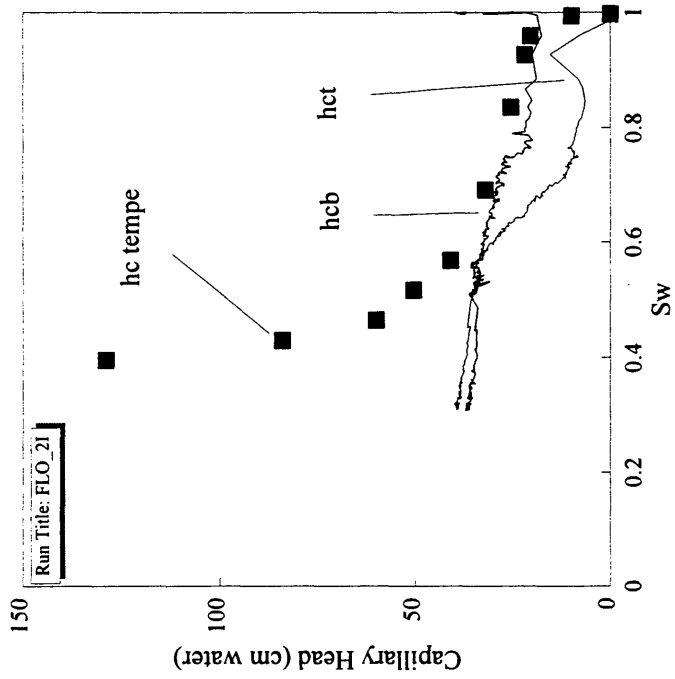
0.33 = porosity

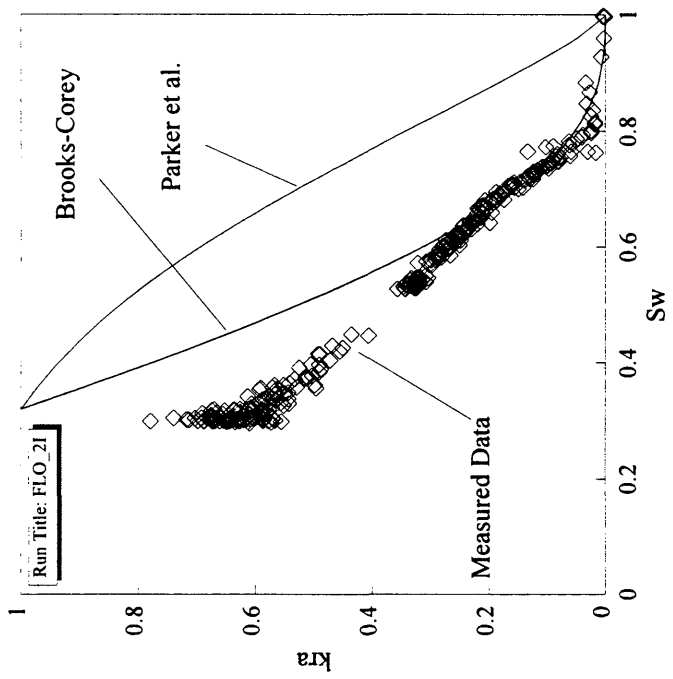
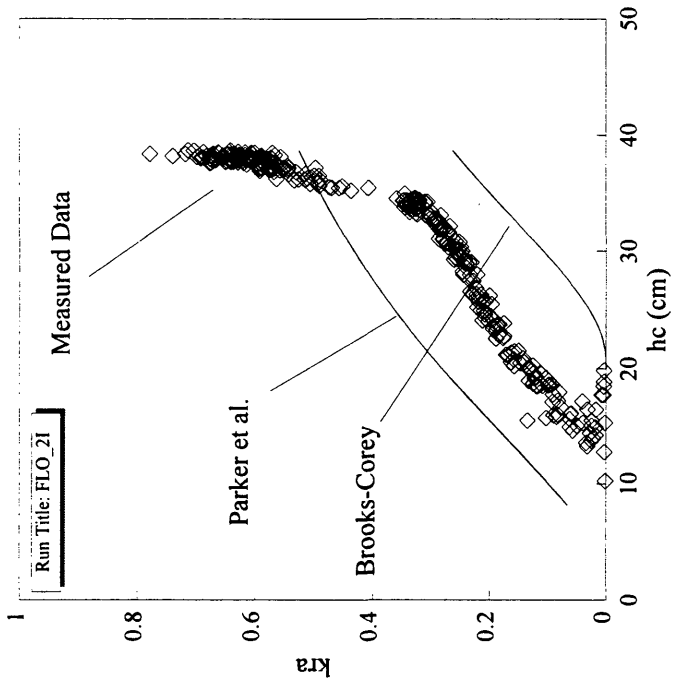
APPENDIX D1

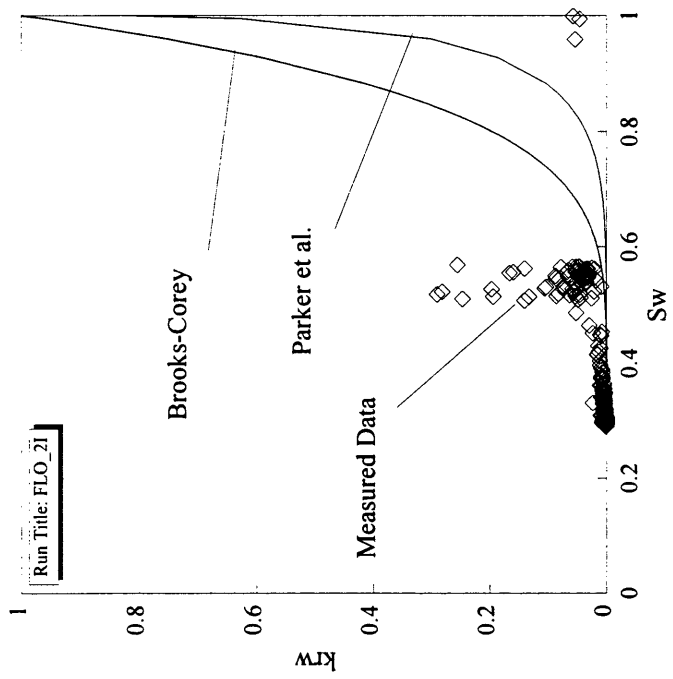
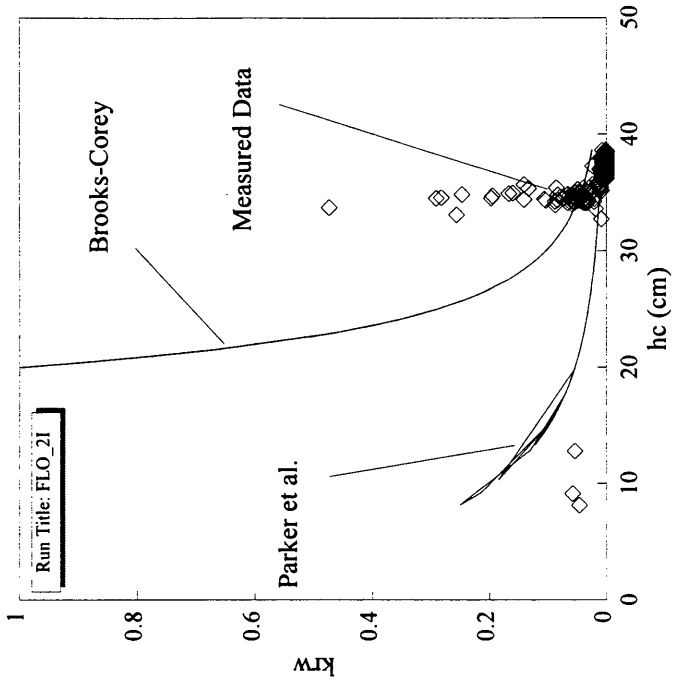
Displacement Experiment Data
Sample FLO

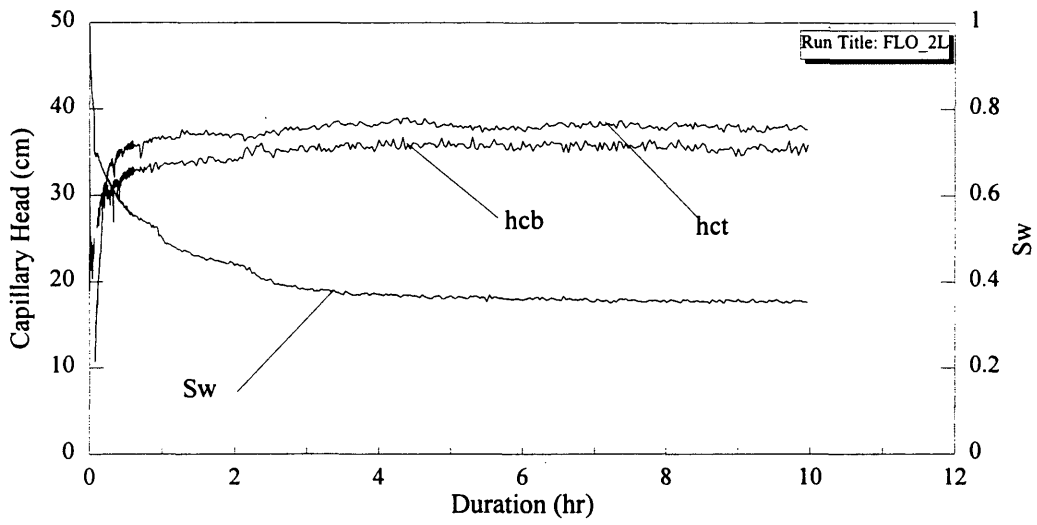
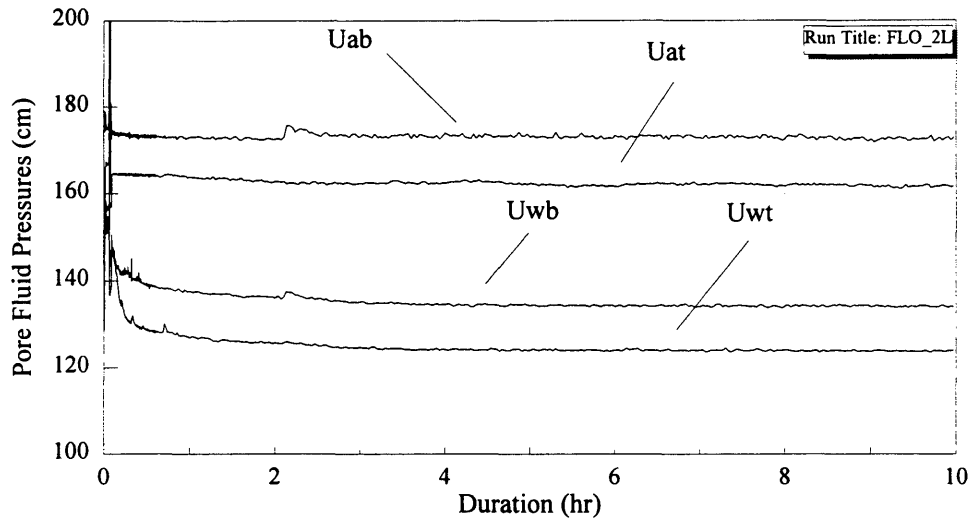


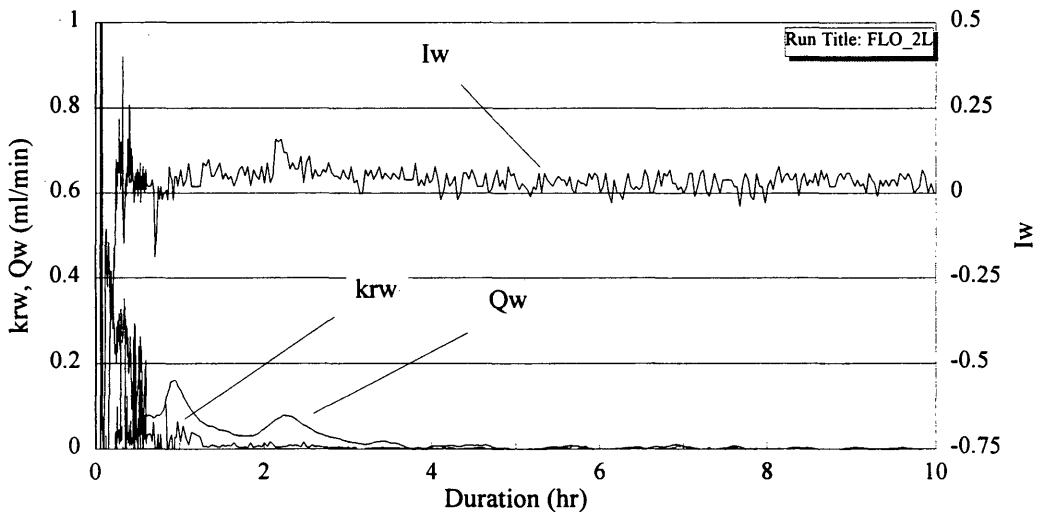
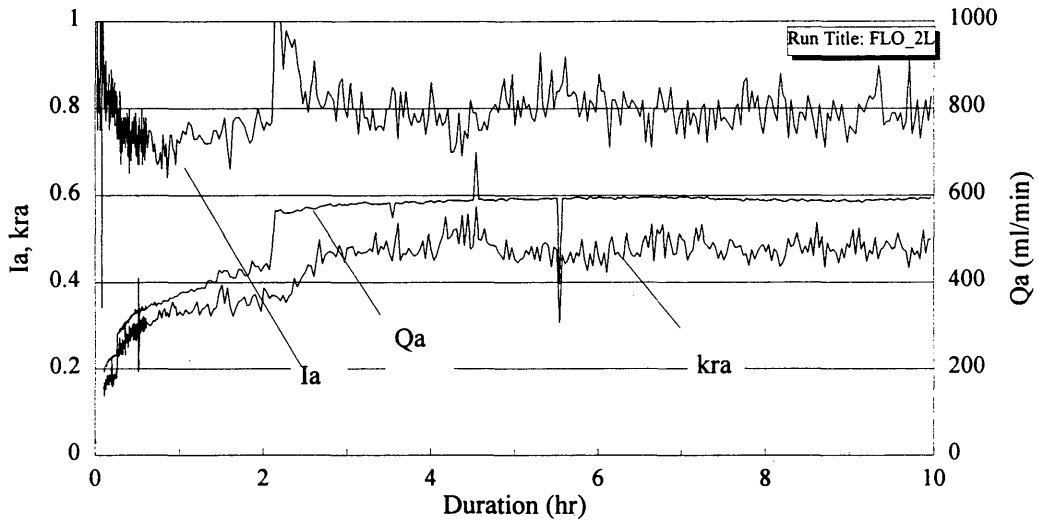


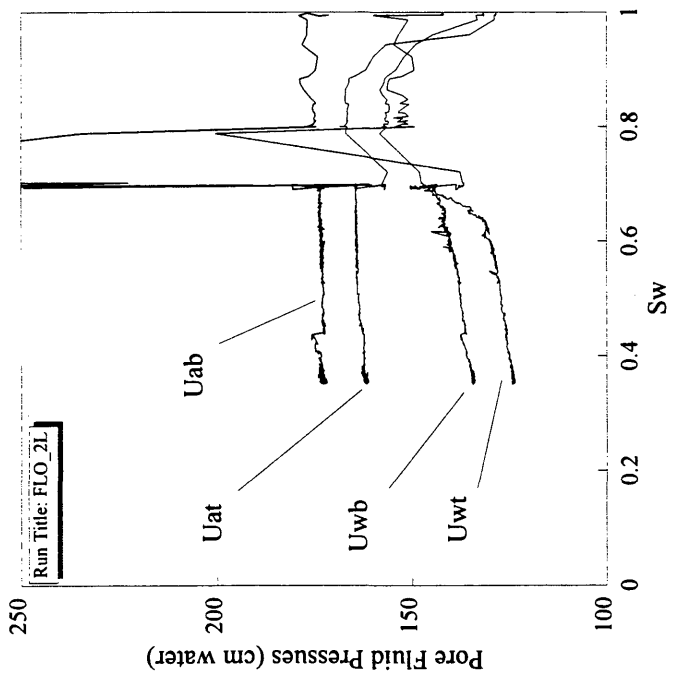
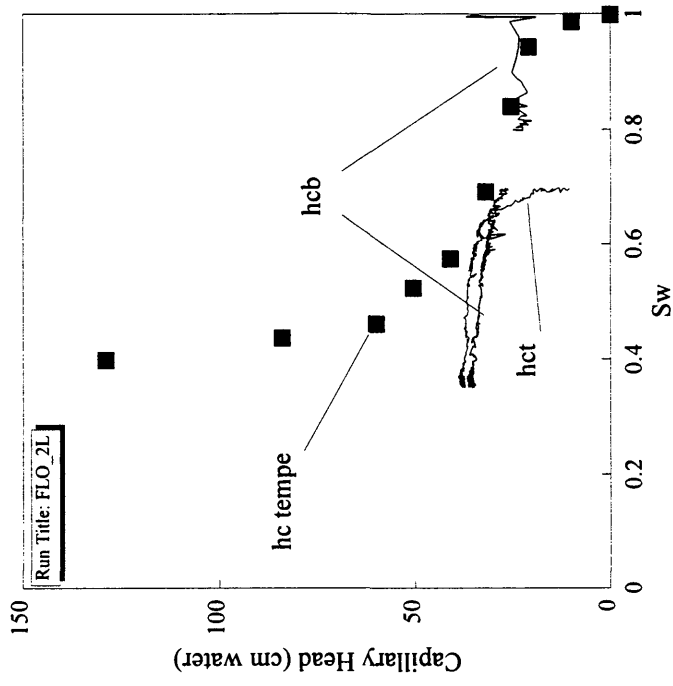


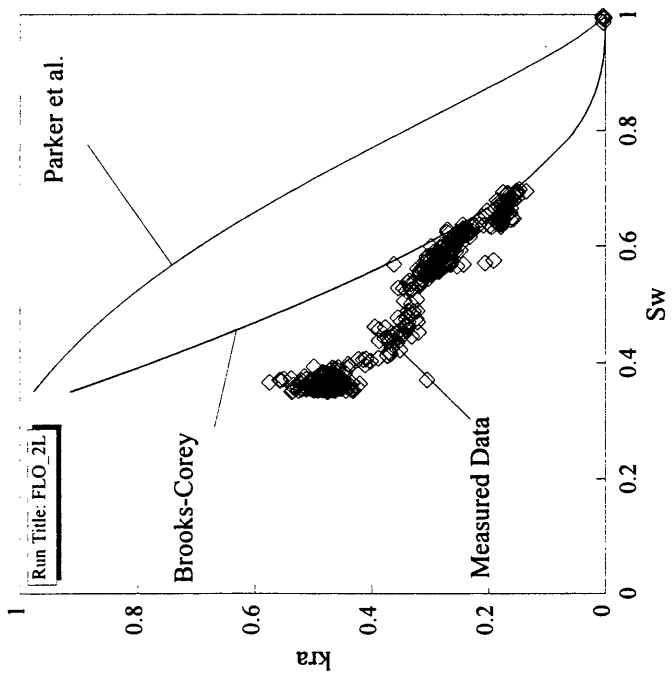
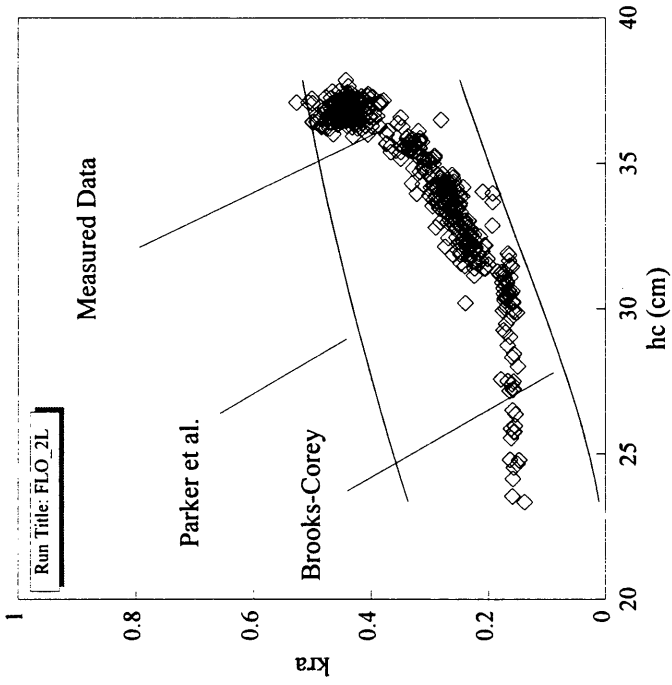


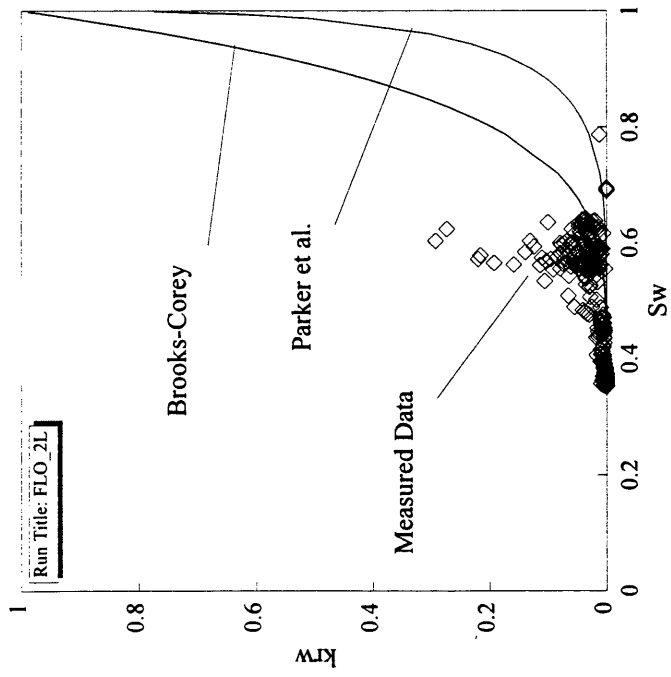
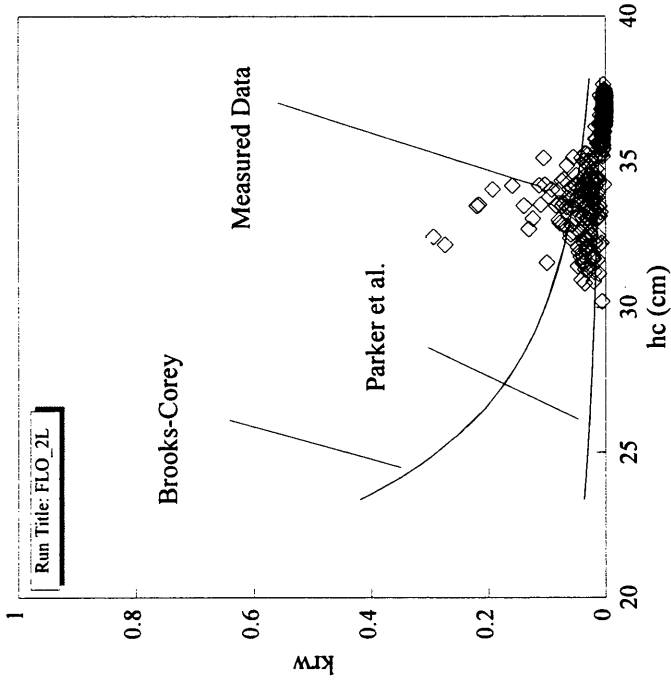


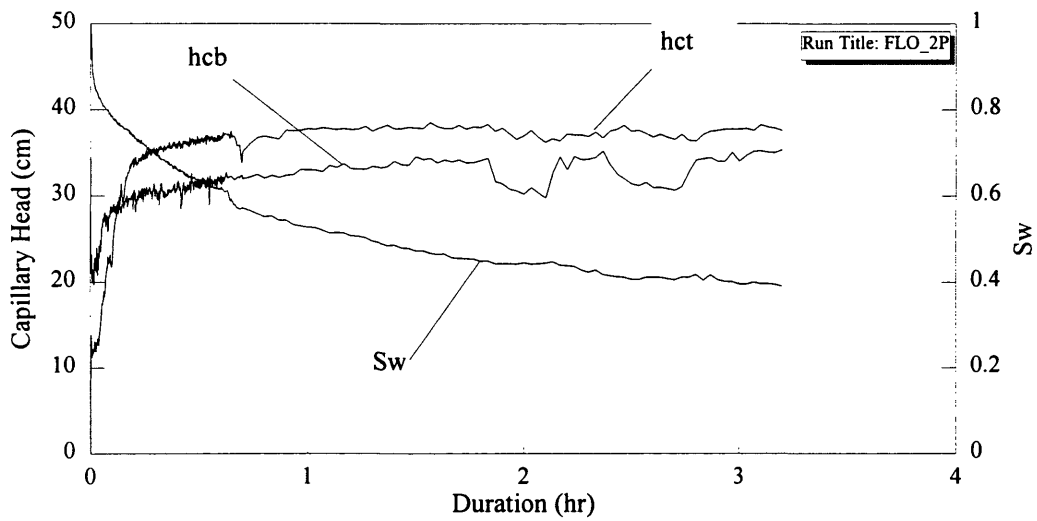
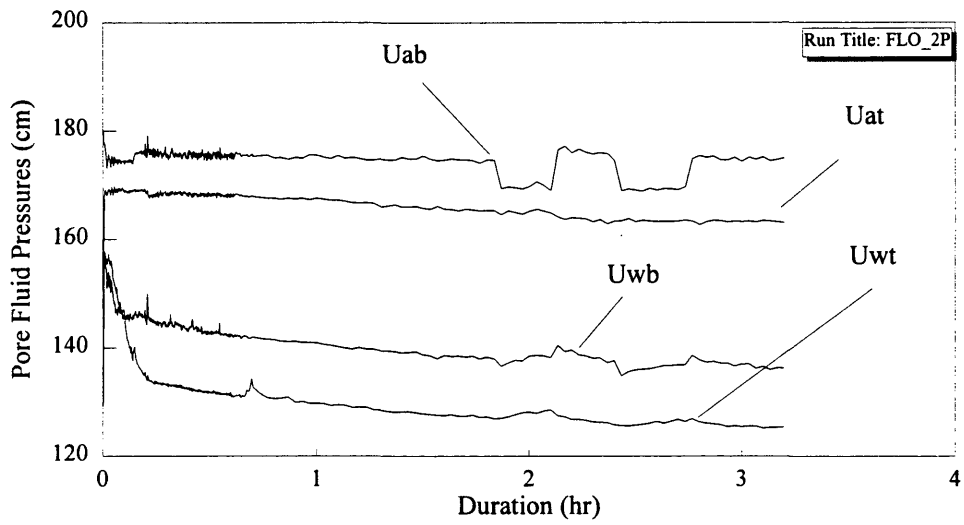


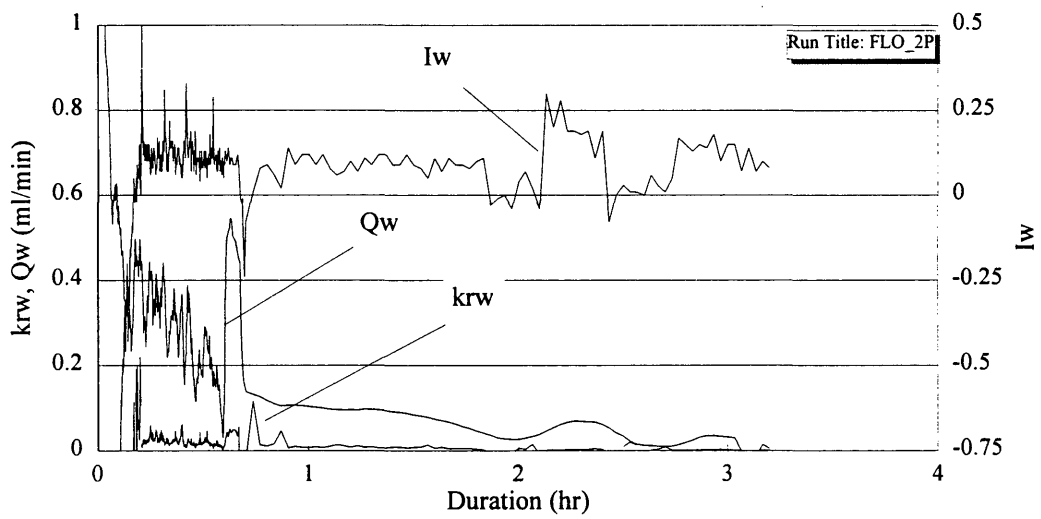
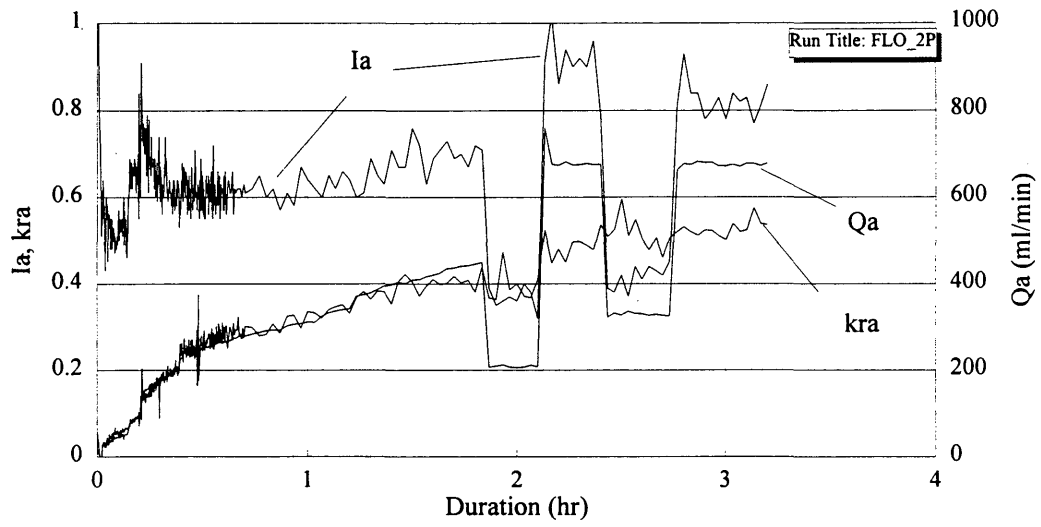


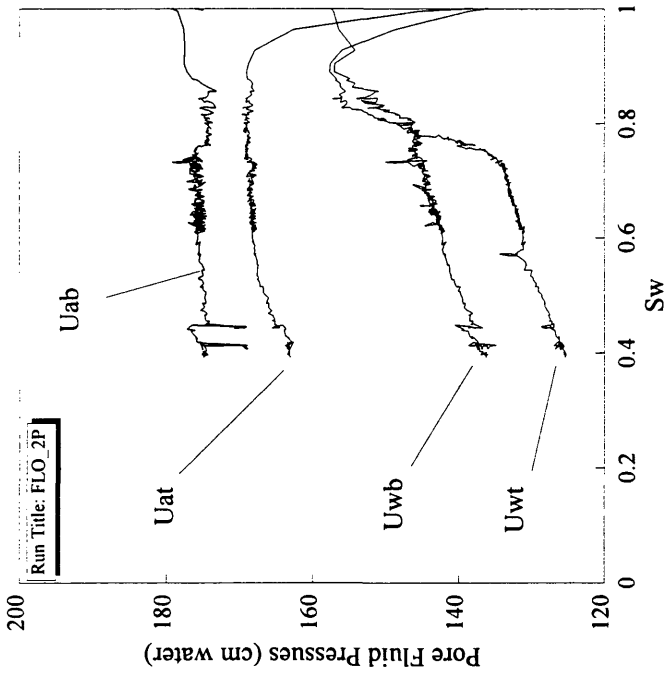
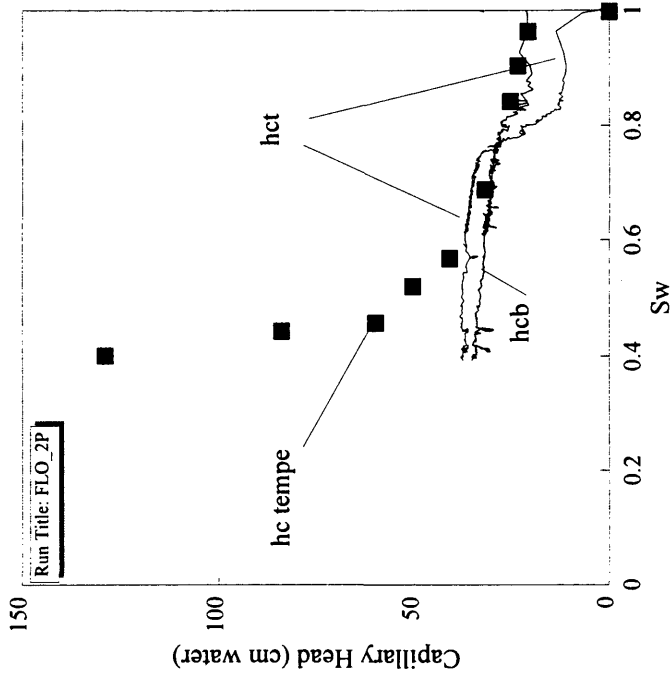


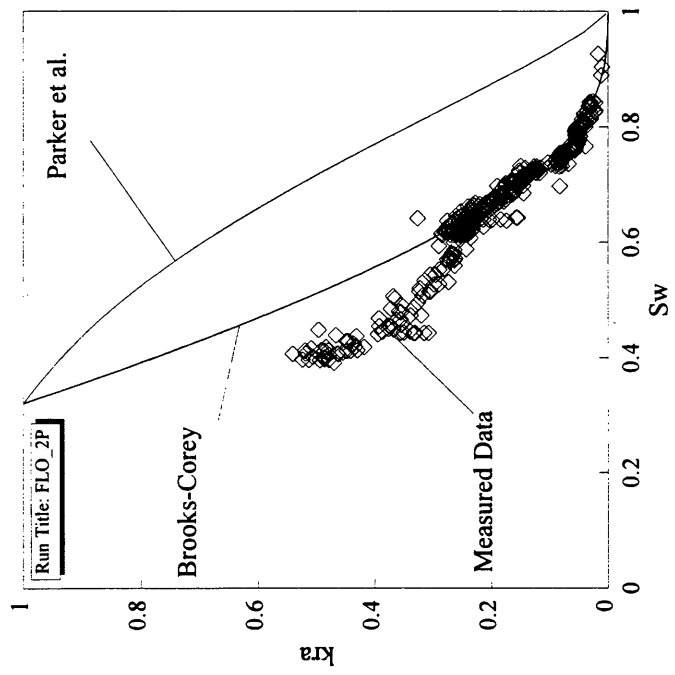
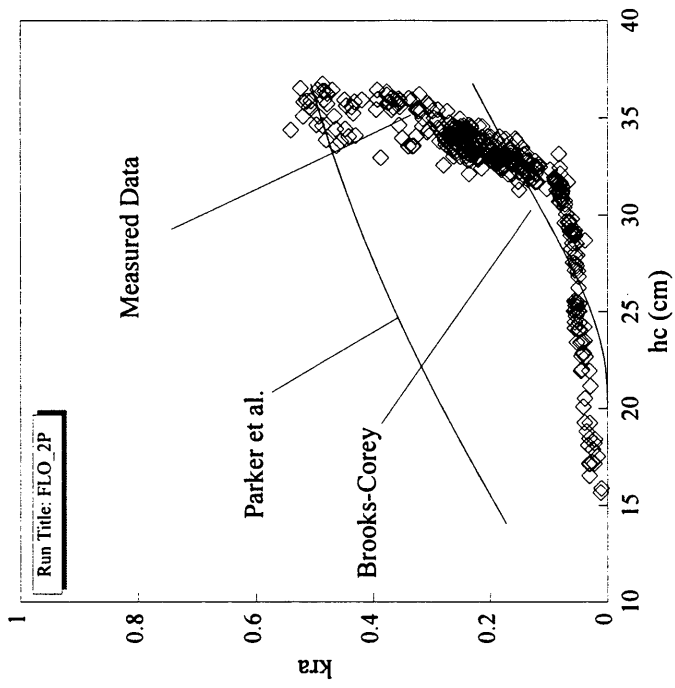


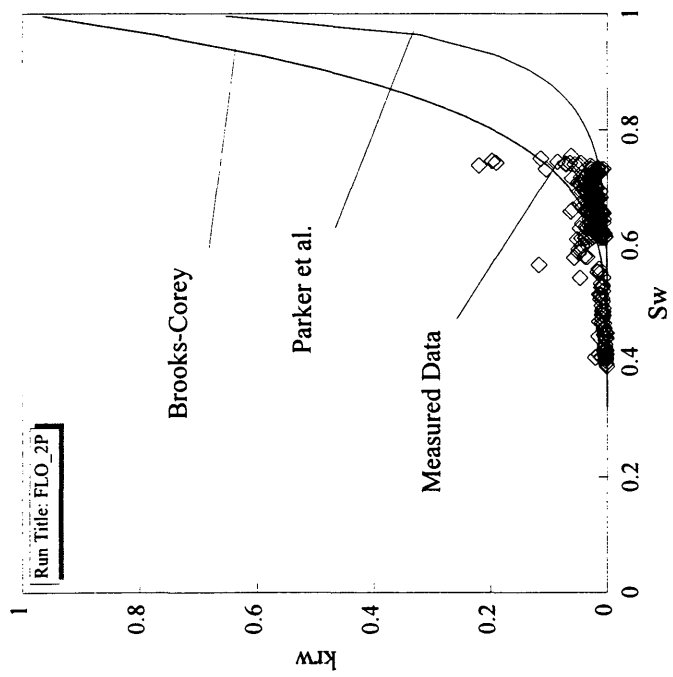
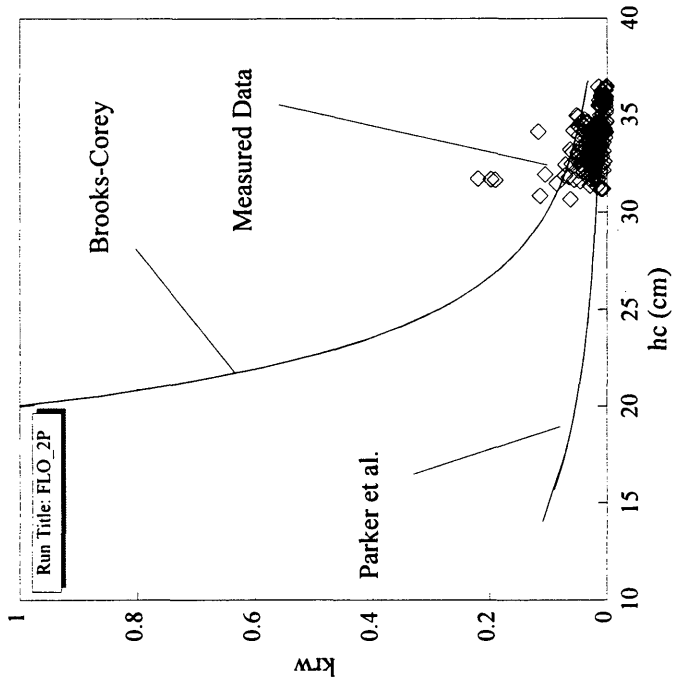


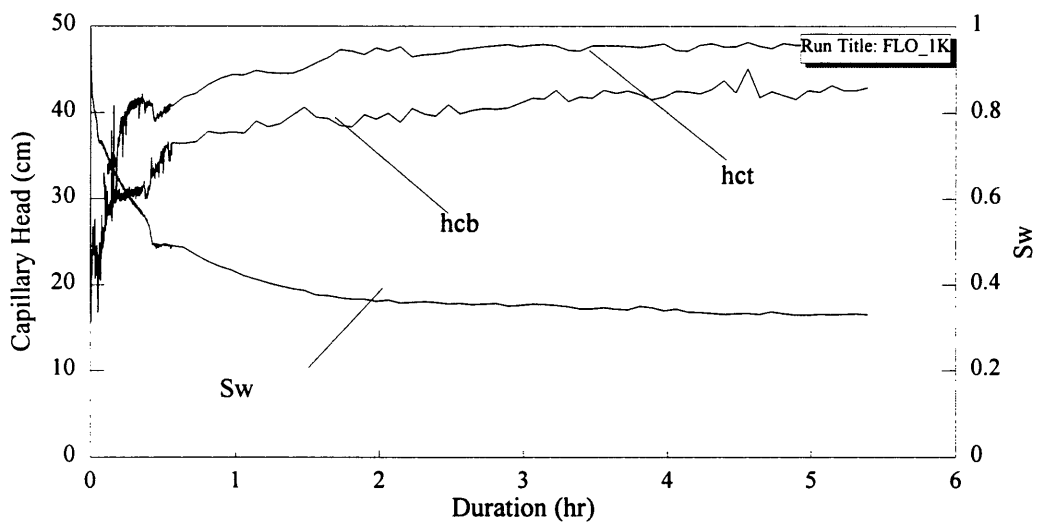
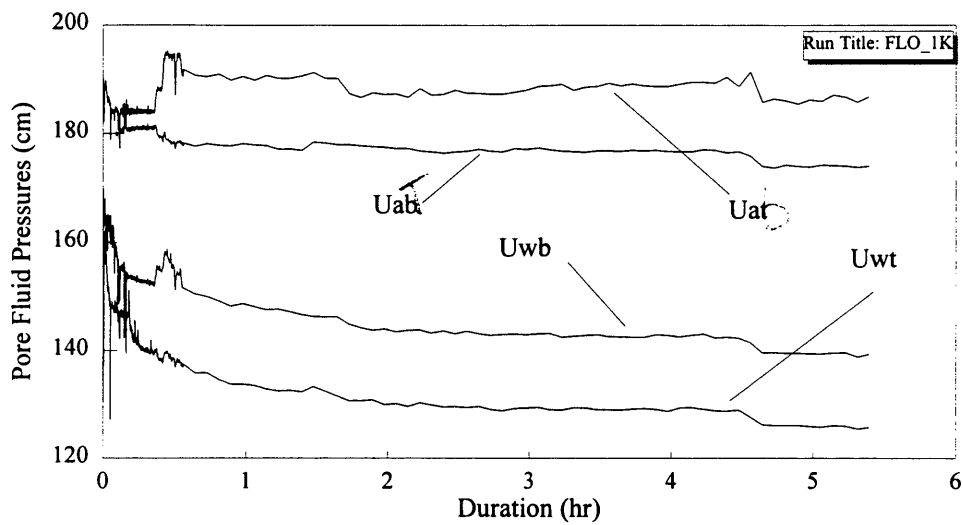


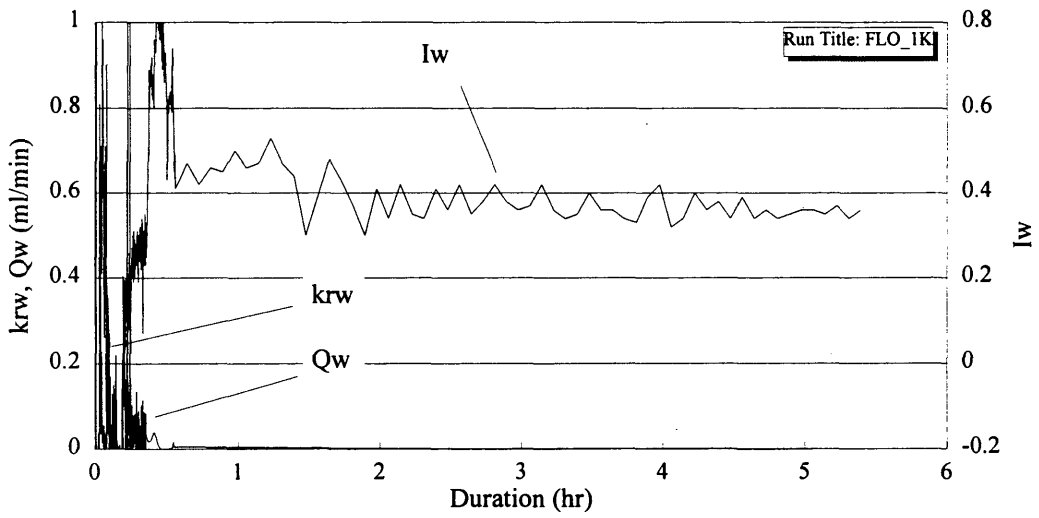
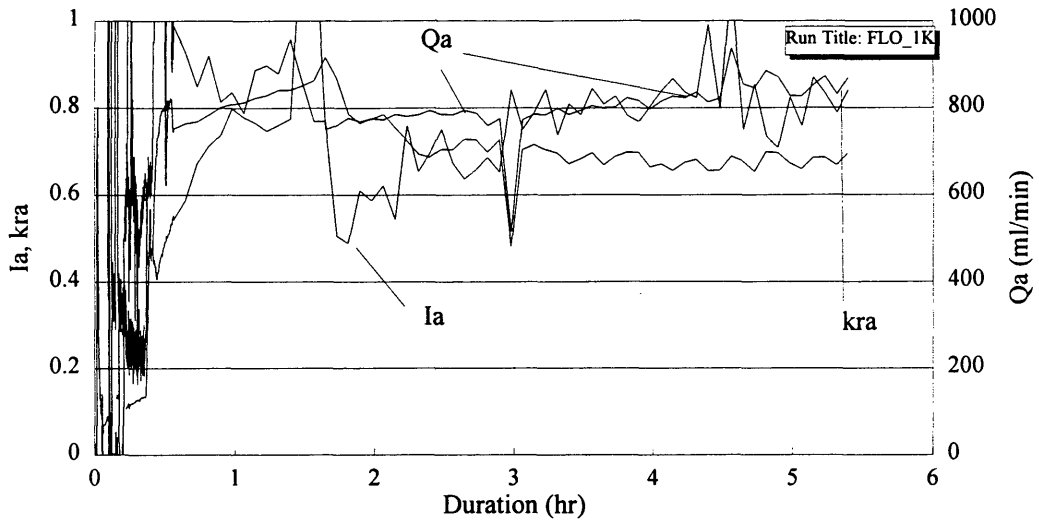


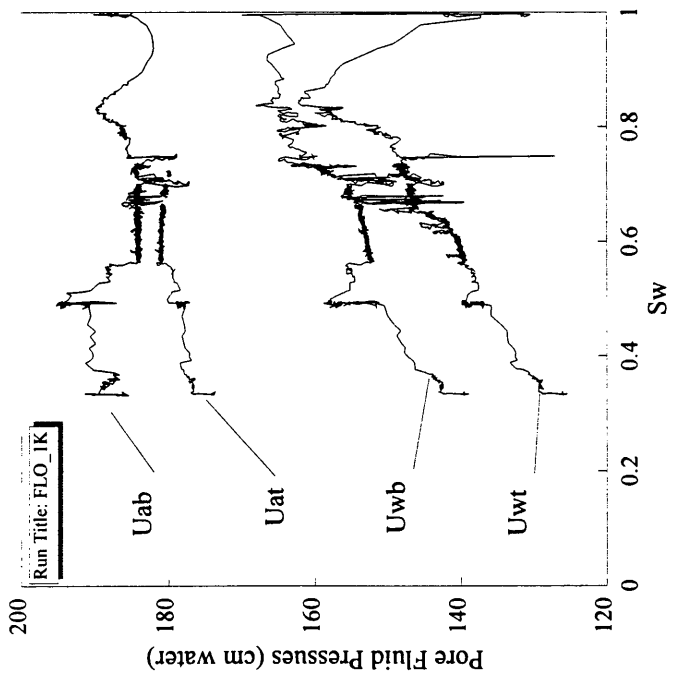
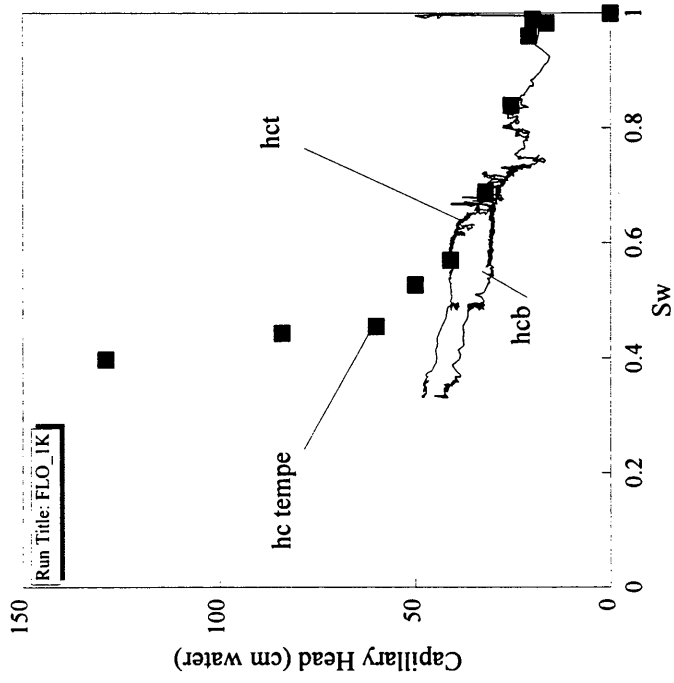


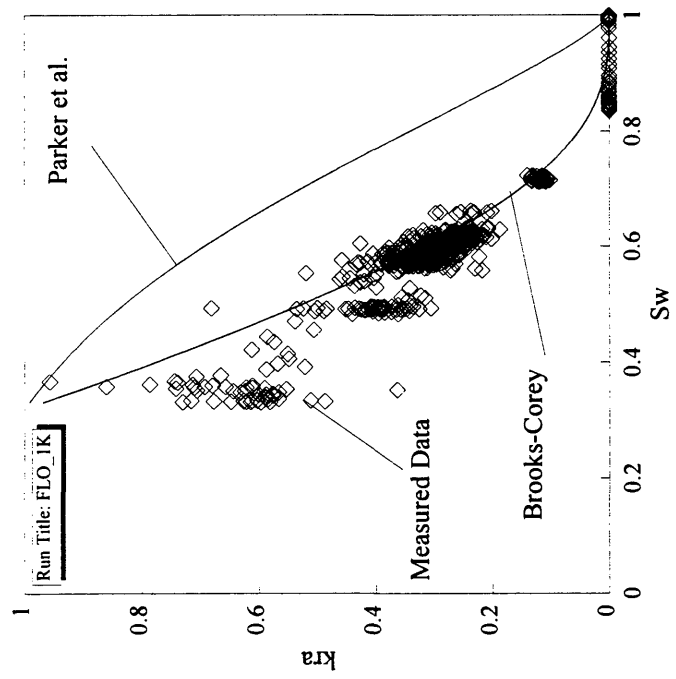
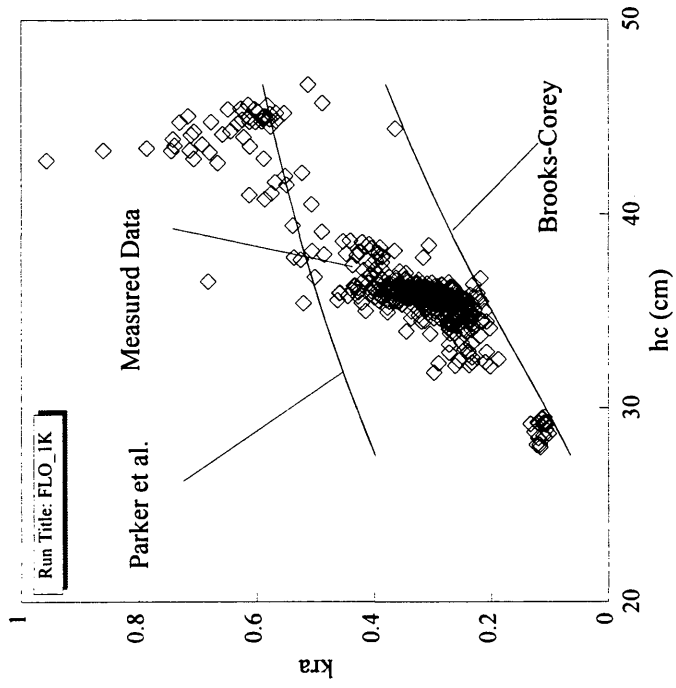


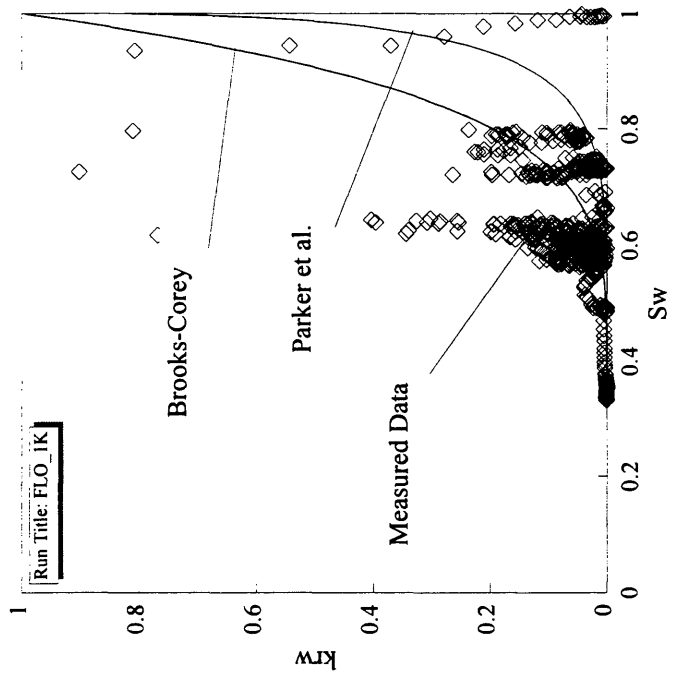
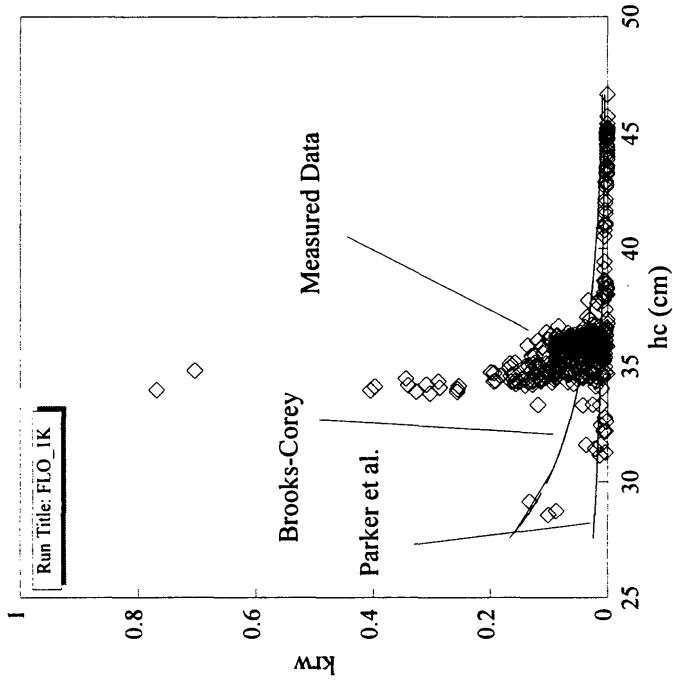






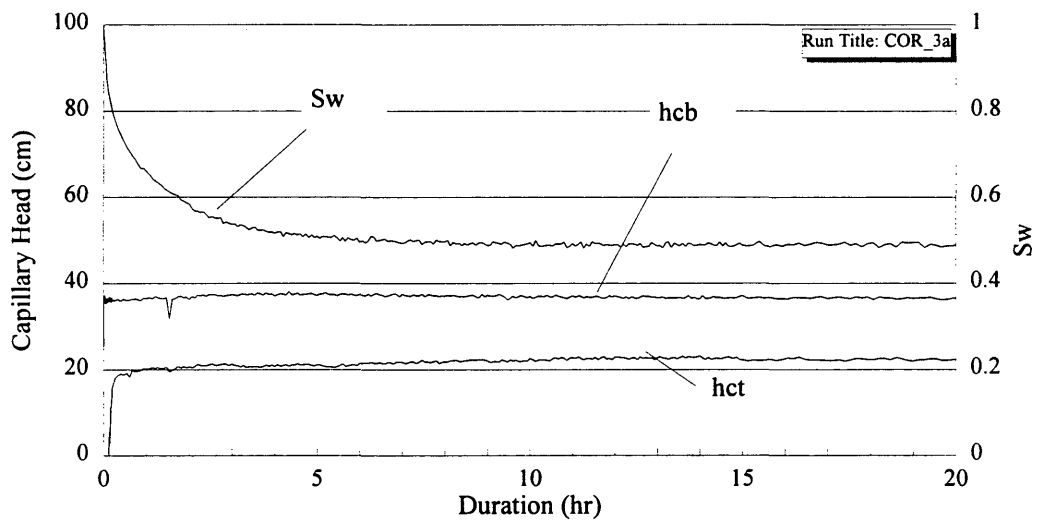
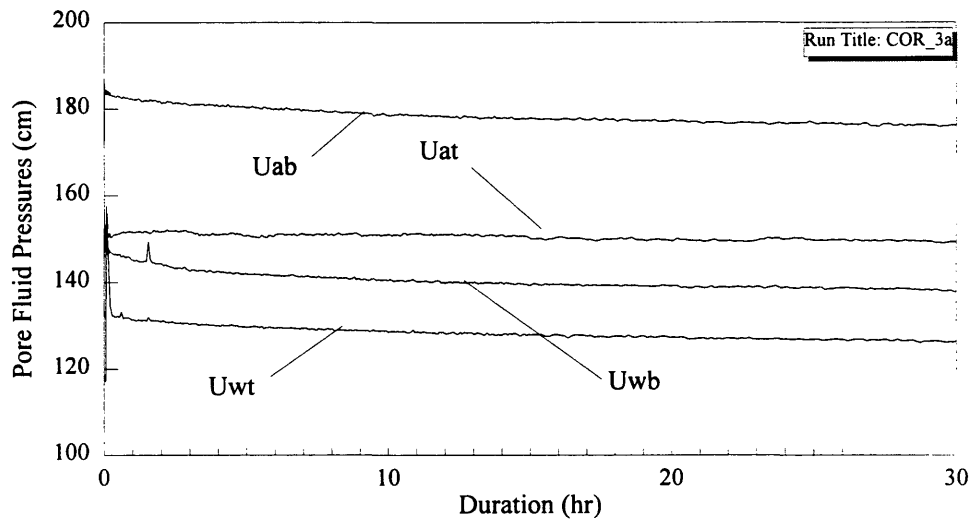


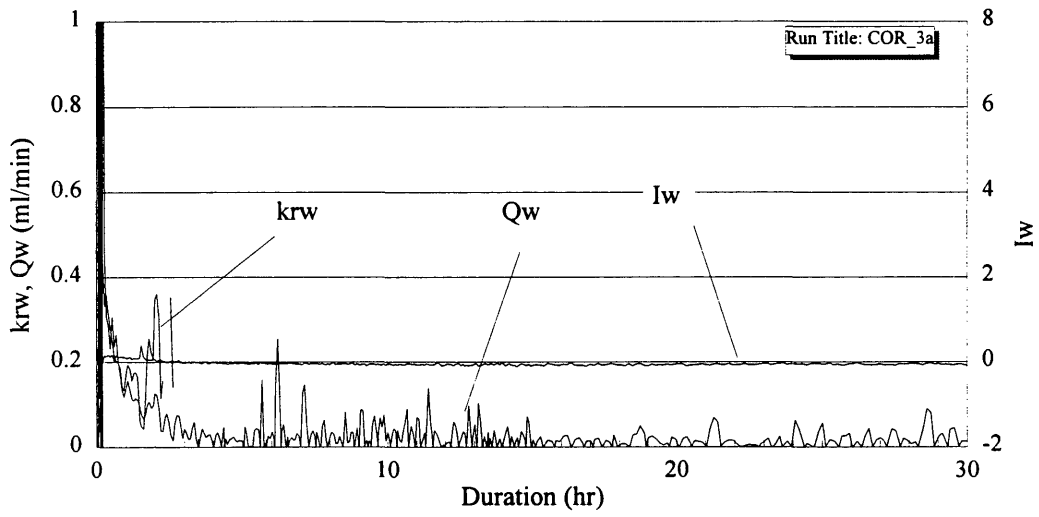
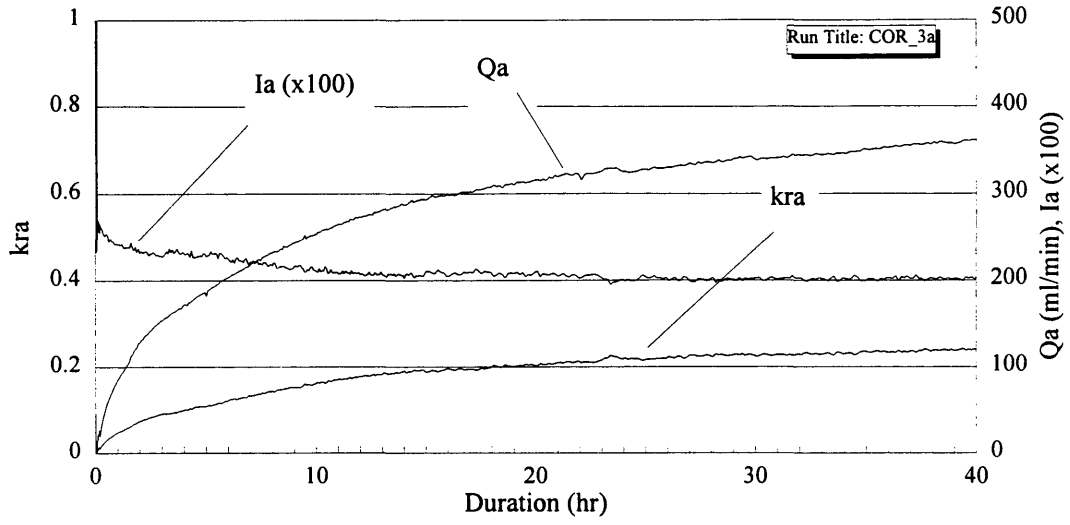


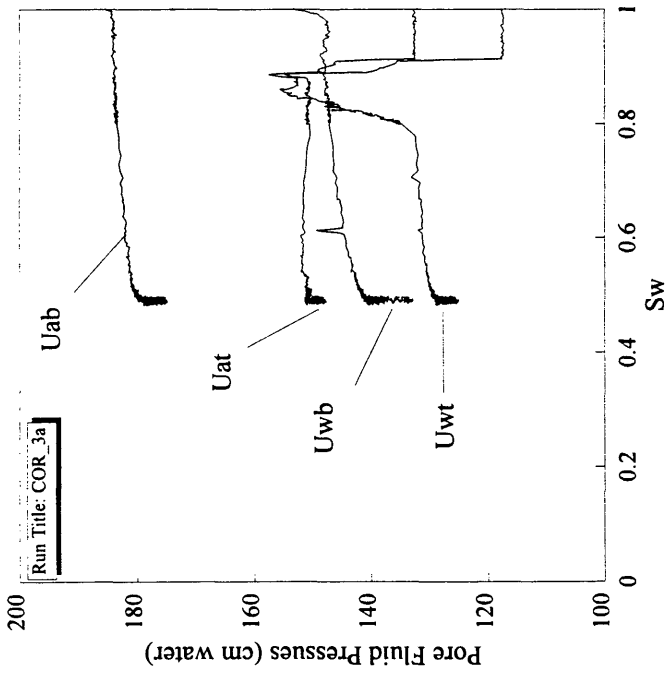
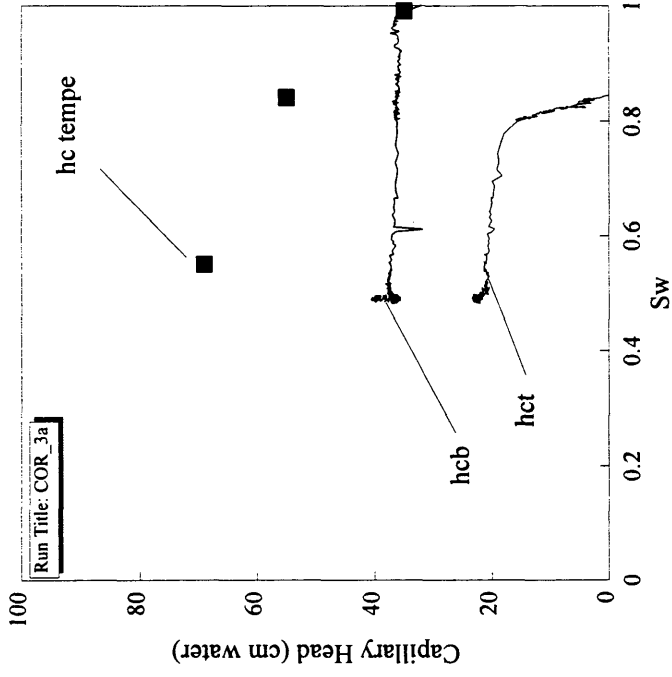


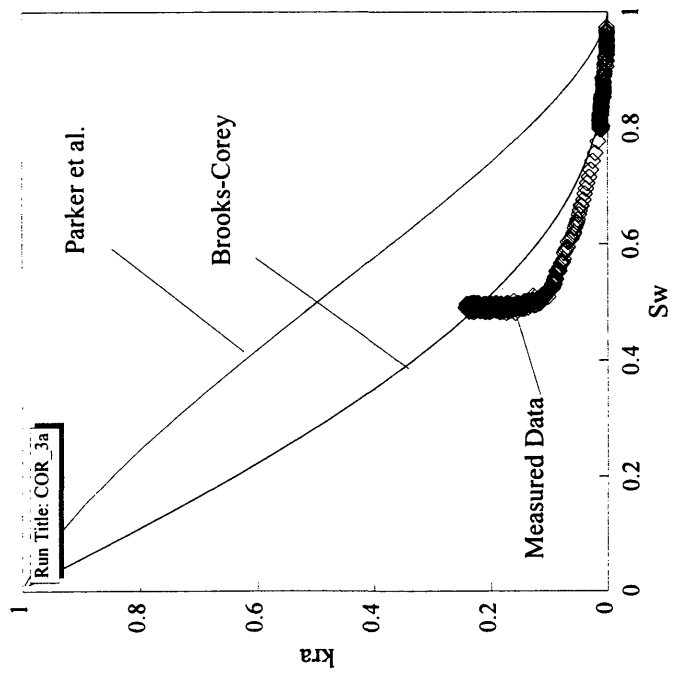
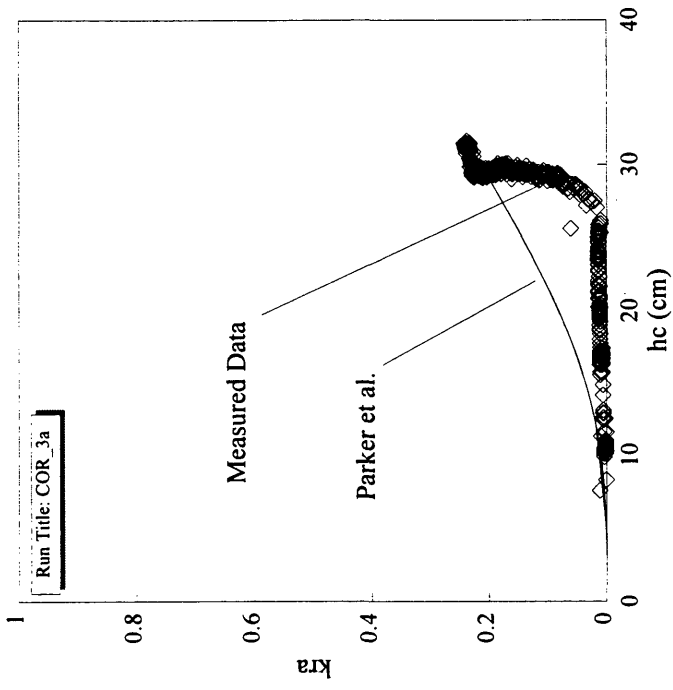
APPENDIX D2

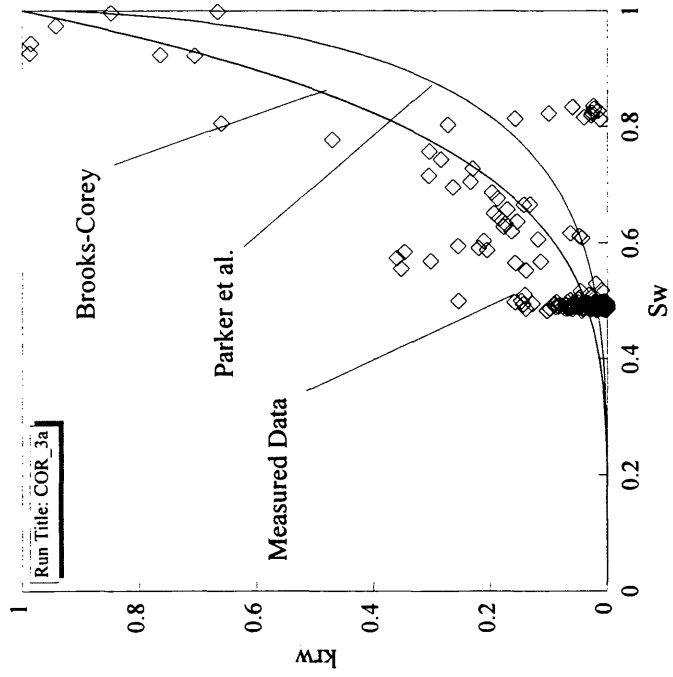
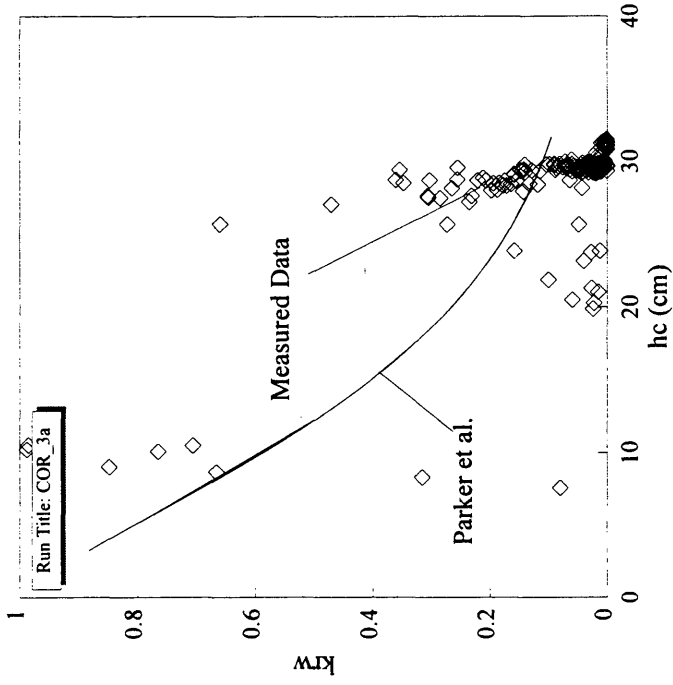
Displacement Experiment Data
Sample COR

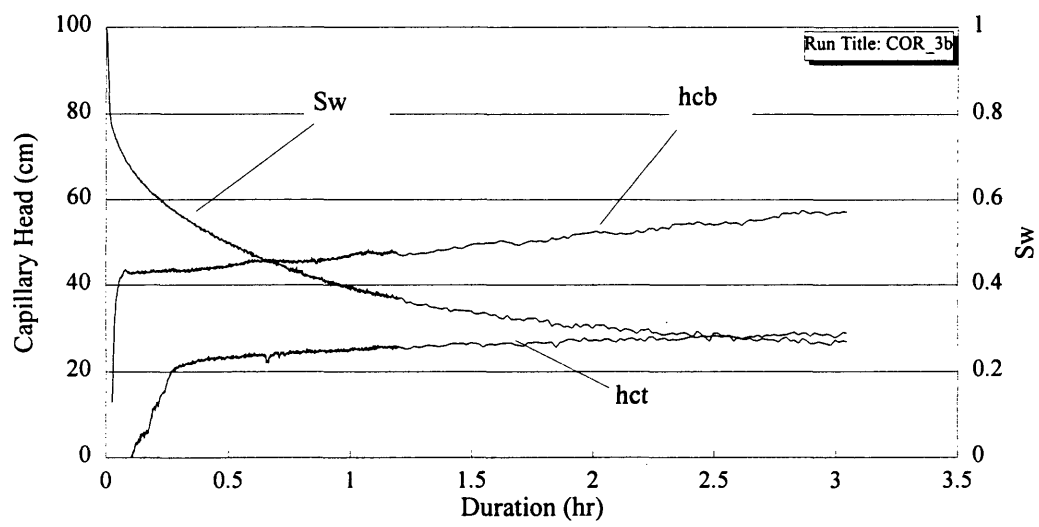
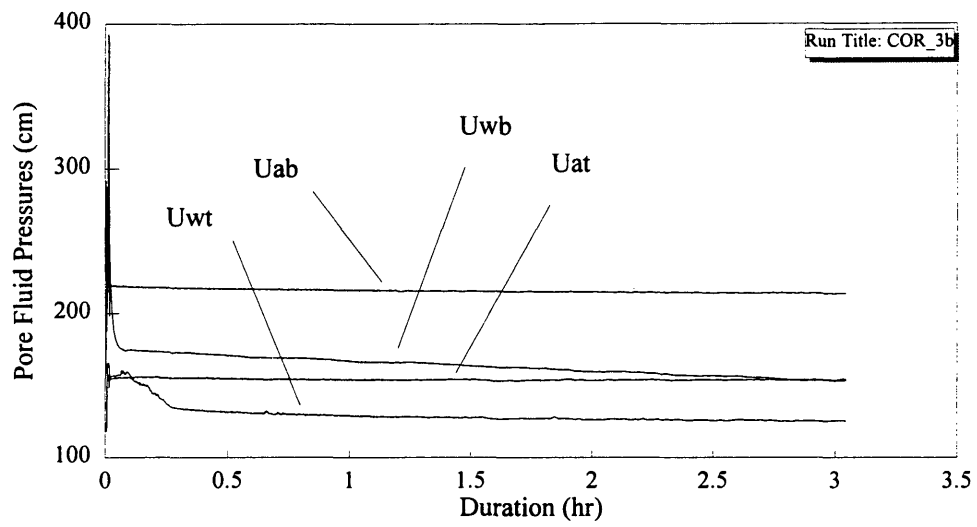


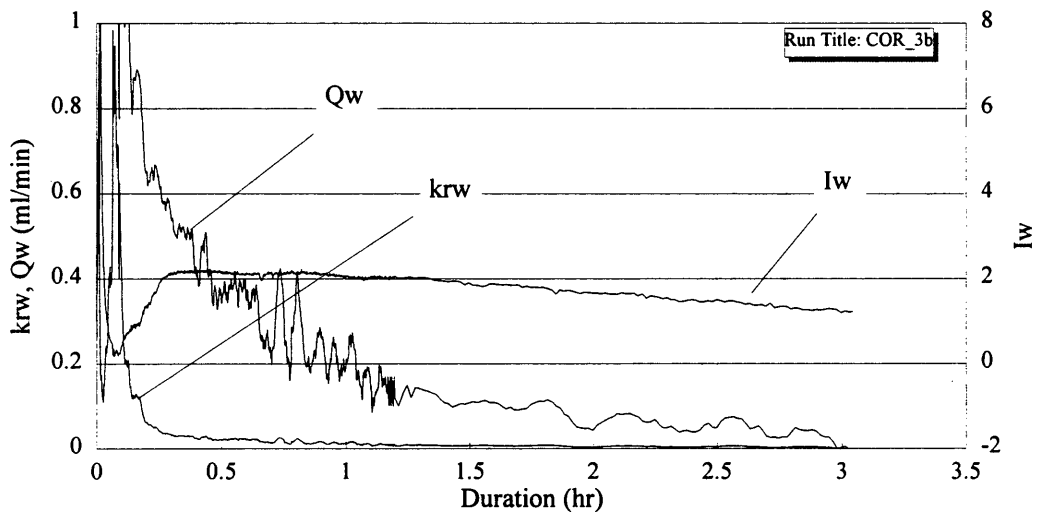
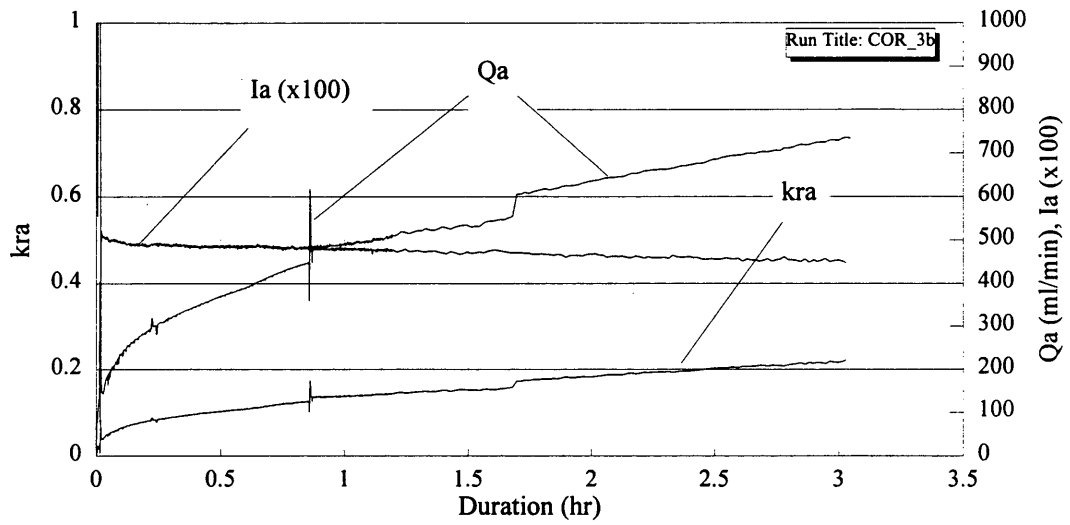


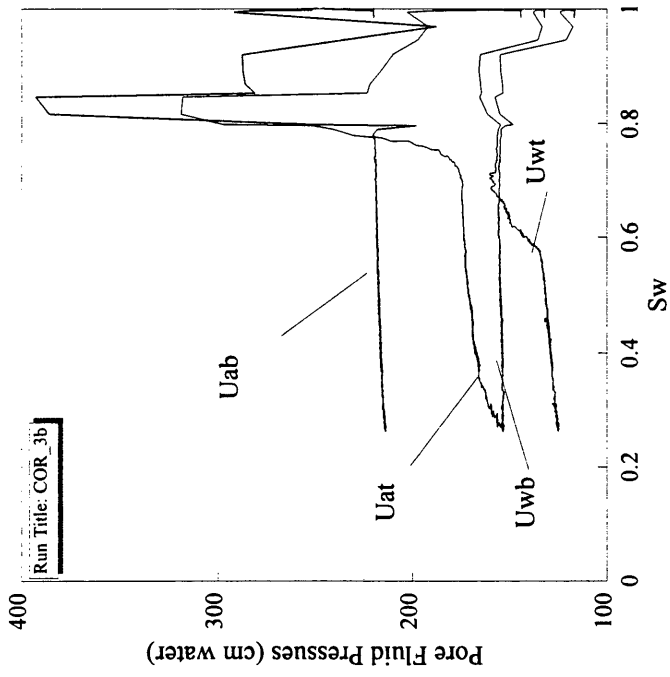
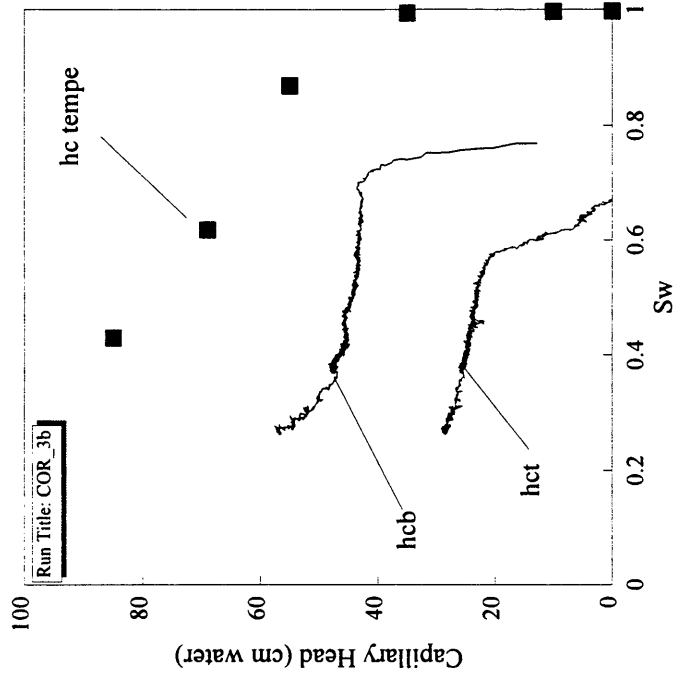


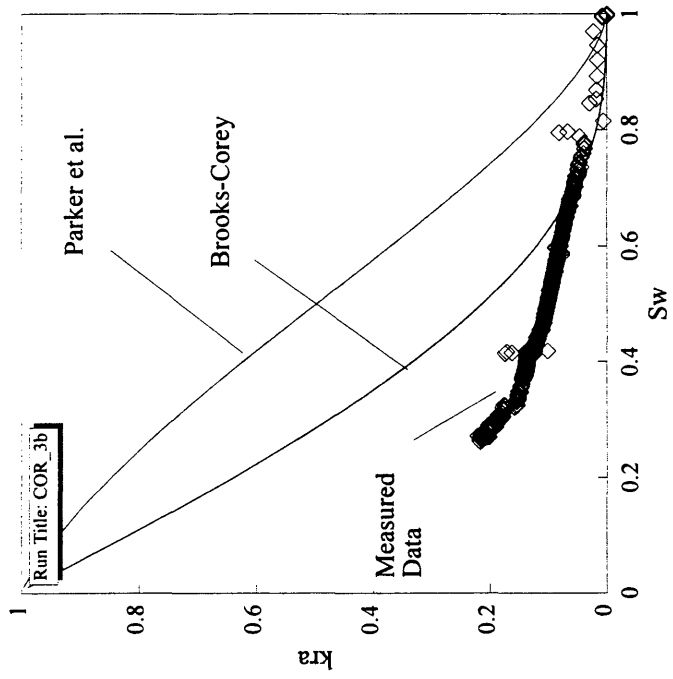
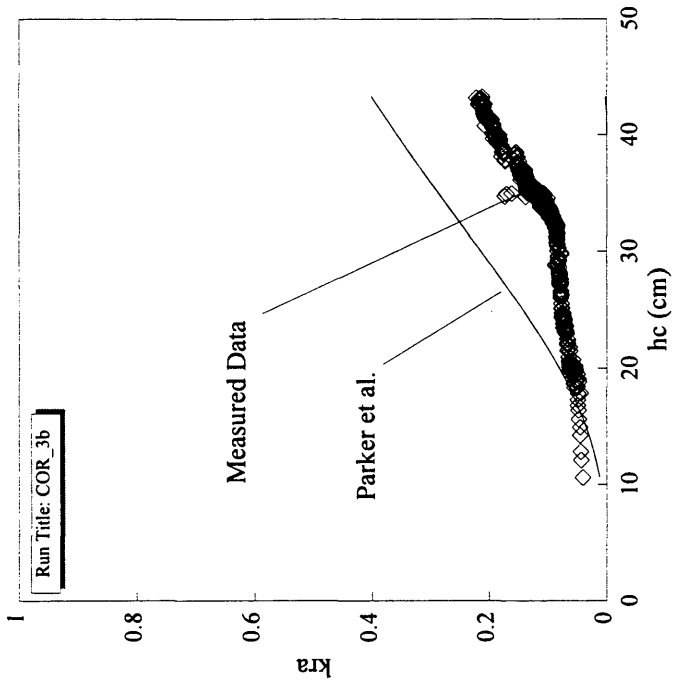


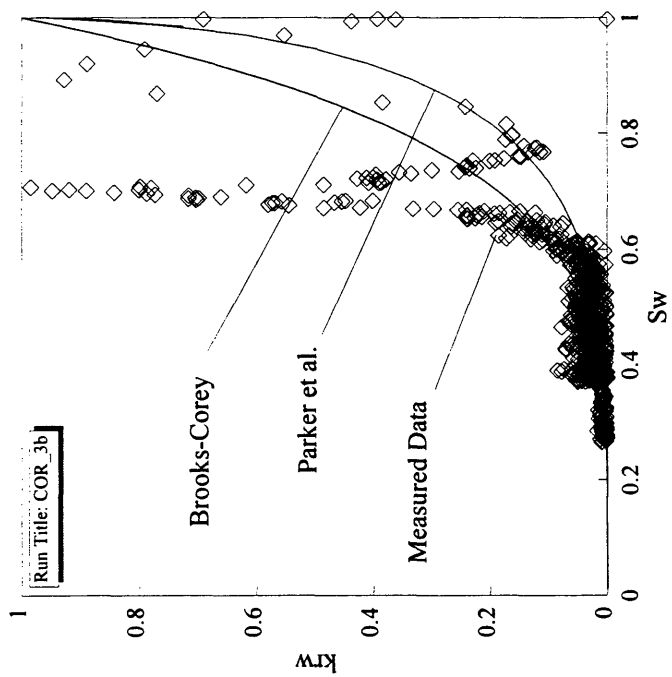
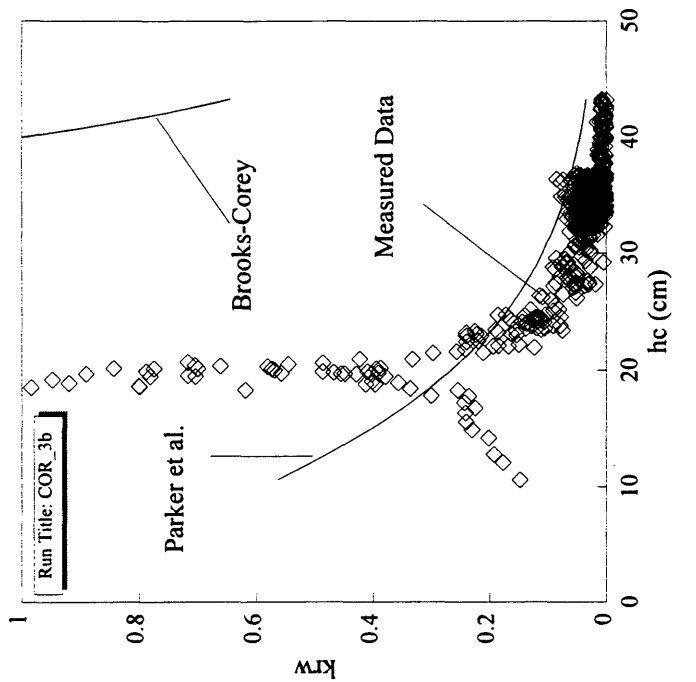


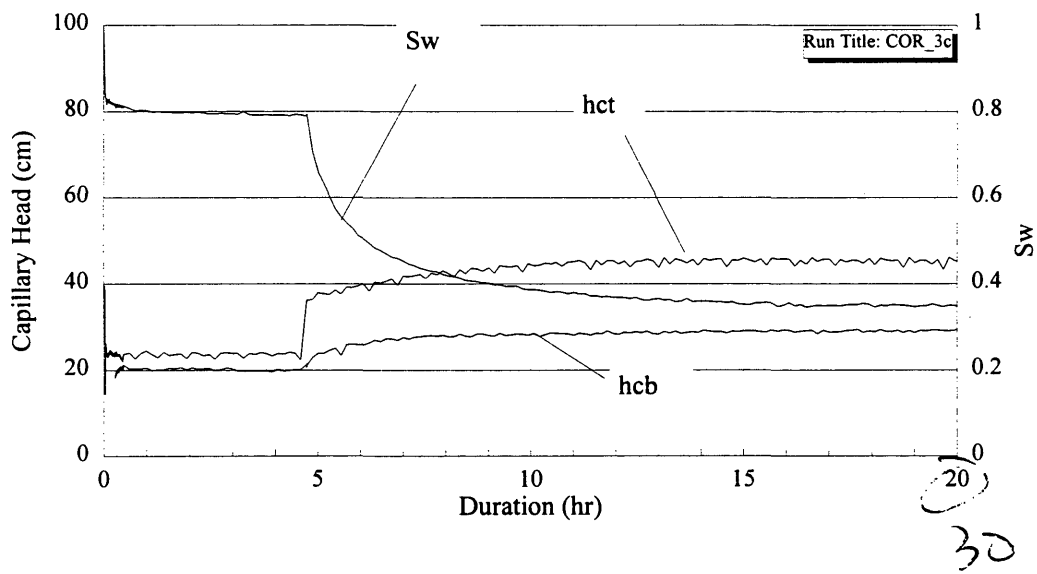
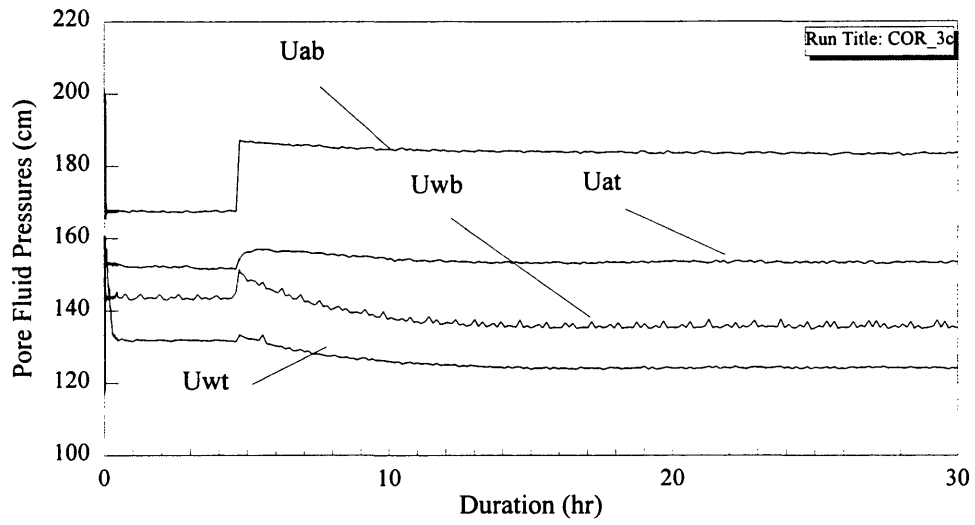


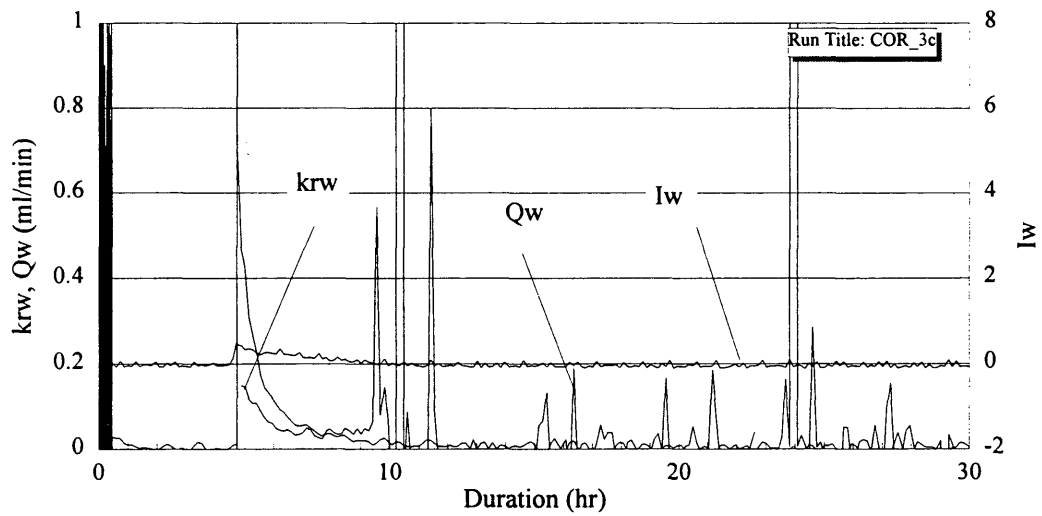
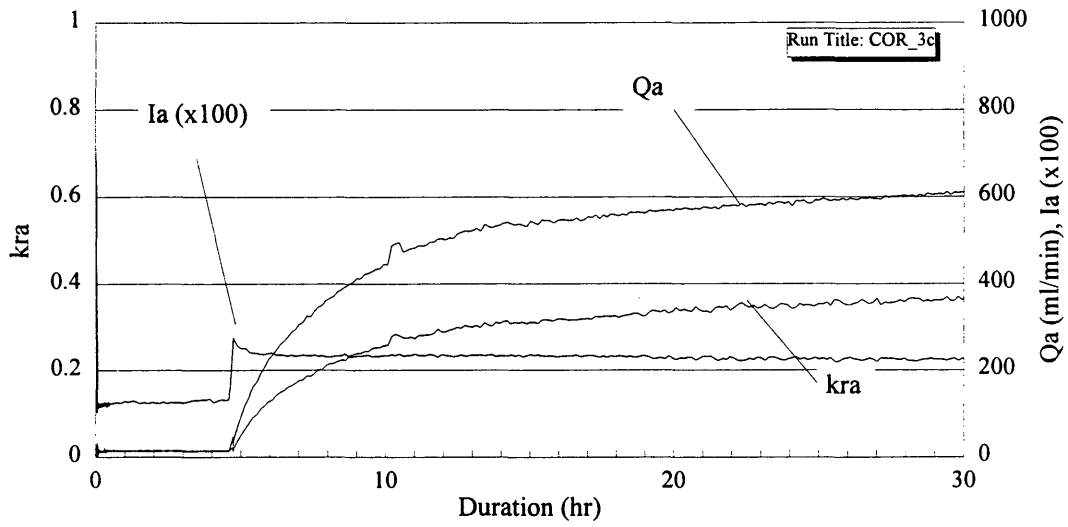


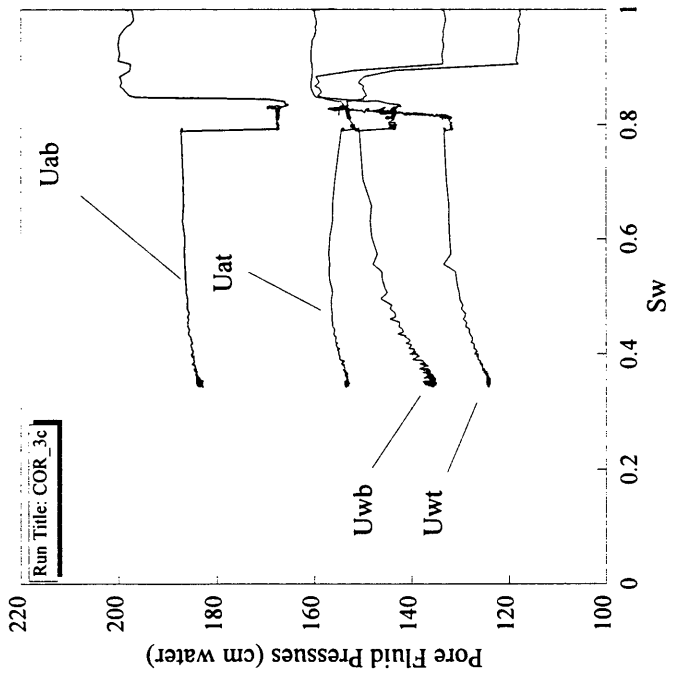
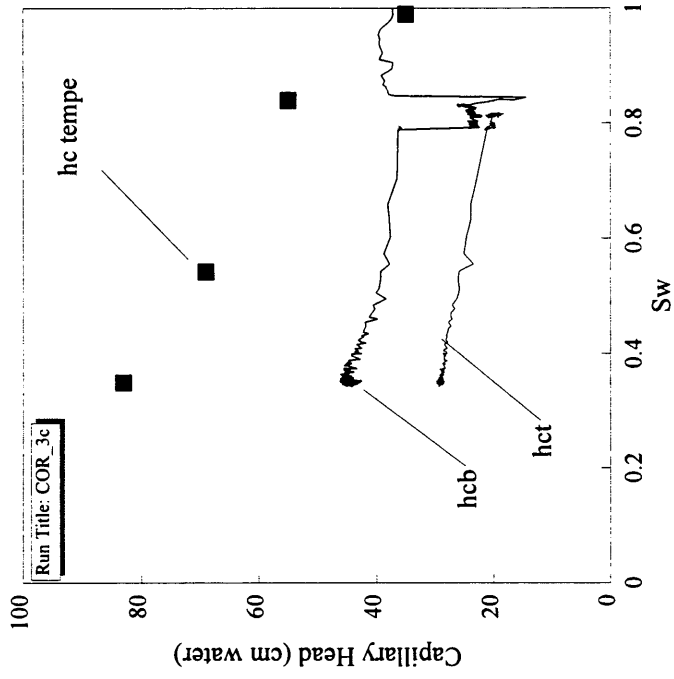


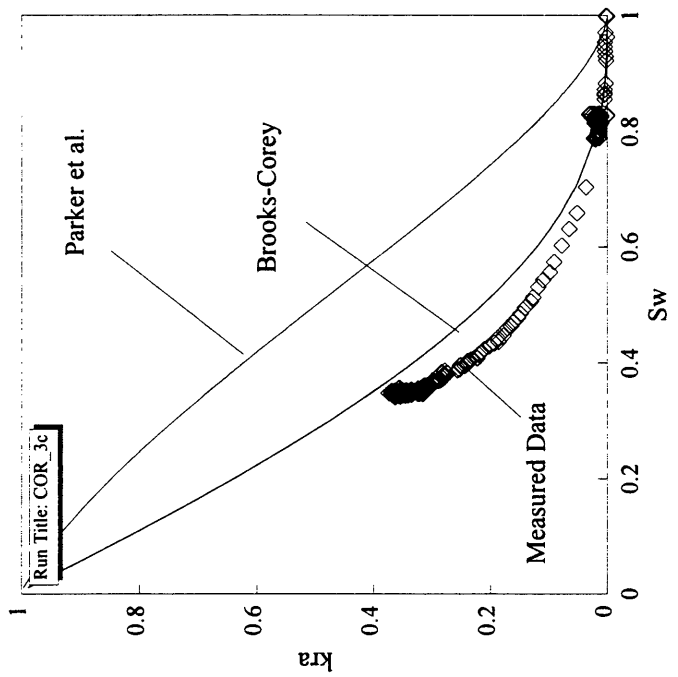
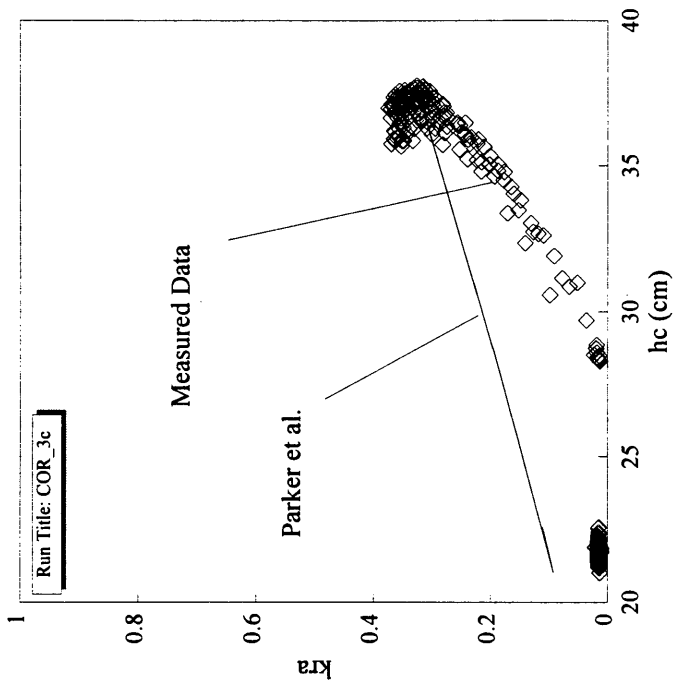


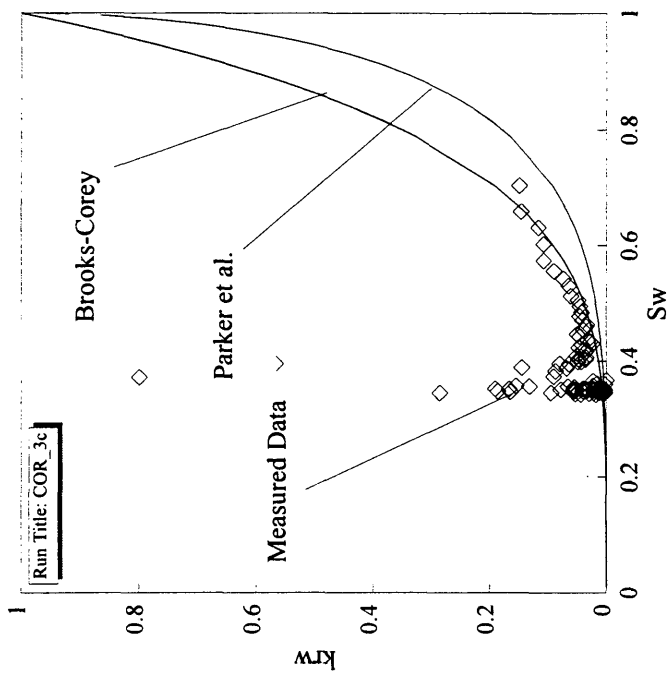
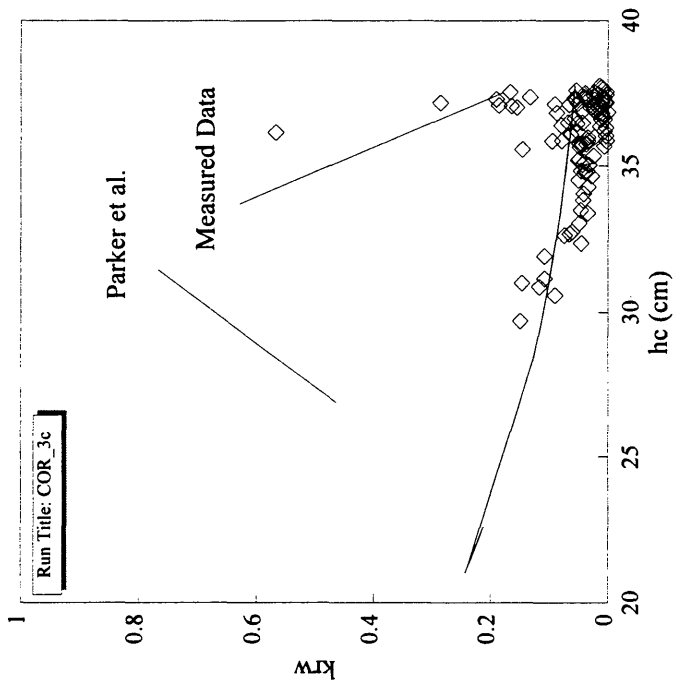


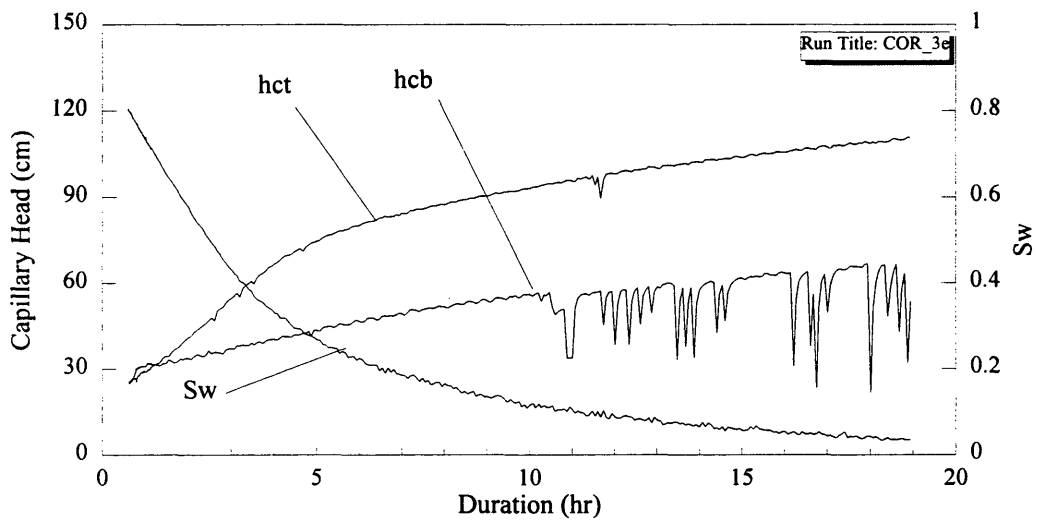
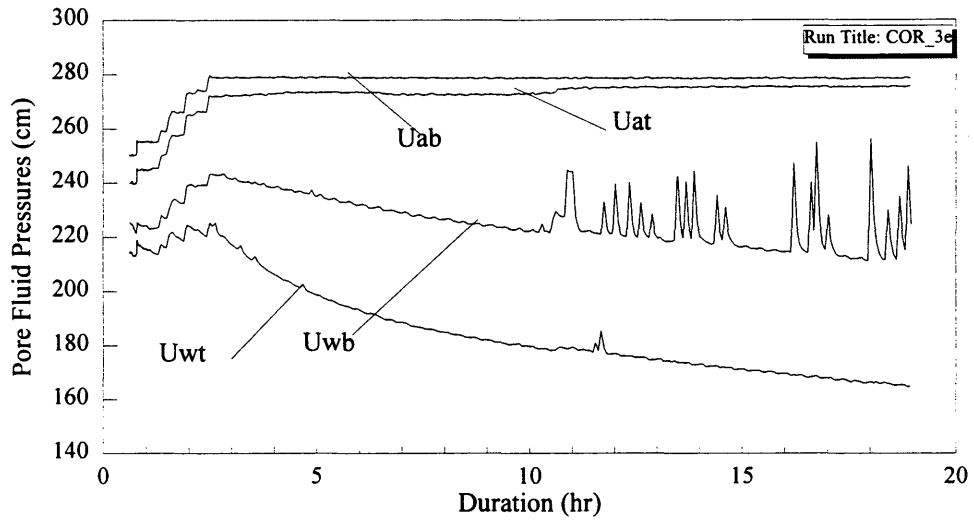


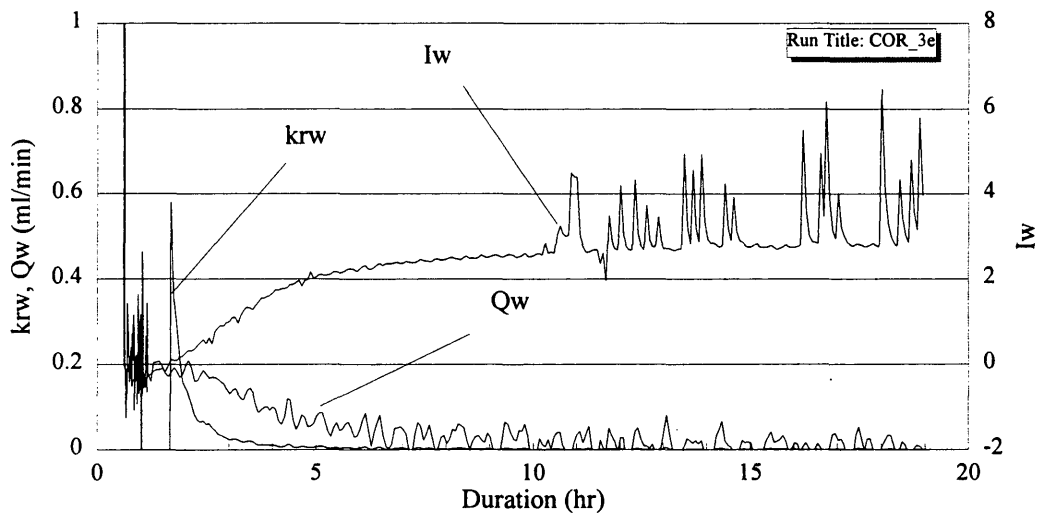
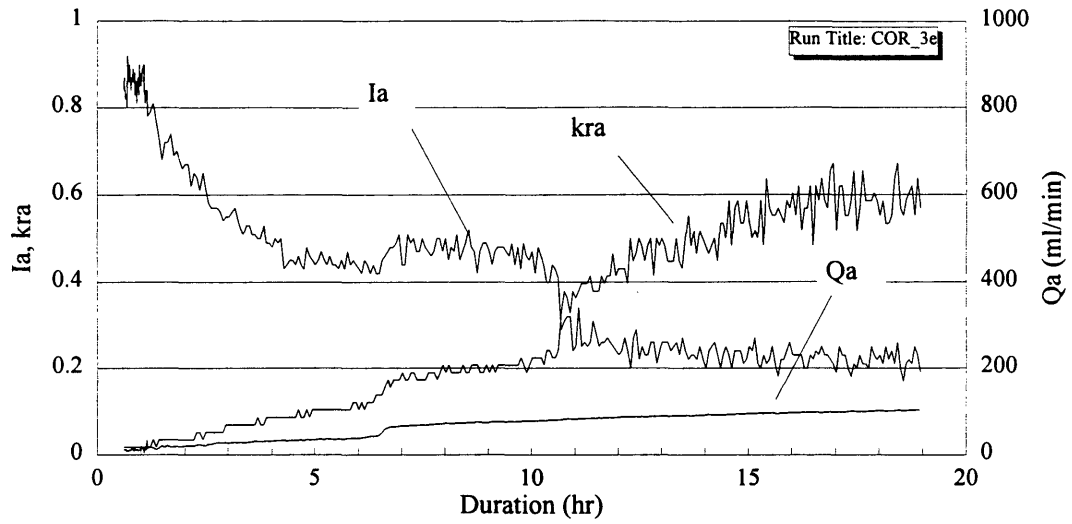


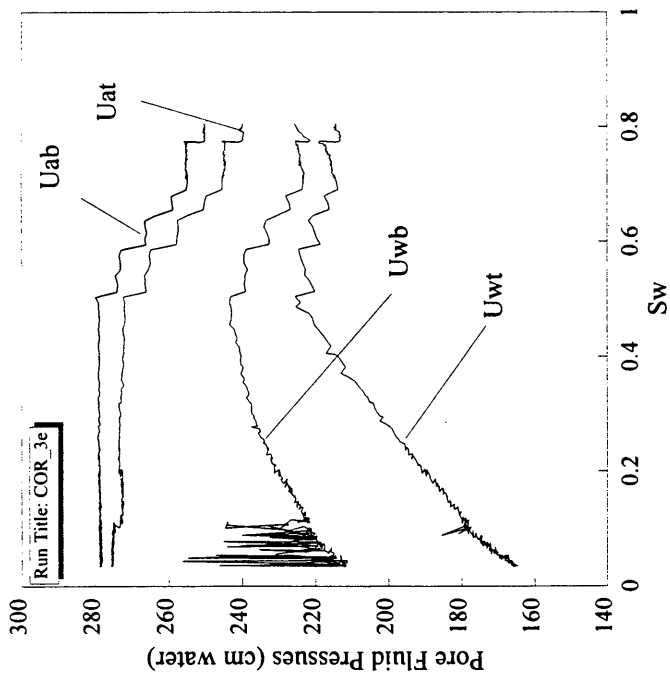
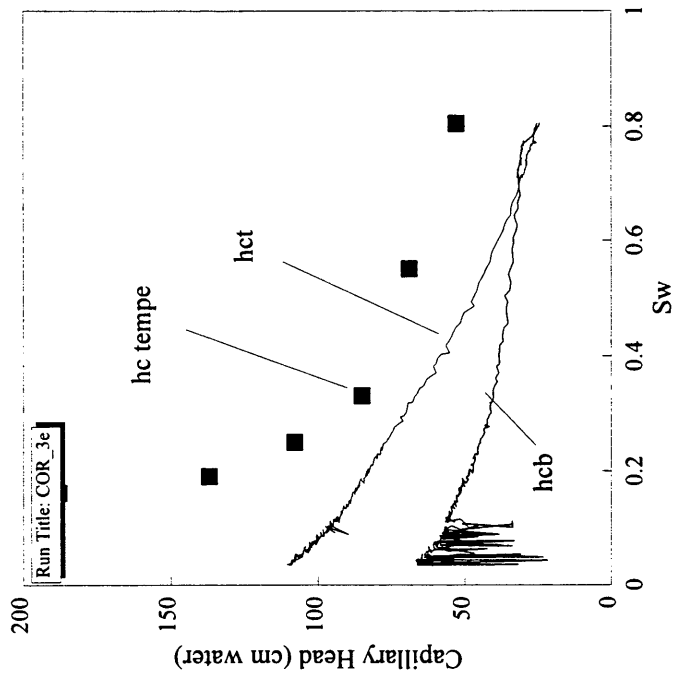


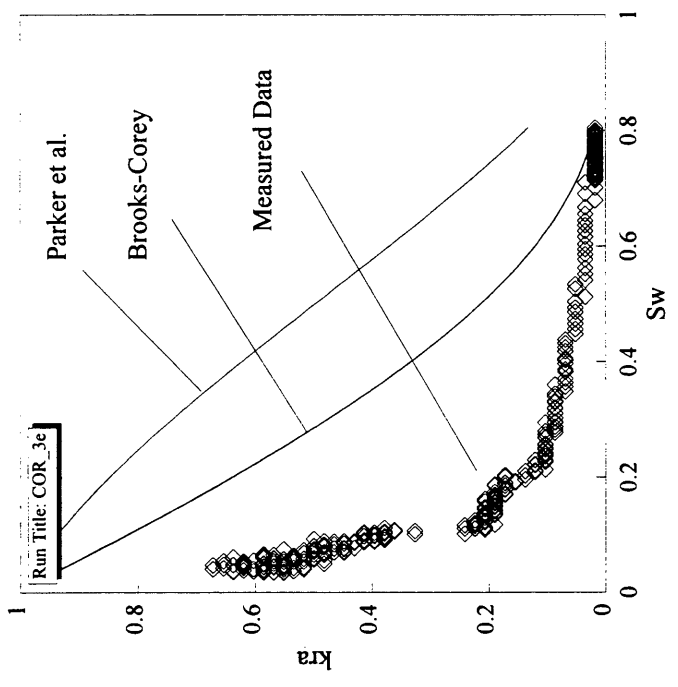
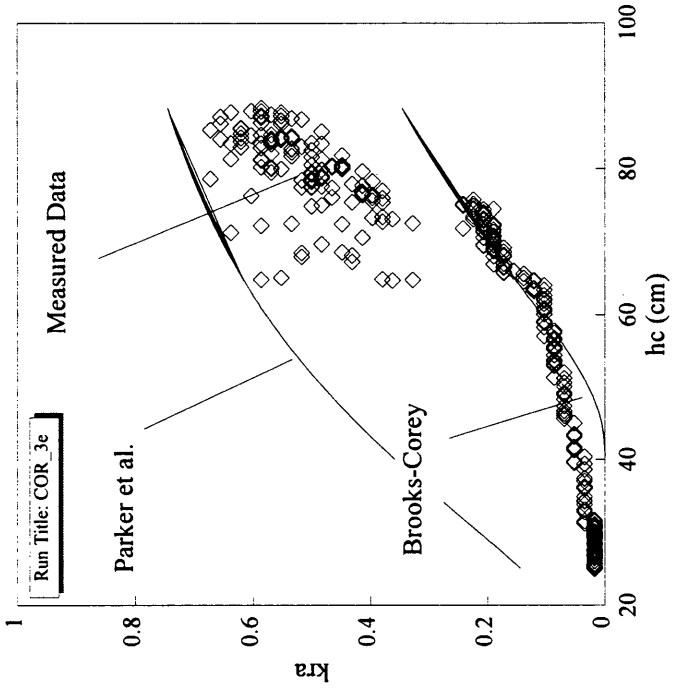


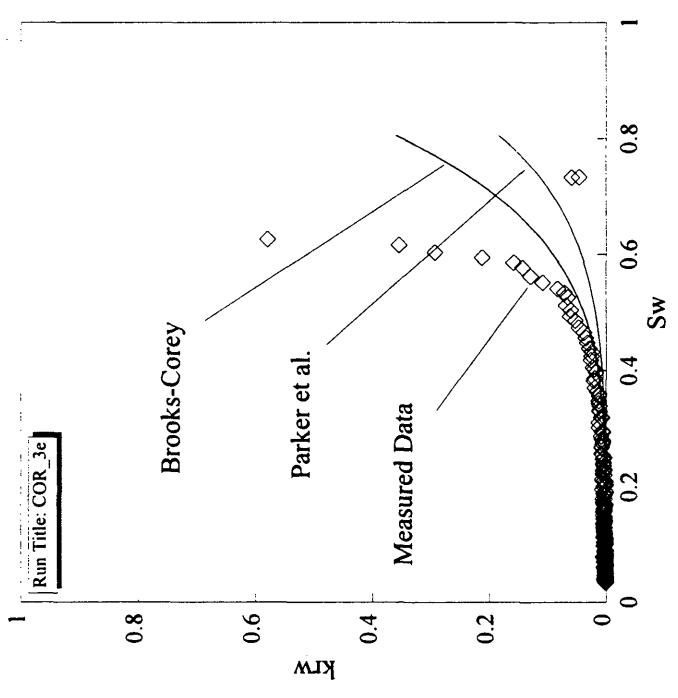
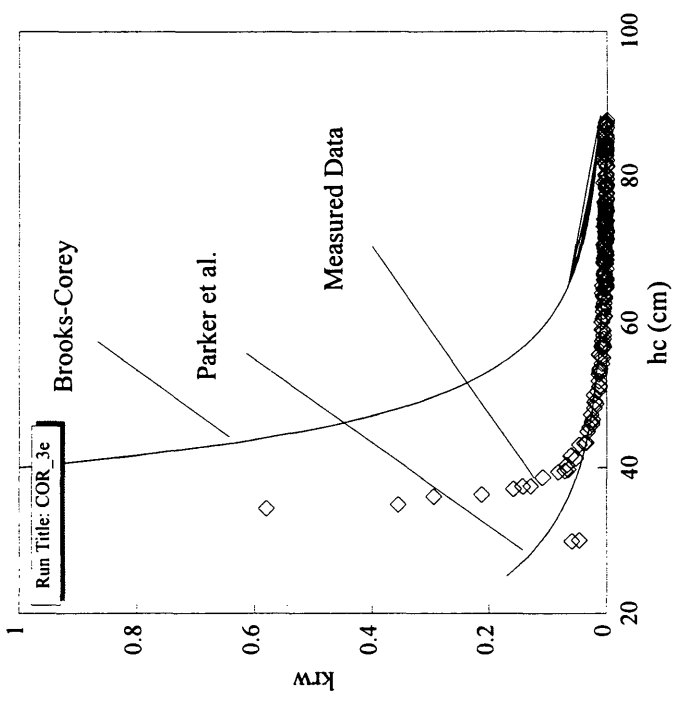






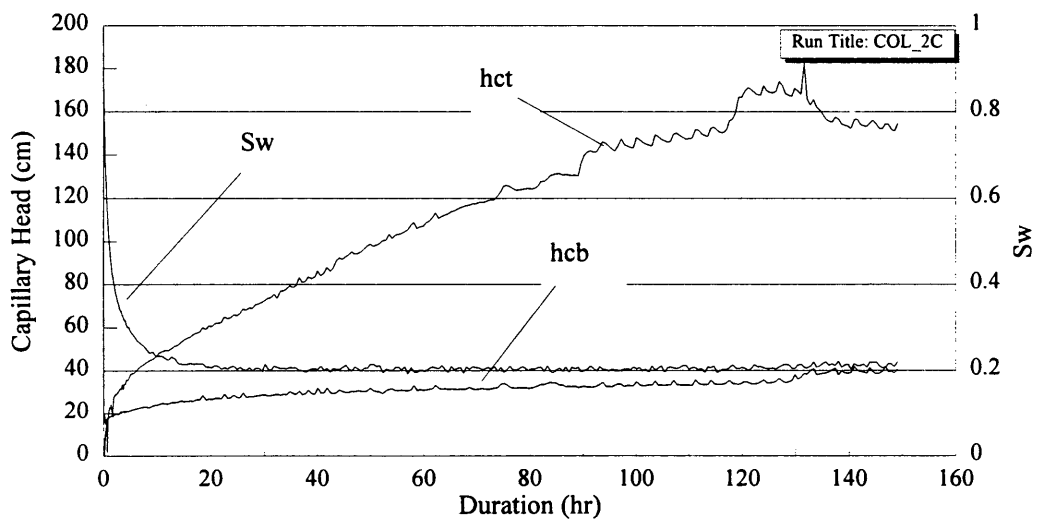
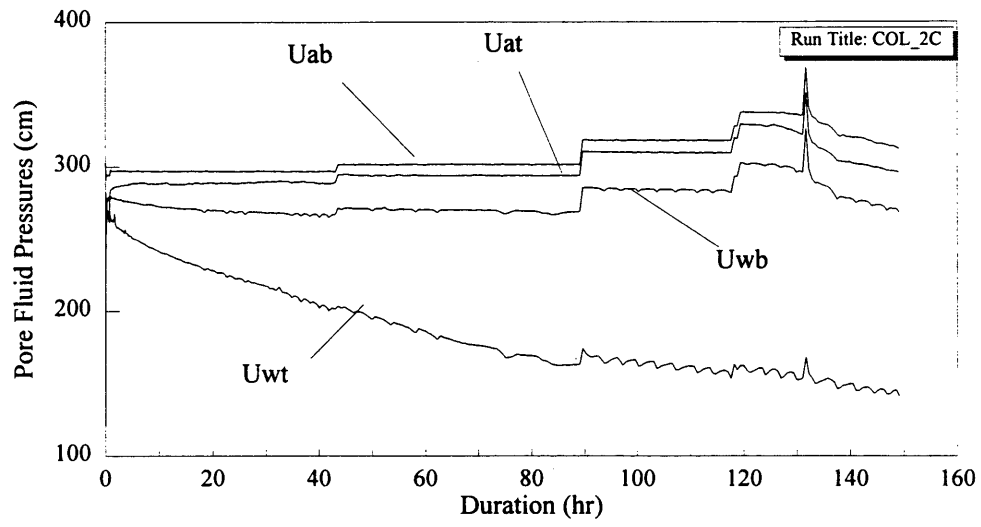


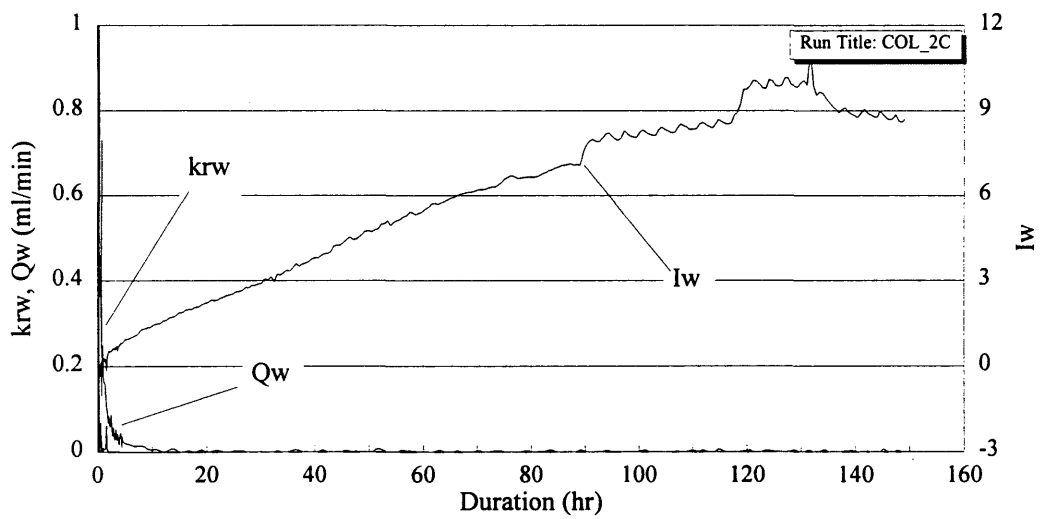
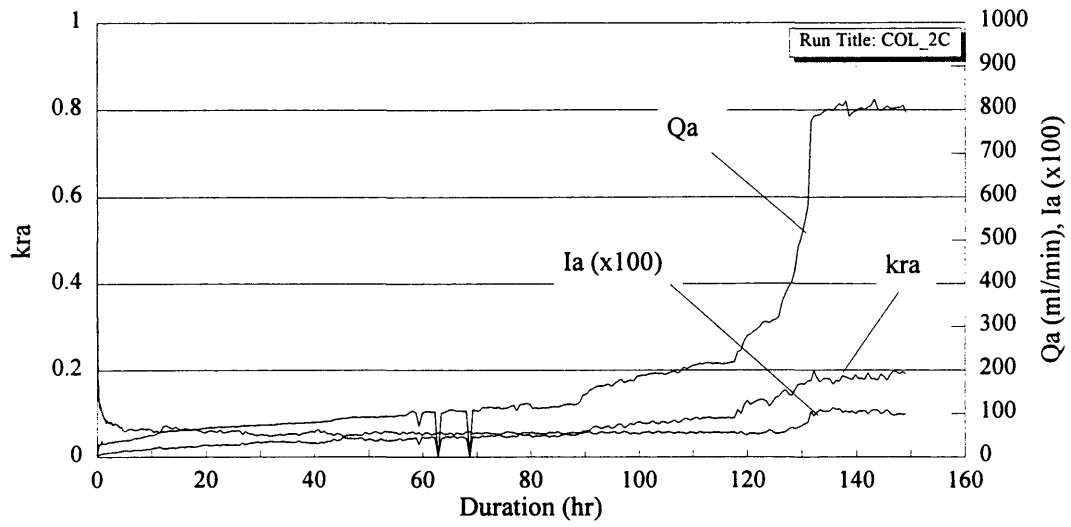


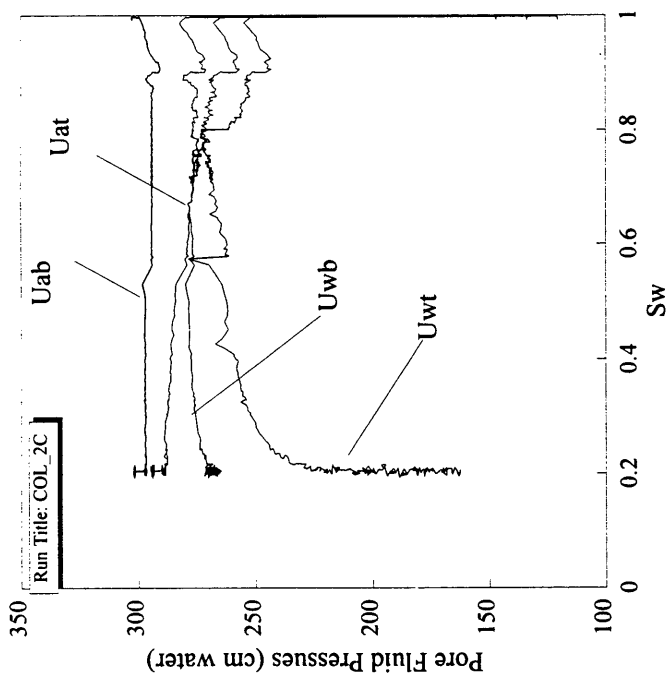
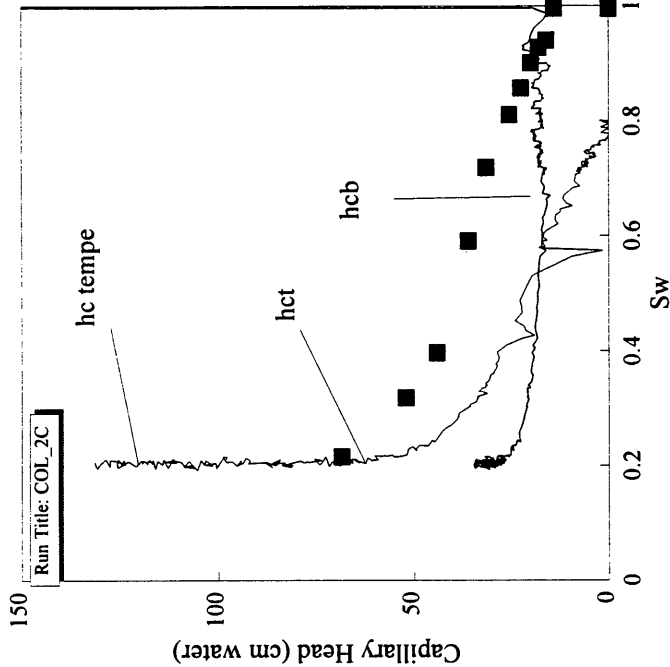


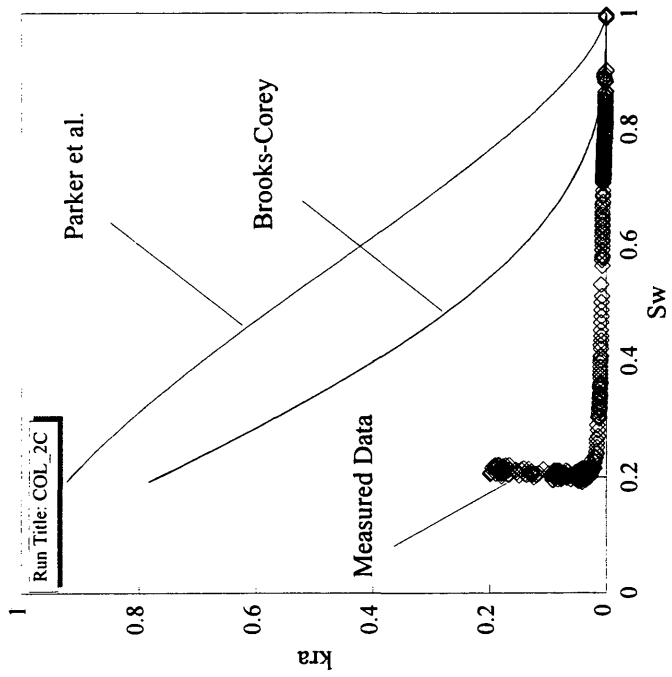
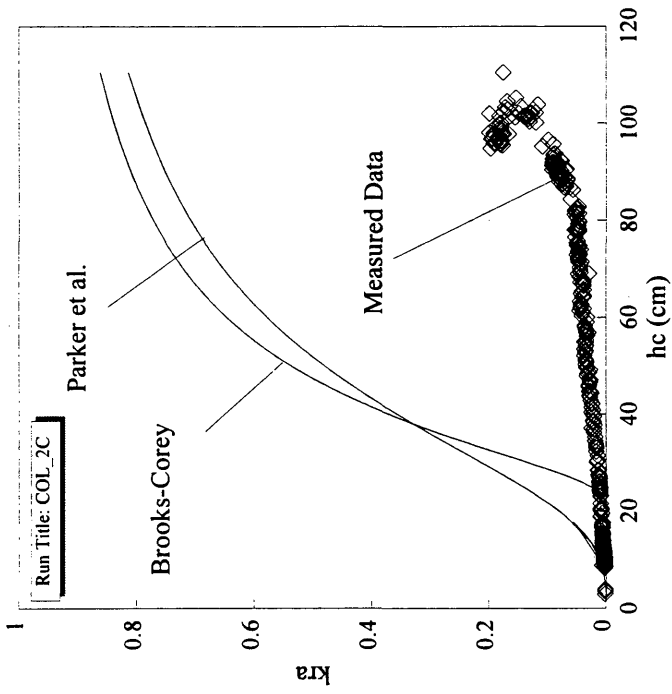
APPENDIX D3

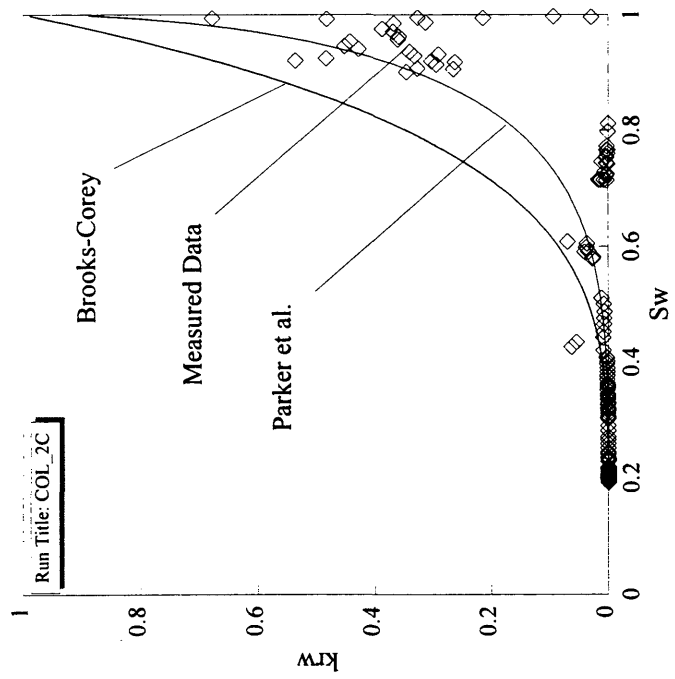
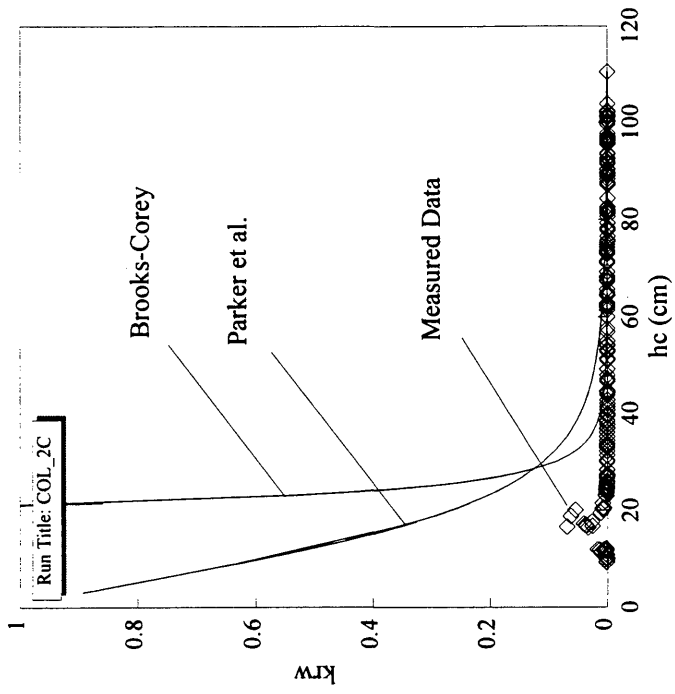
Displacement Experiment Data
Sample COL

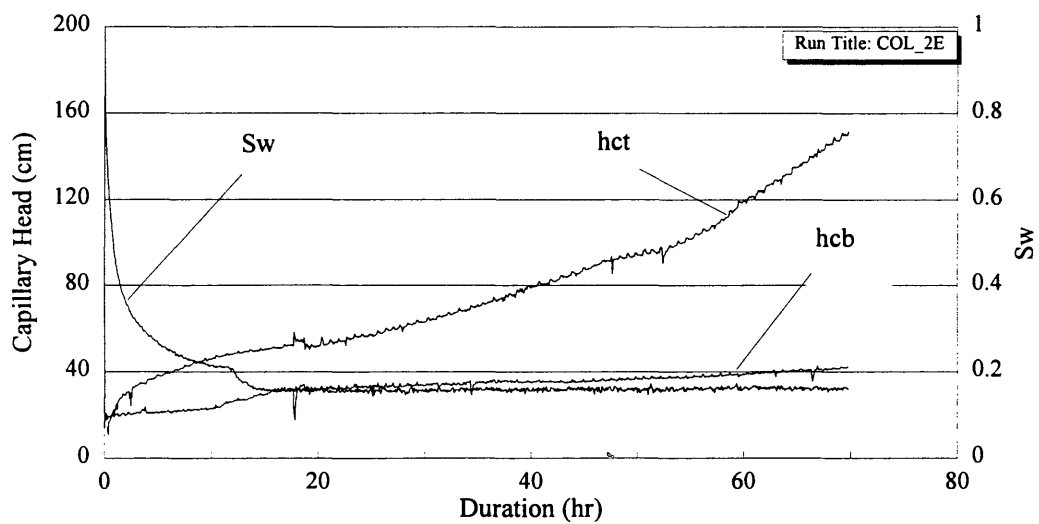
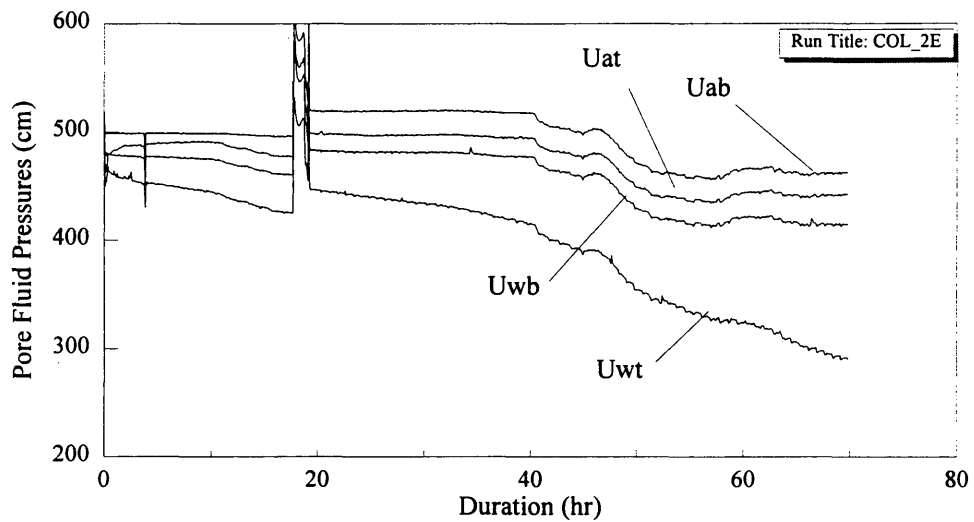


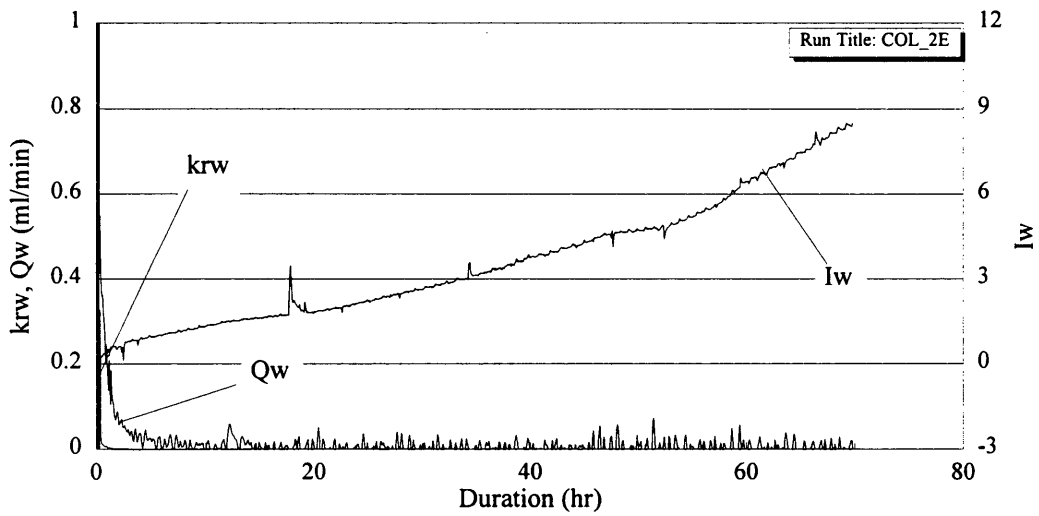
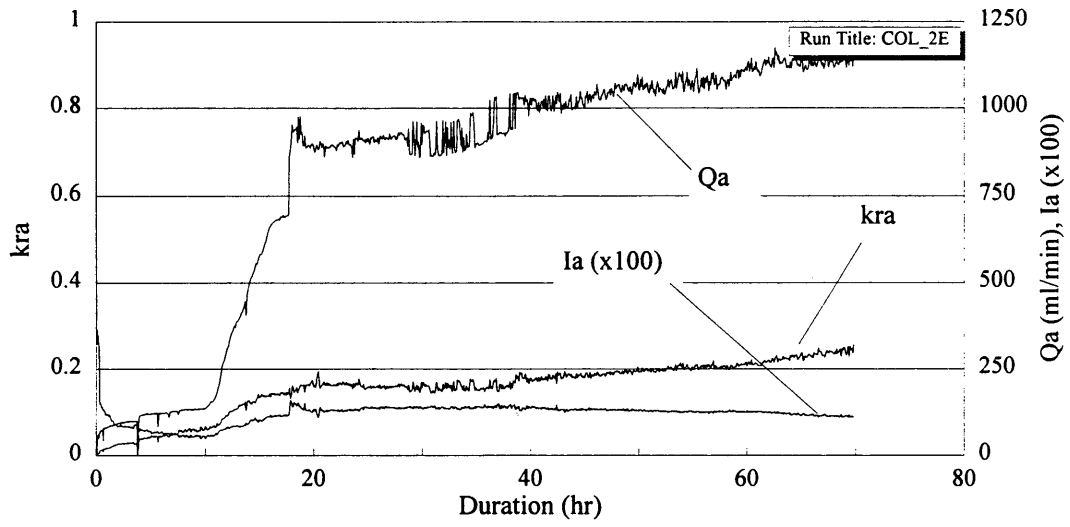


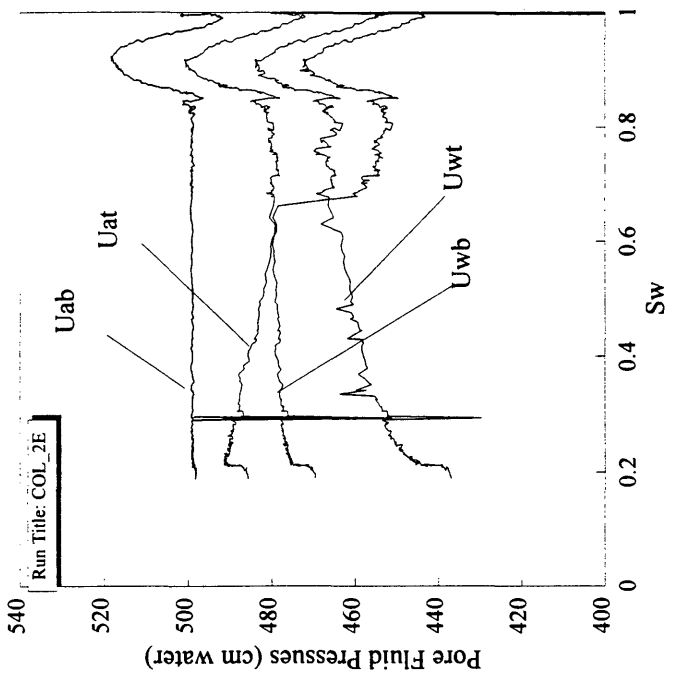
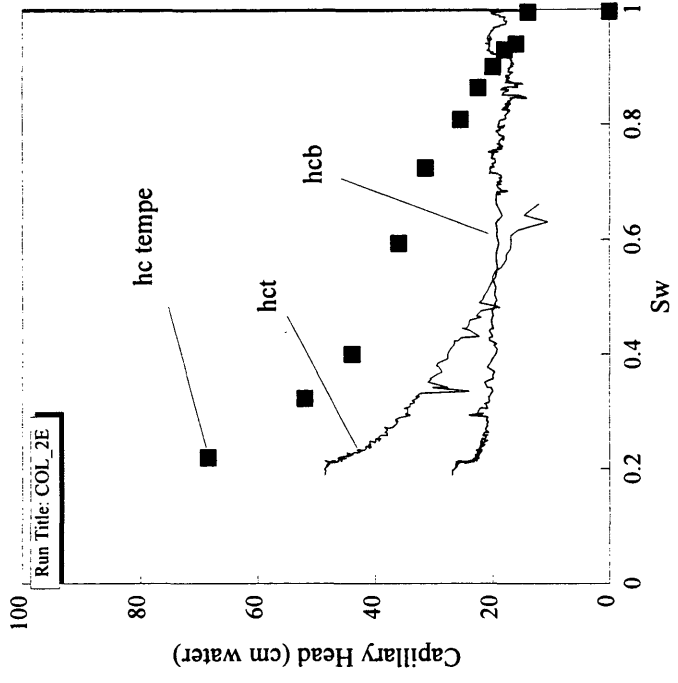


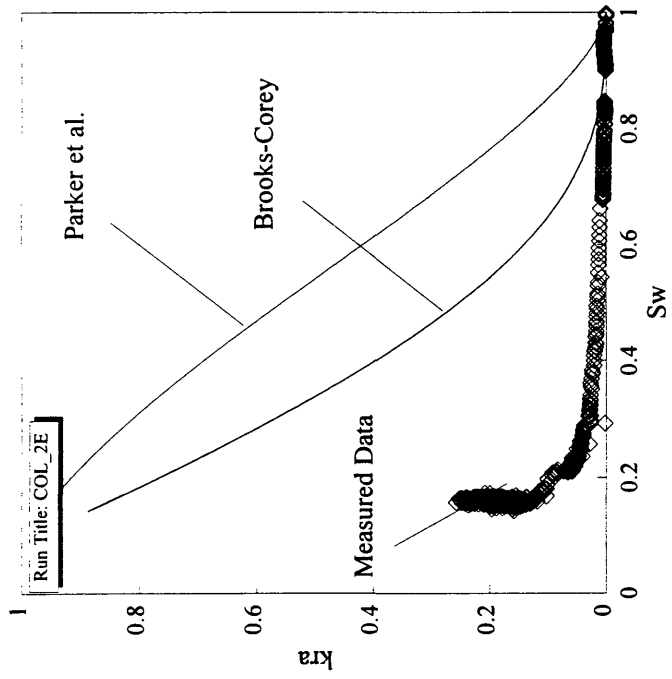
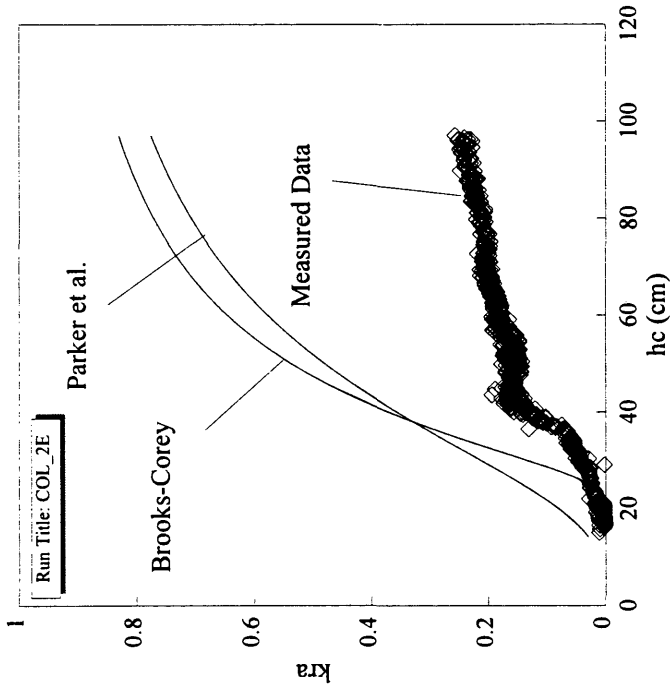


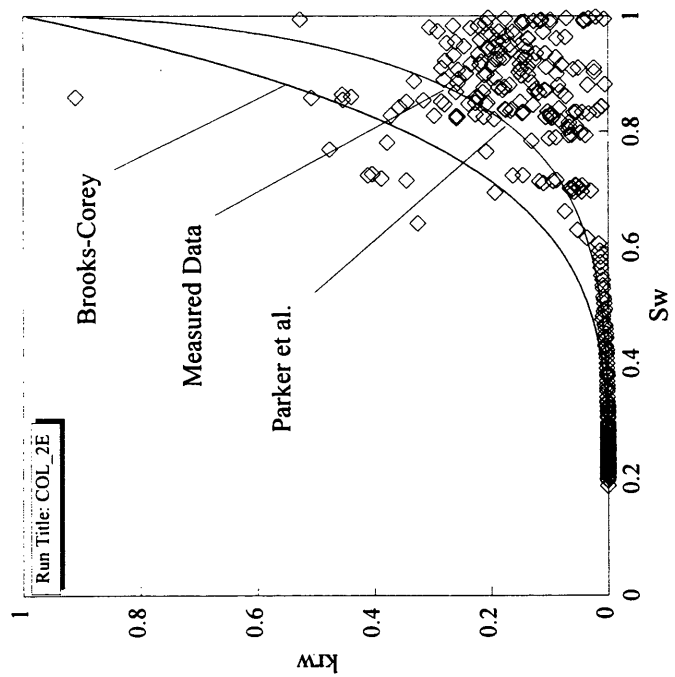
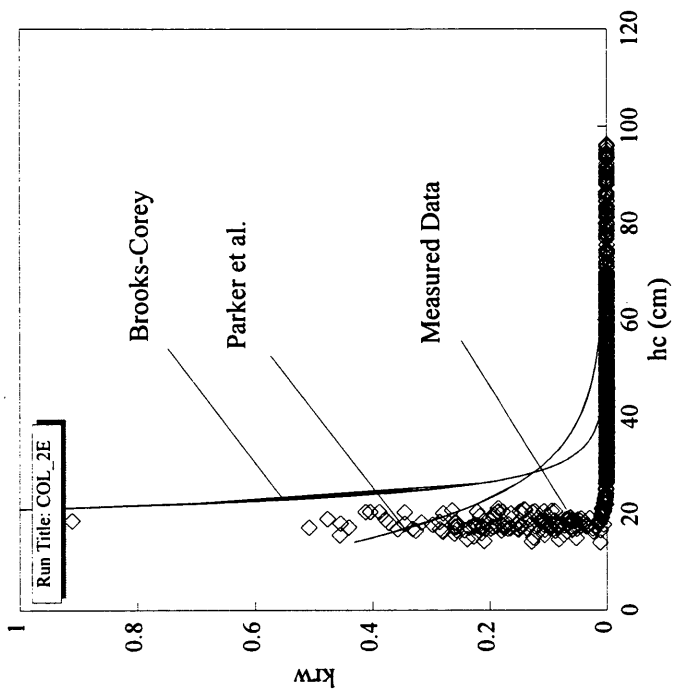


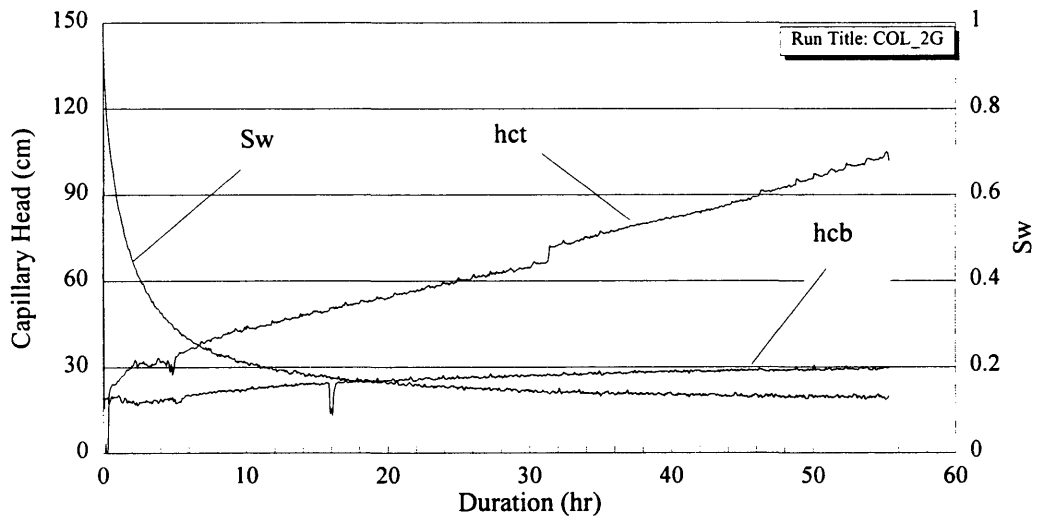
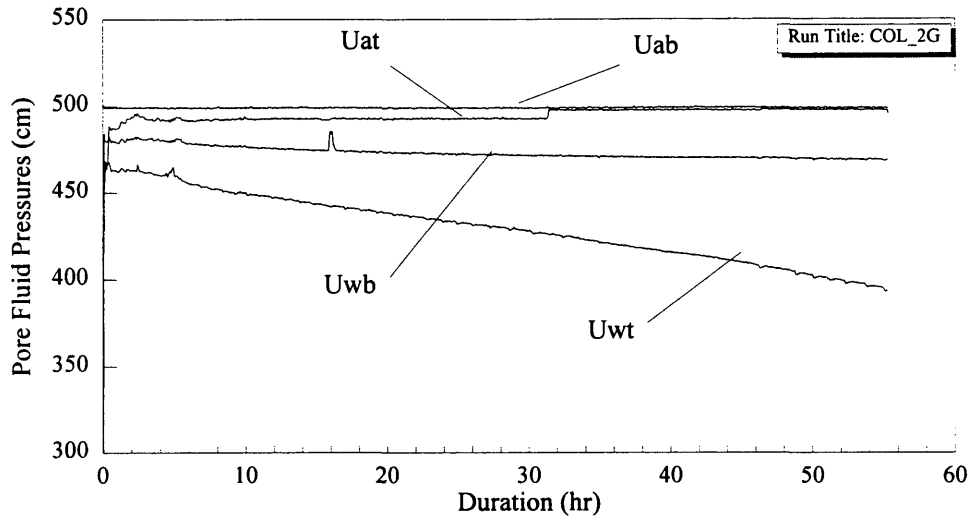


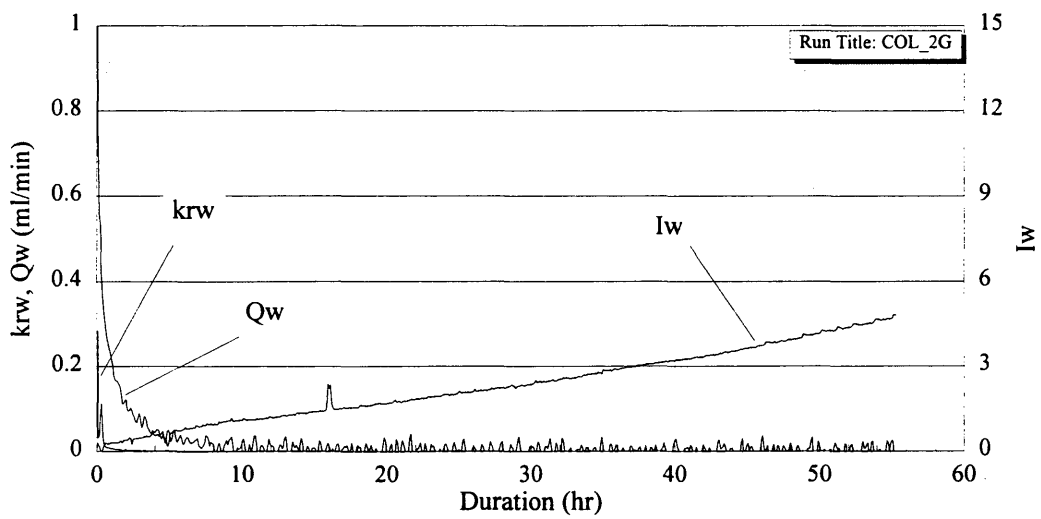
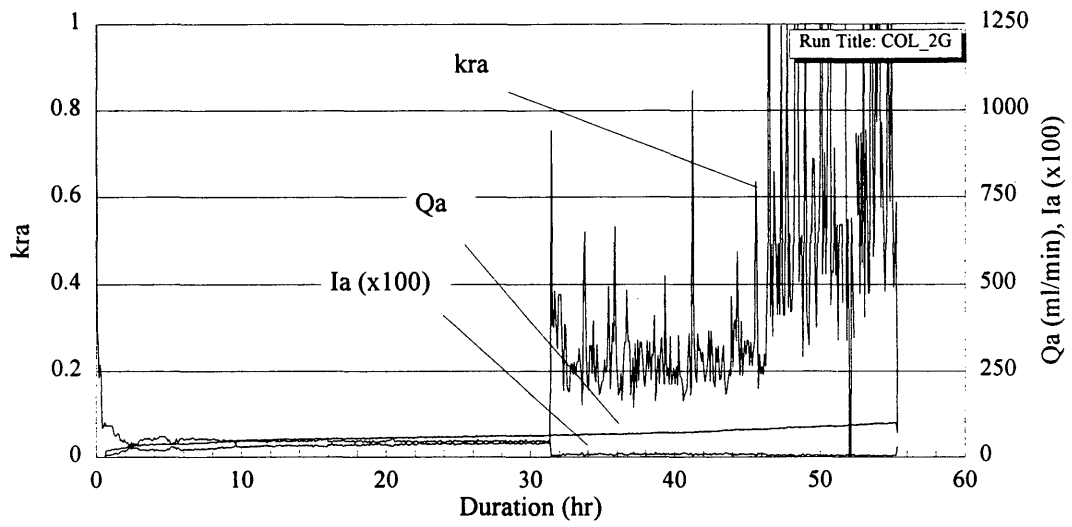


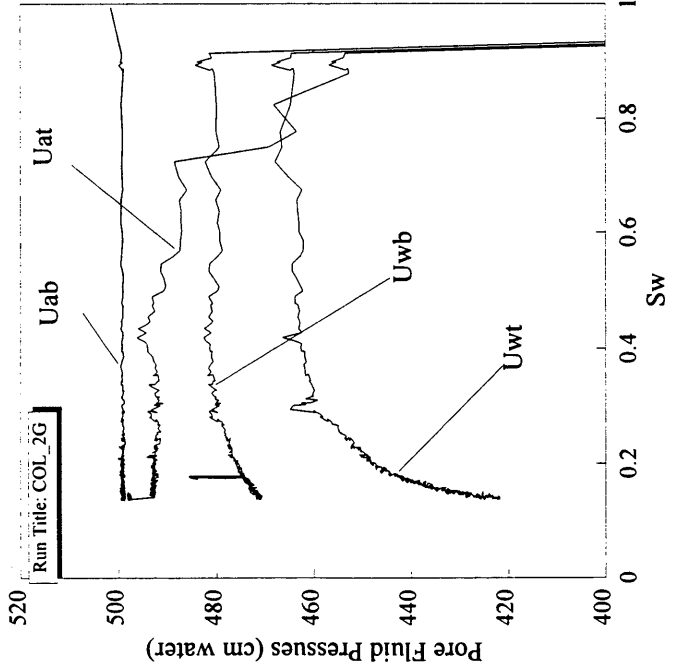
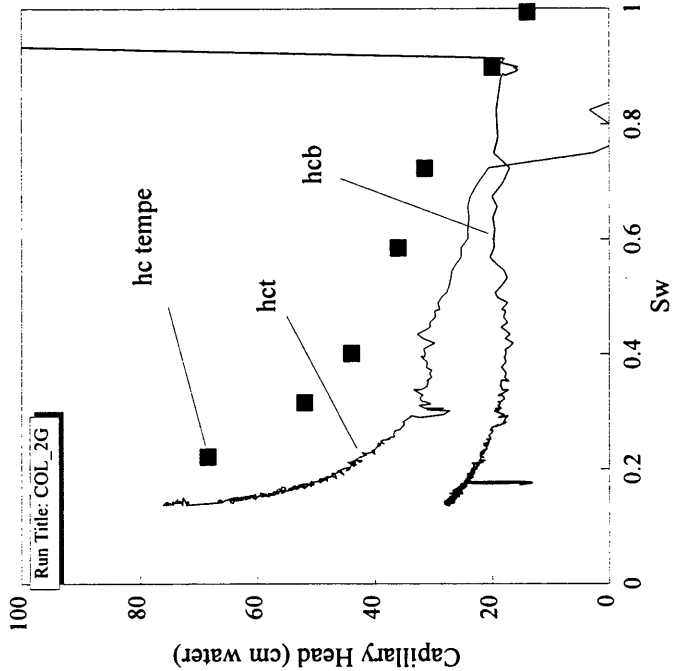


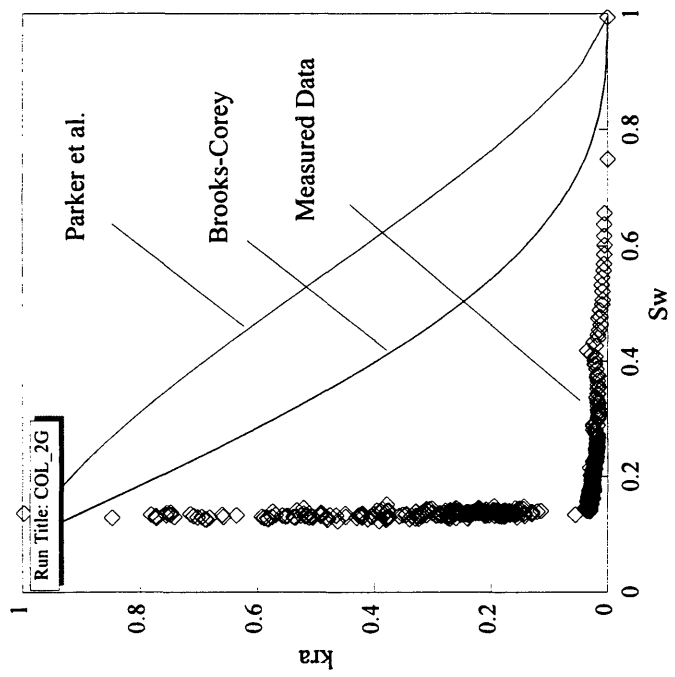
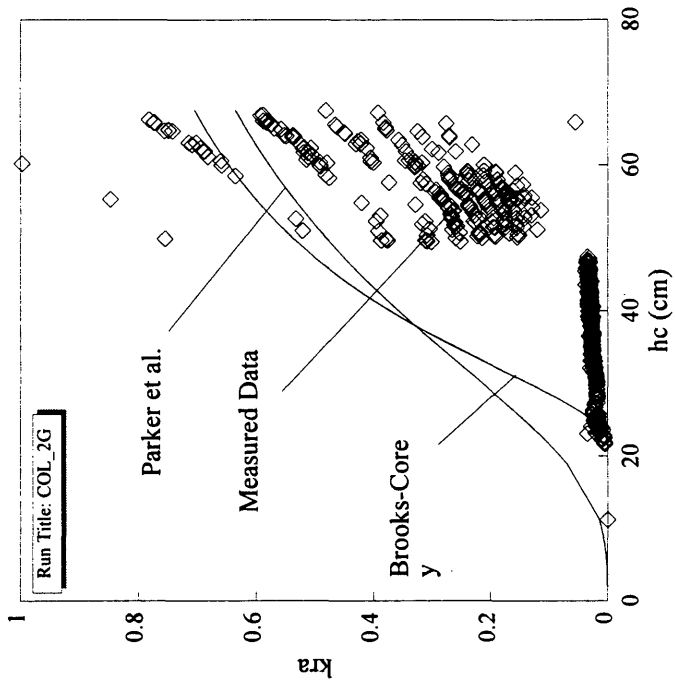


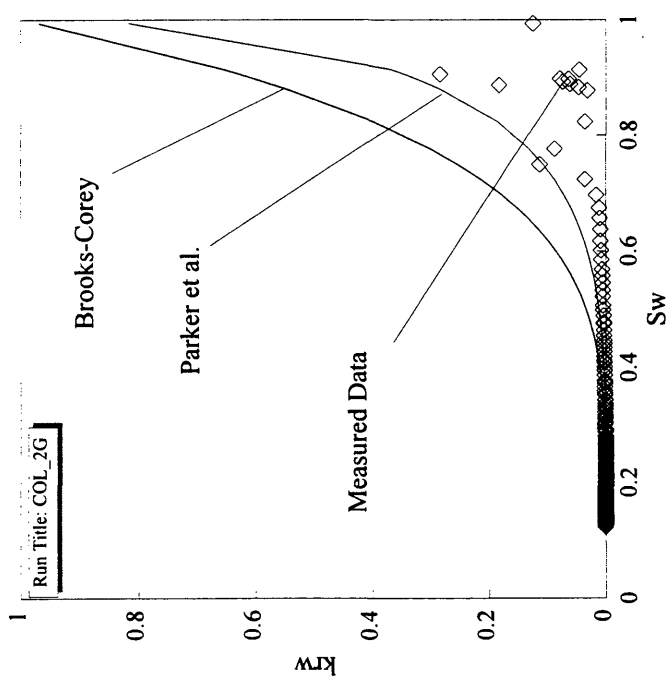
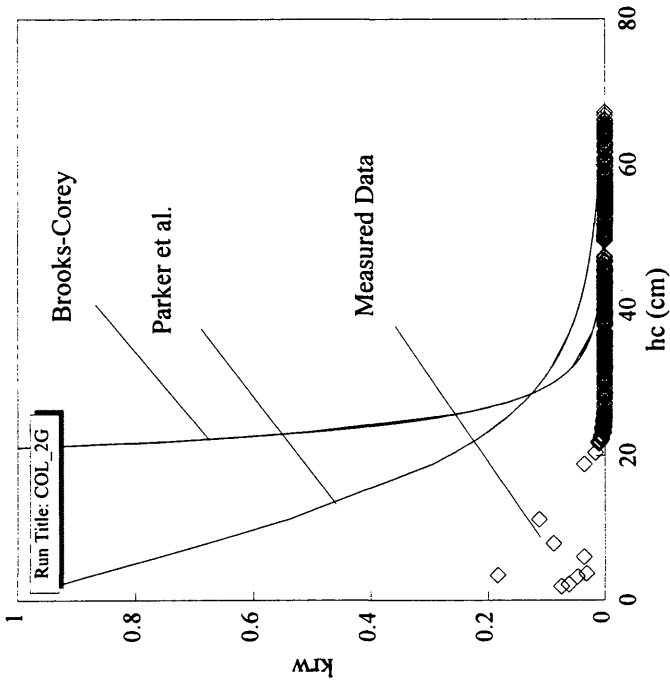


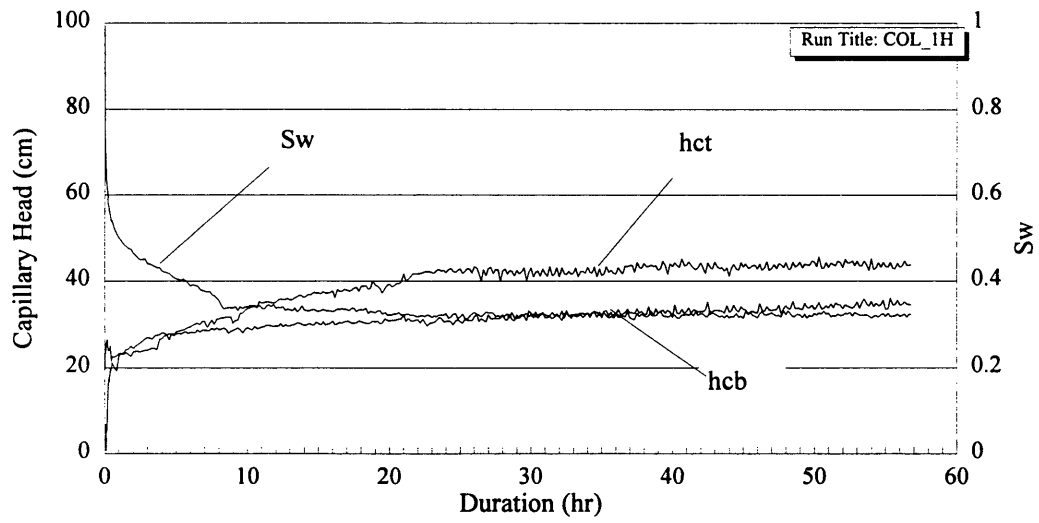
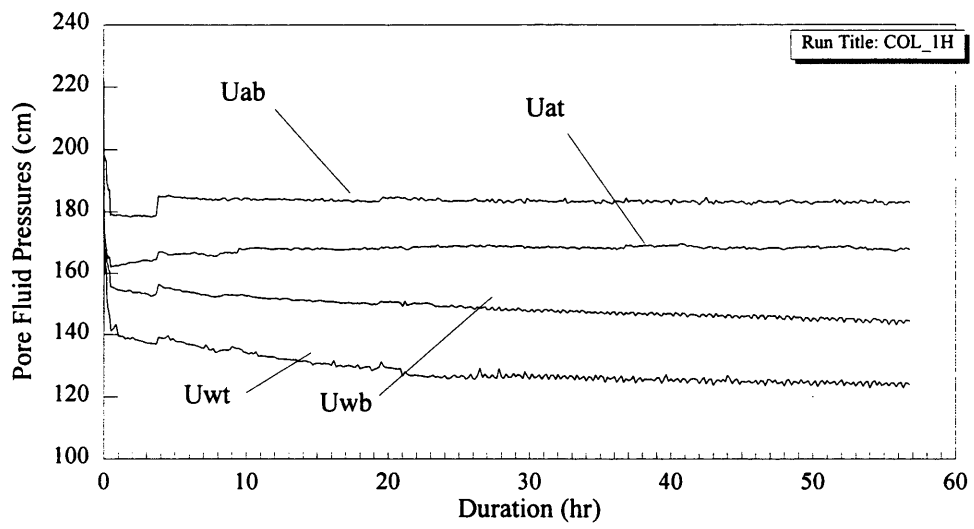


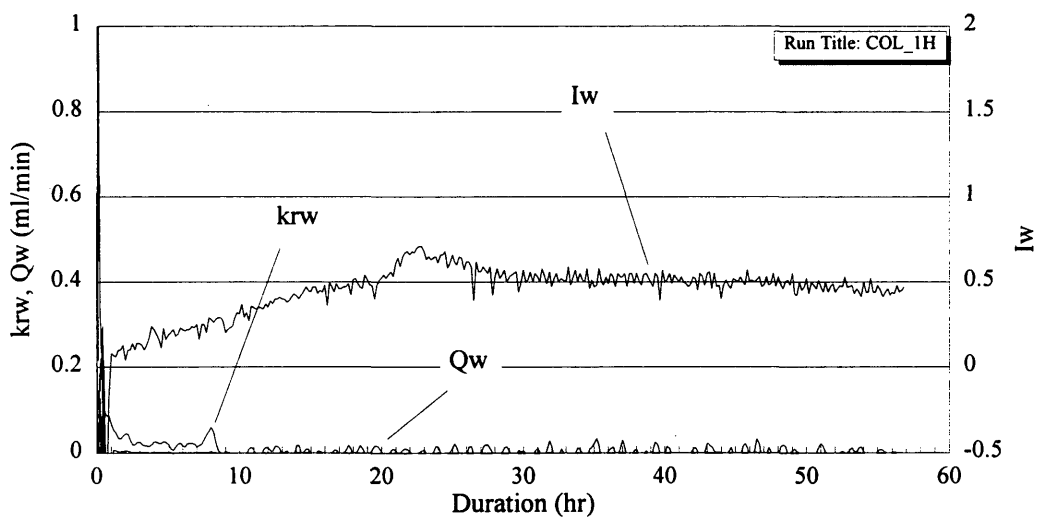
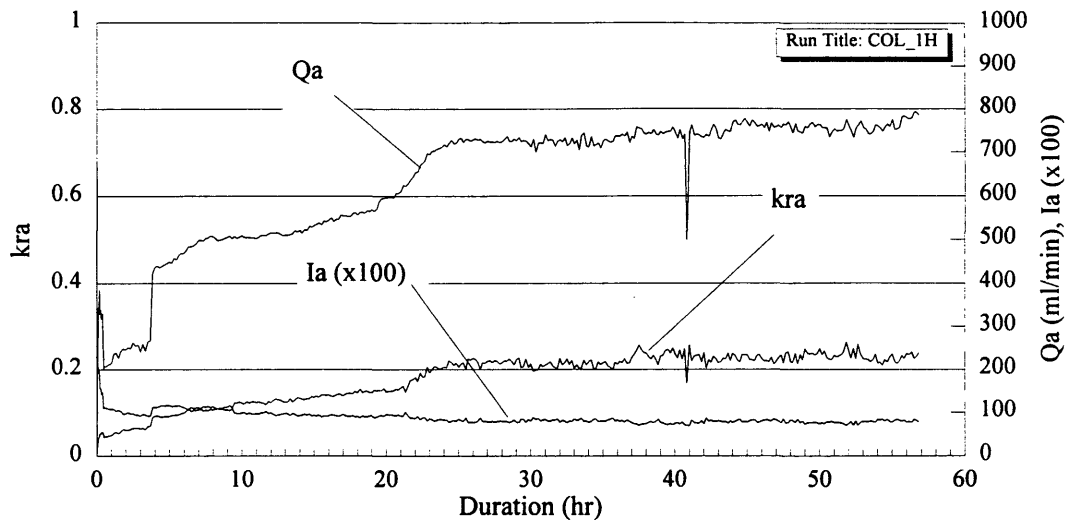


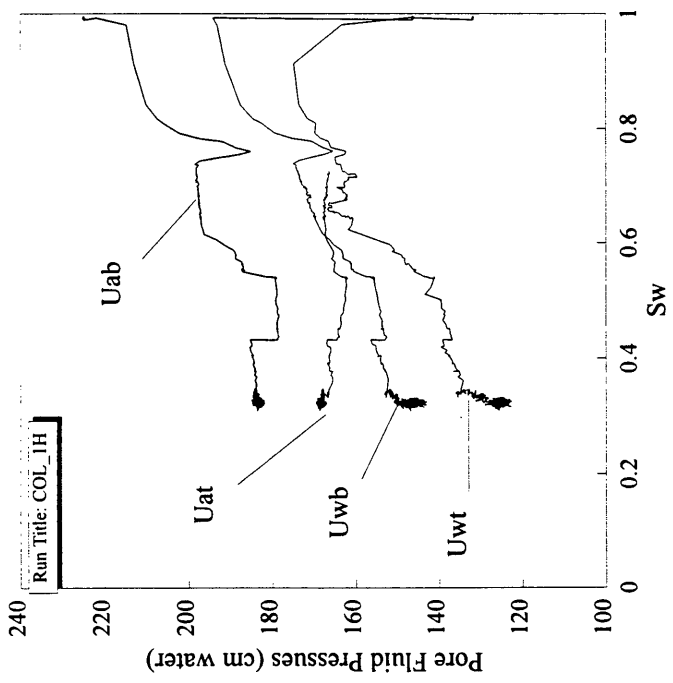
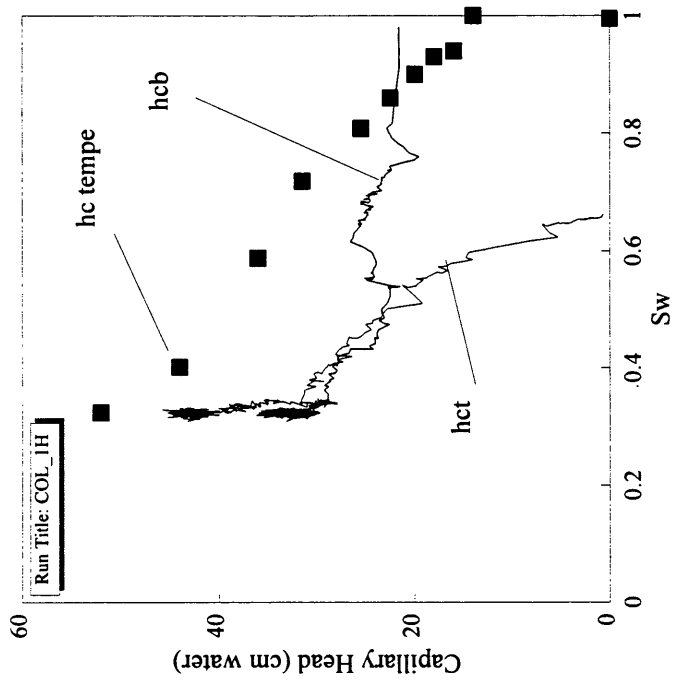


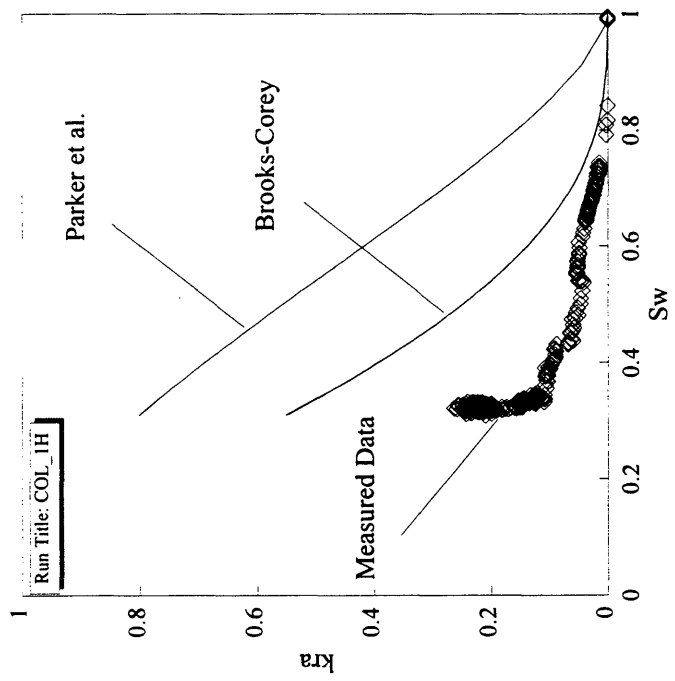
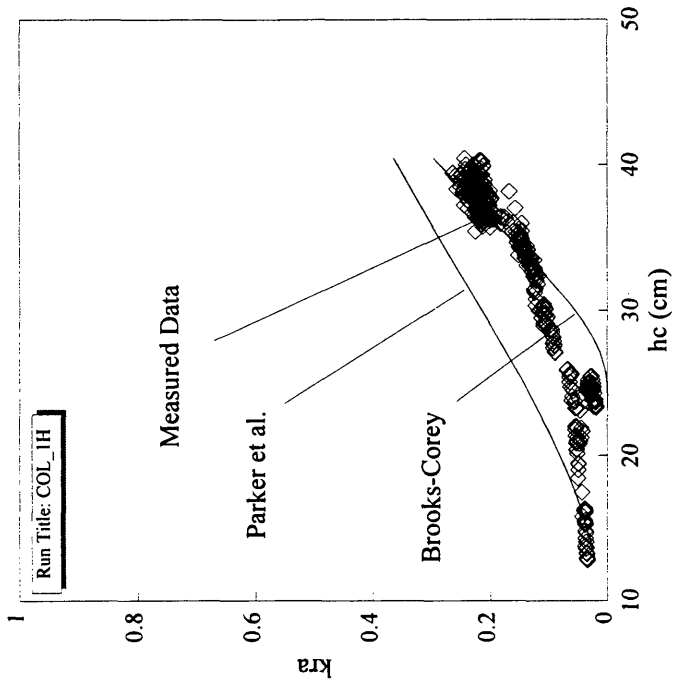


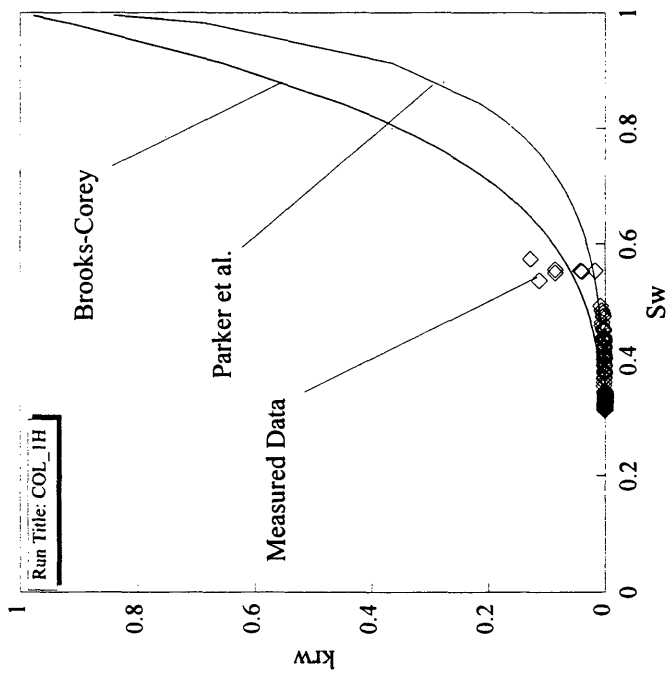
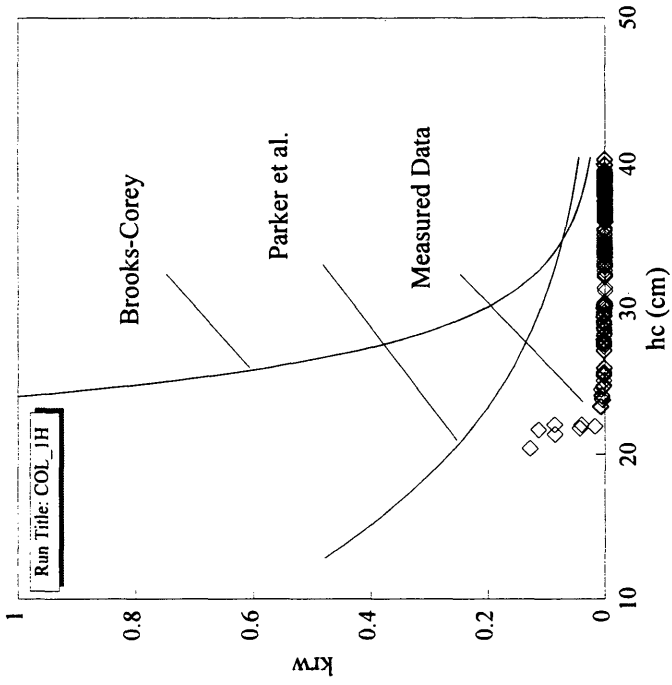


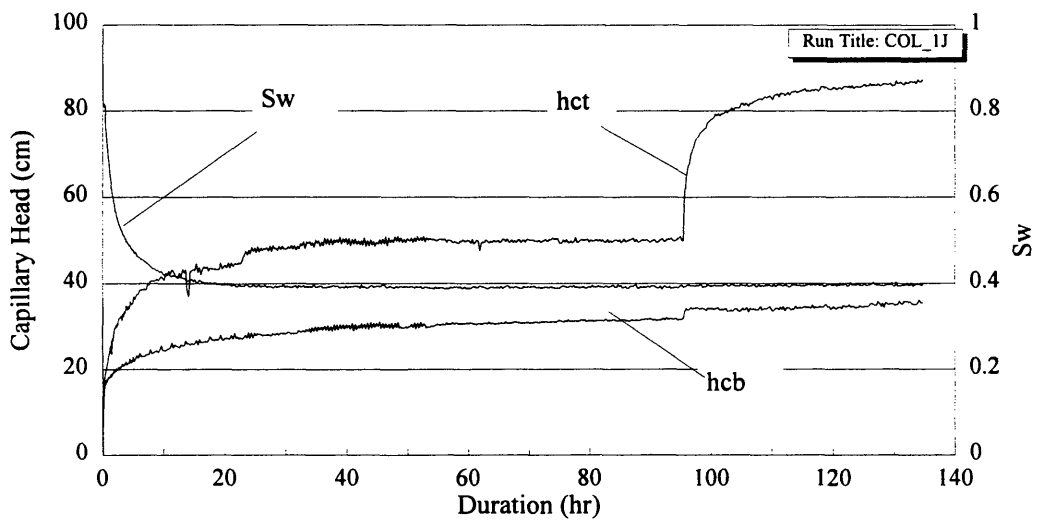
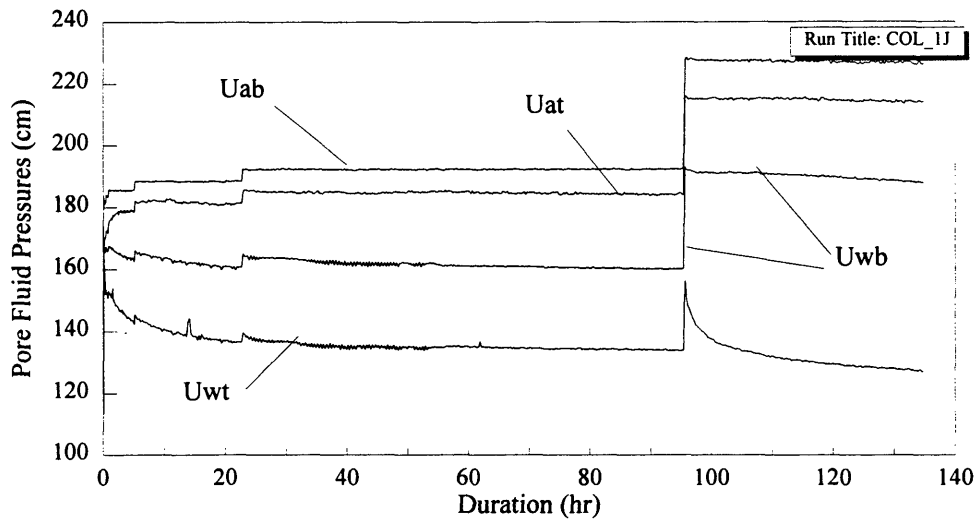


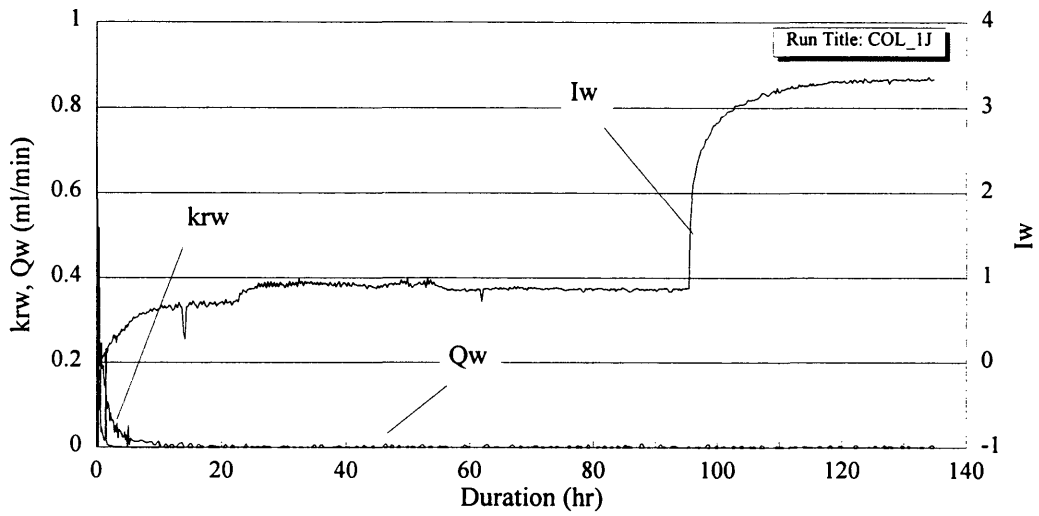
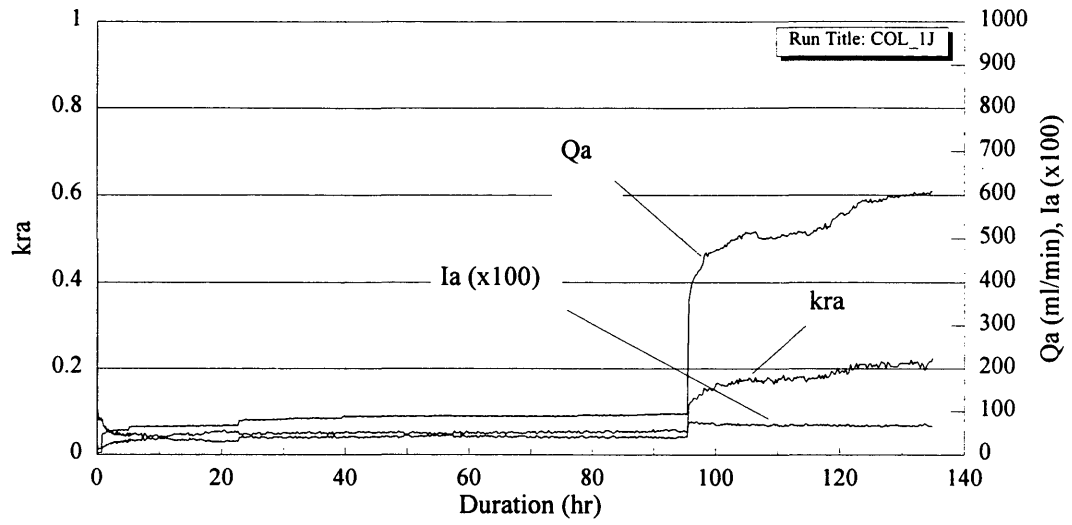


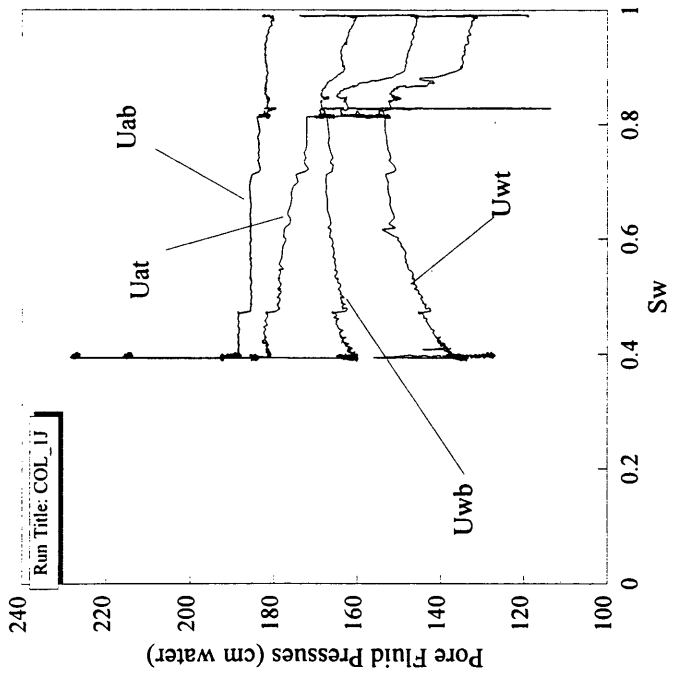
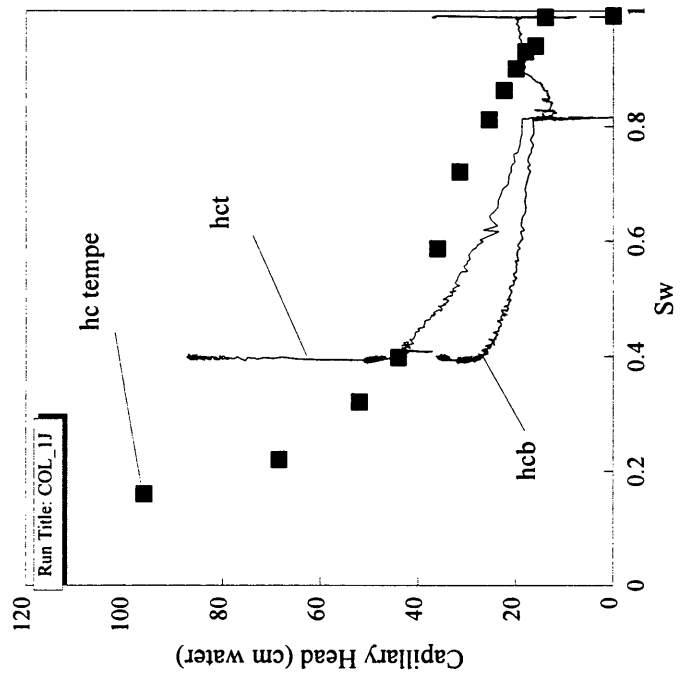


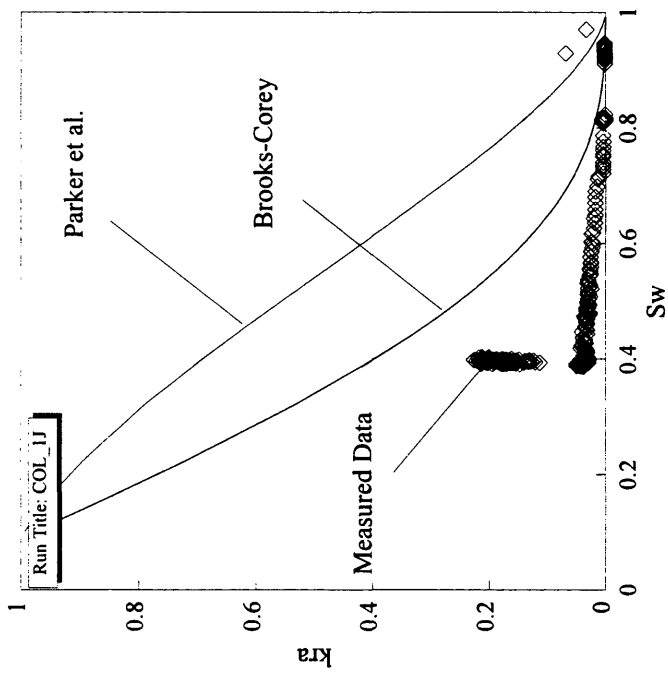
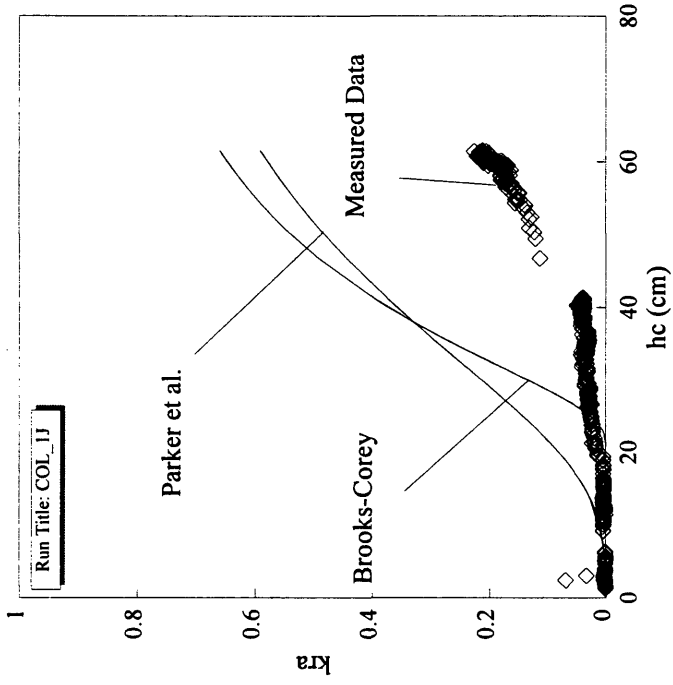


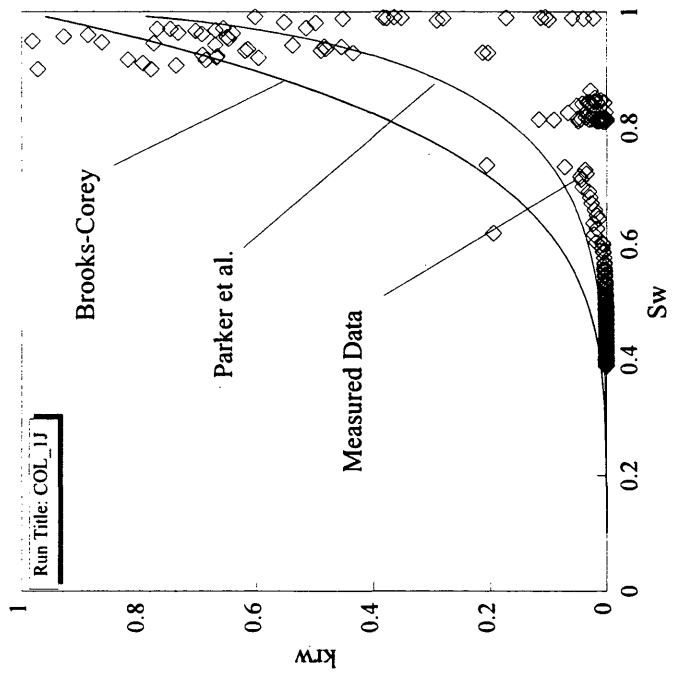
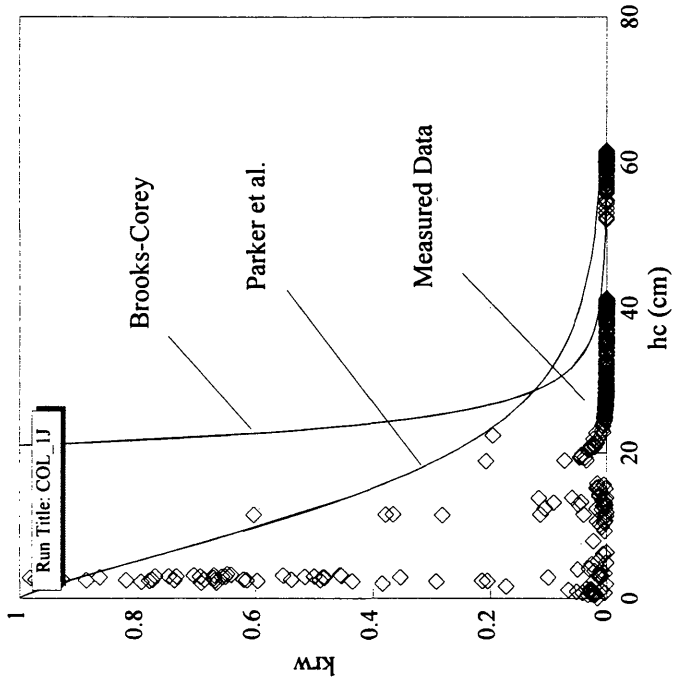






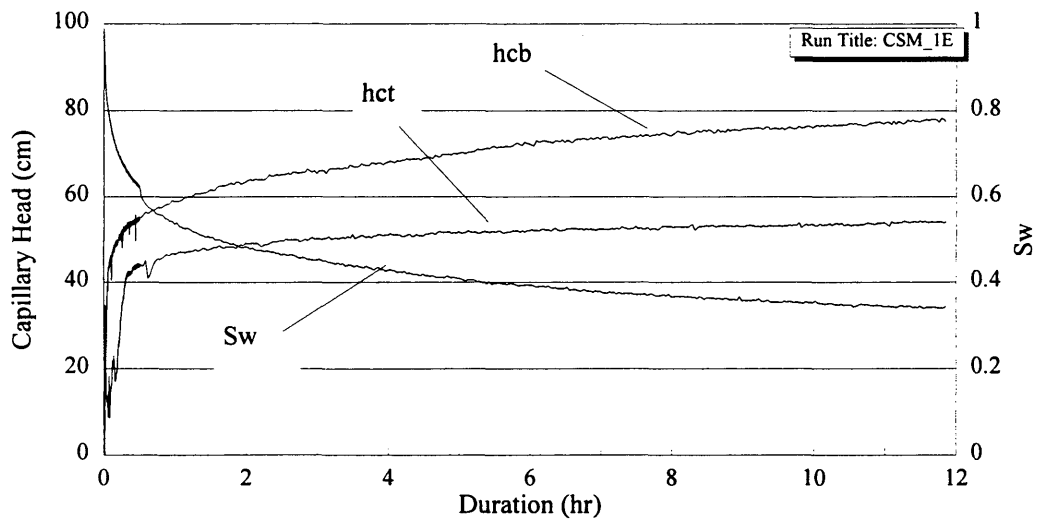
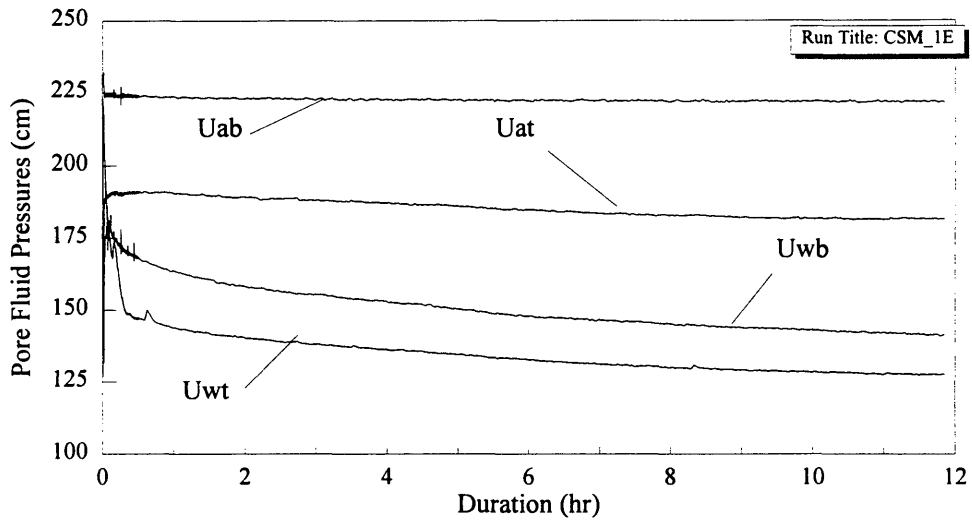


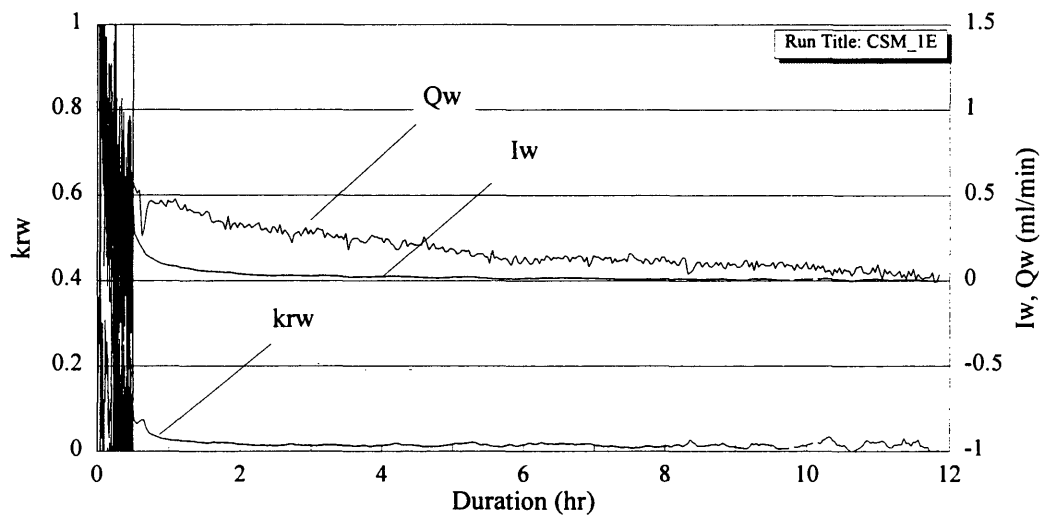
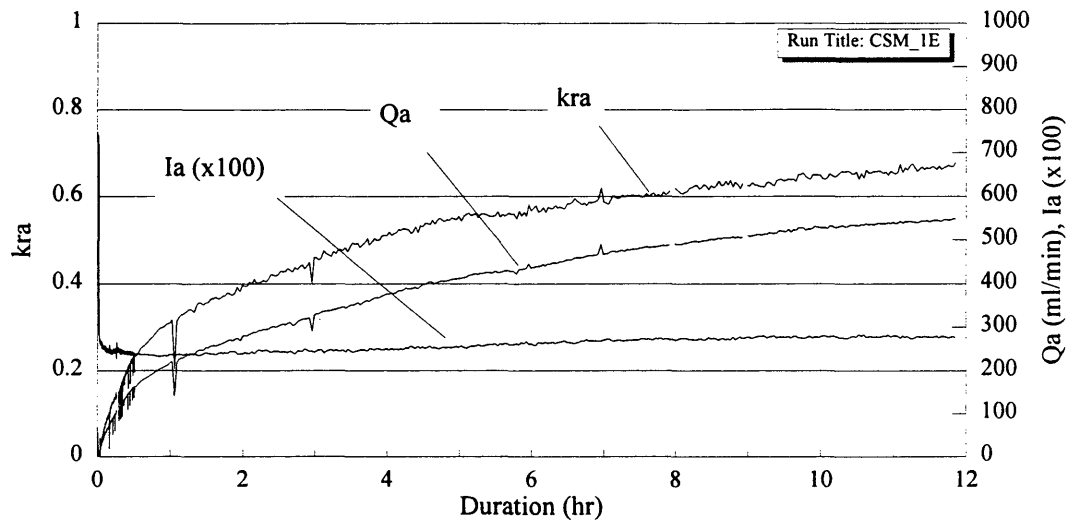


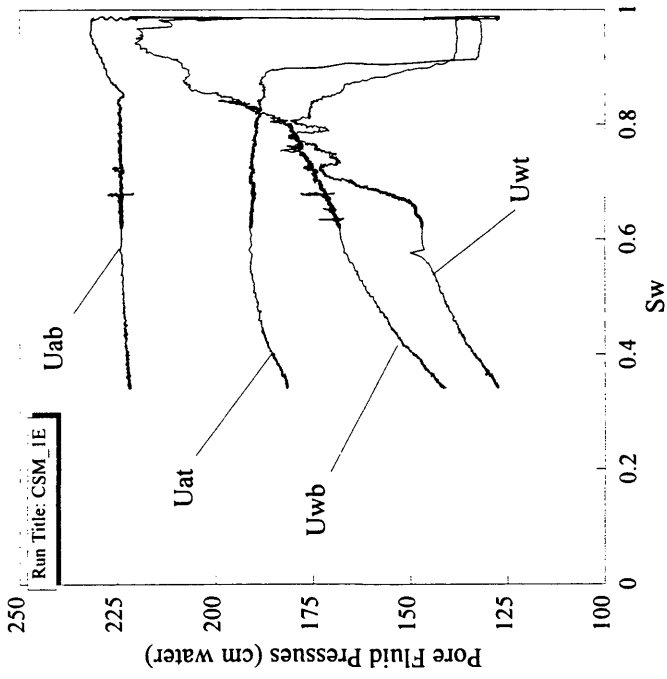
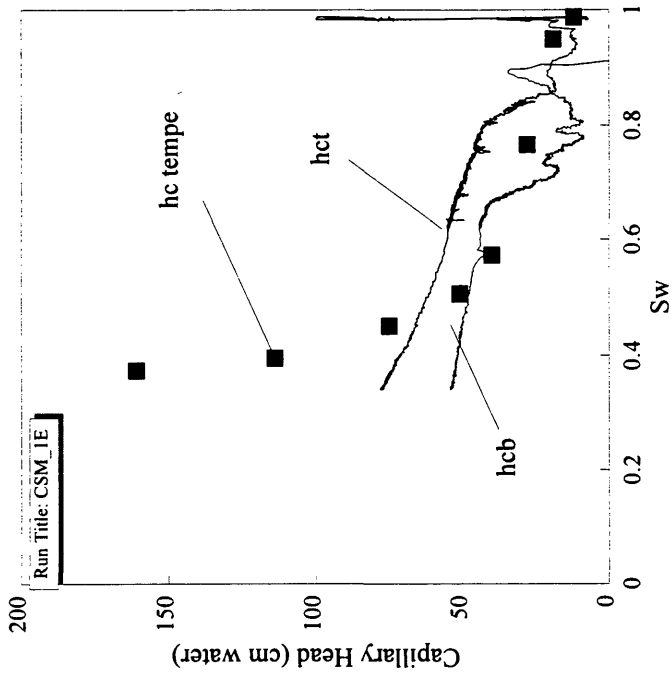


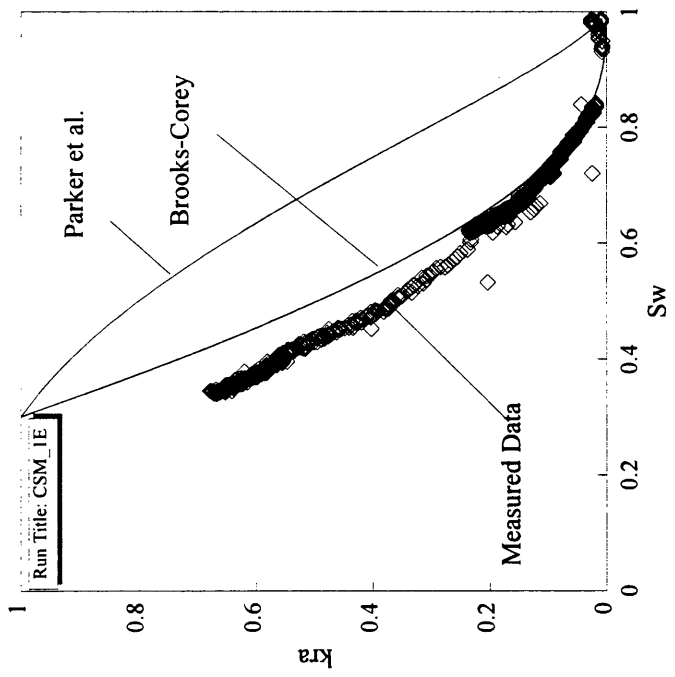
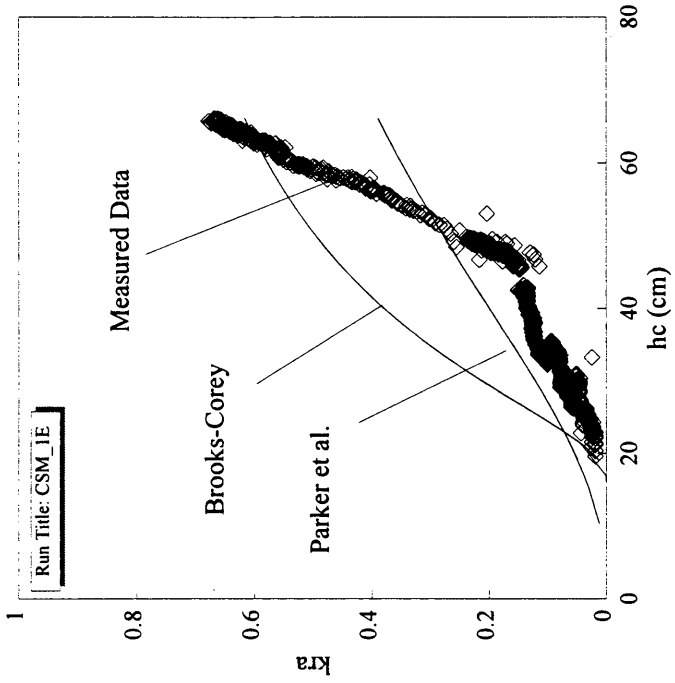
APPENDIX D4

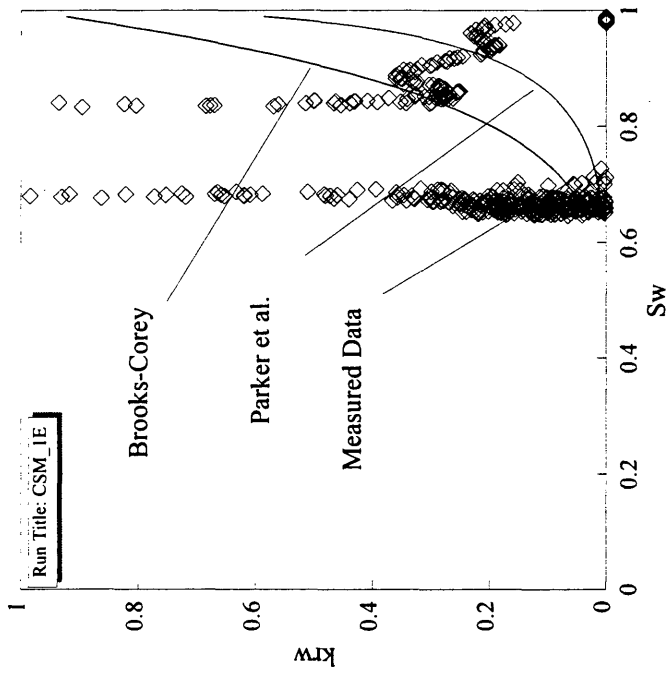
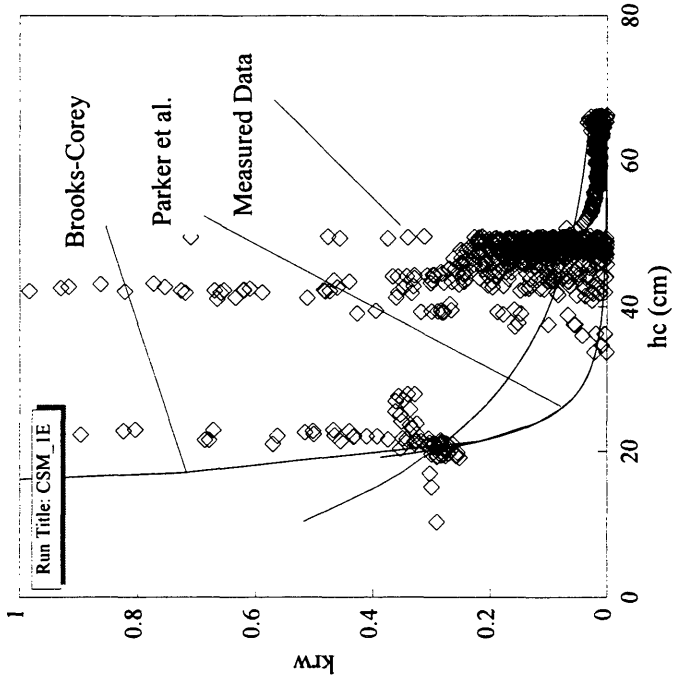
Displacement Experiment Data
Sample CSM

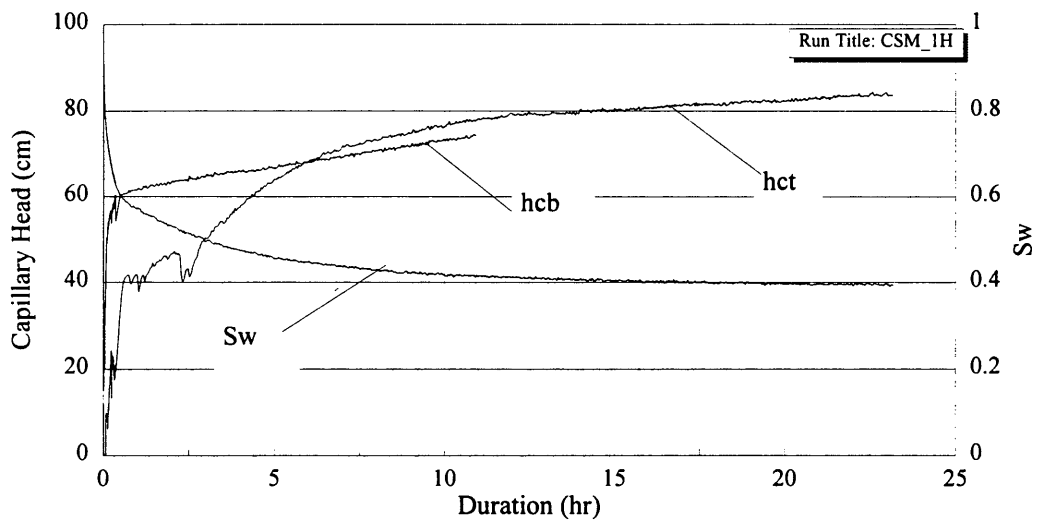
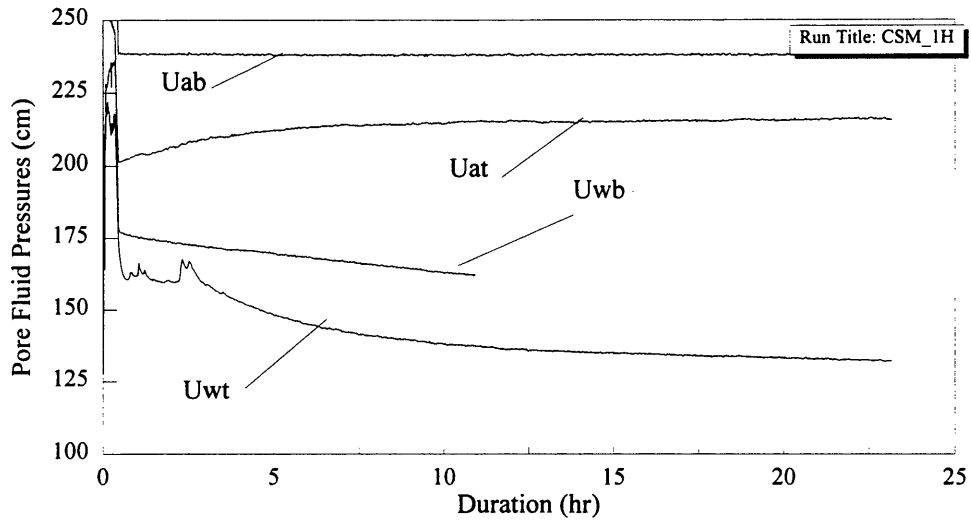


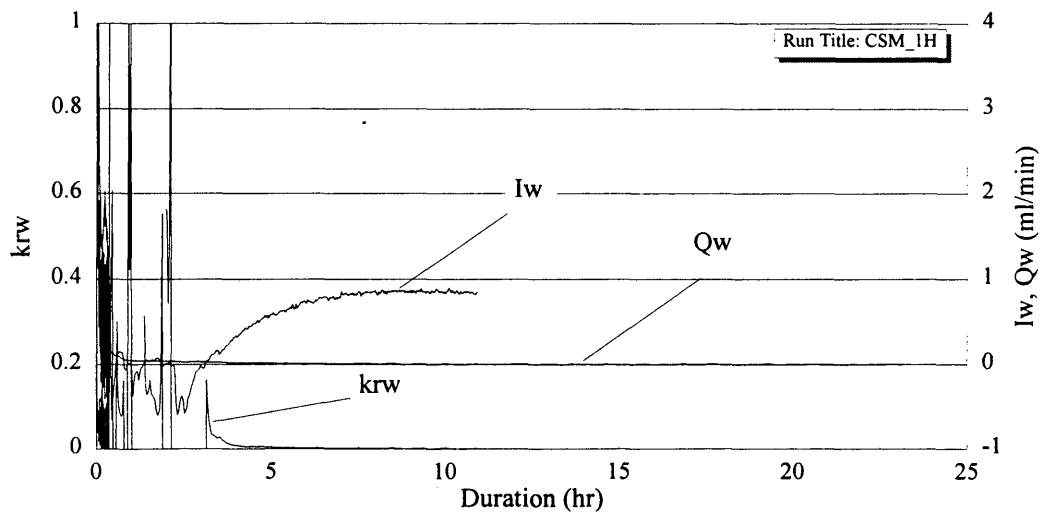
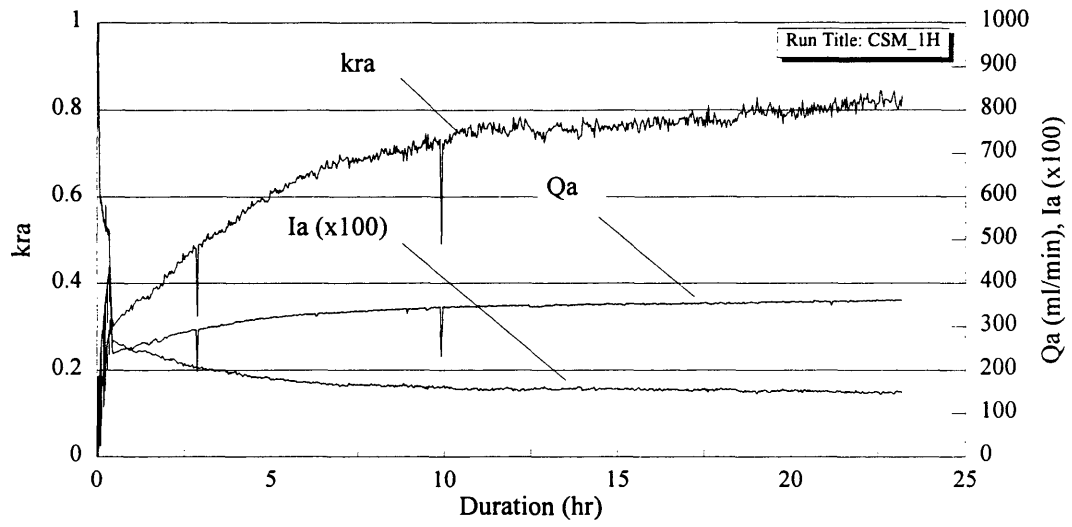


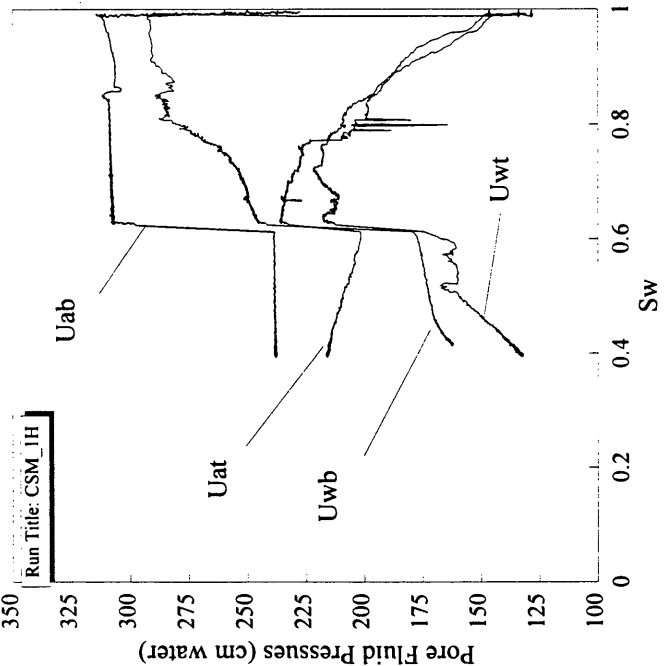
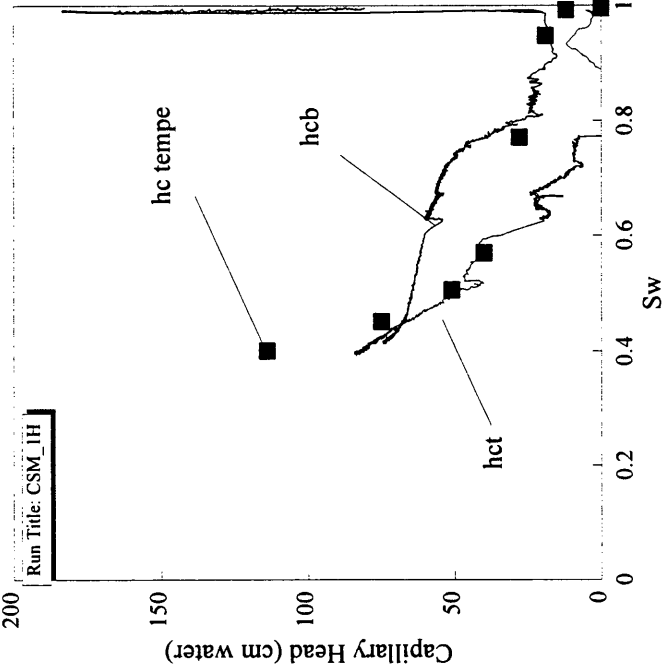


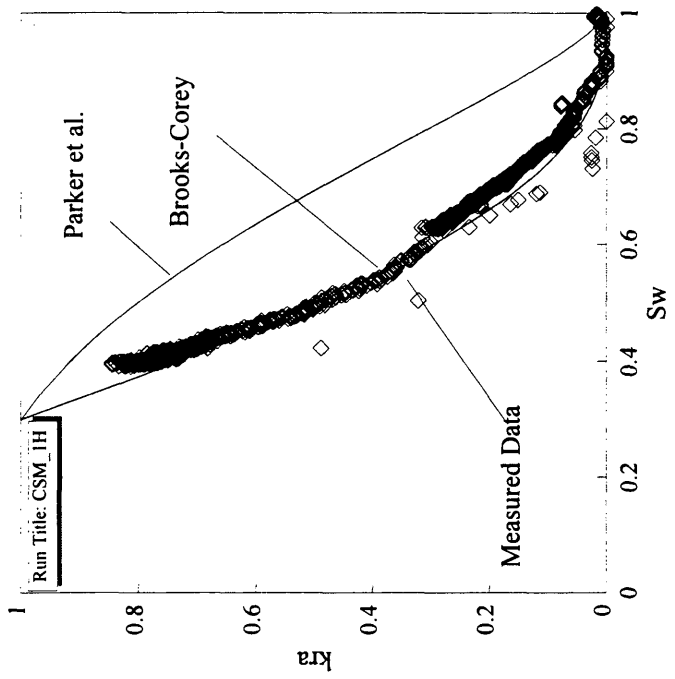
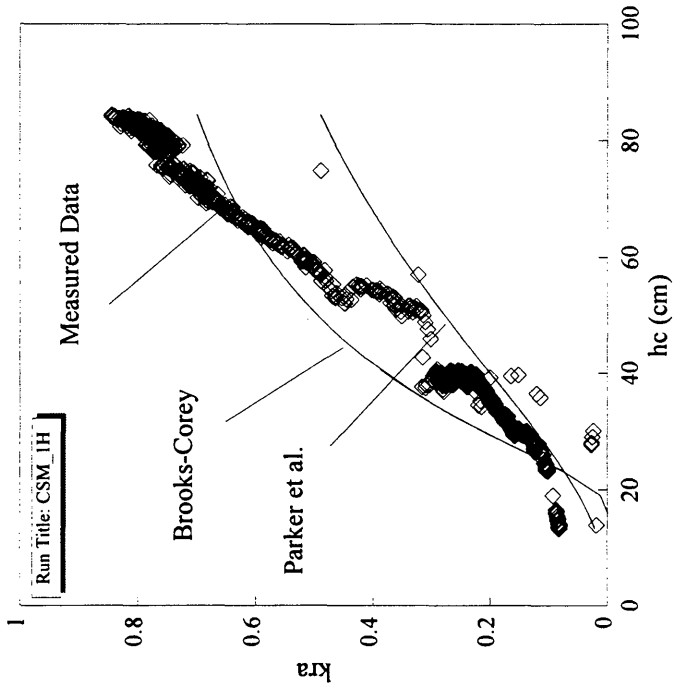


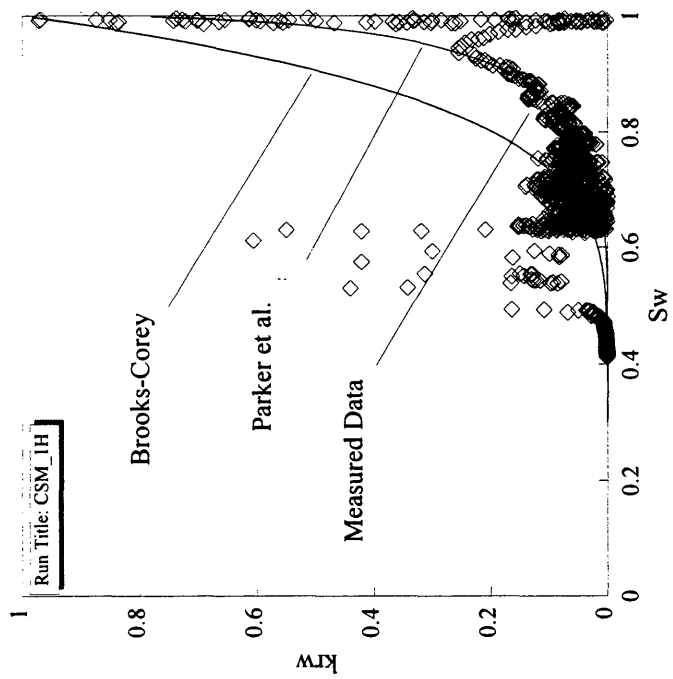
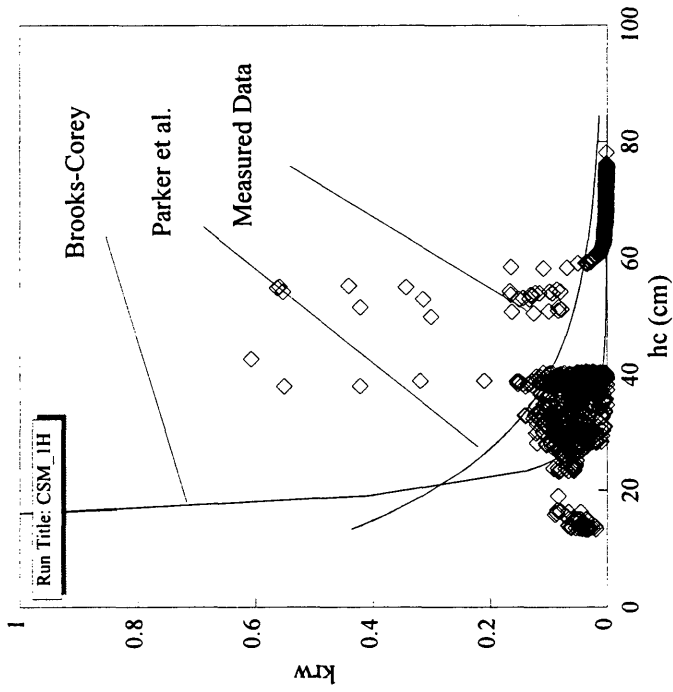






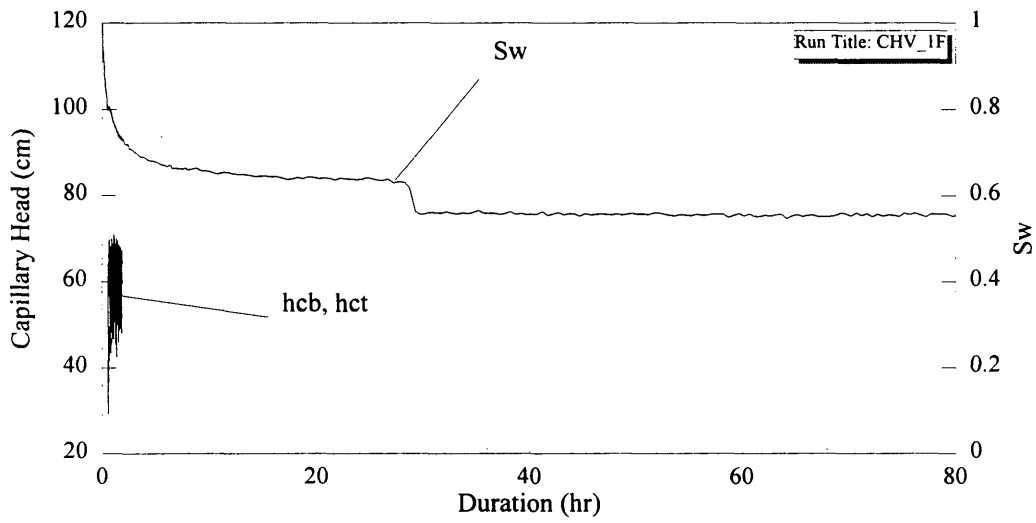
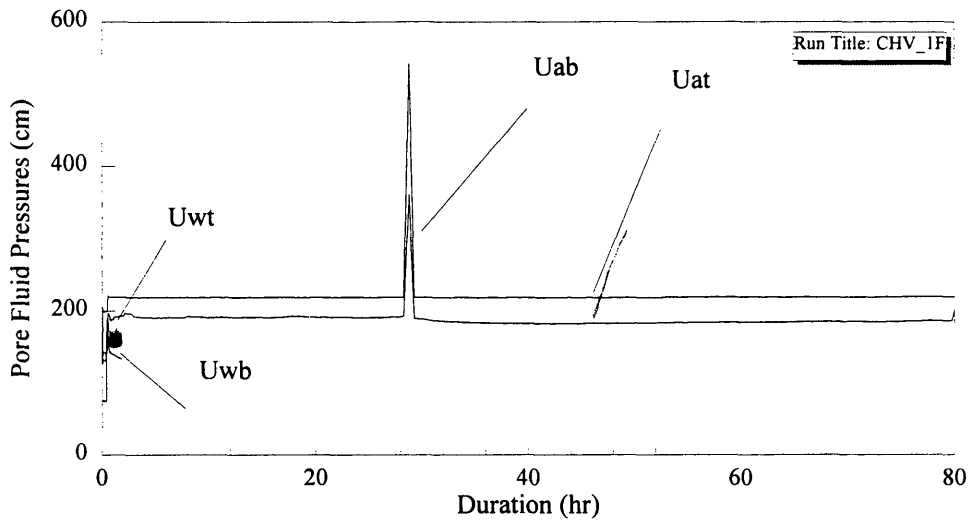


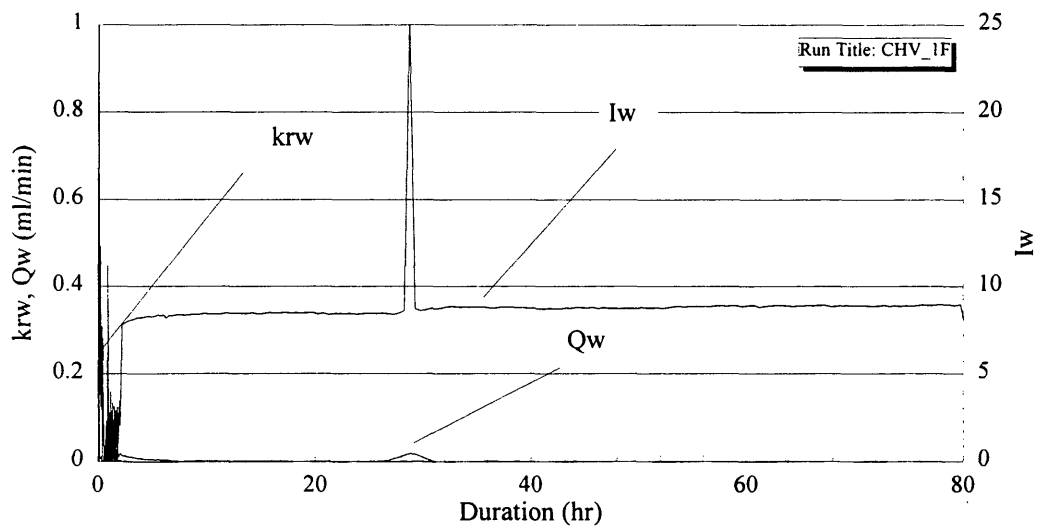
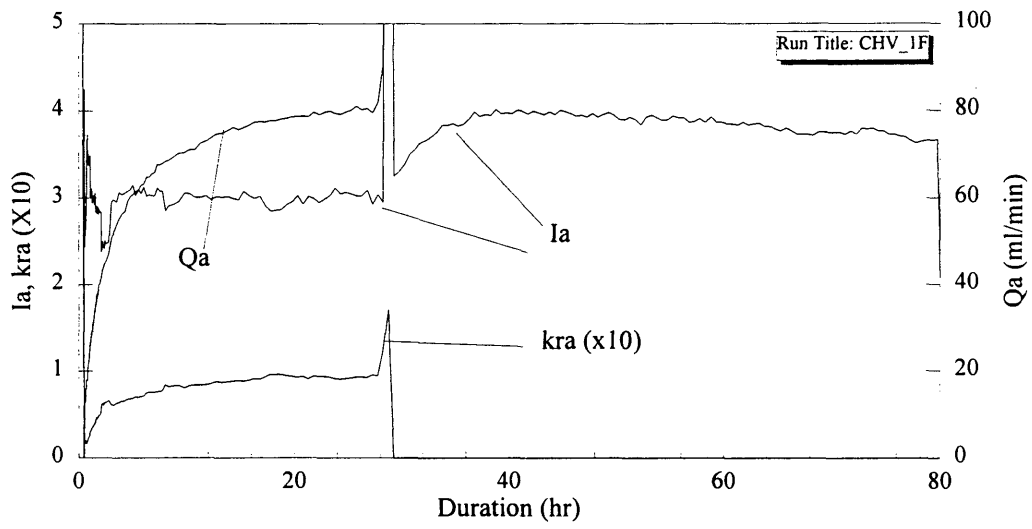


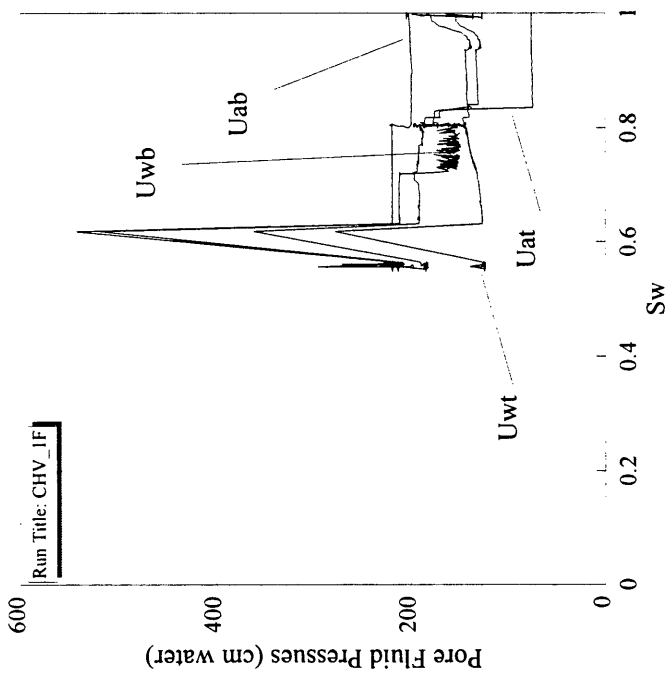
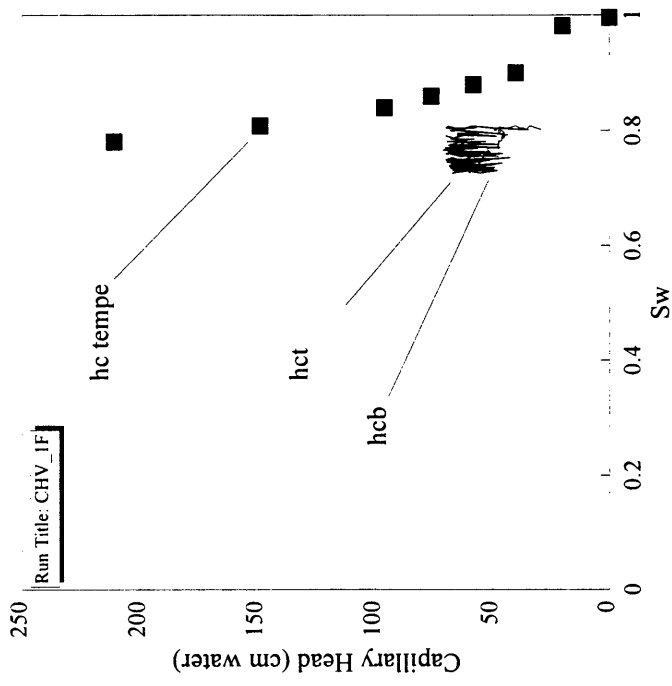


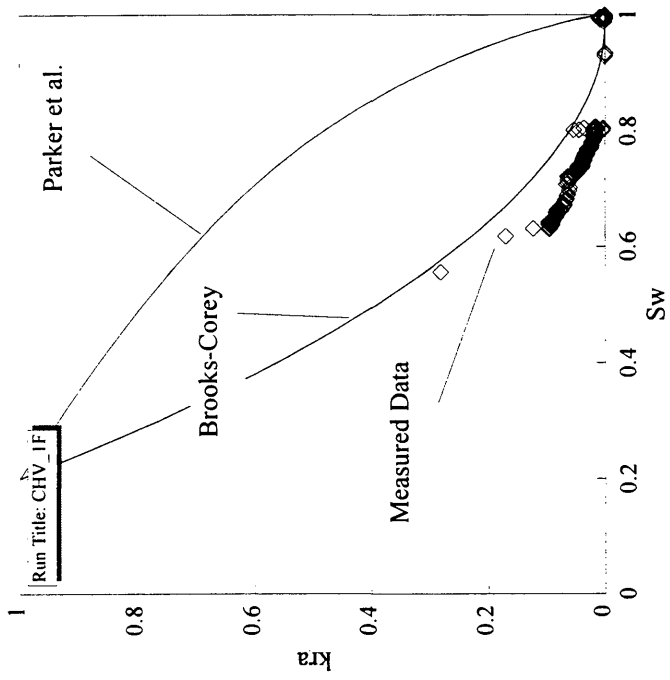
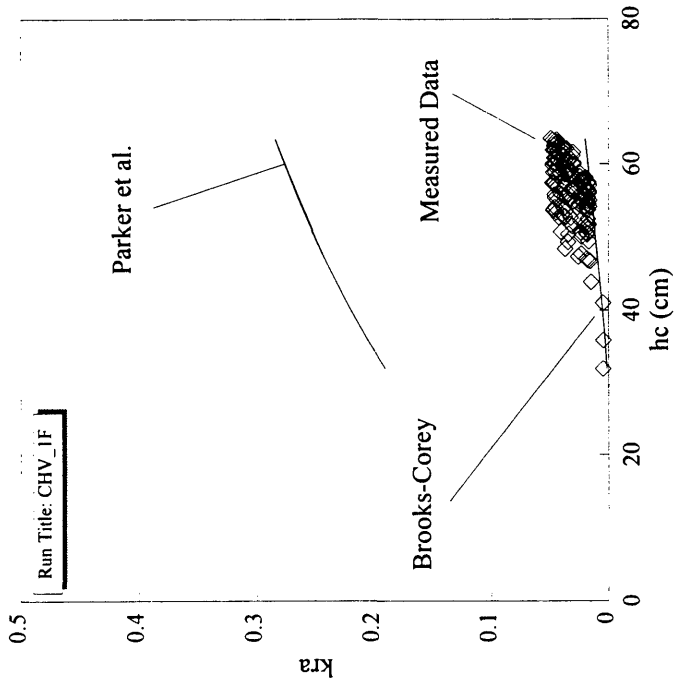
APPENDIX D5

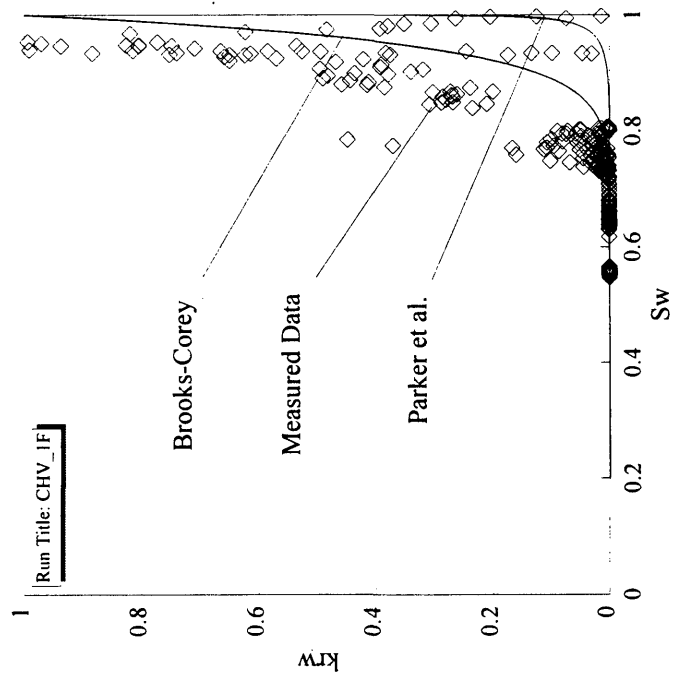
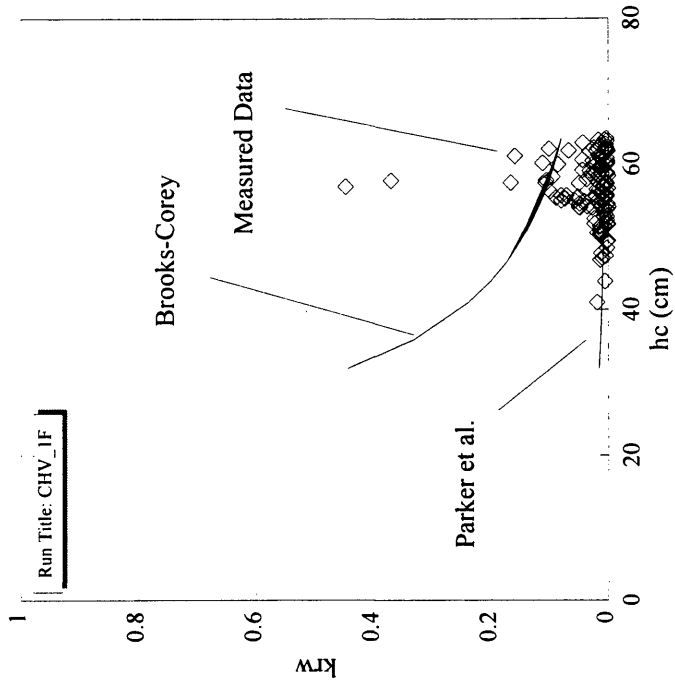
Displacement Experiment Data
Sample CHV

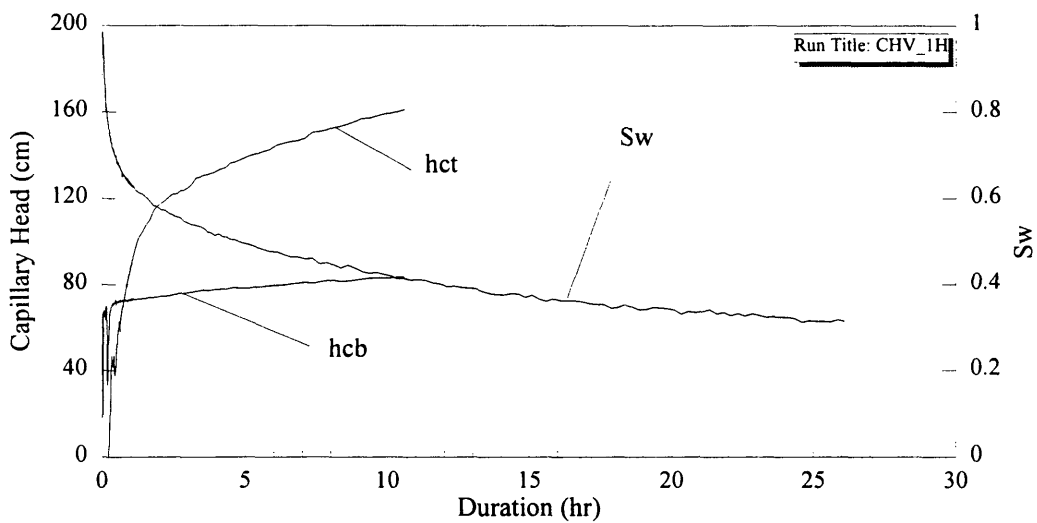
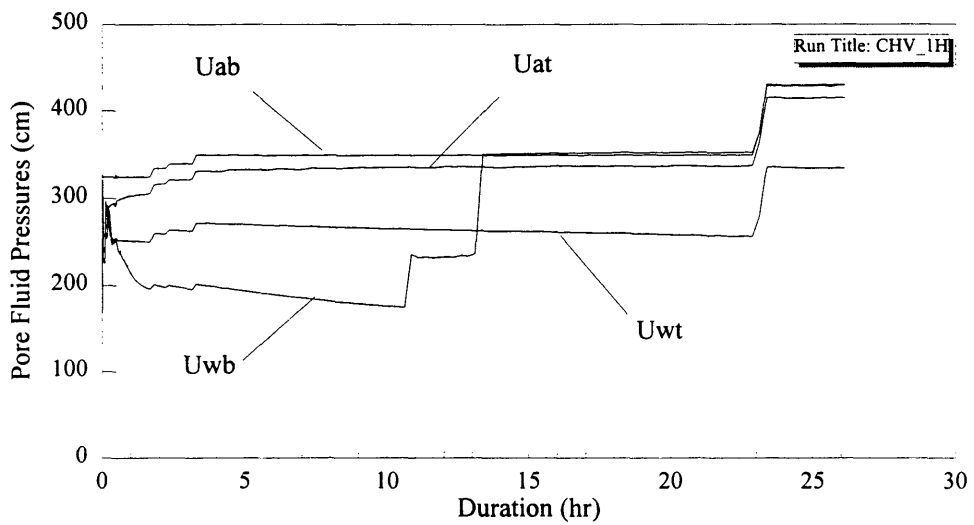


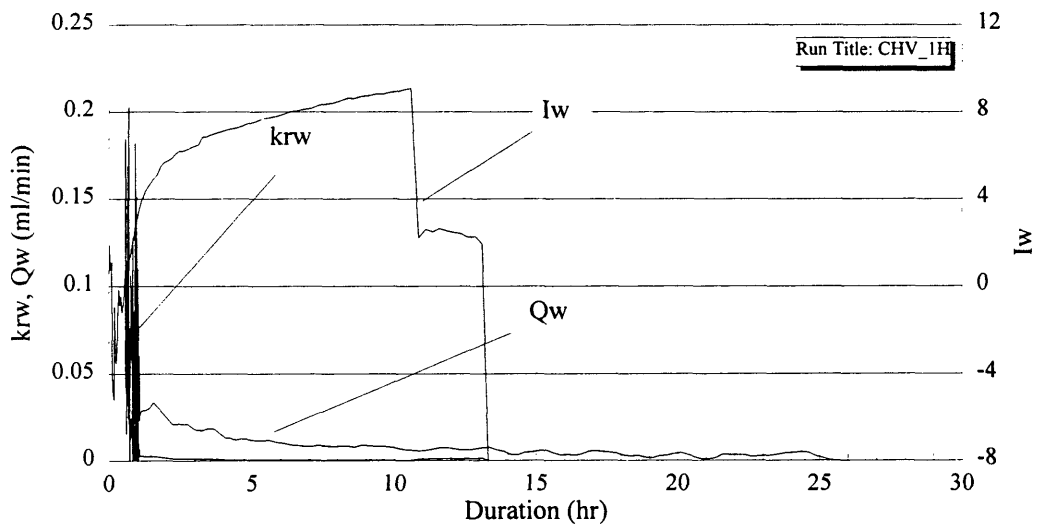
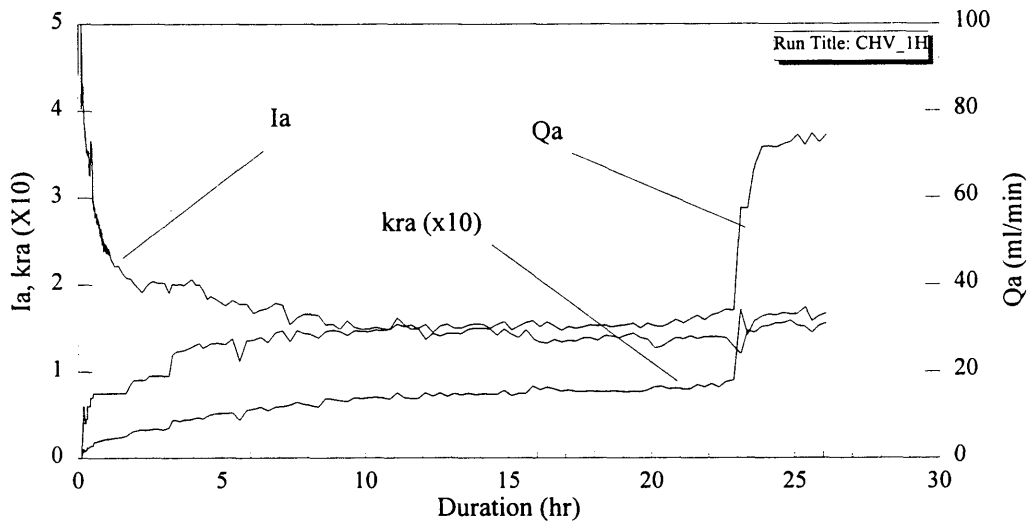


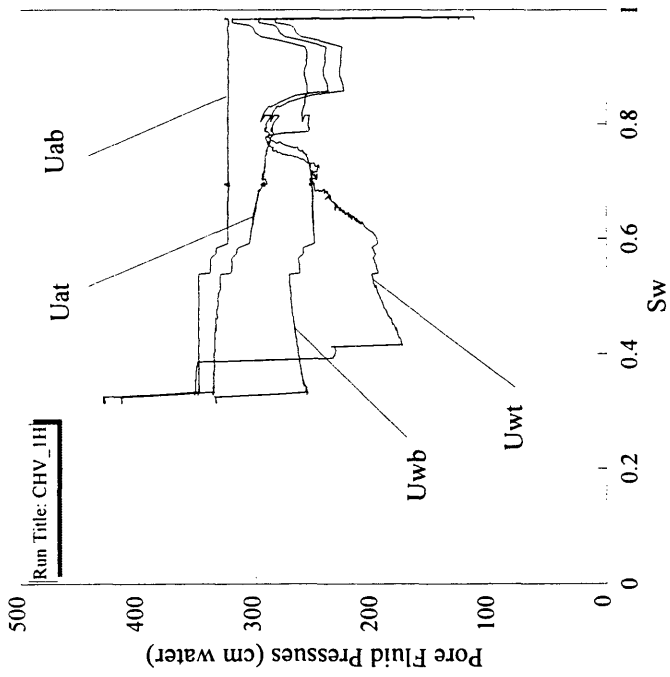
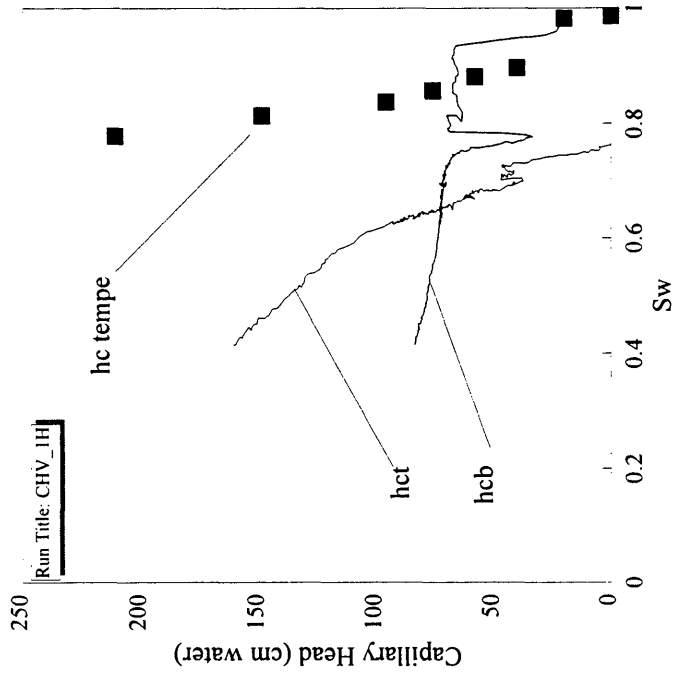


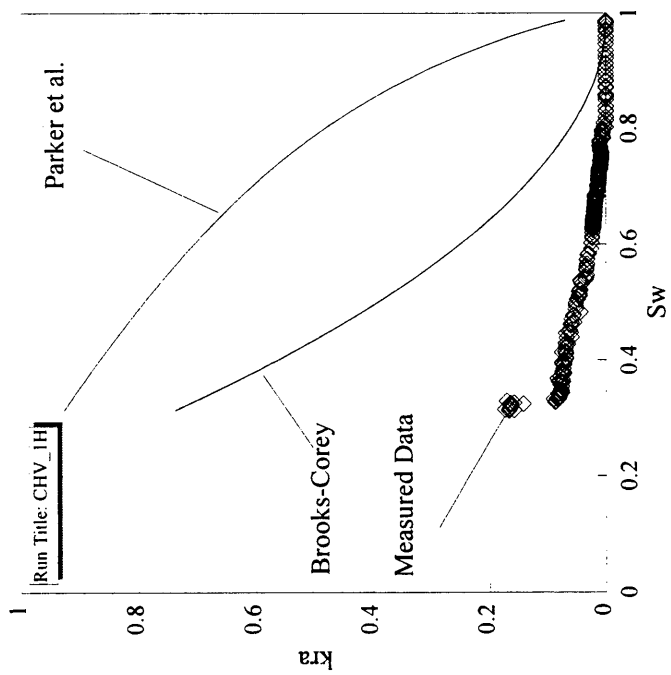
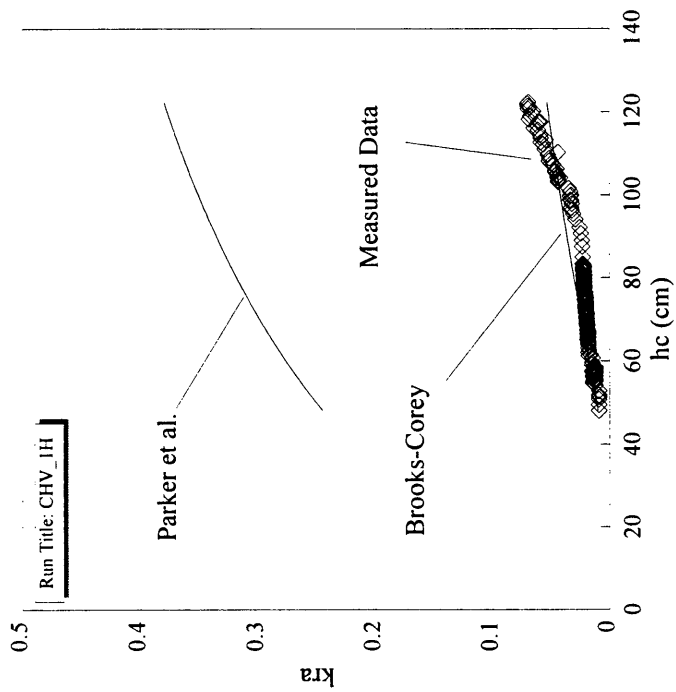


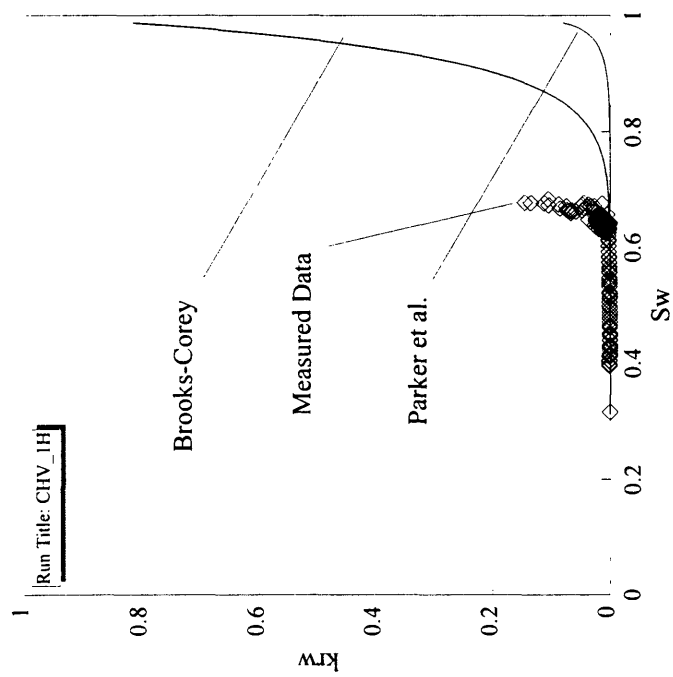
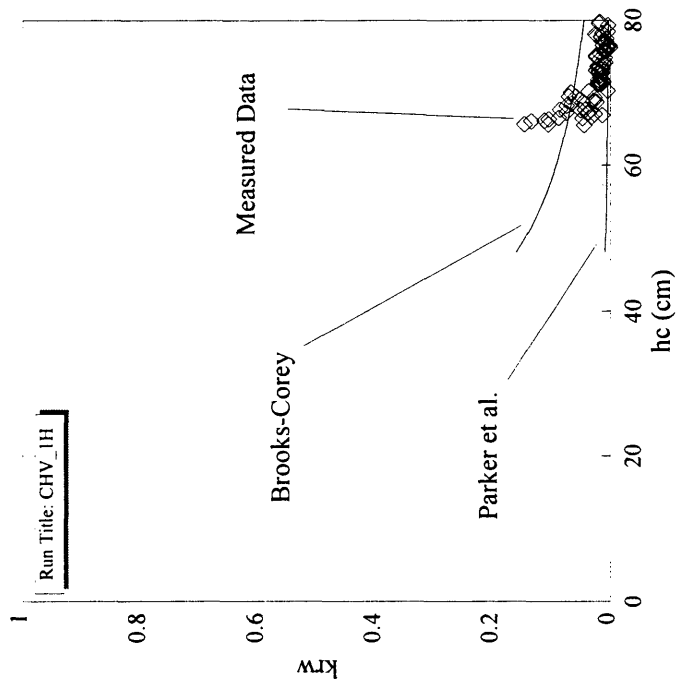


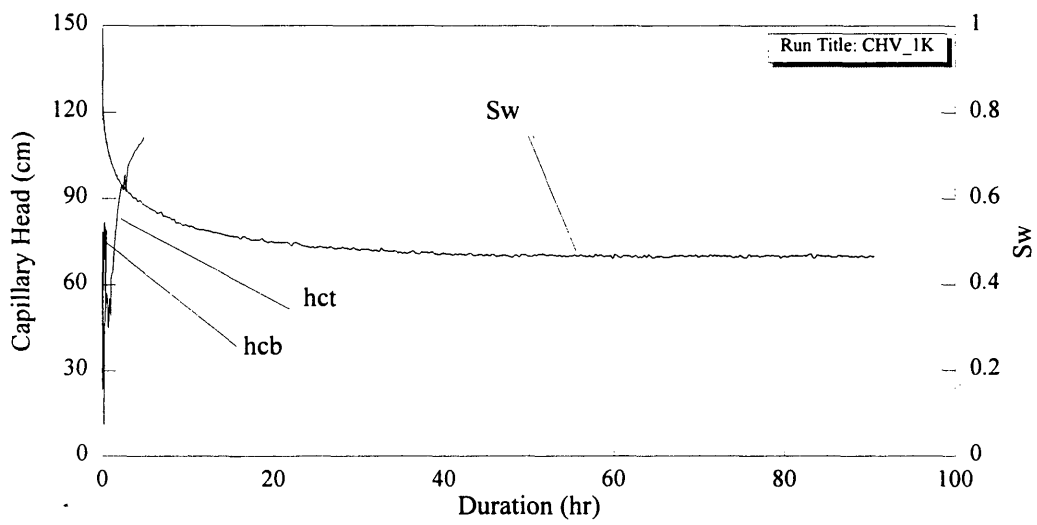
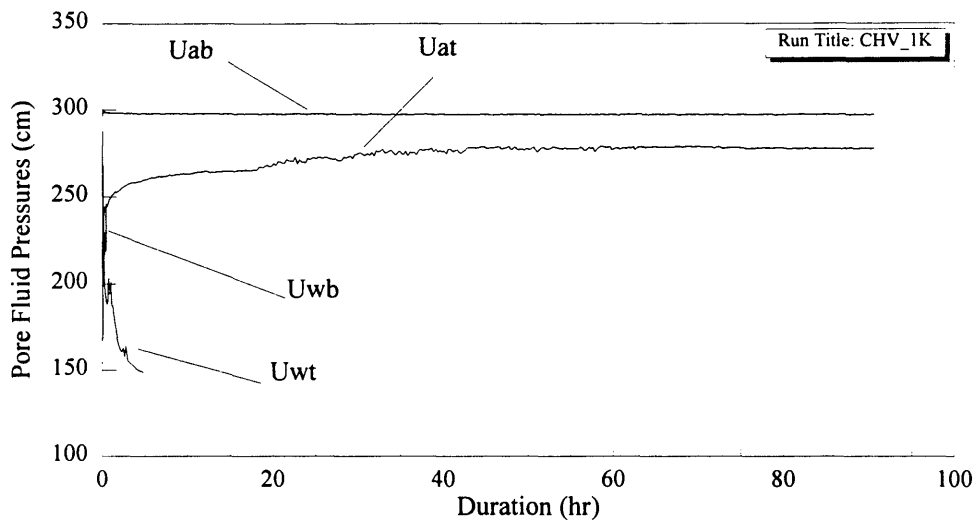


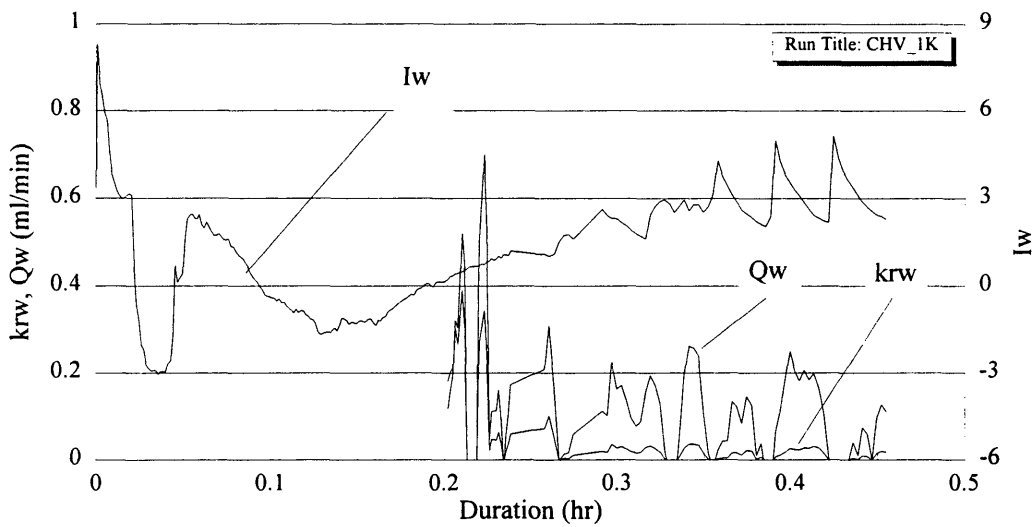
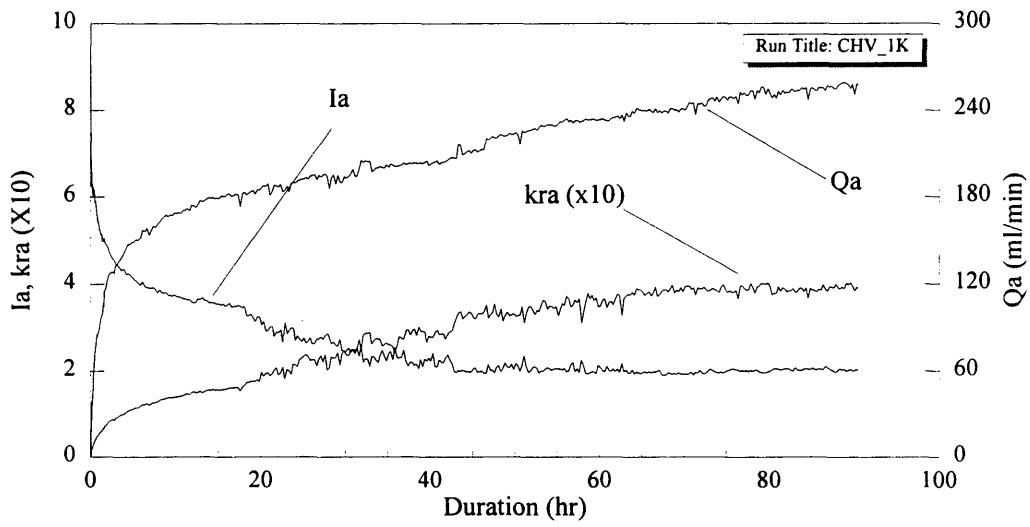


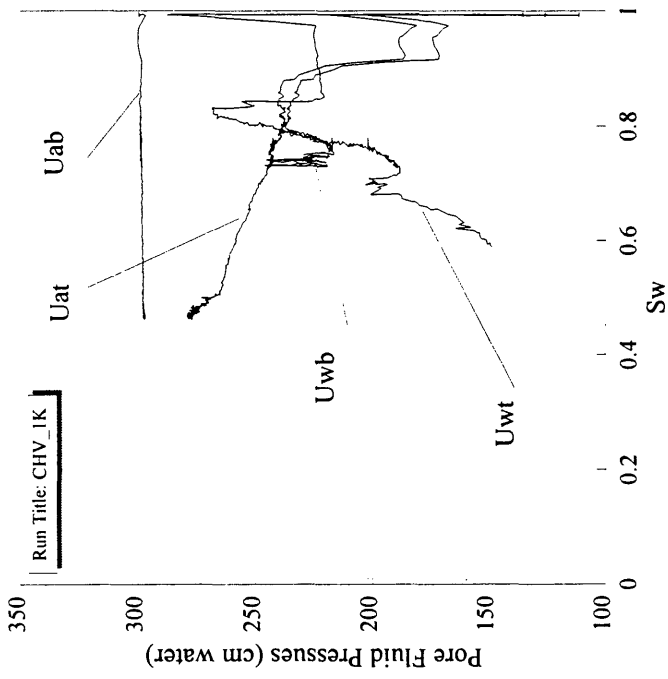
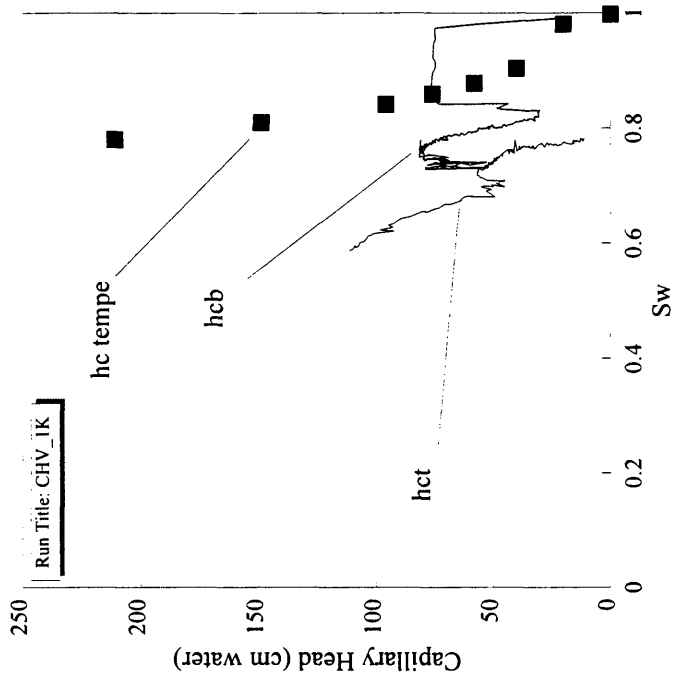


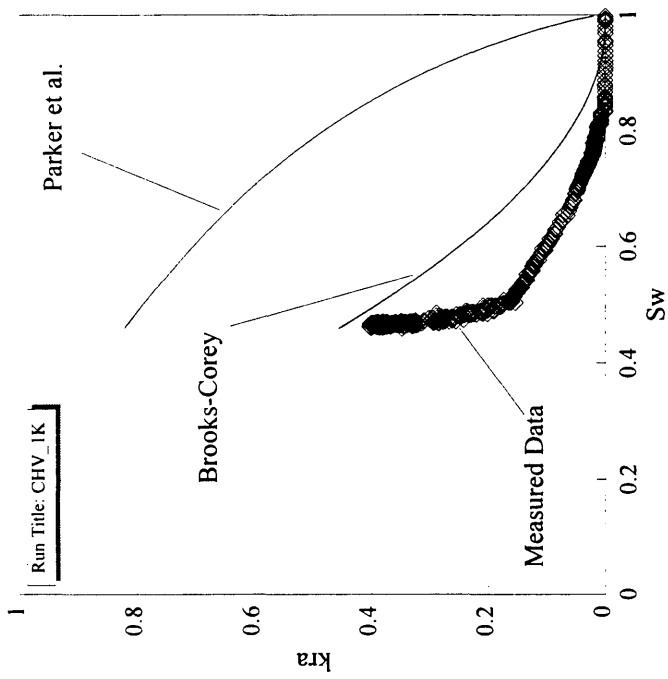
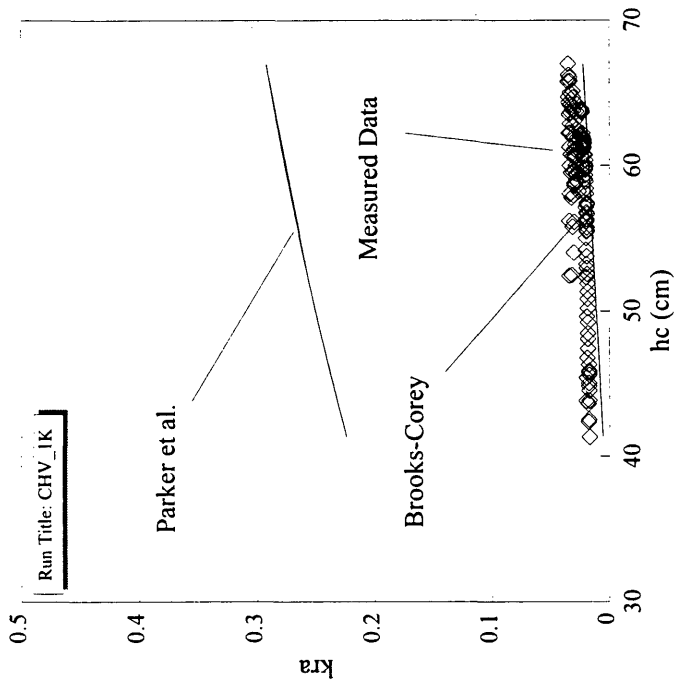


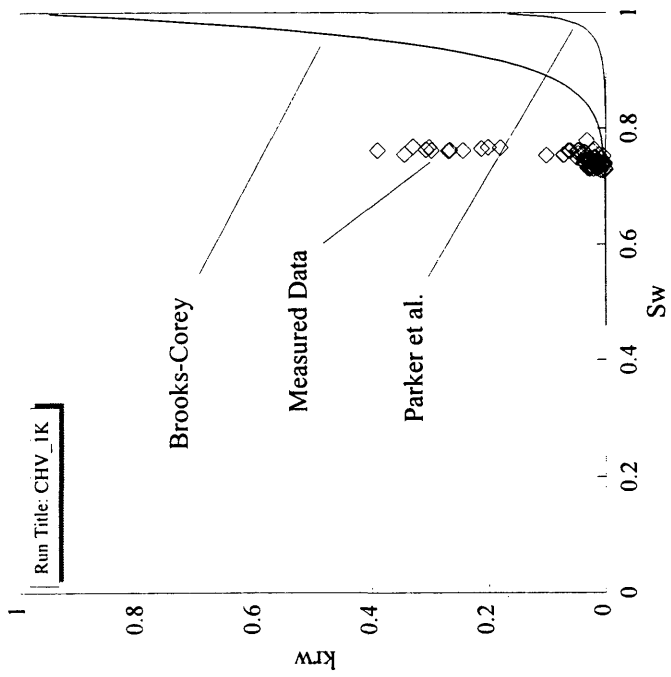
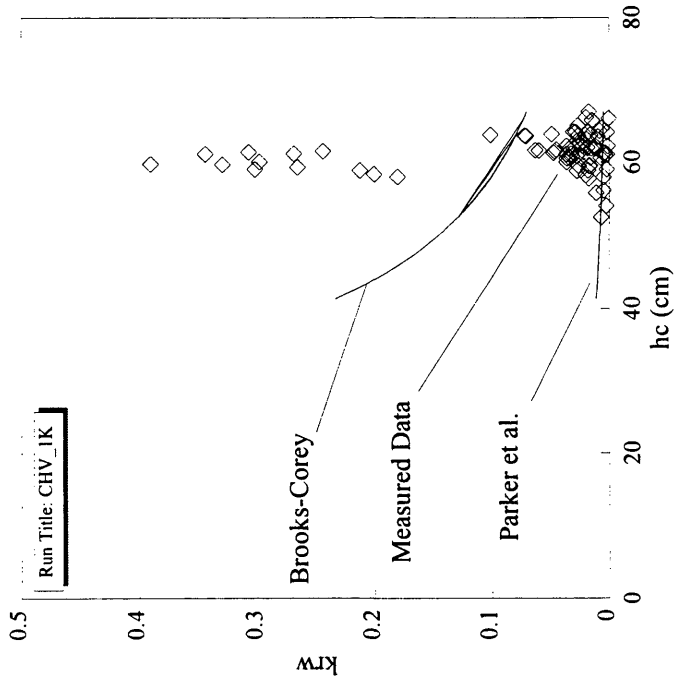












APPENDIX E

Error Analysis of Fluid Non-Uniformity

Run Title: FLO_2P		lambda =	1.2	Sr =	0.32	Hd =	20	Modeled Parameters				Results			
Measured Test Data		hct	hcb	P	Top Sw	Base Sw	Bulk Sw	Bulk kra	kra(Sw)	% error	UEB kra	BC kra			
0.0742	0.800	20.95	27.18	0.5	0.95	0.69	0.849	0.01	0.02	-58.5%	0.08	0.05			
0.1036	0.778	23.84	28.61	0.5	0.81	0.65	0.7992	0.05	0.05	-10.0%	0.06	0.07			
0.1211	0.769	28.44	28.66	0.5	0.66	0.65	0.763	0.08	0.08	-0.0%	0.05	0.08			
0.1542	0.757	30.68	28.52	1.2	0.60	0.65	0.7437	0.10	0.10	-0.9%	0.07	0.09			
0.1803	0.745	33.31	29.64	1.2	0.54	0.62	0.7136	0.13	0.14	-1.6%	0.08	0.10			
0.295	0.697	34.89	30.4	1.2	0.51	0.61	0.6969	0.15	0.16	-1.8%	0.16	0.16			
0.4308	0.655	36.27	31.06	1.2	0.49	0.59	0.6835	0.17	0.18	-1.9%	0.23	0.22			
0.5992	0.615	36.8	32.37	1.2	0.48	0.56	0.6716	0.19	0.19	-1.1%	0.25	0.29			
0.6897	0.568	34.96	32.27	1.2	0.51	0.56	0.6837	0.17	0.18	-0.5%	0.27	0.38			
0.8678	0.544	36.6	32.1	1.2	0.48	0.57	0.6745	0.19	0.19	-1.2%	0.31	0.43			
1.2344	0.507	37.72	33.1	1.5	0.47	0.55	0.6589	0.21	0.21	-1.1%	0.37	0.51			
1.7678	0.455	38	33.89	1.5	0.46	0.53	0.6531	0.22	0.22	-0.8%	0.40	0.63			
2.8011	0.419	36.36	34.15	1.5	0.49	0.53	0.6621	0.21	0.21	-0.2%	0.44	0.73			
3.2011	0.391	37.55	35.34	1.5	0.47	0.51	0.6488	0.23	0.23	-0.2%	0.47	0.80			

Run Title: COR_3e		lambda	1.2	Sr =	0.01	Hd =	20						
Measured Test Data		Modeled Parameters						Results					
duration	Sw	kra	hct	hcb	P	Top Sw	Base S	Bulk S	Bulk kr	kra(Sw)	% error	UEB kr	BC kra
0.659	0.793	0.017	25.76	25.57	1.2	0.74	0.74	0.744	0.04	0.04	-0.03%	0.02	0.02
0.809	0.765	0.017	27.08	30.01	1.2	0.70	0.61	0.662	0.08	0.08	-2.42%	0.02	0.03
0.951	0.742	0.017	28.7	31.04	1.2	0.65	0.59	0.626	0.10	0.10	-1.02%	0.02	0.04
1.118	0.714	0.017	30.17	32.13	1.2	0.61	0.57	0.595	0.13	0.13	-0.50%	0.02	0.05
1.476	0.655	0.034	34.45	31.86	1.2	0.52	0.57	0.548	0.17	0.17	-0.53%	0.03	0.08
1.81	0.604	0.034	38.42	33.66	1.2	0.46	0.54	0.497	0.22	0.22	-0.98%	0.04	0.12
2.143	0.551	0.034	42.83	34.43	1.2	0.40	0.52	0.46	0.26	0.26	-1.95%	0.04	0.16
2.477	0.504	0.052	46.87	36.51	1.2	0.36	0.49	0.422	0.30	0.31	-1.82%	0.06	0.21
2.81	0.456	0.052	51.61	35.38	1.2	0.32	0.50	0.409	0.31	0.32	-3.70%	0.06	0.27
3.21	0.405	0.069	55.18	38.17	1.2	0.30	0.46	0.376	0.36	0.37	-2.60%	0.08	0.33
3.743	0.356	0.069	63.47	38.88	1.2	0.25	0.45	0.347	0.40	0.41	-3.45%	0.08	0.40
4.41	0.302	0.086	70.08	41.13	1.2	0.22	0.42	0.318	0.44	0.45	-3.07%	0.10	0.48
5.344	0.250	0.103	76.82	44.95	1.2	0.20	0.38	0.287	0.49	0.50	-2.23%	0.12	0.56
6.41	0.210	0.138	82.08	47.19	1.2	0.18	0.36	0.269	0.52	0.53	-1.95%	0.15	0.63
8.344	0.151	0.190	88.84	52.82	1.2	0.17	0.31	0.24	0.57	0.58	-1.23%	0.20	0.73
11.14	0.103	0.397	96.7	54.65	1.2	0.15	0.30	0.225	0.59	0.60	-1.23%	0.41	0.82
17.41	0.054	0.655	107.9	64.56	1.2	0.13	0.25	0.191	0.66	0.66	-0.63%	0.66	0.91

Run Title: CHV_1H												
Measured Test Data			lambda			Sr = 0.2			Ho = 23			
duration	Sw	kra	hct	hcb	Top Sw	Base S	Bulk S	Bulk kr	kra(Sw)	% error	UEB kr	BC kra
0.29	0.741	0.009	27.96	68.07	0.97	0.84	0.902	0.01	0.01	-42.0%	0.05	0.10
0.357	0.715	0.012	43.93	70.96	0.90	0.84	0.884	0.02	0.02	-4.8%	0.02	0.13
0.628	0.670	0.019	62.27	71.99	0.85	0.83	0.871	0.02	0.02	-0.3%	0.02	0.17
0.72	0.658	0.020	69.96	72.89	0.84	0.83	0.866	0.03	0.03	-0.0%	0.02	0.18
0.758	0.654	0.020	72.33	72.38	0.83	0.83	0.866	0.03	0.03	-0.0%	0.02	0.19
0.837	0.641	0.020	77.9	72.83	0.82	0.83	0.863	0.03	0.03	-0.0%	0.02	0.20
1.067	0.625	0.023	93.4	73.28	0.80	0.83	0.851	0.03	0.03	-0.9%	0.02	0.22
1.937	0.581	0.031	116.4	74.4	0.77	0.83	0.838	0.04	0.04	-2.6%	0.04	0.27
3.404	0.535	0.044	129.8	77.29	0.76	0.82	0.83	0.04	0.04	-3.0%	0.05	0.34
5.604	0.483	0.044	141.6	79.01	0.75	0.82	0.824	0.04	0.05	-3.5%	0.06	0.42
8.354	0.439	0.059	153.5	81.71	0.74	0.82	0.819	0.05	0.05	-3.7%	0.08	0.49
10.6	0.415	0.069	161.1	83.57	0.73	0.81	0.815	0.05	0.05	-3.8%	0.09	0.53

Run Title: COL_IH		lambda	1.6	Sr =	0.09	Hd =	21						
Measured Test Data		Modeled Parameters						Results					
duration	Sw	kra	hct	hcb	P	Top Sw	Base S	Bulk S	Bulk kr	kra(Sw)	% error	UEB kr	BC kra
0.993	0.501	0.047	22.88	23.39	0.5	0.87	0.84	0.865	0.01	0.01	-1.4%	0.05	0.25
1.993	0.465	0.060	24.45	23.74	1.2	0.78	0.82	0.819	0.02	0.02	-1.8%	0.07	0.30
2.993	0.440	0.063	27	24.03	1.2	0.67	0.81	0.755	0.03	0.04	-12.5%	0.10	0.33
5.326	0.403	0.094	28.69	27.86	1.2	0.61	0.64	0.654	0.09	0.10	-0.3%	0.09	0.39
7.326	0.377	0.104	30.26	28.59	1.2	0.56	0.61	0.619	0.12	0.12	-0.7%	0.11	0.43
10.49	0.342	0.122	34.44	29.63	1.2	0.45	0.58	0.553	0.18	0.19	-2.8%	0.14	0.49
14.99	0.330	0.135	37.39	30.34	1.2	0.40	0.56	0.516	0.22	0.23	-3.8%	0.15	0.51
20.33	0.325	0.150	39.02	31.02	1.2	0.37	0.54	0.495	0.25	0.26	-3.7%	0.17	0.52
26.83	0.330	0.215	41.31	30.6	1.2	0.34	0.55	0.484	0.26	0.27	-5.7%	0.24	0.52
37.49	0.327	0.257	44.45	33.69	1.2	0.30	0.47	0.433	0.33	0.35	-3.0%	0.27	0.52
51.66	0.325	0.242	44.72	34.71	1.2	0.30	0.45	0.423	0.35	0.36	-2.2%	0.25	0.52
56.33	0.325	0.241	44.78	35.29	1.2	0.30	0.44	0.417	0.36	0.37	-1.9%	0.25	0.52